PREDICTION OF RESERVOIR PROPERTIES OF THE N-SAND, VERMILION BLOCK 50, GULF OF MEXICO, FROM MULTIVARIATE SEISMIC ATTRIBUTES

A Dissertation

by

RASHEED ABDELKAREEM JARADAT

Submitted to the Office of Graduate Studies of
Texas A&M University
in partial fulfillment of the requirements of the degree of

DOCTOR OF PHILOSOPHY

May 2004

Major Subject: Geophysics

PREDICTION OF RESERVOIR PROPERTIES OF THE N-SAND, VERMILION BLOCK 50, GULF OF MEXICO, FROM MULTIVARIATE SEISMIC ATTRIBUTES

A Dissertation

by

RASHEED ABDELKAREEM JARADAT

Submitted to the Office of Graduate Studies of
Texas A&M University
in partial fulfillment of the requirements of the degree of

DOCTOR OF PHILOSOPHY

Approved as to style and content by:

Joel S. Watkins (Chair of Committee)	Steven L. Dorobek (Member)
John H. Spang (Member)	Richard A. Startzman (Member)
Mark E. Everett (Member)	Richard L. Carlson (Head of Department)

May 2004

Major Subject: Geophysics

ABSTRACT

Prediction of Reservoir Properties of the N-sand, Vermilion Block 50, Gulf of Mexico, from Multivariate Seismic Attributes. (May 2004)

Rasheed Abdelkareem Jaradat, B.Sc., Yarmouk University;

M.Sc., Yarmouk University

Chair of Advisory Committee: Dr. Joel S. Watkins

The quantitative estimation of reservoir properties directly from seismic data is a major goal of reservoir characterization. Integrated reservoir characterization makes use of different varieties of well and seismic data to construct detailed spatial estimates of petrophysical and fluid reservoir properties. The advantage of data integration is the generation of consistent and accurate reservoir models that can be used for reservoir optimization, management and development. This is particularly valuable in mature field settings where hydrocarbons are known to exist but their exact location, pay, lateral variations and other properties are poorly defined.

Recent approaches of reservoir characterization make use of individual seismic attributes to estimate inter-well reservoir properties. However, these attributes share a considerable amount of information among them and can lead to spurious correlations. An alternative approach is to evaluate reservoir properties using multiple seismic attributes.

This study reports the results of an investigation of the use of multivariate seismic attributes to predict lateral reservoir properties of gross thickness, net thickness, gross effective porosity, net-to-gross ratio and net reservoir porosity thickness product. This approach uses principal component analysis and principal factor analysis to transform eighteen relatively correlated original seismic attributes into a set of mutually orthogonal or independent PC's and PF's which are designated as multivariate seismic attributes.

Data from the N-sand interval of Vermilion Block 50 field, Gulf of Mexico, was used in this study. Multivariate analyses produced eighteen PC's and three PF's grid maps. A collocated cokriging geostaistical technique was used to estimate the spatial distribution of reservoir properties of eighteen wells penetrating the N-sand interval.

Reservoir property maps generated by using multivariate seismic attributes yield highly accurate predictions of reservoir properties when compared to predictions produced with original individual seismic attributes. To the contrary of the original seismic attribute results, predicted reservoir properties of the multivariate seismic attributes honor the lateral geological heterogeneities imbedded within seismic data and strongly maintain the proposed geological model of the N-sand interval.

Results suggest that multivariate seismic attribute technique can be used to predict various reservoir properties and can be applied to a wide variety of geological and geophysical settings.

This dissertation is dedicated to
my beloved wife, Dr. Anne Gharaibeh,
my sweet lovely angels, Rafeef and Abdelkareem,
my parents, AbdelKareem Jaradat and Najwah Hijazi, and
my parents in law, Dr. Ayesh Gharaibeh and Maha Gharaibeh.

ACKNOWLEDGMENTS

I wish to express my sincere gratitude to my advisor, Professor Joel S. Watkins, for his ample guidance, inspiration, friendship, and support throughout the course of this study. Special thanks also go to Professors Steven L. Dorobek, Mark E. Everett, John H. Spang and Richard A. Startzman for their cooperation, support and serving as committee members.

I would like to express my gratitude to Yarmouk University for their valuable sponsorship and providing the financial means to pursuing my degree. A word of thanks goes to the staff of the Department of Geology and Geophysics at Texas A&M University for their partial financial support and help to make this research project reach this final stage. Thanks are due to A2D Inc. for donating well log data. Their contribution represents an integral part to this study.

A similar vote of thanks and appreciation goes to all of my friends and colleagues for sharing tough and sweet moments at Texas A&M University. Special thanks, however, must be given to Dr. Ilyas Najmuddin, Dr. Eyad Masad, Mohammad Mohammad, Aslam Alomary and Mohammad Jaradat for their support and review of the manuscript.

I would like to express my sincere gratitude and thanks to my beloved wife, Dr. Anne Gharaibeh, for her endless support, patience and encouragement and for being a mother and a father to my kids during the past two years.

I would like to extend my thanks and admiration to my parents, my parents-in-law and my sisters for their invaluable support, corporation and sincere prayers. Finally, my sincere admiration goes to my beloved brother, Dr. Mohammad Jaradat, for his love, hospitality and encouragement. This dissertation would have been impossible without his assistance, care and love.

TABLE OF CONTENTS

Page

CHAPTER Page

CHAPTER Page

LIST OF TABLES

LIST OF FIGURES

Page

Page

Page

Page

Page

Page

Page

Page

Page

Page

Page

Page

Page

Page

Page

Page

Page

Page

Page

Page

CHAPTER I

INTRODUCTION

1.1 Preface

Quantitative estimation of the spatial distribution of key reservoir properties such as porosity and permeability has gained momentum in recent years. Integrating well log and seismic information provide a natural and convenient way to extend the knowledge of the reservoir properties gained at well locations to the wider field scale domain (Saggaf et al., 2003). Accordingly, such studies can provide accurate estimates of reservoir properties and also provide important information to make reservoir management decisions and development plans (Kalkomey, 1997).

The utility of seismic attributes is mainly related to their ability to be used as effective discriminators or proxies for certain reservoir properties (Taner, 2001). For example, a drop in instantaneous seismic frequency is associated with horizons immediately beneath gas-bearing reservoirs (Chen and Sidney, 1997). At present, single valued and interval averaged seismic attributes extracted from 3D seismic data are the main inputs for integrated reservoir characterization study.

Seismic attributes are not independent pieces of information but represent various ways to present a limited amount of basic information contained within seismic data (Barnes, 2001). Many attributes contain redundant information contained in other attributes. The amount of information contained in a seismic attribute, and how this information is linked to or contained in other attributes is not always clear. The use of multivariate statistics can help to understand these relations and to reduce redundancy between seismic attributes.

Principal component analysis (PCA) reduces the dimensionality of a dataset without losing much of the information contained in the variables and permits derivation

---

This dissertation follows the style and the format of the Bulletin of American Association of Petroleum Geologists (AAPG).

of a new set of multivariate seismic attributes from the original various input variables (Marcoulides and Hershberger, 1997). This method decomposes the variance of a data matrix into uncorrelated or independent orthogonal principal components (PCs), which are linear combinations of the original variables. On the other hand, principal factor analysis (PFA) determines how many meaningful principal factors (PF's) are needed to explain the amount of the shared variance among original attributes. Factor analysis produces another set of multivariate seismic attributes, which are a function of the factors responsible for the interrelations among original inputs (Marcoulides and Hershgerger, 1997).

In this study, I have investigated the use of multivariate seismic attributes in the predication of key reservoir properties, including: gross thickness, average gross effective porosity, net thickness, sand volume fraction and net reservoir porosity thickness product, rather than using the original seismic attributes. Our main goal is to reduce dimensionality and redundancy between the original seismic attributes, and to identify new attributes that can improve the correlation to well log measurements.

To test this approach, I applied it to estimate the above mentioned reservoir well log properties across the N-sand interval of the Tiger Shoal and Vermilion Block 50 (Vermilion 50) fields, Gulf Coast of Mexico. Eighteen different attributes were extracted and gridded across the interval of interest. These attributes were: arc length, biased bandwidth rating, debiased bandwidth rating, half energy, mean instantaneous frequency, mean instantaneous phase, maximum amplitude, maximum magnitude, mean amplitude, mean magnitude, mean trough amplitude, minimum amplitude, number of zero crossing, polarity ratio, root mean square (rms) amplitude, sum of amplitudes, sum of magnitudes and sum of negative amplitudes.

The results of PCA and PFA were used to calculated new multivariate seismic attribute grid maps, PC’s and PF’s. Subsequently, I investigated the relationships between each of the well log reservoir properties and the original seismic attributes and the newly created multivariate seismic attributes. Attributes indicating good correlation

were then used to estimate log reservoir properties by using collocated cokriging mapping methods.

Collocated cokriging is a geostatistical method used to integrate well log-derived reservoir properties and seismic attributes (Doyen et al., 1996). This algorithm predicts the spatial distribution of the various reservoir properties away from sparse well locations. The results include distribution and standard deviation maps for the estimated reservoir property.

1.2 Purpose of the study

The purpose of this study is to use seismic attribute technology to revisit these mature fields in order to define new hydrocarbon potentials. Recent increase in demands for energy in the United States has focused exploration of the Gulf of Mexico, this in turn has resulted in increased activity in historically producing areas of the shelf and new frontiers on the continental slope (Seni, 1997). Oil and gas production from the Tiger Shoal field dates back to the 1950's. There is a total of 103 wells, while Vermilion 50 has produced gas from 53 wells since its discovery in 1975 (Hentz and Zeng, 2003).

It is hoped that conducting a multiattribute seismic analysis for the N-sand interval, a middle-Miocene major producing interval penetrated by the wells of the Tiger Shoal and Vermilion 50 fields, new bypassed hydrocarbon reservoirs will be defined. In order to reach this goal, this study will attempt to build a comprehensive framework that integrates the geological, petrophysical and geophysical information of the study area. Conducting a multiattribute study to predict reservoir properties in areas away from well control, and maintaining the consistency of the geological and structural developed knowledge, will enhance hydrocarbon prospectivity evaluation.

1.3 Significance of the study

The integration of well data and seismic data has been a consistent aim in reservoir characterization studies. This has been increasingly important during the recent few years with a pronounced shift from frontier exploration to redevelopment of existing fields.

Johnston (1989) stated that analyses by the Bureau of Economic Geology indicate that up to 80 billion barrels (bbl) oil and 180 trillion ft^3 gas can be added to current US onshore reserves by infill drilling, extension drilling, and well recompletion, but only if this work is built on detailed geologic evaluations.

The enormous information complied over the production history of mature fields coupled with the advent and continuous technological progress in seismic exploration prompted the quest to revisit these fields. Additionally, the economics of exploration in new frontiers of the deep sea is another factor urging the need to revisit mature fields to push the limits of production and exploration within existing fields.

Siliciclastic deposits of the Miocene are currently the most productive unit in the northern Gulf of Mexico's (GOM) stratigraphic column. For the central part of GOM, Miocene deposits account for 40% of all hydrocarbon proved-reserves and more than 40% of all remaining proved reserves (Figure 1). Remaining proved reserves are the quantities of proved reserves currently estimated to be recoverable. Estimates of remaining proved reserves equal proved reserves minus cumulative production (Crawford et al., 2002).

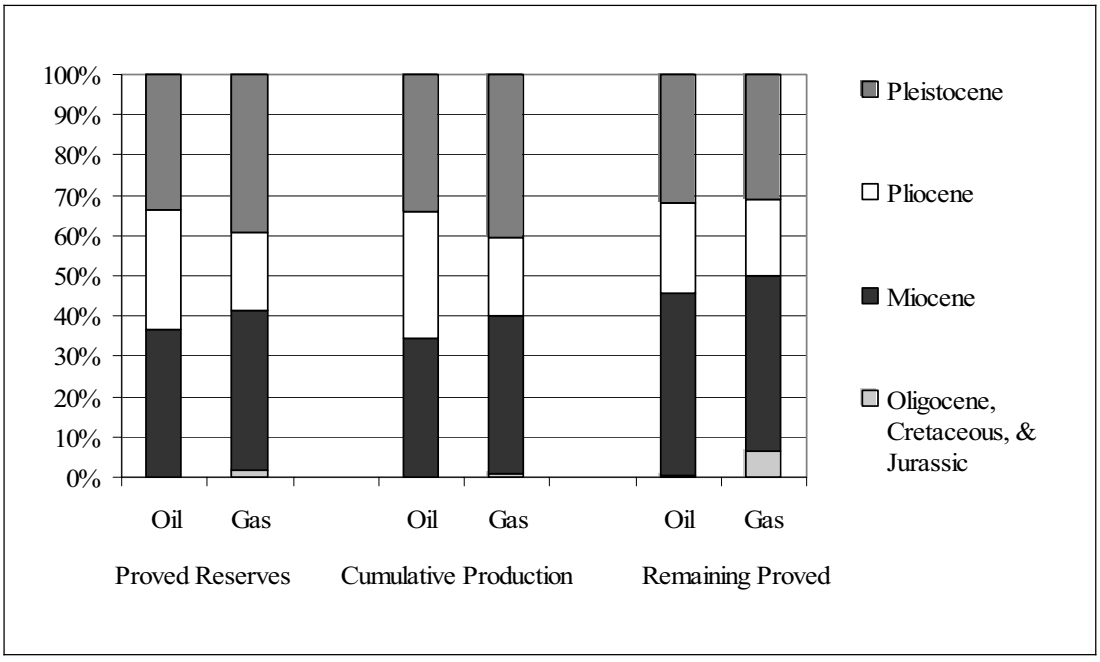

Figure 1. Distribution of reserves and production data by geologic age of central GOM region.

The N-sand interval is typical of productive sands throughout the northern Gulf of Mexico (Shelby, 1988). It is proposed to conduct this study for the N-sand's characteristic wide spatial distribution across the study area. Hydrocarbon production from this interval was reported from adjacent fields, Lighthouse Point, Mound Point and south Marsh block 236, to the fields of Tiger Shoal and Vermilion 50 of the South Marsh Island exploration area (Shelby, 1988). Earlier production within the N-sand interval was mainly restricted to structural closures associated with growth faulting. However, production from stratigraphic traps was also reported from the Upper Miocene deposits (Ray and Pearcy, 1988).

Seni (1997) believes that plays based mainly on structural reservoirs are of limited exploration use in mature areas, emphasizing that depositional/stratigraphic reservoirs remain a robust attribute, and they allow possibilities for predicting reservoirs in lightly drilled areas. Recently, Hentz and Zeng (2003) indicated that there are significant untapped hydrocarbon accumulations in nonstructural traps within the Miocene third-order lowstand systems tracts of the Tiger Shoal and Vermilion 50 fields. Accordingly, the use of N-sand interval provides a basis for the development of new hydrocarbon reserves both within the study area and in other mature and unexplored Miocene strata of the northern Gulf of Mexico shelf province.

1.4 Objectives of the study

The major objective of this study is to investigate the use of multivariate seismic attributes in order to obtain better spatial estimates of key reservoir properties of the N-sand interval of Tiger Shoal and Vermilion 50. These properties include: gross thickness, average gross effective porosity, net thickness, sand volume fraction and net reservoir porosity thickness product. In order to accomplish our main objective, the following specific objectives are to be met:

- Conduct structural and stratigraphic interpretation of the N-sand interval using 3D seismic and well log data.
- Generate multivariate attributes using multivariate statistical methods.
- Estimate key well log-derived reservoir properties across the N-sand interval.

- Provide a general workflow for use in similar reservoir localities.
- Predict and map the lateral variations of reservoir properties using collocated cokriging.

1.5 Location of the study area

The study area lays on the outer shelf off the Louisiana shore line in northern central Gulf of Mexico (Figure 2). It is located to the south of Marsh Island between 29º 15` to 29º 38` (N) and 91º 49` to 92º 17` (W). Water depths in the region range from a few feet to 20 ft.

1.6 Data base

The data base consists of 3D seismic and well data. The seismic data is from to the federal lease OCS 310 located to the south of central Louisiana shore lines. The data were poststack time migrated. CDP spacing is equal to 112.61 by 109.83 ft. The sampling rate of the seismic data is 2 ms. The deepest imaged time is 6.0 seconds of two-way travel time (TWTT). A subset of this data base is included in this study. It represented a seismic coverage of approximately 246.5 km^2, which is bounded between 1081 to 1432 in-lines and 152 to 802 cross-lines (Figure 3).

Well data consists of logs from 42 wells. Each well is given a distinctive name composed of the block number and the well number. For example, well number 4 of block 30 is named as 30-4. These wells are essentially restricted to the producing fields of Tiger Shoal and Vermilion 50. The well data includes a variety of digital well logs, ranging from electric to full suite logged wells. In addition, the well data base includes 8 wells with paleontological data (30-4, 31-3, 31-1, 31-14, 210-95, 211-6, 217-15, and 231-2), and 10 with check-shot velocity surveys.

The seismic data was donated by Texaco and well log data are donated by Texaco and A2D Inc. Velocity surveys, deviation surveys, culture data of lease block grids, and well's upper and down hole well coordinates are provided by the Mineral Management Services. Paleontological data is provided by Texaco and the Mineral Management Services (www.mms.gov).

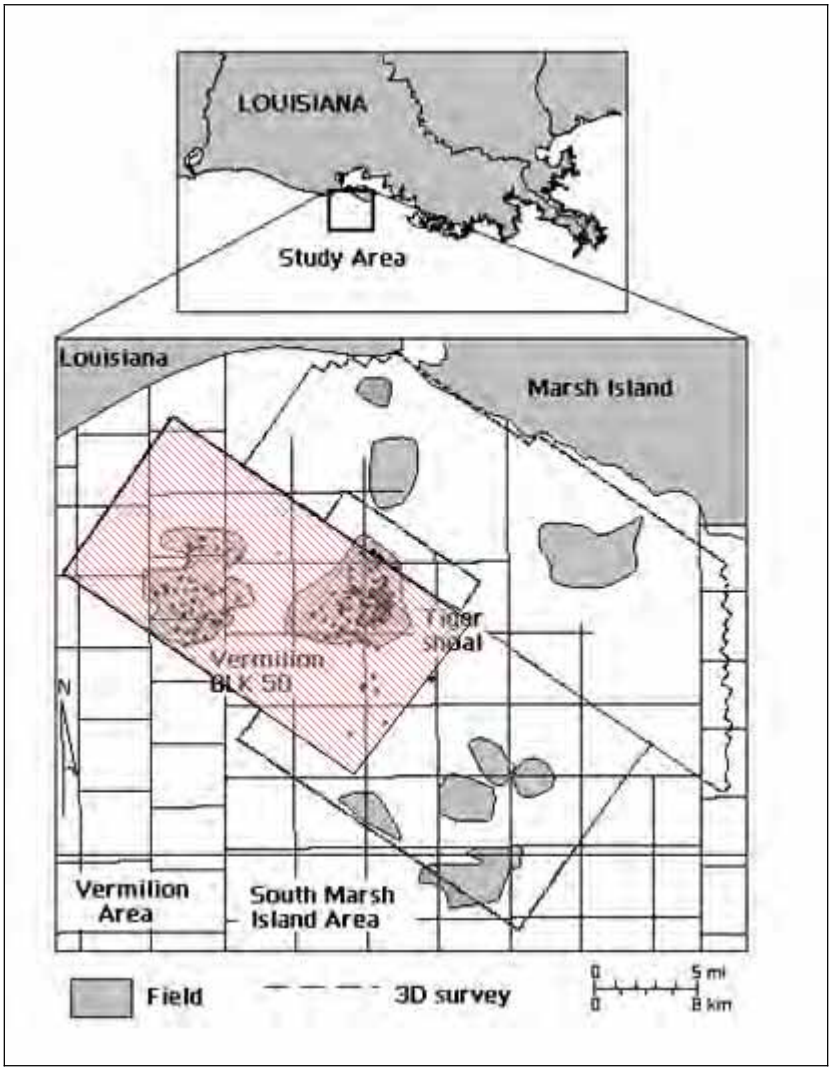

Figure 2. Location of the study area. The seafloor is less than 20 ft deep and is just a few miles south of the coasts of Louisiana. Area shaded in red denotes the portion of the seismic data used in this study (after Zeng et al., 2001).

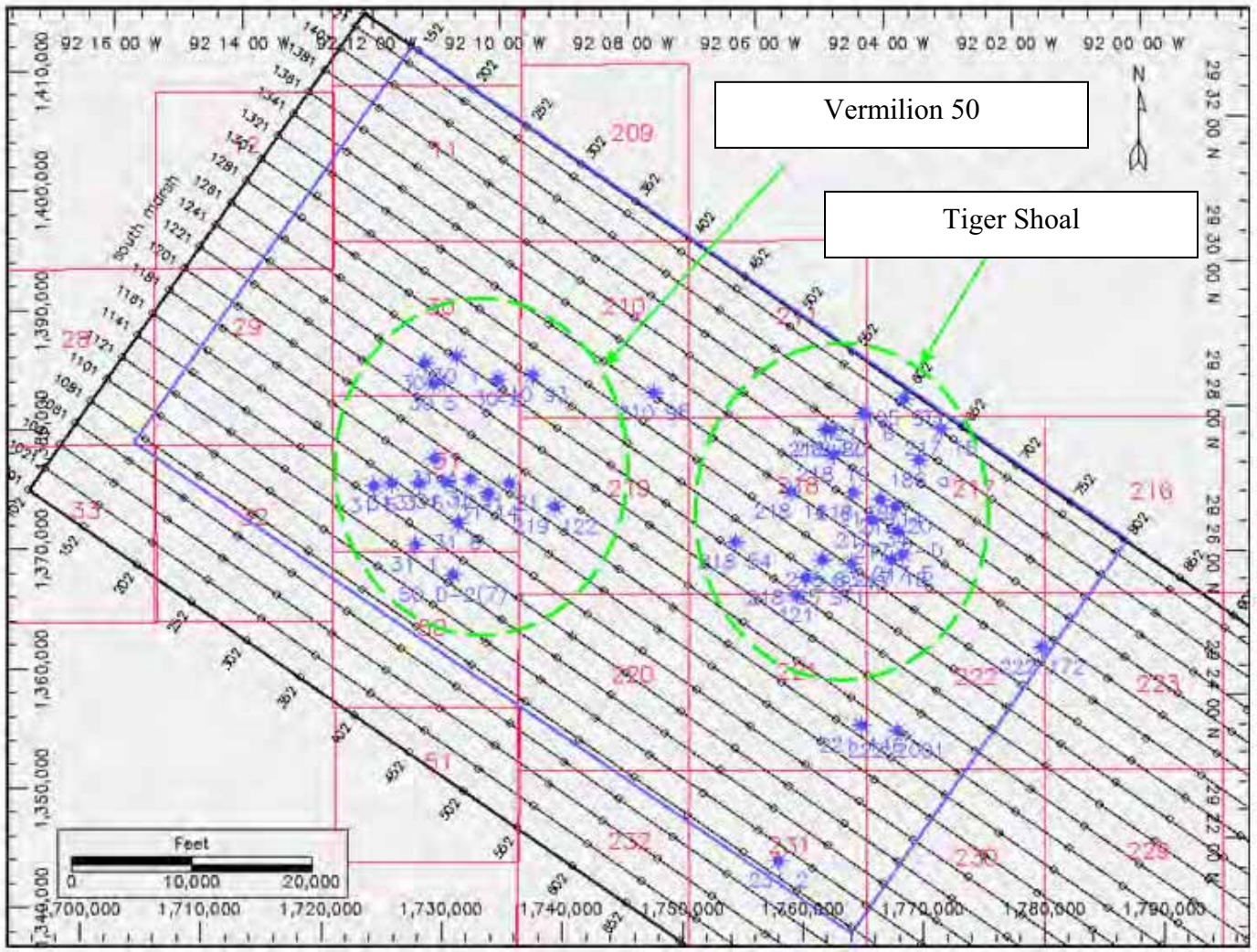

Figure 3. Seismic basemap, limits of the area of interest (shown in blue border line), lease blocks and wells of Vermilion 50 (left) and Tiger Shoal fields (right).

CHAPTER II

BACKGROUND

2.1 Seismic attribute technology

2.1.1 Introduction

Reservoir characterization is a systematic process for quantitatively describing reservoir properties. Usually, this process requires a multidisciplinary approach that integrates a wide array of data of various scales and sources.

The traditional function for using seismic data to reservoir seismology is mainly restricted to structural applications. However, recent advances in seismic technology have opened new doors for nontraditional uses of seismic data. The increasing demand for using seismic data as a predictive tool for the estimation of reservoir properties is mainly attributed to the advent of seismic attributes technology.

The general definition of seismic attributes defines any piece of information derived from seismic data as a seismic attribute. These attributes are function of some numerical measures of characteristics of the seismic data (Hart, 1999). Taner (2001) extended this definition to incorporate all possible information without any preference to their origin, “all the information obtained from seismic data, either by direct measurements or by logical or experience-based reasoning”.

Until early 1960’s, the use and the interpretation of seismic reflection data was largely a matter of mapping events and converting these events into depth maps to determine the geological structure of the subsurface (Barnes, 2001). Advances in the field of electronics and computing allowed the computation of seismic attributes, mostly derived from the basic seismic measurements of time, amplitude, frequency and attenuation (Brown, 1996). Figure 4 shows a general classification of the main seismic attributes derived from post-stack seismic data.

Seismic attributes can be divided into volume-based seismic attributes and map-based seismic attributes. Map-based attributes are considered as a major tool for a

detailed reservoir-level analysis (Brown, 2001) offering superior resolution and computational efficiency (Barnes, 2001). Not only had this shifted the interest in exploration seismology from a qualitative tool into a pure quantitative tool but also it shifted the scale of investigation from wide basin-scale studies into more detailed reservoir-scale studies.

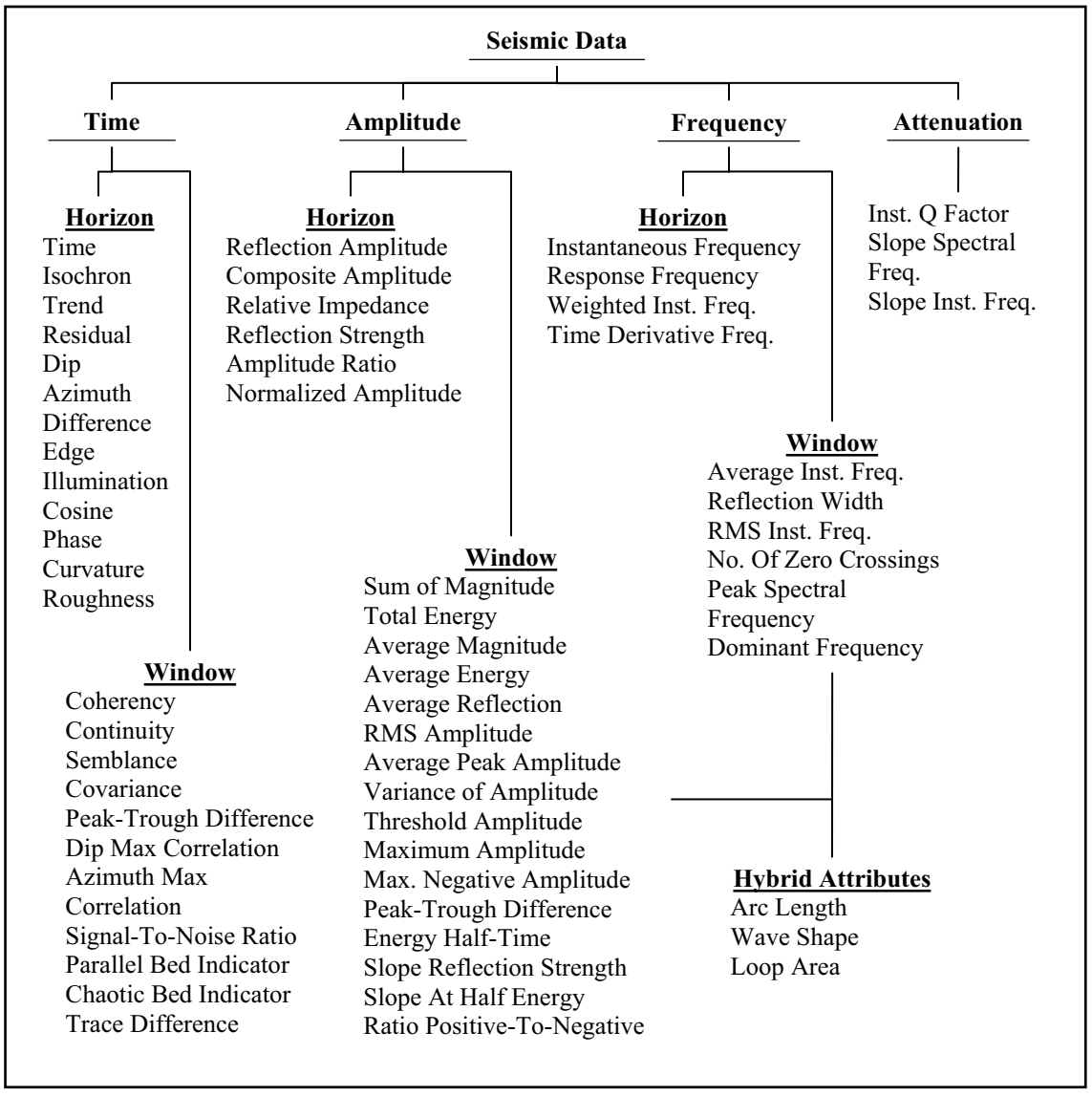

Figure 4. The various types of post-stack seismic attributes derived from the basic seismic information of time, amplitude, frequency, and attenuation. The window can be a constant time interval, a constant interval hung from one horizon, or the interval between two horizons or depth (after Brown 2001).

2.1.2 The use of seismic attributes to predict reservoir properties, a quantitative interpretation approach

The famous “bright spot” technology of the late 1960’s and early 1970’s is one of the earliest direct applications of a seismic attribute to predict reservoir properties (Barnes, 1999). Ever since, the use of seismic attributes in reservoir characterization has drawn substantial interest because it provides better insight into the internal geological characteristics of a reservoir and its derived properties.

The two primary sources of data in reservoir characterization are well and seismic data. The integration of these two data inputs has been a consistent aim in reservoir characterization studies. Owing to the dense coverage of seismic data, seismic attributes can help to interpolate between sparse well data if it is possible to build a correlation between these two data types.

In a reservoir characterization seismic attribute study, an attempt is made to establish a statistically acceptable correlation between one or a group of seismic attributes with well log measured reservoir properties. A correlation, if found, can be used to predict the behavior and the distribution of the modeled reservoir property in areas outside well control (Schultz et al., 1994; Russell et al., 1997; Hart, 1999). Several methods are available for finding the transform that best predicts the targeted reservoir property. Methods of linear and non-linear regression, geostatistics and neural networks are among popular approaches (Russell et al., 1997; Hirsche et al., 1997; Kalkomey, 1997; Gastaldi et al., 1997).

In some situations, however, correlations between seismic attributes and reservoir properties can be misleading. Spurious correlations, as apparent correlations between uncorrelated variables, can lead to erroneous predictions. Kalkomey (1997) and Hirsche et al. (1998) showed that the probability of observing spurious correlations can be quite large if the number of well measurements is small or the number of attributes is large. Russell et al. (1997) stated that extra caution should be exercised when using more than one attribute and that there is an optimum number that should not be exceeded.

In the midst of these uncertainties, it is obvious that the selection of an appropriate seismic attribute or a set of attributes is important. The degree of confidence in the proclaimed correlation model is another important point to be considered.

The following two conditions are fundamental in an integrated reservoir characterization study (Kalkomey, 1997; Hirsche et al., 1998; Hart, 1999). First, the optimum seismic attribute or attributes are those which have a physically justifiable relationship with a modeled reservoir property, especially when the number of wells is small. Second, the results of the correlation must be geologically reasonable, "geology should play a key role, Hart (1999)", where predicted results must honor the existing geological model characteristics.

The sensitivity in prediction using the optimal selection of attributes requires assessment of validity and consistency. A common practice usually involves the use of a cross-validation scheme, where each well is removed sequentially, and its property is predicted using information from the remaining wells (Gastaldi et al., 1997; Hirsche et al., 1998; Hart, 1999). Another approach uses standard deviation maps. Comparing variance or standard deviation maps of kriging and collocated cokriging estimates can determine how reliable the estimates are at any geographical location, within the study area. The closer the estimation point is to a sampled point, the lower the standard deviation (Flores-Garnica and Omi, 2003).

In summary, reservoir characterization using seismic attributes requires a thorough geological understanding and accurate and representative well log-derived reservoir properties. Additionally, although it is not always feasible, such studies should demonstrate the physical meaning of the seismic attribute used in the integration process.

2.1.3 Understanding seismic attributes

Over the past few years, seismic attributes have established themselves as a valuable tool in reservoir studies, possessing the ability to provide quantitative information about lateral variations in the seismic data.

In reflection seismology, the response of the earth to seismic wave propagation is recorded in terms of events of seismic reflectivity data. To varying extents, this response is also documented by the extracted seismic attributes.

Physical factors including the various elastic properties of a rock system, such as rigidity, incompressibility, porosity, pore fluid, clay content, lithology, and gas saturation, and tend to interact mutually in response to wave propagation (Wang, 2001; Chambers and Yarus, 2002). These factors can be classified into three groups or properties which are: rock properties; fluid properties; and environmental properties. However, they are often interrelated or coupled such that changing one factor will change others (Wang, 2001). The effects of changes on seismic data can be additive or subtractive. Figure 5 illustrates the degree of interaction and how complicated the task can be if we try to isolate and study the response of each factor individually. (See Wong, 2000 for a discussion about the effect of these properties on seismic data).

Accordingly, rock physics has been always an instrumental tool, bridging between seismic data and reservoir properties (Wang 2001; Castagna, 2001). Elasticity theory (Hilterman, 2001) provides the basis to model the seismic velocities of P and S waves in terms of different elastic rock constants, such as the bulk modules (κ), shear modules (μ), poisson ratio (σ), lamé's constant ($\lambda = \kappa - 2\mu/3$), and density ($\rho$) (Sheriff, 1991; Yang and Stewart, 1997; Chambers and Yarus, 2002):

$$\text{e.g., } Vp = \sqrt{(\lambda + 2\mu/\rho)},\ Vs = \sqrt{(\mu/\rho)},\ \text{and } Vp = \left[\frac{1-\sigma}{0.5-\sigma}\right]^{0.5}.$$

The relationships between seismic velocities, porosity and fluid properties are usually approached by using Gassmann's equation, (Gassmann, 1951):

$$\rho V_P^{\ 2} = K_{dry} + 4/3\mu_{dry} + \frac{(1 - K_{dry}/K_{ma})^2}{(1 - \phi - K_{dry}/K_{ma})1/K_{ma} + \phi/K_{fl}}$$

where K_{dry}, K_{ma}, K_{fl}, are the bulk modulus for dry-rock, matrix, and pore fluid, respectively, and μ_{dry} is the dry-rock shear modulus value.

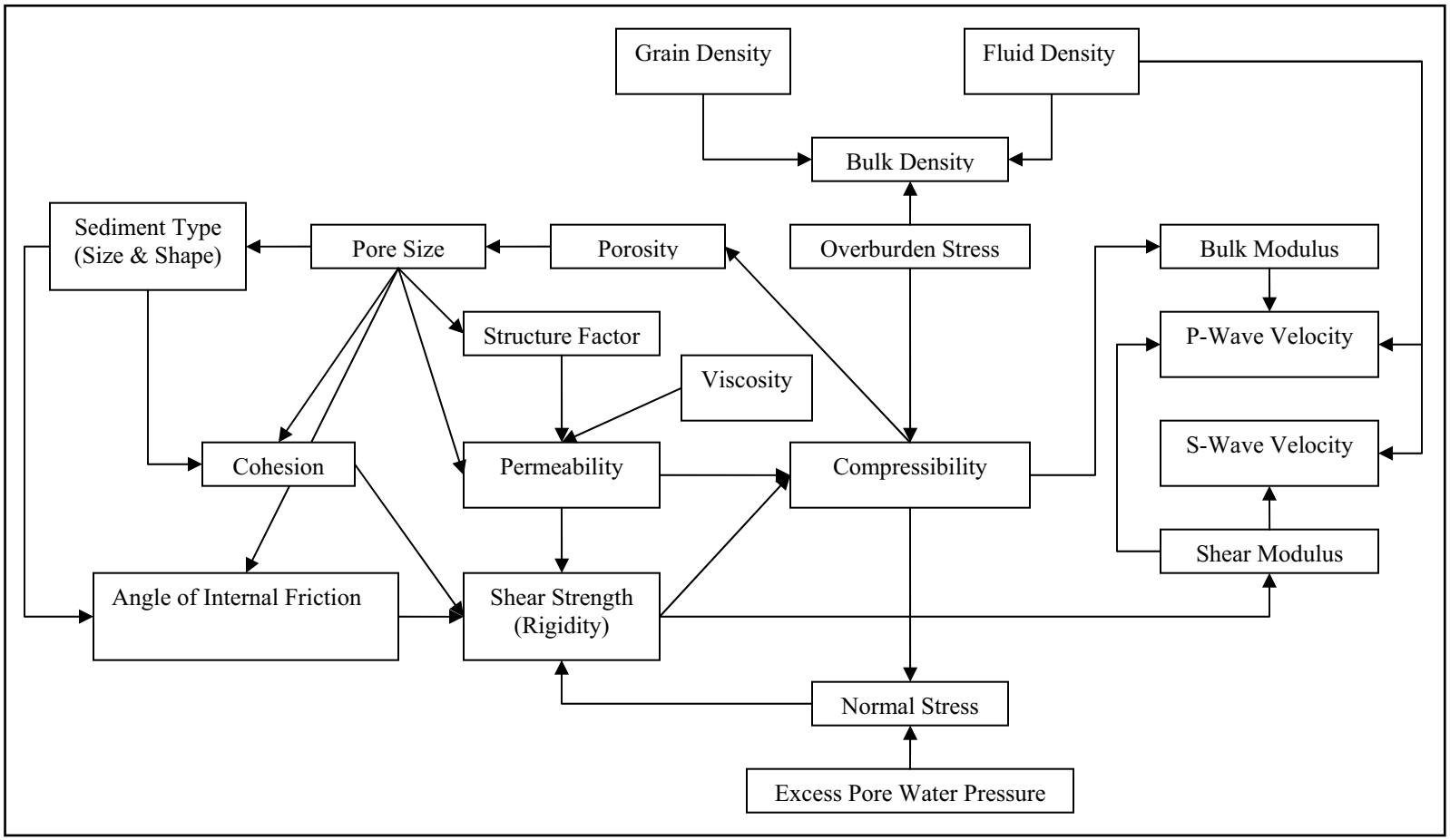

Figure 5. Schematic representation showing the complex relationships between the different physical factors affecting seismic properties.

The third main addition was introduced by Biot (1956), which is considered as a major refinement for the Gassmann's equation by incorporating the effect of viscosity of the pore fluid (Biot, 1956). However, Hilterman (2001) described Biot's equation as not intuitive to understand and that its parameters are difficult to derive. The effect of porosity (ϕ) was simplified using a simple solution to the velocity-porosity relationship (the time-average equation) proposed by Wyllie and others (1956):

$$\frac{1}{V} = \frac{\phi}{Vf} + \frac{1-\phi}{Vm}$$

where ϕ is the porosity, Vf is the velocity of the pore fluid, and Vm is the velocity of the rock matrix.

These formulas identify the basic relations between the various factors that play a major role in understanding the principles of wave propagation through rock media. Other important factors, such as the effect of temperature or pressure on elastic properties, are too large to be ignored (Gregory, 1977; Wang, 2001).

Over the past years, rock physics provided an ample number of mathematical models to define the relations between seismic velocities and rock properties. To some extent, these relations are all valid; however, many of them fail to fully illuminate all physical principles involved (Dewar, 2001).

To use seismic attributes as a tool for a quantitative prediction of reservoir log properties, it is important to keep these relations in mind, because they can help to understand the physical meaning between a seismic attribute and the various reservoir properties (Chambers and Yarus, 2002).

A less demanding approach to elucidate the possible geological significance of seismic attributes, involves the use of forward seismic modeling to ensure that there is a physical and meaningful relationship between reservoir properties and selected seismic attributes.

Hart and Balch (2000) used seismic attributes extracted from synthetic seismic data produced by forward modeling. The goal was to build direct inferences between log measured porosity and modeled seismic attributes. Applying these inferences to seismic

attributes extracted from the real data showed the feasibility of this approach to produce accurate reservoir property maps. Moreover, it ensures that the predicted results are also geologically plausible.

In order to achieve improved quantitative parameter estimation of reservoir properties, Castagna (2001) stressed the need to (1) use and integrate all available data, (2) continue to make progress in understanding of rock physics and its applications to seismic interpretation, (3) recognize the earth's complexities and anisotropies, (4) properly deal with associated uncertainty and nonuniqueness, and (5) bring in additional independent information by exploiting as much of the full seismic wavefield as possible and making time-lapse measurements.

2.1.4 Potential challenges in reservoir characterization guided by seismic attributes

Unfortunately, the quest to use seismic attributes in reservoir characterization has not always been a straightforward mission due to a number of key challenging points. The number of assumptions employed, the scale difference between seismic and well data, and the physical meaning of seismic attributes are among the most important challenges. The following discussion sheds light on these challenges that tend collectively to obscure the process of integration between seismic and well data.

"The rock-fluid system is so complicated that virtually all the theories for such a system have to make major assumptions to simplify the mathematics" (Wang, 2000). The various types of assumptions having major impacts on the results of seismic guided reservoir study can be classified into two main levels.

The first level of assumptions is related to the fundamental mathematics describing the interaction between seismic waves and rock-fluid response. As an example, Dewar (2001) explained six different fundamental assumptions used to constrain the equation of Gassmann's. A full discussion regarding these assumptions can be found in Wang (2001). Other assumptions used in petrophysics, such as those used in Archie's equation (Archie, 1942) to estimate water saturation, fall under this category of assumptions.

The second level of assumptions is more statistical. They are set to ensure the validity of the general statistical argument that is used to build a representative model by integrating well and seismic data.

In reservoir characterization studies, it is not always a plausible option to collect additional data. Therefore, it is generally assumed that the size and the quality of the collected data are sufficient to define a representative model.

In addition to a high signal-to-noise ratio, which is seen as a major prerequisite, Chambers and Yares (2002) stated that success in such studies depends on many factors related to the quality of seismic data, such as proper zero-phase seismic processing, true-amplitude recovery of seismic data, and sufficient frequency content at a reservoir level. On the other hand, it is also essential to assume that the available well data is considered as a representative subset of a larger reservoir population.

Scale related heterogeneities are the second main challenges faced in integrated-reservoir characterization study. The integrated data represent a collection of different sourced information that mainly includes seismic data, its attributes, well log data and other core-measured reservoir properties. Consequently, these data are collected at various scales. Figure 6 outlines the projected amount of variation in scale or frequency between the core derived measurements, well log measurements and seismic derived attributes.

The resolution of well logs and cores are less than 0.3 meters, while seismic resolution is often no better than 15 meters (Dewar, 2001). In terms of the frequency ranges, seismic data or seismic derived attributes are measured as functions of continuous frequency of (10–200 Hz), log data of (~ 10 kHz), and laboratory-measured properties of (100 kHz–2 MHz) frequency bands (Wang 2001).

The band-limited nature of the seismic data frequencies (typically of 10-80Hz) has a major impact on the sensitivity of seismic attributes. The low frequencies are usually missing from the seismic data. These frequencies are extremely important if a quantitative interpretation is claimed (Latimer et al., 2000). Finally, averaging a reservoir property and a selected seismic attribute over a delimited window adds a new

component of complexity to establish good correlation between seismic attributes and well data measurements.

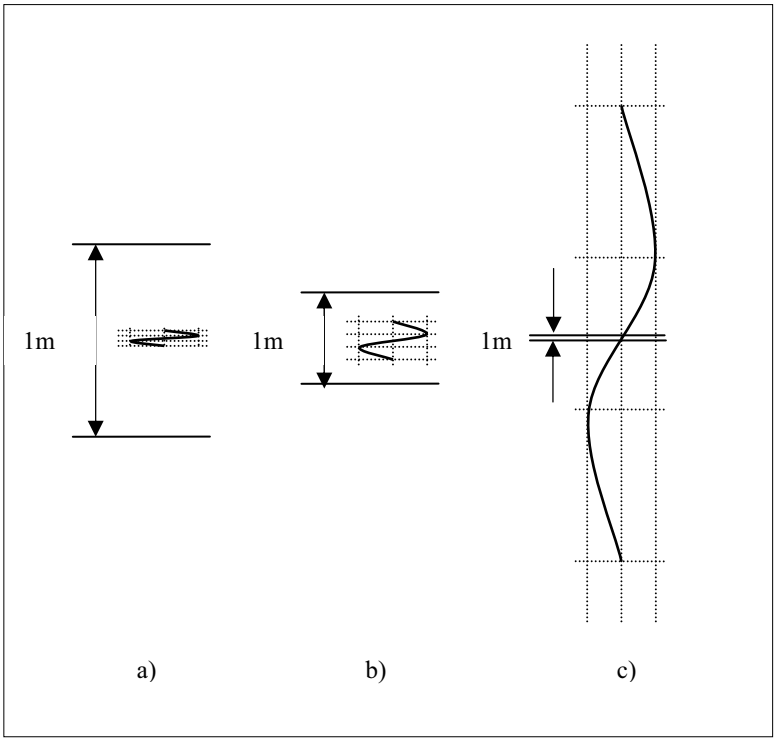

Figure 6. Schematic wavelet of typical wavelength for a) laboratory measurement, b) sonic logging tool, and c) seismic data (after Yang and Stewart, 1997).

The third type of challenges facing a researcher in using seismic attributes is strictly related to seismic attributes and their physical meaning. Unfortunately, most of the seismic attributes, used in reservoir seismology, are not conclusive from geological or petrophysical point of views. Failing to establish solid relationships has led to more confusion in understanding these attributes and their use (Chen and Sidney, 1997). Among many reasons, this inherited ambiguity may be related to the fact that seismic attributes are not independent pieces of information but, they represent various ways to portray a limited amount of basic information or a subset of the total information (Barnes, 2001). The amount of information contained in a seismic attribute is not clear, and how this information are linked to or contained in other attributes is ambiguous. The

confusion is simply attributed to the fact that a given seismic attribute can describe seismic data by quantifying specific data characteristics.

Recent estimates indicate current technology allows calculating several hundred seismic attributes (Chambers and Yares, 2002), which is seen as a major drawback. From an interpretational point of view, it can be said that the more seismic attributes available, the more difficult it becomes to select representative or appropriate attributes.

Furthermore, the vast number of available attributes has caused many of the seismic attributes to be duplicates of each other. Many different names describe the same information (Barnes, 2001). As an example, seismic amplitude can be computed in terms of its mean, rms, minimum, maximum, etc. A cross-plot of the mean and the rms amplitudes will not provide additional information. Additionally, extracting seismic attributes across a limited window may lead to the same effect. The minimum amplitude and the maximum negative amplitude attribute maps will be identical if we set a window across the central trough portion of the seismic signal.

The difficulty in establishing a physical linkage between seismic attributes and well measured reservoir properties, providing that they are statistically correlated, is another major hurdle to make sound generalizations. Few direct relations can truly be established between most of the available attributes and the physical or the geological properties (Chambers and Yares, 2002).

Acoustic impedance, the product of density and velocity across a given interface, is one of the important seismic attributes. It can be conclusively and meaningfully related to many reservoir properties like lithology, porosity and pore fill (Latimer et al., 2000). This unique criteria possessed by acoustic impedance is mainly attributed to the fact that acoustic impedance is considered as a layer or rock property, which makes this attribute very close in nature to all of the log measured reservoir properties (Latimer et al., 2000). On the other hand, seismic derived attributes are described as interface properties. Most of the seismic attributes are portrayed as interface attributes. As a result, the information contained in a seismic attribute reading across an interface is very condensed and delimited to the region defined by a definite sample interval.

In summary, recent knowledge gained from reservoir characterization studies proved the ability of seismic attributes to provide insight into the data. Despite their inherent ambiguities, experience showed that it is possible to associate certain seismic attributes with certain physical reservoir properties. While no precise relationships have been established between the majority of known attributes and the physical or geological characteristics of the earth, Taner (2001) explained that the power of seismic attributes is contained in their ability to be used as effective discriminators.

2.1.5 General review of seismic attributes applications

Among their different applications, seismic attributes have been used in previous geophysical investigations to address various tasks in reservoir seismology. Among their many applications are:

1. Structural and stratigraphic interpretation

Since the very beginnings, structural interpretation of reflection seismic data has been always our main goal. The use of the instantaneous phase or its cosine, coherency-based attributes, spectral decomposition, dip and azimuth etc. allowed for a more accurate picture about the subsurface structures and stratigraphy. Moreover, it provides supremacy to visualize and understand complex features of faulting, fault sealing, subtle stratigraphic changes or lateral facies relationships (onlaps, downlaps and etc.).

The work presented by Bouvier and others (1989) is one of the very early classical examples to use the effectiveness of using three-dimensional seismic survey to provide detailed reservoir structural framework. This detailed information improved confidence in the identification of highly prospective, partially tested and untested closures, highlighted by stacked amplitude anomalies (Bouvier et al., 1989).

MacRae and Watkins (1993) conducted detailed seismic structural interpretation to study the basin architecture, salt tectonics of the Desoto Canyon Salt Basin, Northeastern Gulf of Mexico. Additionally, the use of seismic derived information was very instrumental in understanding the effect and mechanisms of growth faulting and its consequence impacts on hydrocarbon exploration (Watkins et al., 1996).

2. Lithologic identification

The use of seismic attributes to illuminate lithology within a reservoir unit is very important. Acoustic impedance and AVO attributes demonstrated excellence in relating lithologic information of reservoirs (Castagna, 2001; Latimer, 2000). Number-of-zero crossings, arc-length, coherency-based attributes and polarity ratio are very powerful attributes that reflect the degree of heterogeneity within a specified interval due to lithology or stratigraphy variations (Chen and Sidney 1997).

3. Direct hydrocarbon indicators

The use of seismic attributes as direct hydrocarbon indicators has been successful. Amplitude variation with offset (AVO), instantaneous frequency, acoustic impedance and interval velocity inversion results, Bright and dim spots of the instantaneous amplitude, etc., are among the many attributes used in this task (Chen and Sidney 1997; Castagna, 2001).

4. Reservoir production monitoring (Dynamic reservoir characterization)

It is of prime importance to detect changes within producing zones and to delineate producing related features, such as steam or fluid injection fronts and temperature changes. Time-lapse seismic reservoir monitoring (also known as 4D seismic surveys) has advanced rapidly over the past decade (Lumley, 2001), to provide important answers to enhanced oil recovery strategies by studying changes in seismic derived attributes extracted from repetitive seismic surveys (Wang, 1997).

5. Fractured reservoirs

Once again, seismic attributes provided the ability to detect the existence of natural fractures. Natural fractures are a critical component for economic oil and gas production, especially in tight sand and mud rocks (Li et al., 2003). Over the past few years, there has been a consistent increase in using 3D P-wave data to characterize fractured reservoirs (e.g. Lynn et al., 1996; Smith and McGarrity, 2001), by providing fracture intensity maps or 3D volumes that are valuable sources of information to layout future of production and development strategies.

6. Geohazard reduction tool

Using seismic attributes allows early detection and delineation of both surface and subsurface geologic drilling hazards that are risky to the stability of future production facilities. Haskell and others (1999) demonstrated the ability of using seismic attributes to detect geology related hazardous features that include faults, dewatering structures, salt and shale diapirs, shale ridges, pockmarks, buried channels, gas chimneys, shallow gas pockets, and slump features.

Geopressuring is another example of geology related hazards. It poses significant threats to drilling safety, especially in deepwater settings. Seismic attributes (amplitude, velocity, coherency, etc.) can detect the effect of geopressuring when the effective or differential stresses acting on the sedimentary column are very low (Dutta, 2002). These attributes obtain signatures of overpressure or lack of fluid transport over the geologic time both qualitatively and quantitatively. Using the seismic signatures, it is possible to map hazardous zones of trapped fluids and overpressured compartments.

2.2 General geology and stratigraphy of the study area

The Gulf of Mexico (GOM) basin is the most prolific gas and oil province in the United States of America. It represents one of the most thoroughly studied sedimentary basins in the world. At the same time, it is considered one of the most structurally complex basins. The joint effects of growth faulting, salt diaprism, gravity flows, and massifs produce complex near-surface deformation patterns that mask the origins of many structures (Worrall and Snelson, 1989).

During the early Cenozoic, in response to Laramide orogenic activity in the western interior of the North American continent, large volumes of clastic sediments were deposited in the northern and western regions of the GOM in a rapidly subsiding basin (Martin, 1978; Winker, 1982; Ray and Pearcy, 1988; Worral and Snelson, 1989). High rates of deposition formed very thick clastic depocenters along the northern marginal shelf of the GOM. The Cenozoic section of the northern GOM is characterized by cyclic clastic sediments that are repeatedly interrupted by shaly marine transgressions due to rises in sea level (Ray and Pearcy, 1988; Seni, 1997).

The rate of sedimentation exceeded the rate of subsidence, causing the northern Gulf margin to prograde basinward for a distance of 400 km, Figure 7, from the edge of the Cretaceous carbonate shelf to the present position of the continental slope (Ray and Pearcy, 1988). Simultaneously, the centers of main depocenters shifted eastwards in response to a shift in source of sediment supply from the western Rio Grande in southern Texas to the Mississippi River drainage basin in Louisiana (Martin, 1978; Ray and Pearcy, 1988; Hunt and Burgess, 1995). Thus, the thickest lower Tertiary strata accumulated in the Rio Grande embayment, while the thickest Miocene strata are found in the onshore and offshore of southern Louisiana (Woodbury et al., 1973).

The structural styles within the GOM reflect extensional tectonics dominated by growth faulting, which result from gravitationally induced gliding and gravity spreading of thick depocenters over mobile salt or overpressured shale. Worrall and Snelson (1989) differentiated two fundamental styles of growth faulting existing within the prograding Cenozoic shelf margin. These two fundamental styles are a very long, coast parallel, basinward dipping linear and listric growth faulting that dominate the Texas offshore and nearshore regions (the Texas-style), and a short, arcuate growth faulting dominates the central offshore Louisiana (the Louisiana-style). In contrast with the former style, Louisiana-style faults result from point source loading by rapidly shifting deltaic depocenters associated with massive loading of the Mississippi River subdelta (Seni, 1997).

Watkins and others (1996) indicated that arcuate faults of the Louisiana style are associated with salt substrate, whereas elongated linear faults of Texas detach into linear geopressured shale ridges. Initial investigations of this study indicated that faults within the study area are of the Louisiana-style and they tend to sole out at the top of a geopressured zone at 12000 ft. It is obvious that these faults played a major role in accumulating hydrocarbons within the Miocene deposits, by providing a suitable trapping mechanism.

The present study area is located within the limits of the Miocene production trend of the northern Gulf of Mexico (Figure 7), dominating the central region of the

GOM basin. This region is characterized by large scale, down-to-the-basin listric faults that sole on a regional detachment zone above the Oligocene section (Diegel et al., 1995; Dutton and Hentz, 2002). The Miocene time was significantly affected by sea level fluctuations. However, it is marked by a steady prograding shelf edge of thick offlapping wedges (Martin, 1978; Ray and Pearcy, 1988).

The Miocene succession in Vermilion 50 and Tiger Shoal fields represents an overall regressive record of ~10,000 ft of thickness and more than 15m.y of depositional history. Benthic paleoenvironmental indicators within the study area show a general upward-shallowing trend (Table 1) that coincides with the general Miocene interval of the northern offshore GOM (Seni et al., 1997).

Published studies of Vermilion 50 and Tiger Shoal fields are very rare. Yang and others (1992) studied Miocene system tracts of East and West Cameron areas, offshore western Louisiana. This area is located directly to the west of our study area, and they share similar characteristics of relatively high sediment rates of deposition, pronounced structural control by growth faulting and to a lesser extent through salt diapirism. Moreover, seismic reflection configurations share the same patterns which are dominated by parallel and sub-parallel reflections.

The lower Miocene sediments are restricted to the western portion of the recent Louisiana shelf in a localized region near the Texas-Louisiana border to the west of the study area (Hunt and Burgess, 1995). Within the study area, the upper lower Miocene is a deeply buried thin section characterized by ~ 2000 ft of mostly lowstand basin-floor-fan, slope fan, and prograding-wedge deposits (Dutton et al., 2002)

Combellas-Bigott1and Galloway (2002) investigated the depositional history by studying the genetic sequence stratigraphic framework of the middle Miocene depositional episode of south Louisiana. The middle Miocene is delimited by two main transgressive marine faunal tops, the *Amphistegina* B (15.5 Ma) and the *Textularia* W (12.5 Ma).

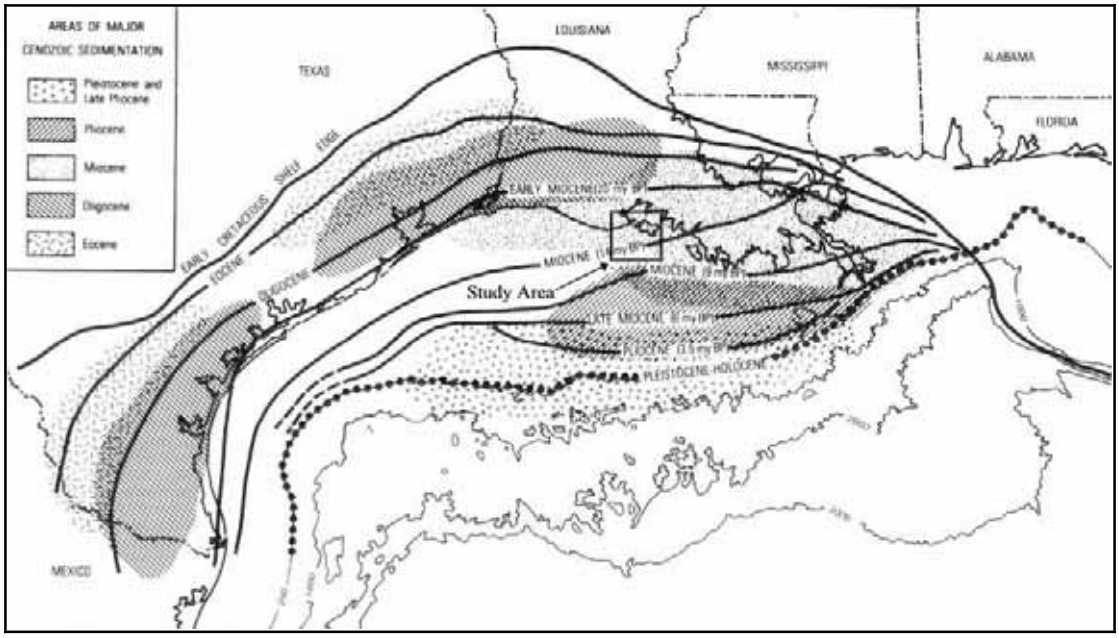

Figure 7. Map showing the regional distribution of major Tertiary depocenters in the northern Gulf of Mexico. Study area location is outlined on the map rectangle. (after Martin, 1978).

According to Combellas-Bigott1and Galloway (2002), the middle Miocene interval is characterized by four regressive cycles separated by maximum flooding surfaces (Table 1): Cycle-1 (*Amphistegina* B – *Cibicides opima*), cycle-2 (*Cibicides opima* – *Cristelaria* I), cycle-3 (*Cristelaria* I - *Bigenerina humblei*), and cycle-4 (*Bigenerina humblei* - *Textularia* W). These regressive cycle facies were modified by high-frequency sea level fluctuations. A fluvial dominated platform and shelf margin deltas of mixed-load sediments, feeding the central Mississippi fluvial system in the western and central provinces, are the characteristic depositional system in cycles 1 and 2. During cycle-2, collapse of the shelf margin developed a retrogradational delta fed apron, bounded by a structurally controlled gorge that fed a long-standing submarine fan.

During cycle3, main deltaic depocenter shifted eastward, fed by the eastern Mississippi fluvial system, while extensive shore-zone-shelf system tracts occupied most of the western and central provinces. During the final forth cycle; submarine canyons started feeding the eastern portion of the submarine fan.

Table 1. Paleobathymetric zones of indicator faunal assemblages of the study area, showing a clear upward-shallowing trend within the entire logged interval of middle and upper Miocene succession. *

Biostratigraphic Fauna	Age Ma**	Paleobathymetric zones			
		Inner Neritic	Middle Neritic	Outer Neritic	Bathyal
1. *Robulus* E	6.15				
2. *Bigenerina* A	6.91				
3. *Bigenerina* B	9.10				
4. *Textularia* L	9.50				
5. *Cibicides inflata*	10.60				
6. *Cibicides carstensi*	10.85				
7. *Textularia* W	12.5				
8. *Bigenerina humblei*	12.85				
9. *Cristellaria* I	13.55				
10. *Cibicides opima*	14.90				
11. *Amphistegina* B	15.50				
12. *Robulus* L	15.85				

* Paleobathemtry data compiled after Breard et al., 1993.

** Age data compiled after Paleo-Data Inc., 2003 (www.paleodata.com).

Xinxia and Galloway (2002) studied the upper Miocene depositional history of central GOM basin that is defined by *Textularia* W (12.5 Ma) and *Robulus* E (6.5 Ma) transgressive events. They divided the upper Miocene into 5 genetic subsequences displaying an overall progradational stacking pattern.

Recently, Hentz and Zeng (2003) published a detailed high-frequency sequence stratigraphy of the Miocene sediments of these fields. By dividing the study interval into distal, medial, and proximal third-order sequences, they were able to define ten major third-order sequences representing a generalized Miocene shelf-to-basin depositional profile. The following text summarizes the Miocene general stratigraphy of the Vermilion 50 and Tiger Shoal fields. It is mainly based on the work published by Hentz and Zeng (2003). Figure 8 shows a dip oriented seismic section of the total Miocene succession penetrated by the wells of Vermilion 50, showing a clear transition from deep slope deposits into proximal shelf depositional settings.

The distal interval is composed of two third-order sequences (sequences 10 and 9), representing the upper lower Miocene section (Figure 8). According to Hentz and Zeng (2003), distal intervals are characterized by thick shale lower sections, containing periodic, interbedded shaly-sands of upward-fining and upward-coarsening trends.

The basal shale interval is overlain by interstratified upward coarsening progradational shale and sandstone units of transgressive systems tracts. Thin retrogradational shale units conclude the progradational shale units that are difficult to identify in distal sections. The basal sand units of sequence 10 exhibit thick aggradational sand units of blocky-serrate log motifs.

Loading the unstable outer shelf and slope areas with vast sediments accentuated fault systems lead to a prominent regional shelf hypersubsidence and collapse deformation (Gallowy et al., 2000). The lower part of Figure 8 shows a swarm of blind extensional faults that are mainly developed in response to regional shelf/slope edge failure. Morton and Jirik (1989) indicated that a marked increase in the number of faults and an abrupt increase in stratigraphic thickness define the transitional boundary separating outer shelf and upper slope environments.

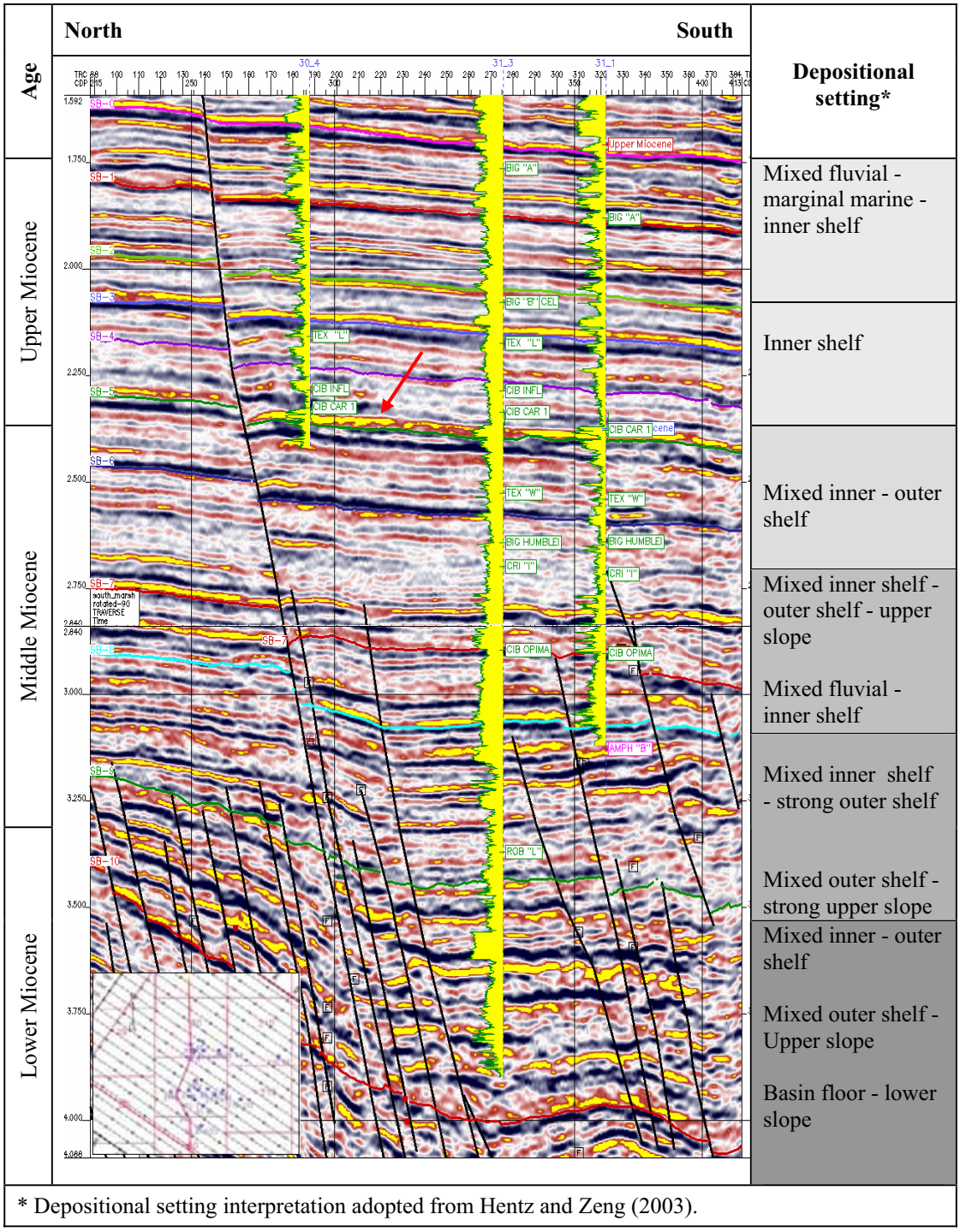

Figure 8. Dip oriented seismic section of the total Miocene succession penetrated by the wells of Vermilion 50, showing a clear transition from deep slope deposits into proximal shelf depositional settings. Color scale indicates the following upward-shallowing trend; Slope, near shelf edge, distal shelf, middle shelf and proximal shelf. N-sand interval is highlighted by the red arrow at the upper/middle Miocene boundary. Black indicates positive seismic polarity

The N-sand interval is located within the medial third-order sequence region that belongs to the middle Miocene interval. Hentz and Zeng (2003) stated that each medial sequence (8-4) is composed of three third-order sequences; a lower succession of aggradational and progradational units that are overlain by thick shale dominated upward-fining retrogradational middle section, and an upper section of progradational units of thick shales and sandstones. These three stratigraphic divisions represent third-order lowstand, transgressive, and highstand systems tracts, respectively. Medial sequences accumulated in upper slope/outer shelf to fluvial environments in marine water depths that ranged from upper bathyal to marginal marine.

The third-order sequences (4-1) of the upper Miocene proximal interval are very thin but very similar to the antecedent medial sequences. Each of the proximal sequences consists of three stratigraphic units (Hentz and Zeng, 2003): a lower succession of aggradational or progradational units, a locally thick upward-fining retrogradational shale-dominated section in the middle, and an upper section of typically two to five mostly progradational units of thicker shales and sandstones. The lower and upper progradational and aggradational units are interstratified with thinner retrogradational intervals. The proximal sequences are differentiated from the medial ones by having a higher proportion of blocky and blocky-serrate aggradational sandstones and thinner progradational units that contain a higher percentage of sandstone. Meanwhile, the retrogradational units in the lower and upper units also contain a higher percentage of sandstone than those in the medial sequences but are of comparable thickness.

The lower, middle, and upper stratigraphic units of the proximal sequences represent a sequence of third-order lowstand, transgressive, and highstand systems tracts, that are deposited in inner-shelf to fluvial settings in marine water depths that ranged from middle neritic to marginal marine shallower marine environments (Hentz and Zeng, 2003). Moreover, the third-order lowstand systems tract is overlain by the third-order transgressive systems tract and fourth-order highstand systems tracts that are of locally incised by valley fills (Figure 9) and interstratified with thin transgressive

systems tracts, composing a progradational sequence set, forms the third-order highstand systems tract (Hentz and Zeng, 2003).

In summary, the succession of Miocene sediments encountered within the fields of Vermilion 50 and Tiger Shoal are indistinguishable from the stratigraphy and geology of the great northern GOM basin. The terrigenous sediments in the northern and western part of the Gulf of Mexico were mainly deposited during sea level lowstands. During those periods, coarse-grained sediments were transported to the outer shelf and upper slope, causing shelf-edge progradation, subaerial erosion, slope instability, and sediment gravity flows in the deep sections (Beard et al., 1982). During periods of transgression and sea level highstands, marine and reworked fine-grained sediments formed a thin hemipelagic and pelagic layer in the deepwater areas (Bryant et al., 1995), and more pronounced thickness in proximal regions which provide suitable sealing conditions above low stand terrigenous deposits.

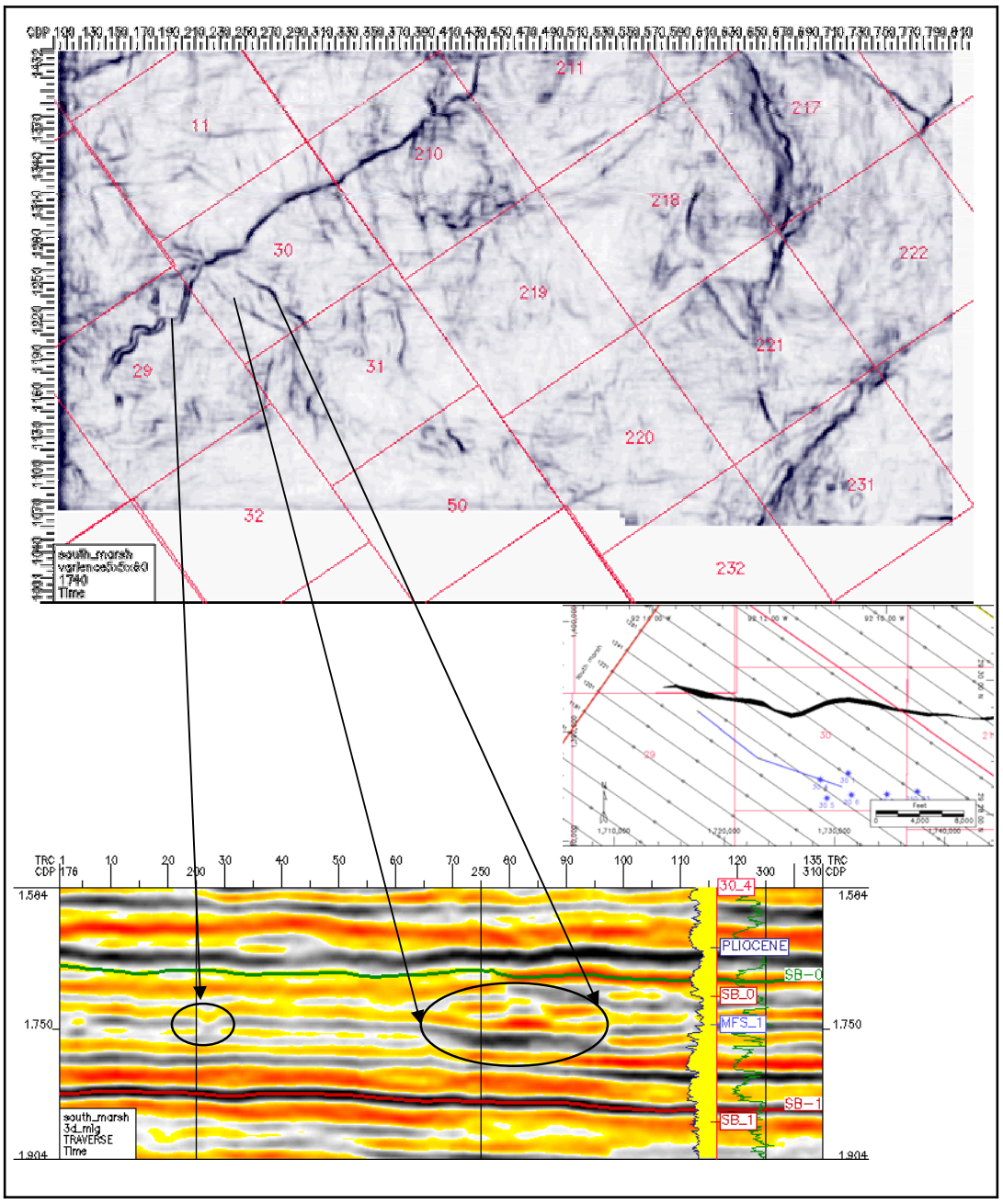

Figure 9. Dip oriented seismic section of the proximal shelf of the upper Miocene, showing various patterns of channeling and incision within a marginal marine setting. Horizontal scale = 20 trace/inch and vertical scale = 7.5 inches/second. Time slice horizontal scale = 100 trace/inch.

CHAPTER III

METHODS OF INVESTIGATION

To achieve the objectives of this study, a collection of procedures is put together in a flow-chart pattern. Figure 10 summarizes the general workflow of procedures. Figures 11 and 12 summarize the different workflows of two main sub-procedures; the *Seismic Attributes Analyses* and the *Upscaling Using Geostatistics*, respectively.

3.1 Data loading and quality control

This step represents the commence point of this study. Seismic data were loaded in a 32 bits mode. This was necessary in order to ensure that the numeric significance is maintained during all subsequent computations and attribute extraction and to avoid data clipping (Brown, 1996). Subsequently, well logs data, check shot data, deviation surveys, available core data and paleo-data were loaded.

Seismic data were checked for any possible errors during the loading process. Each well was checked for its proper loading, surface and subsurface locations and proper loading of directional surveys. Due to the fact that well data were provided by many vendors, log curves were checked for unit consistency, log-depth matching, and core to log alignment.

Log-depth matching check is an important process to make sure that all log curves of the same well are aligned in depth. For the necessity of consistency, alignment is based on the response of at least two logs that have a similar trend, such that one of them is a reseistivity log.

3.2 Post stack seismic processing

3.2.1 Polarity definition

Knowledge of the polarity convention is essential in order to correlate and tie data properly as part of the interpretation of seismic data. The conventional definition adopted by the Society of Exploration Geophysicists (SEG) specifies polarity convention

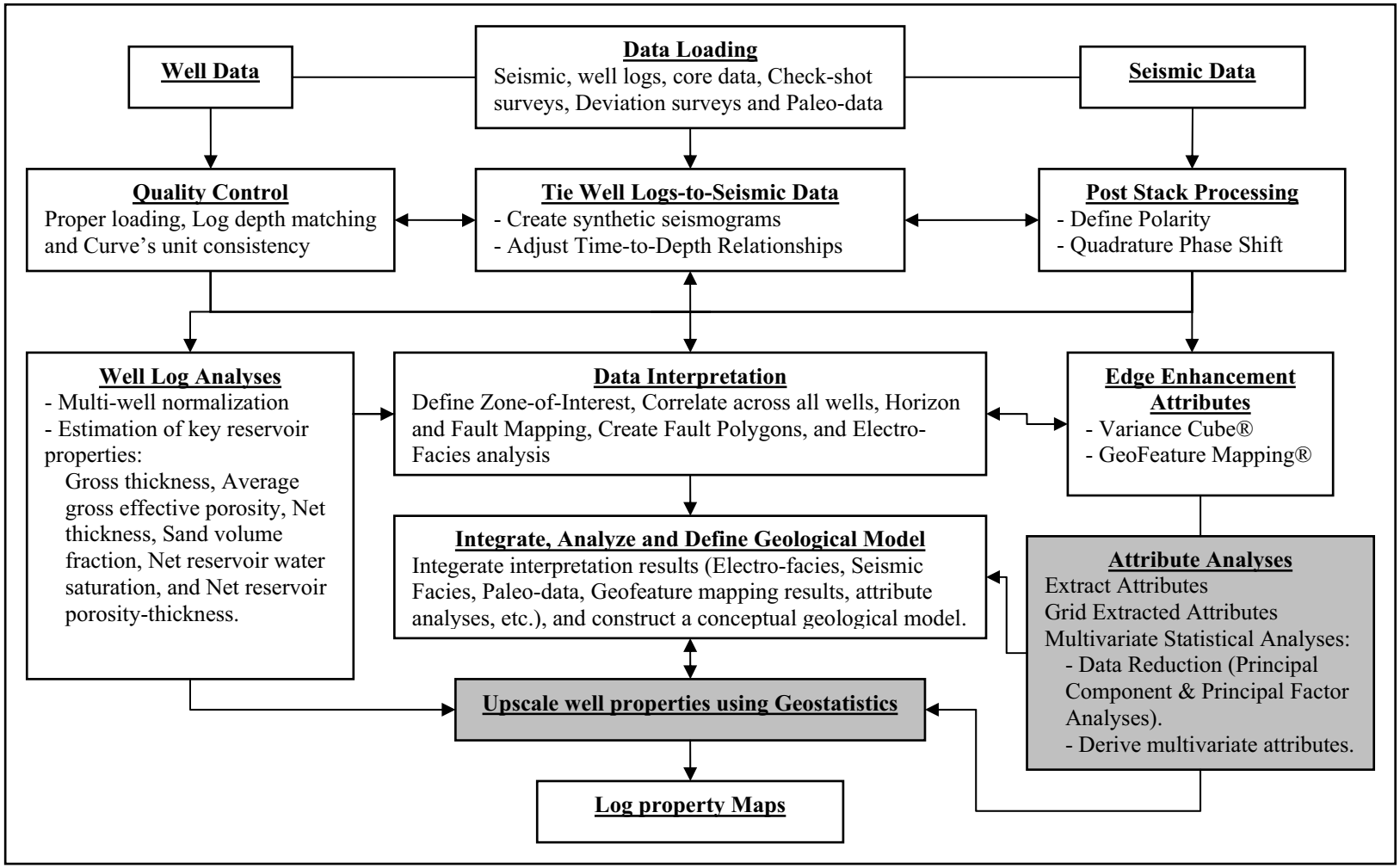

Figure 10. A schematic workflow outlining the main procedures involved in this study. Shaded procedures have their detailed workflows, illustrated in Figures 11 and 12. The double-headed arrows indicate a two-way feedback process.

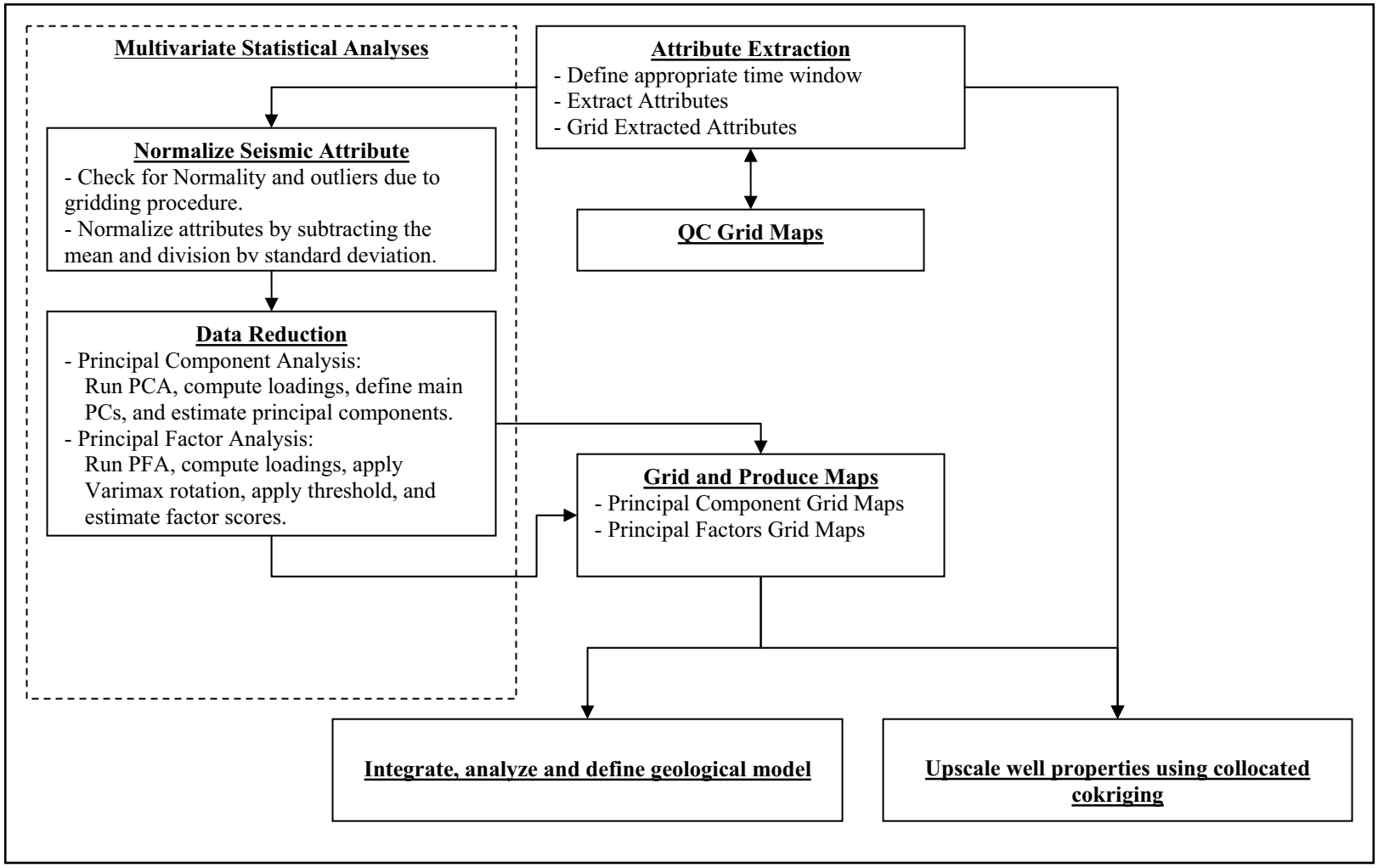

Figure 11. A schematic workflow outlining the main steps of the seismic attribute analysis procedure. The double-headed arrows indicate a two-way feedback process.

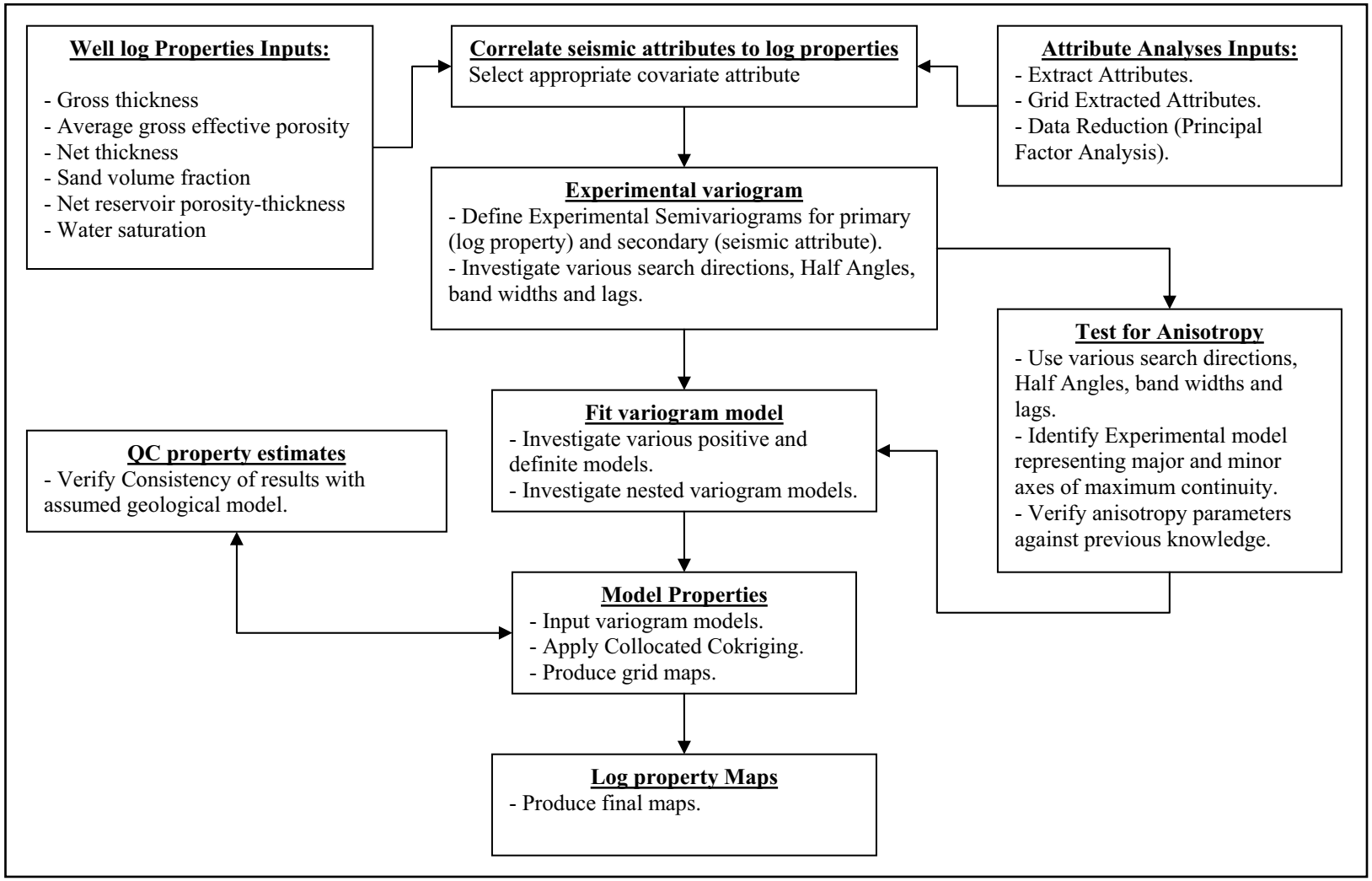

Figure 12. A schematic workflow outlining the main steps of upscaling procedure by using collocated cokriging method. The double-headed arrows indicate a two-way feedback process.

and the procedure to display zero-phase seismic data (Sheriff, 1991). If the signal arises from a reflection indicates an increase in acoustic impedance, the polarity is *positive or normal* and it is displayed as a *trough*. Otherwise, the polarity is *negative or reverse* and it is displayed as a *peak* (Figure 13). However, this convention is not always followed, and consequently, it is necessary to check the processing documentation to verify the polarity definition of the seismic data.

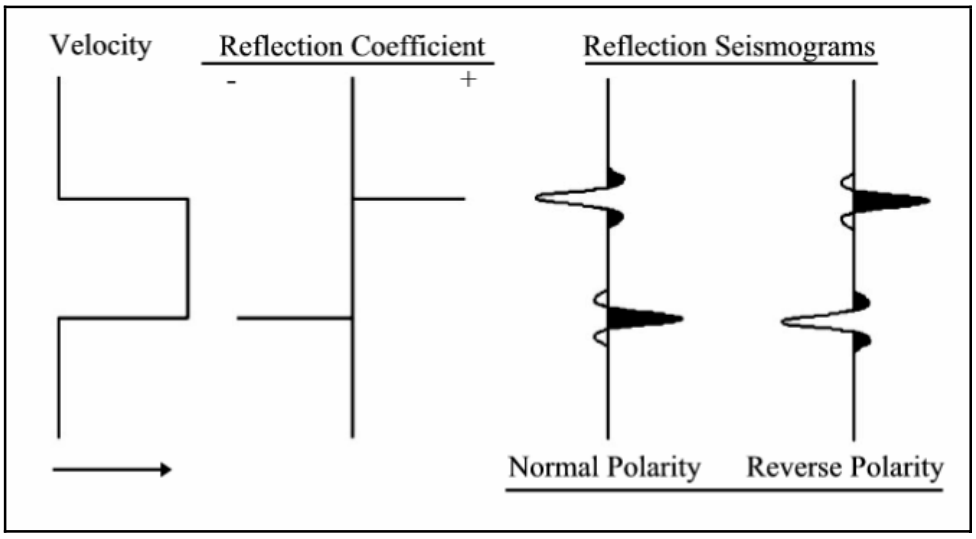

Figure 13. The conventional detention of seismic polarity adopted by the Society of Exploration Geophysics (SEG).

Unfortunately, the polarity of the seismic data used in this study was not clear as information such as acquisition and processing reports were not available. However, the investigation of the wavelet extracted from the seismic data could assist in determining the data polarity convention. Figure 14 shows a typical wavelet extracted from the data set. It suggests that the seismic data is processed to a zero-phase, where most of the energy is concentrated in a central trough. This strongly indicates a reverse polarity seismic definition that is opposite to that specified by the SEG (Sheriff, 1991).

Forward seismic models are essential interpretational tools. They make it possible to correlate observed reflections and geologic interfaces, and verify that the

seismic responses of interpreted conceptual geologic models are consistent with the actual seismic data (Anderson and Cardimona, 2000).

Modeling of the real seismic data, (Figure 15), shows that the N-Sand reservoir ties well to the trough only when using a Ricker wavelet or a reverse wavelet (180° phase shifted). Accordingly, it is concluded that the data is really of a reverse polarity definition, and that sandstone packages will tie to the peak portion of the seismic signal if their resolution is higher than their tuning thickness (< λ/4).

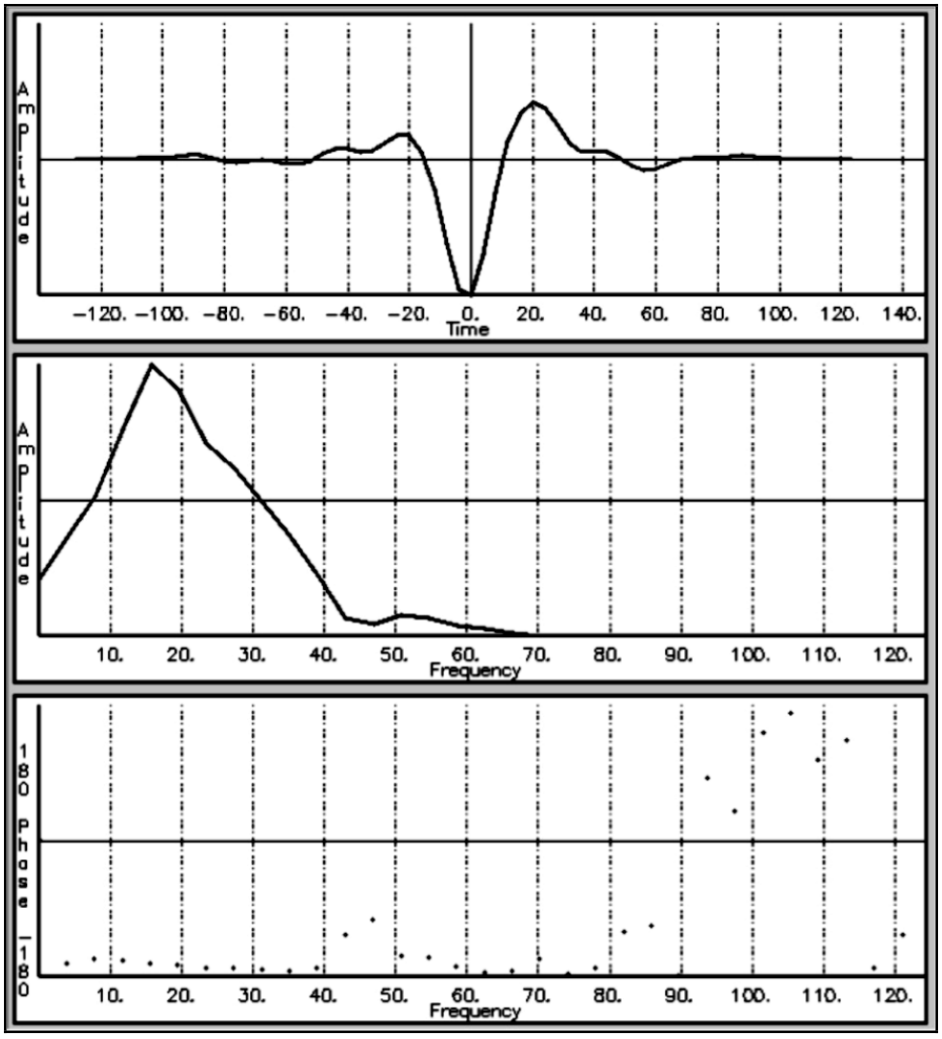

Figure 14. A deterministic wavelet extracted in the region of well 31_6 with a dominant frequency of 17Hz, suggesting a reverse polarity definition and that the data is processed to an almost zero-phase state.

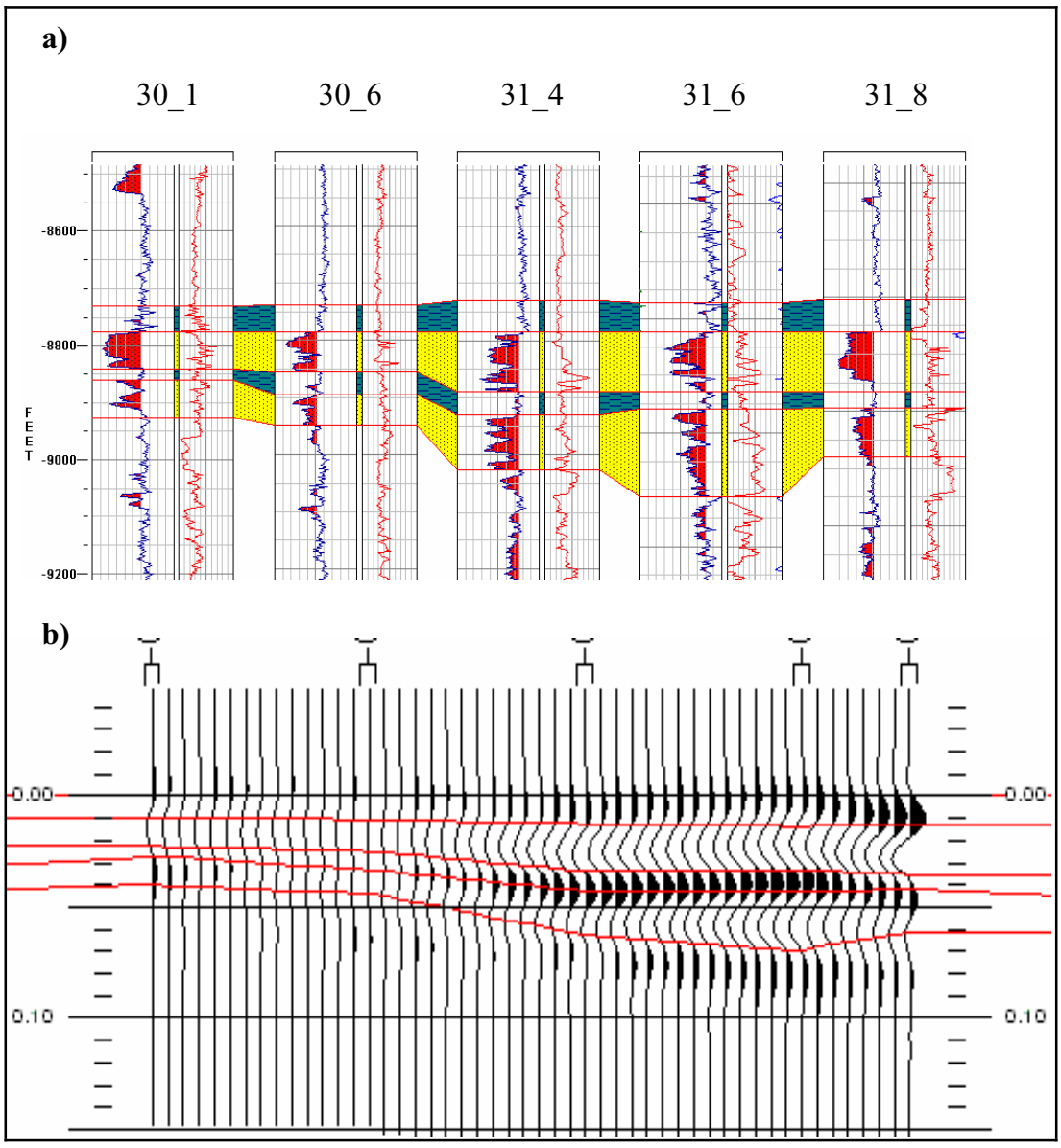

Figure 15. Synthetic 2D-forward modeling of a seismic response of N-sand reservoir produced by a reversed polarity Ricker wavelet and a dominant frequency of 20MHz. Notice the good match between the N-sand reservoir and the trough of the seismic signal. a) The geological model used as an input (blue curve represents a Gamma-ray, and red curve represents delta-time log), and b) represents the results of the GMAplus 2D seismic modeling.

3.2.2 Quadrature phase shift

The extracted wavelets from the data set indicate a zero-phase well processed data (Figure 14). According to Knapp (1993), zero-phase wavelets have the minimum energy envelope width, minimum time dispersion and, therefore, the maximum resolving power. Because a zero-phase wavelet shares its amplitude envelope with a class of wavelets that differ by only a constant phase shift, all wavelets of the class also have the same maximum resolving power within the suite. He concluded that applying a constant phase shift of +/- 90° produces a quadrature-phase wavelet that shares with the zero-phase wavelet its maximum resolving power. Additionally, this can enhance the interpretability of thin beds, where the resulting trough or peak represents the response of the total bed.

Accordingly, a constant shift of -90° was applied to the whole data set. Yet, it is important to prove that this procedure provides an accurate well-to-seismic tie, and eventually enhances the interpretation process. Accordingly, a comparison between the characteristics of two wavelets extracted from the original data set and a -90° phase shifted data is made.

A seismic derived wavelet can be extracted using statistical and deterministic methods. The statistical method produces a zero-phase wavelet with an average frequency derived from the seismic window specified by the interpreter. In the deterministic method, however, no constraint is imposed on the data. This method extracts the frequency content and keeps the phase of the input data so the output wavelet has the same phase of the seismic data. The reflection coefficient (RC) series from the borehole is cross-correlated with each of the traces from the input seismic data in search of the best match position between them to extract the wavelet. The result of the cross-correlation is shown on a correlation energy map, defining the variation of correlation energy with trace number plotted against seismic lag. The software indicates the point of highest correlation energy with a blue crosshair, the point from which the wavelet is extracted (Figure 16). Still, it is important to determine whether this wavelet is statistically valid and can adequately represent the data. Kearney (2001) gave a

comprehensive discussion about deterministic extraction of wavelets and listed a number of points to test the validity of the extracted wavelet.

To assess the potential of using a quadrature phase data in comparison to the original data, two average wavelets, defining a region of 50 traces in radius, were extracted from both data sets adjacent to well 31-6. All other variables were kept. The results of the two wavelets are shown in Figures 16 and 17. Both wavelets are statistically valid (Kearney, 2001). A comparison between the characteristics of these wavelets indicates that:

- A -90° phase shift wavelet has a much smaller time lag value of 8ms whereas for the original data it is 48ms. This suggests that a very minor time shift will be needed to match this new volume of seismic data to well logs. A positive lag indicates that the borehole data must be shifted down to match the seismic.
- A -90° phase shift wavelet has a higher Signal-to-Noise ratio (N/S) of 0.36 whereas for the original data it is 0.24, indicating that the new data has real advantage over the original one from an interpretation point of view. The signal-to-noise ratio indicates how much of the seismic signal can be predicted using the extracted wavelet convolved with the RC series.
- A -90° phase shift wavelet has a significantly greater signal-to-noise than its minimum value, 0.36/0.189 whereas for the original data it is 0.24/0.178. Ideally, it is favorable to have the wavelet's signal-to-noise value to be significantly greater than its minimum value.
- A -90° phase shift wavelet has a smaller range for the estimates of the normalized mean square error (NMSE), compared to that shown by the original data (Figures 16 and 17).

The above points demonstrate that applying a constant phase shift of - 90° can enhance the interpretability of the seismic data. Its higher signal-to-noise ratio suggests that seismic attributes extracted from this data will be helpful in prediction of well log reservoir properties due to the higher signal-to-noise ratio.

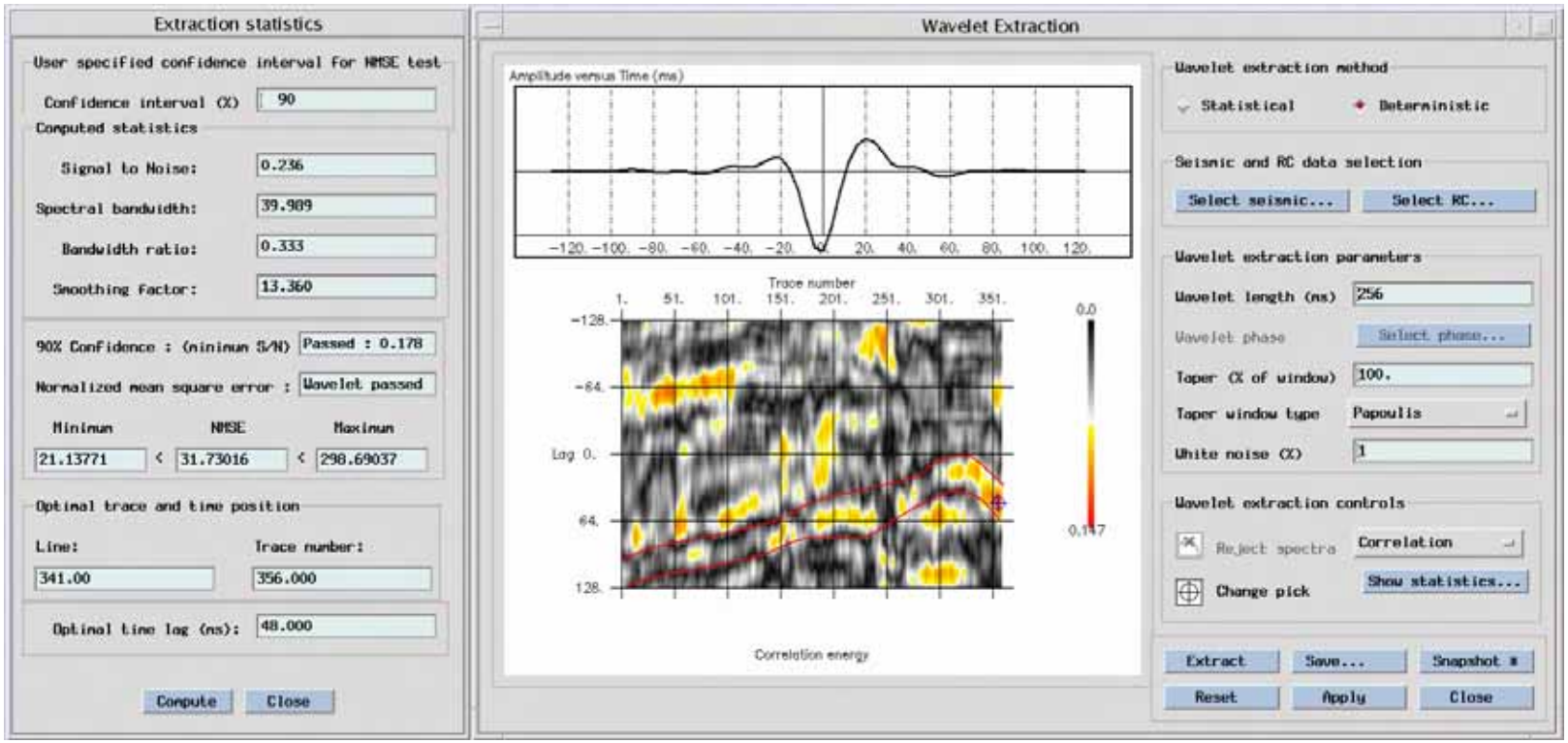

Figure 16. A time domain representation of the extracted wavelet of the original data set. The best-fit location (where the correlation reaches a maximum is marked by the blue crosshair), is located around the trace 356 and optimal lag of 48.0ms. This defines the location of best match between the seismic and the reflection coefficient series from the borehole.

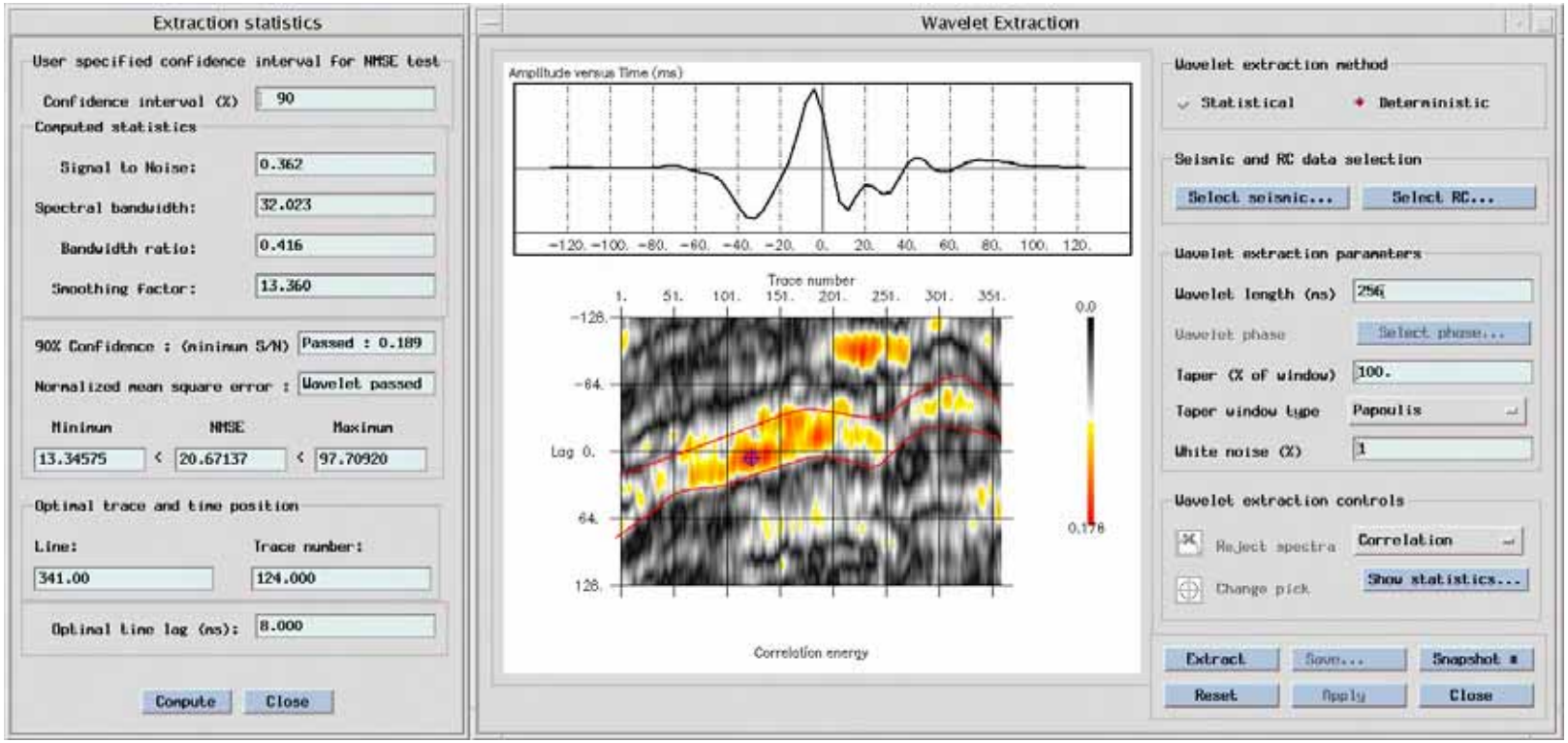

Figure 17. A time domain representation of the extracted wavelet of the -90° phase shifted data set. The best-fit location (where the correlation reaches a maximum is marked by the blue crosshair), is located around the trace 124 and optimal lag of 8.0ms. Compared to the Figure 5, it is clear that a quadrature phase shifting will enhance the process of interpretation and tie between wells and seismic data.

3.3 Tying well-to-seismic data (synthetic seismograms)

The initial interpretive step required for an accurate seismic reservoir characterization study involves the generation and calibration of accurate synthetic seismograms. A synthetic seismogram is computed for each well with a sonic and/or density log in order to maximize the use of available data. The goal of using synthetic seismogram is simply to represent the seismic data in terms of depth units rather than using the original time domain. According to Liner (1999), the major use for using synthetic seismograms is to match the stratigraphy as seen from well logs or outcrops to seismic field data.

Because the velocity model used during the processing is not fully representative of the medium, depths at which events occur after time-to-depth conversion may not be exact. Accordingly, the correlation between the time of seismic data and depth of well logs is not precise. In seismic attribute studies, the importance of correlation between time and depth information can not be stressed enough.

Creating synthetic seismograms involves the use of sonic and density logs, representative wavelets, and representative check-shot surveys. A reflection coefficient series (RC), usually named as RC stick, is calculated based on the contrast between the acoustic impedance values across an interface between two layers according to the following mathematical relationship:

$$RC = \frac{\rho_2 v_2 - \rho_1 v_1}{\rho_2 v_2 + \rho_1 v_1}$$

where ρ = rock density and v = rock P-wave velocity.

Finally, the synthetic seismogram is a product of the convolution between the causal wavelet, usually extracted from the seismic data near to the well location, and the reflection coefficient stick, as follows:

$$T(t) = R_o(t) * w(t) + n(t)$$

where:

T(t) = seismic trace,

Ro(t) = reflection coefficient series (spikes) as a function of time,

* = convolution function,

w(t) = wavelet,

n(t) = noise.

The degree of match between the synthetic seismogram and the real data depends on the quality of all inputs (logs, wavelet, and time-depth relationship). Usually we do not have the check-shot survey and time-depth relationship for each well bore in the study area. Accordingly, there is a need to borrow a neighbor survey to represent the depth-time relationship, or to use the available sonic log after applying a drift correction between the sonic and any available check-shot survey.

Tying well data to seismic data is a very crucial process. Not only does this process enable us to place the sandstone reservoirs against their true seismic response, but also to fix time-depth relationships, which are finally used to convert interpretations from the time domain to the depth domain.

The N-Sand interval is the main interest of this study. Initial investigations indicate that this interval is roughly located around 8700~9000ft. The fact that the depth of geopressuring is located at ~ 12,000ft, much deeper than our depth of interest, and that the seismic volume does not indicate the existence of complex structures and faulting, leads to the conclusion that the velocity model will exhibit a very uniform pattern. Figure 18 shows a very uniform behavior of velocity for all the check-shot surveys available in this study.

It is extremely important that the amount of adjustment needs to be kept to as minimal as possible in order to maintain the uniformity and the smoothness of the velocity model. This can be achieved by very fine time shifting or/and zonal stretching and squeezing over a very limited interval centered on the interval of interest. In concordance with our previous wavelet analysis, a representative wavelet was extracted for each well from the -90° phase shifted seismic data. As a result, a very minute time shift was adequate to bring a perfect match between well data and their seismic responses. The typical range of time shift, needed to establish a good match, was between 0 and 12ms at most.

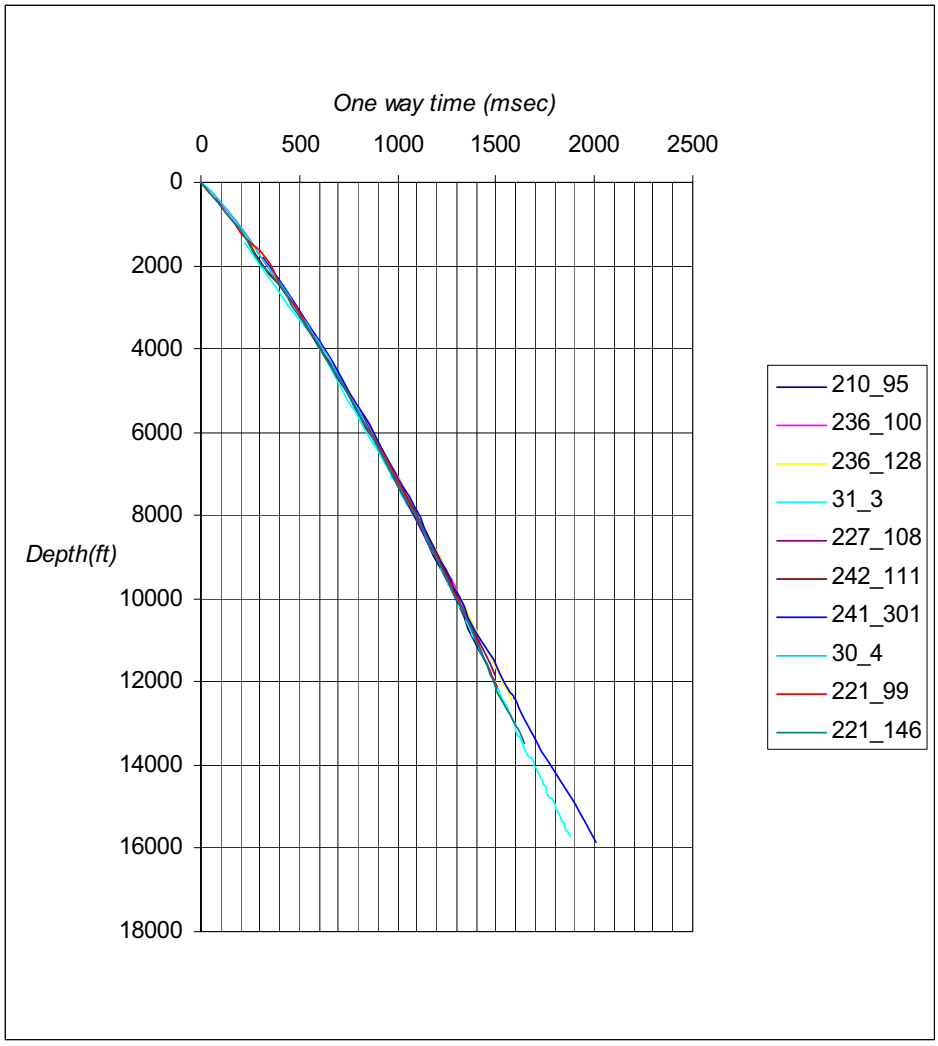

Figure 18. The original check-shot survey data, 10 wells, representing the whole area of seismic coverage. Surveys from adjacent blocks (236, 241, and 242) showing the same trend as well, indicating a very smooth velocity model. Well names are shown on the legend. 221_99 is an average survey model supplied by TEXACO.

Figure 19 shows an example of a final synthetic seismogram of well 31-6. The final results indicate that the processing quality is very good, such that there is no need to input a component of seismic multiples in the model. A sample interval of 4 ms was used to generate the RC series. The final time-to-depth relation was updated and saved. This new relation was used for adjacent wells missing check-shot surveys, and for final time to depth conversion.

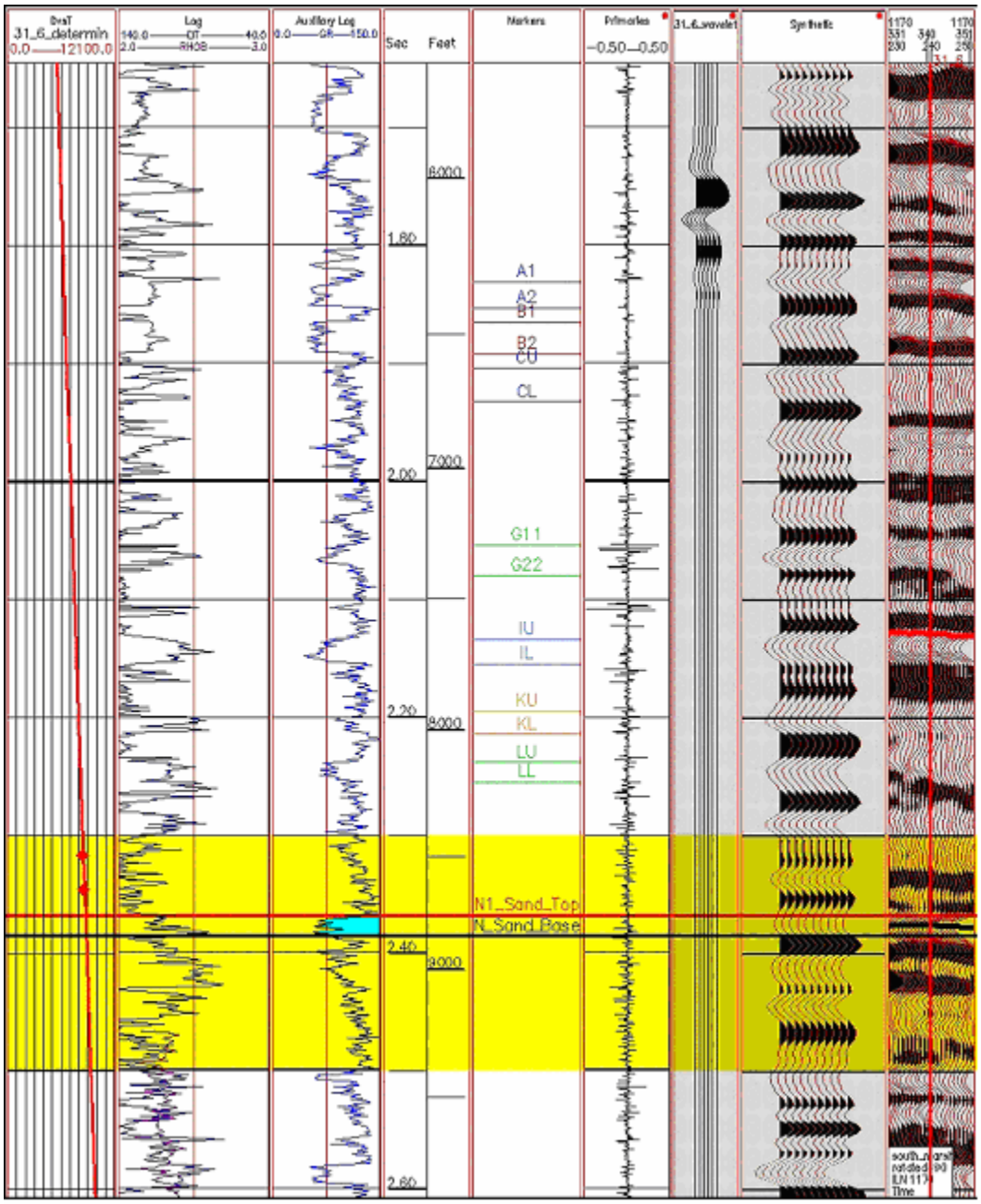

Figure 19. A typical synthetic seismogram of well 31-6. N-Sand is highlighted by cyan color.

3.4 Edge enhancement attributes (variance cube and geoFeature mapping)

3.4.1 Variance cube

Variance cube is a volume-based seismic attribute. This method behind this attribute is different from the coherency cube attribute (Bahorich et al., 1996), in view of the fact that it calculates the direct measurement of dissimilarity rather than the inferred similarity of seismic data (Van Bemmel and Pepper, 2000). It produces much sharper and more distinct terminations than those poorly seen on traditional amplitude displays. Interpretation using variance cube data increases the speed and accuracy of structural and stratigraphic interpretations.

Based on a predefined window length, the 3D amplitude volume is divided into a number of parallel and horizontal time slices. A time slice is divided into a number of cells. Each cell contains a predefined number of amplitude data points. These data points represent the amplitude values of the inline and the cross-line across a given time slice, within each cell (Figure 20). The variance values are calculated from the sum of the difference between interval amplitude and the average amplitude squared, divided by the sum of the squared amplitudes, as follows (Van Bemmel and Pepper, 2000):

$$V = \sigma_t^2 = \sum_{j=t-L/2}^{j=t+L/2} \left[w_{j-t} \bullet \frac{\sum_{i=1}^{I} (x_{ij} - \bar{x}_j)^2}{\sum_{i=1}^{I} (x_{ij})^2} \right]$$

where:

V = a variance value,

w_{j-1} = a triangular weighting function. Its sum is equal to unity to yield smooth variance values between 3 successive time slices,

i = a particular seismic trace number,

j = the time index and refers to a particular time slices within a time window (L),

x_{ij} = the seismic amplitude at time "j" of trace "i" in a cell,

$\bar{x}_j$ = the average seismic amplitude at time "j" for all the traces in a cell.

The final results of variance computation are assigned to the center location of the cells on the time slice. Each cell contains 3x3, 5x5, 7x7, 9x9 traces, or a combination of them. In addition to the two normal directions of inlines and cross-lines, this technique allows the computation of the variance values for the seismic traces in the diagonal directions, enabling a spatial search in all possible directions (Figure 20).

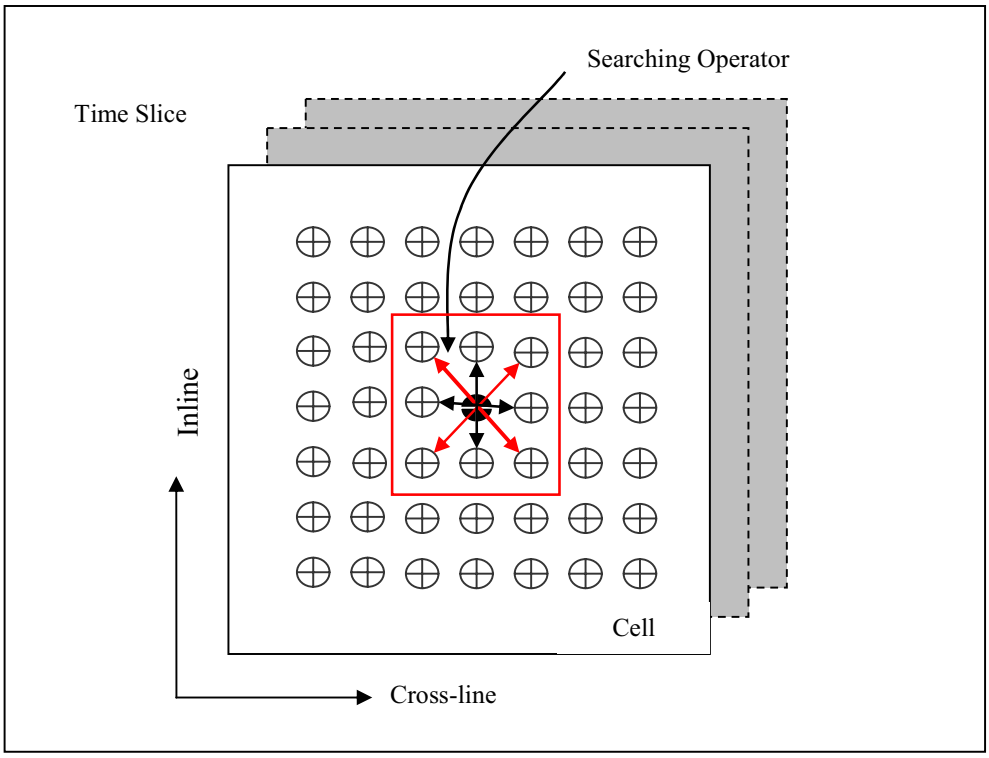

Figure 20. A schematic presentation of the different components used in variance cube computation. Each cell is composed of 3, 5, or 7 traces or a combination of them. The searching operator shows the possible spatial options to compute the variance values.

Various time windows and spatial search scenarios were run over the main area of interest. Best results were achieved using a time window of 50ms, and a cell size of 5x5. A searching operator was set to search in all possible directions (2 normal and 2 diagonal directions). The final variance cube data were sliced using a time interval of 4ms, for the section between 1 and 3.5ms.

The use of variance cube, which can be viewed on a time slice and a vertical seismic section or visualized in a 3D visualization system, improves the accuracy of the

structural interpretation. Variance cube time slices have the superiority in illuminating discontinuities more sharply than the original data time slices. Figure 21 shows a comparison between the original amplitude data and the variance cube data. The inline number is 1351, and depth of the time slice is 2012ms.

3.4.2 GeoFeature mapping (MG)

GeoFeature mapping (MG) is another seismic attribute interpretation tool used to enhance edge terminations. Similar to the variance cube tool, the results of MG help to detect subtle changes in the seismic signature of adjacent traces due to any structural and stratigraphic effects. Compared to the 3D variance cube technique, GM is a 2D based attribute. Its attributes are computed based on adjacent trace cross-correlations, which are finally saved as horizon attributes.

The computed attributes measure the similarity between adjacent seismic traces, based on wavelet shape comparisons. A high correlation indicates that the traces match well (i.e. homogeneous facies); a low correlation indicates that they are dissimilar (i.e. heterogeneous facies). Based on adjacent trace comparisons, a number of different attributes can be estimated, which includes: quality factor, amplitude ratio inclusive, amplitude ratio exclusive, amplitude delta, time/depth delta and time/depth value. Table 2 shows a description of each attribute.

GeoFeature mapping attributes may be extracted between depth-to-depth, or horizon-to-depth intervals. Figure 22 shows the difference between the two methods. Trace correlations are estimated across a predefined correlation window, which is attached to a certain datum, and a certain number of steps. Each step produces a 2D horizon attribute of trace correlations. A datum can be a time slice, similar to the variance cube tool, but it is also possible to select an interpreted horizon as a datum. A wide range of spatial operators are available (Figure 23). These different search options help to illuminate obscured features oblique to the normal seismic inlines and cross-lines.

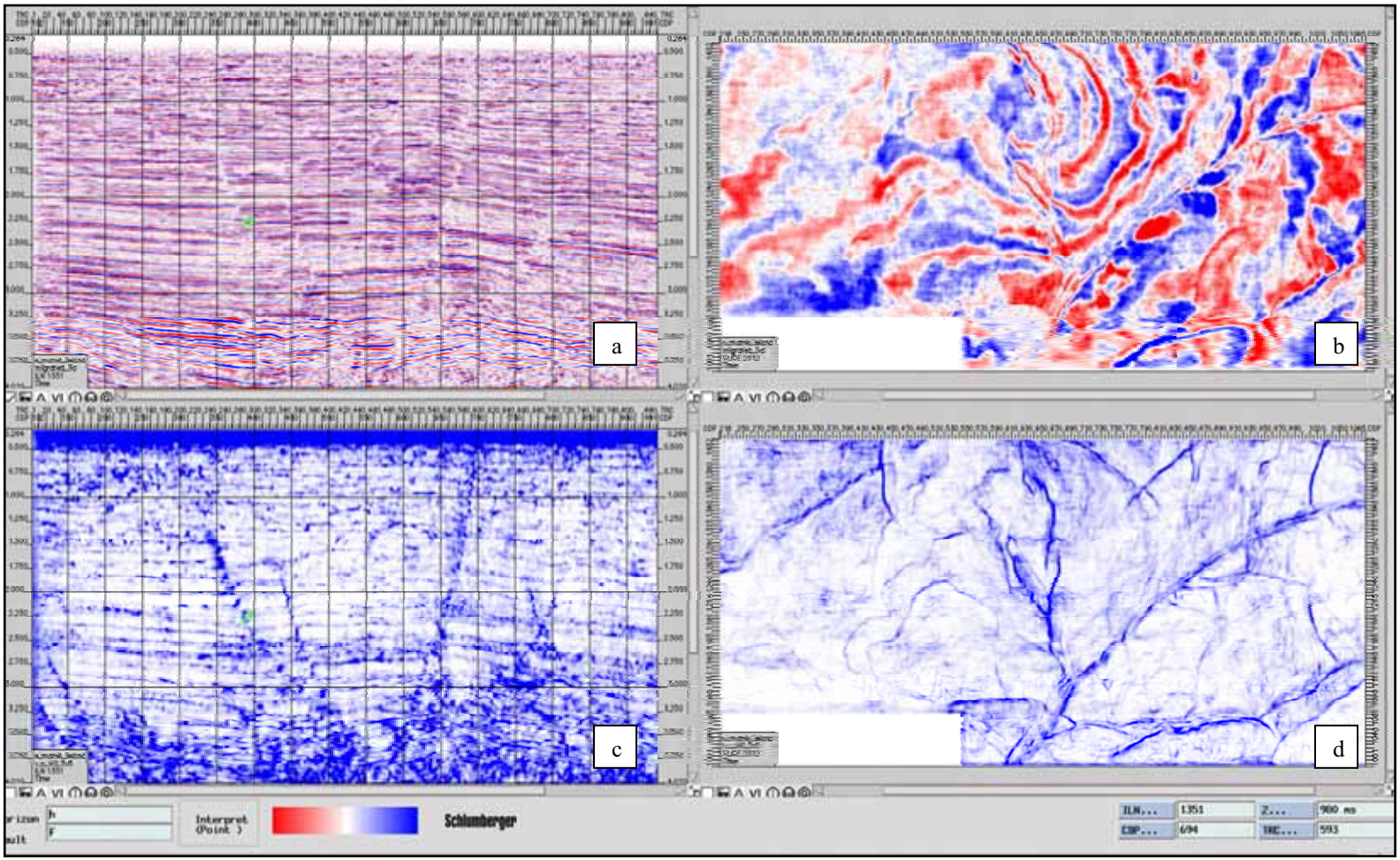

Figure 21. A 4 layout comparison between the original (a&b) and variance cube (c&d) data. The posted inline is inline number 1351, and depth the time slices is 2012ms. Variance cube data improves the accuracy of structural interpretation. Variance cube time slices (d) have the superiority in illuminating discontinuities more sharply when compared to the original data time slices (b).

Table 2. GeoFeature Mapping allows different attributes to be computed within limits of a correlation interval. This table lists the different attributes and their description.*

Attribute	Description
Quality Factor	Measures shape similarity of wavelets between adjacent traces. A value of 1 means very similar traces, whereas a value close to 0 indicates two very dissimilar traces.
Amplitude Ratio Inclusive	Measures the maximum amplitude ratio of the center trace and the selected adjacent trace. Only a defined range of values is posted and outside the range are set to null.
Amplitude Ratio Exclusive	Measures the maximum amplitude ratio of the center trace and the selected adjacent trace. A defined range of values between a minimum and a maximum is set to zero, whereas all values below a minimum are set to minus one, and all values above a maximum are set to one.
Amplitude Delta	Measures the difference in amplitude between the previous trace and the selected adjacent trace.
Time (or Depth) Delta	Measure the correlation lag to align adjacent traces.
Time or Depth	Measure of time or depth of the correlated traces.

*summarized from GeoFrame 4.0 bookshelf documentation.

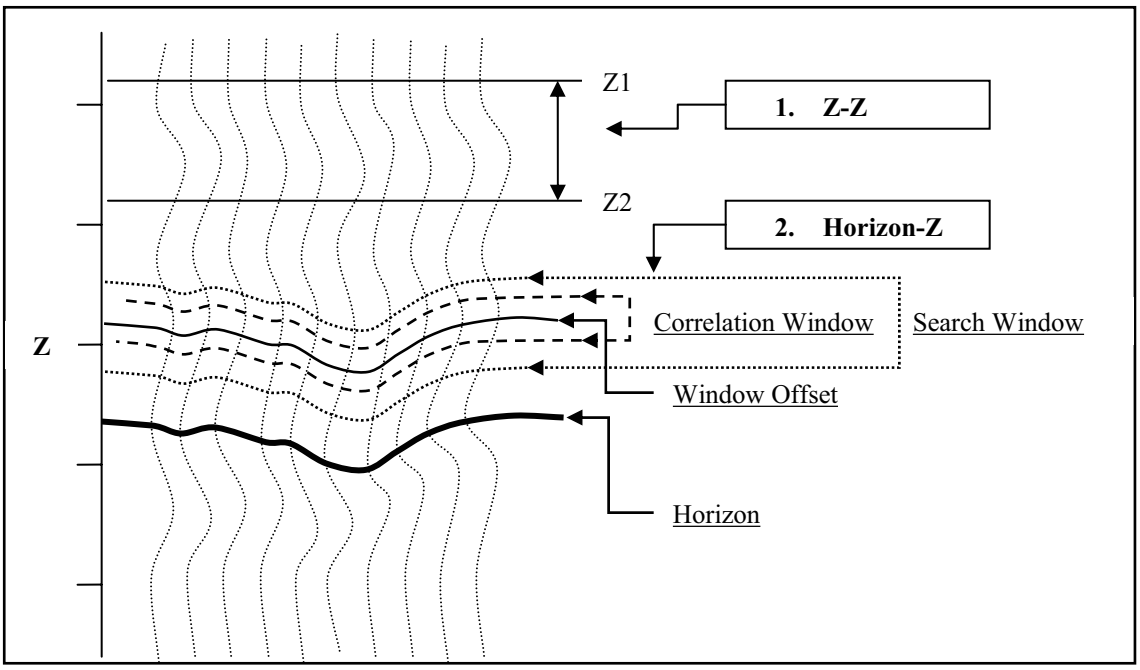

Figure 22. A schematic diagram showing the 2 different options of datum selection available in GeoFeature mapping tool. 1) the Depth-to-Depth and 2) the Horizon-to-Depth options.

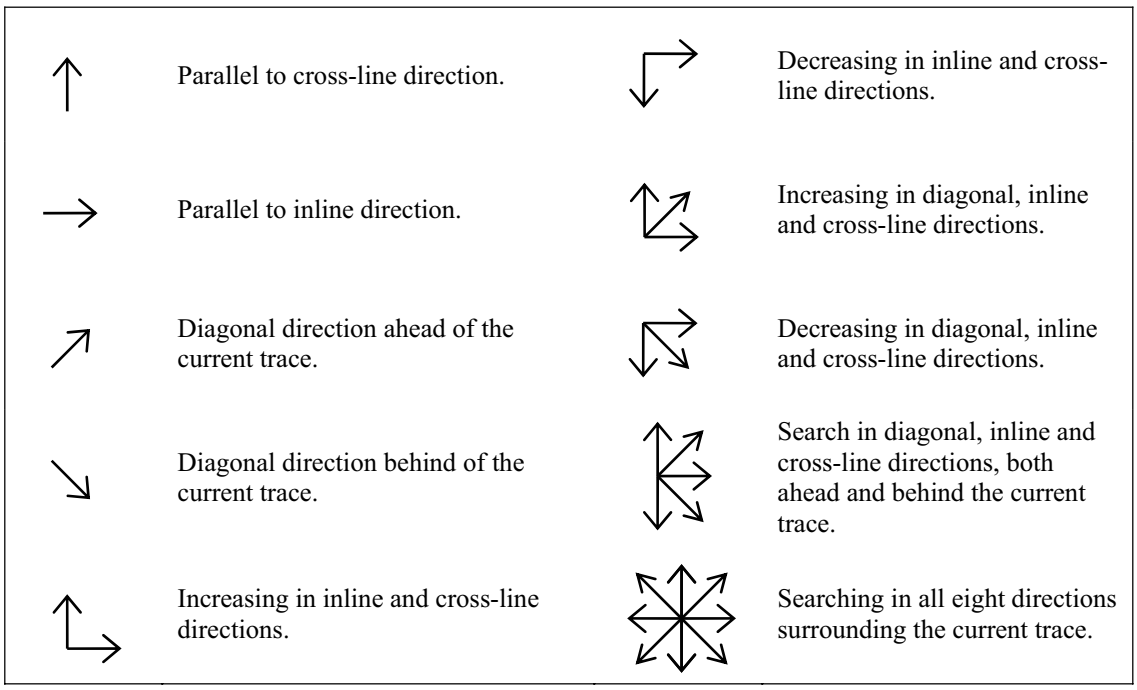

Figure 23. The different spatial search directions available in GeoFeature Mapping tool. These different searching patterns allow illuminating obscured features oblique to the normal inline and cross-line seismic lines.

Correlations estimated across interpreted horizons, such as sequence boundaries, constitute a very valuable tool. They can help in revealing and understanding the stratigraphy of the interval of interest as a stratal slicing method. Figure 24 shows a sequence of quality factor attribute maps produced above the N-sand interval. It illustrates the progress of valley incision and channeling across ancient shelf deposits of the late middle Miocene of the South Marsh Island area.

Different scenarios were investigated to understand the geology of the N-sand Interval. Quality factor attribute, which measures wavelet similarity between adjacent traces, proved to be the best attribute to expose subtle and obscured features embedded within the adjacent seismic traces of the N-sand interval. A datum is an offset above the N-sand interval horizon by 100ms.The correlation window is set to 25ms. A search window is set to 10ms. One half of this window will be placed above the correlation window, and one half will be placed below this window. This makes the correlation window to be equal to 35ms, which enhances the probability to find highly correlated traces. Finally, the step window is set to 5ms, and the number of steps is set to 40ms. An increasing in diagonal, inline and cross-line directions spatial search operator is used (Figure 24).

An attribute map is created every 5ms, covering an interval of 200 ms, centered on the N-sand interpreted horizon. The final attribute maps have a much higher lateral resolution than the conventional time slices. They are more intuitive to understand in terms of geology and stratigraphy, hence, they do not cut through seismic reflectors and they honor the conceptual models of sequence stratigraphy, when a datum is superimposed over a sequence boundary.

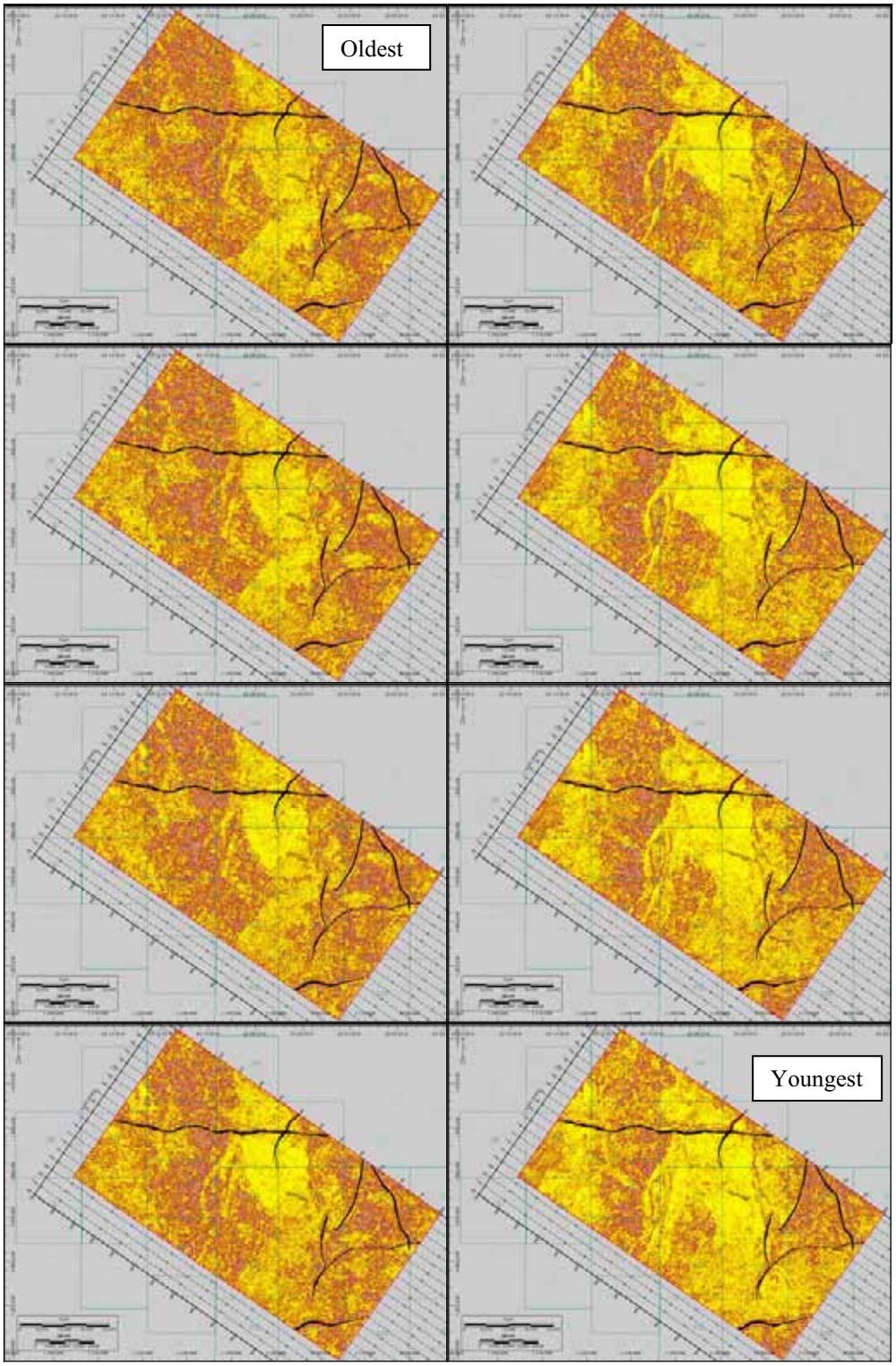

Figure 24. A quality factor attribute map created using a window offset of 100ms above the N-sand interval, showing the progress of valley incision and channeling patterns (yellow color) across an ancient marine shelf substrate (red color). Each map represents a window step 5ms.

3.5 Seismic attribute analyses

The different procedures used in seismic attribute analyses are shown in Figure 11, (see page 46) and are presented in the following sections.

3.5.1 Seismic attribute extraction

Seismic attributes are extracted as a result of mathematical operations performed on a typical seismic trace. In map-based seismic attributes, an attribute can be precisely extracted at an interpreted seismic event, or can also be extracted through a defined time window. Often, this time window may be specified between 2 interpreted horizons, from one seismic horizon to a certain time value, or between two time/depth values.

In order to control the extraction process, two phantom horizons were created above and below the N-sand interval (Figure 25). The two phantom horizons delineate an envelope centered on an interpreted event of the N-Sand, defining the upper and lower boundaries for attributes extraction.

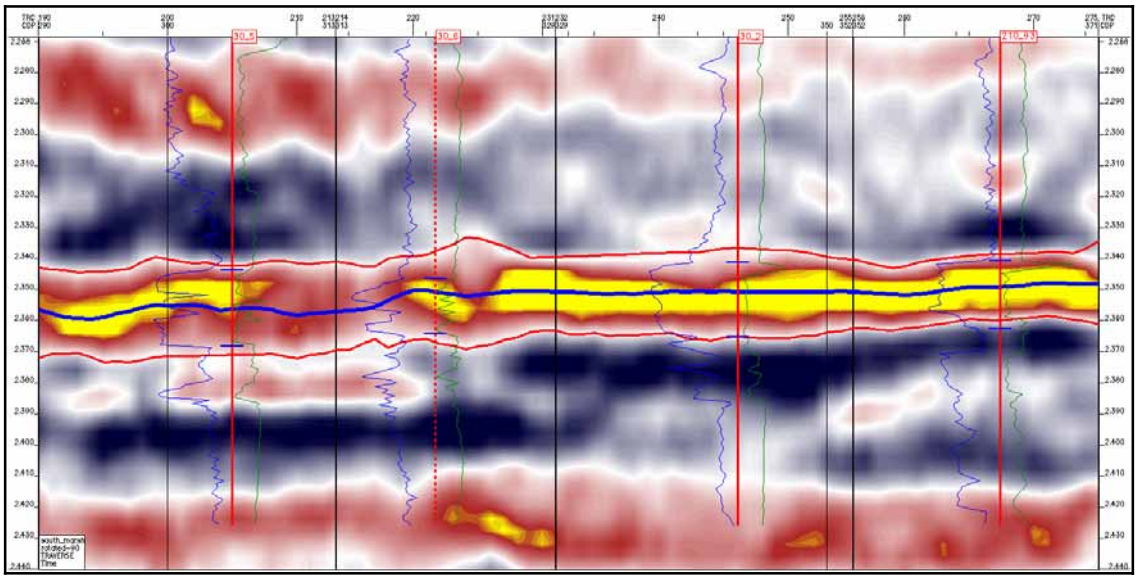

Figure 25. Vertical seismic section showing the two phantom horizons, in red color, centered on an interpreted blue event of the N-Sand. These two phantoms are used to define the upper and the lower boundaries for attributes extraction. (Troughs appear in hot color shades).

An a priori step for this procedure involves the accurate interpretation of the N-sand interval across the seismic survey. The classical approach of horizon tracking across inlines, cross-lines and closed loops is followed. Arbitrary traverses, normal to fault traces, are created, in order to track horizon interpretations across faulted surfaces (Figure 26). Subsequently, the autopicking tool is used to fill-in the gaps between interpreted inlines and cross-lines. The final product of autopicking is quality controlled and refined for accurate autopicking performance. Figure 27 shows a quality control map for the autopicking process, demonstrating the accurate autopicking result. Eighteen different attributes were extracted within an interval defined by 5ms above the upper phantom horizon and below the lower phantom horizon, shown in Figure 25. Finally, grid maps were created for each seismic attribute using a grid cell of 200x200ft, and the entire grid maps were quality controlled for any possible inadvertent errors. The extracted attribute maps successfully identified many anomalies regions that were also associated with previous drilling activities (Figure 28).

Table 3 shows a list of these attributes, a summary of their description, and their possible applications. The extracted seismic attribute maps are available in Appendix.

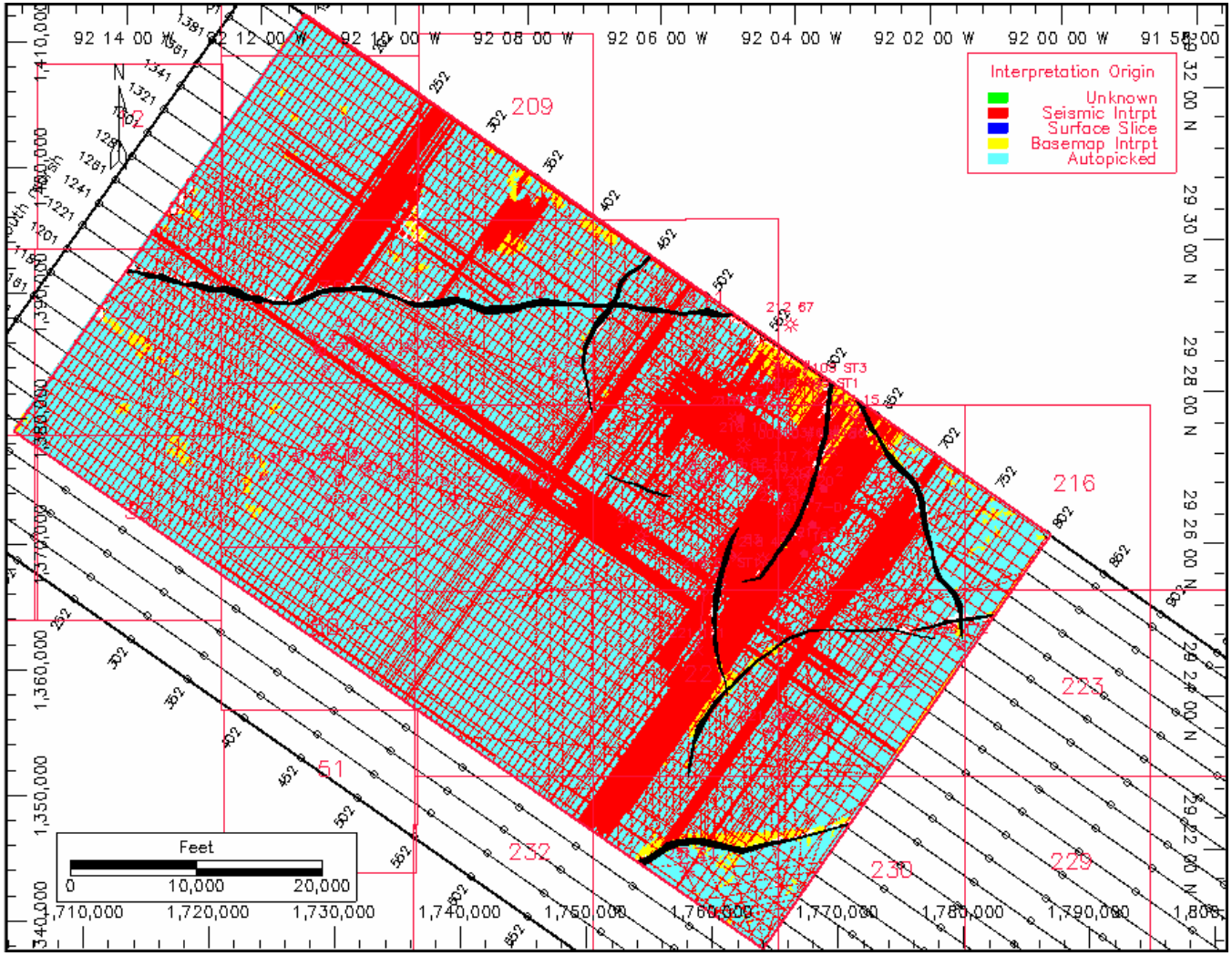

Figure 26. A map representation showing the origin of interpretation. Interpretation shown in red represents the manually picked seismic traces. Densely picked areas represent the regions of weak signal-to-noise ratio, low lateral continuities, due to attenuation or fault distortion.

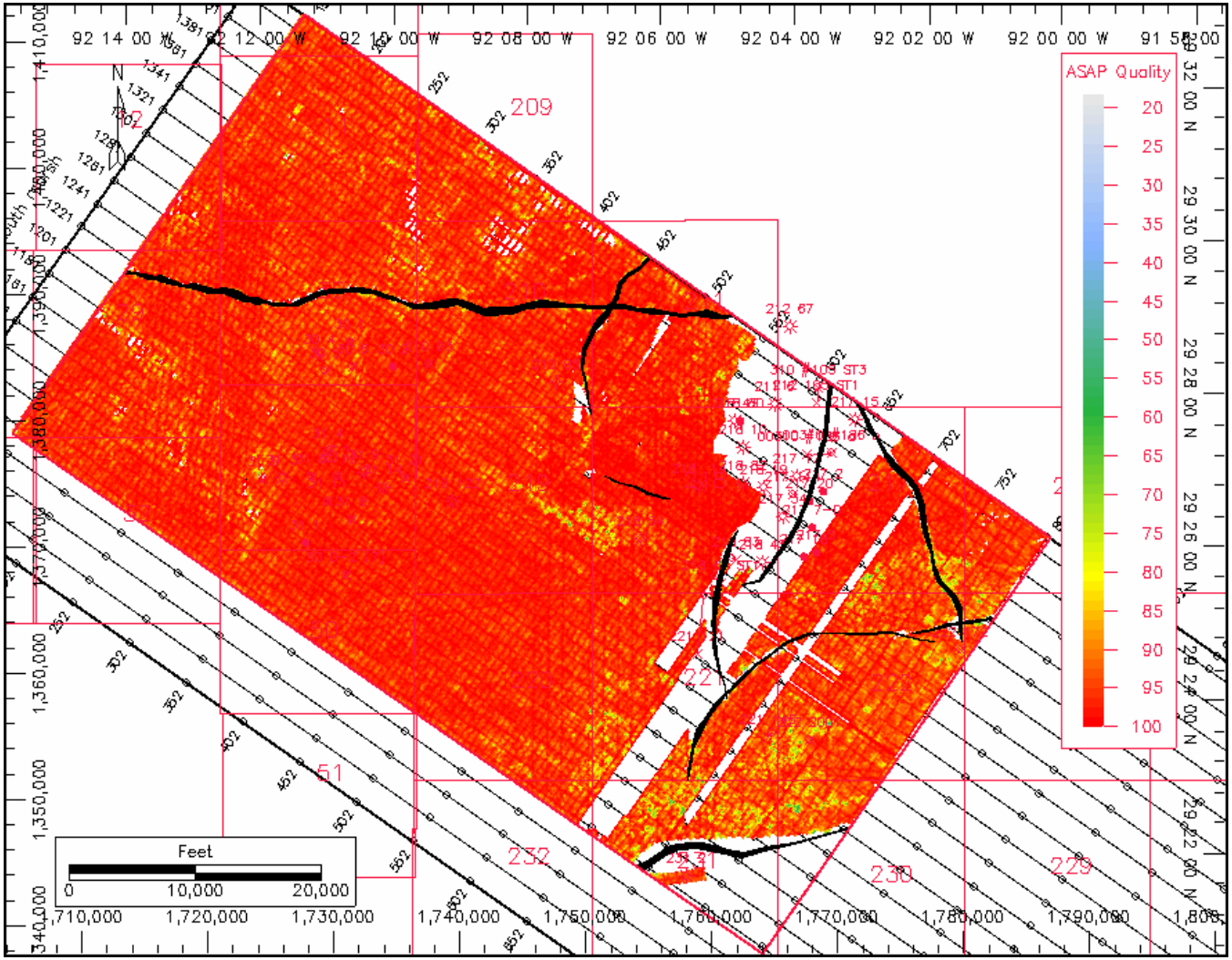

Figure 27. A map representation showing of the quality of the autopicking process. It is a measure of the correlation between autopicked interpretations and adjacent manually picked traces. The quality of the autopicking is highly correlated to its seedpicks (generally >90%).

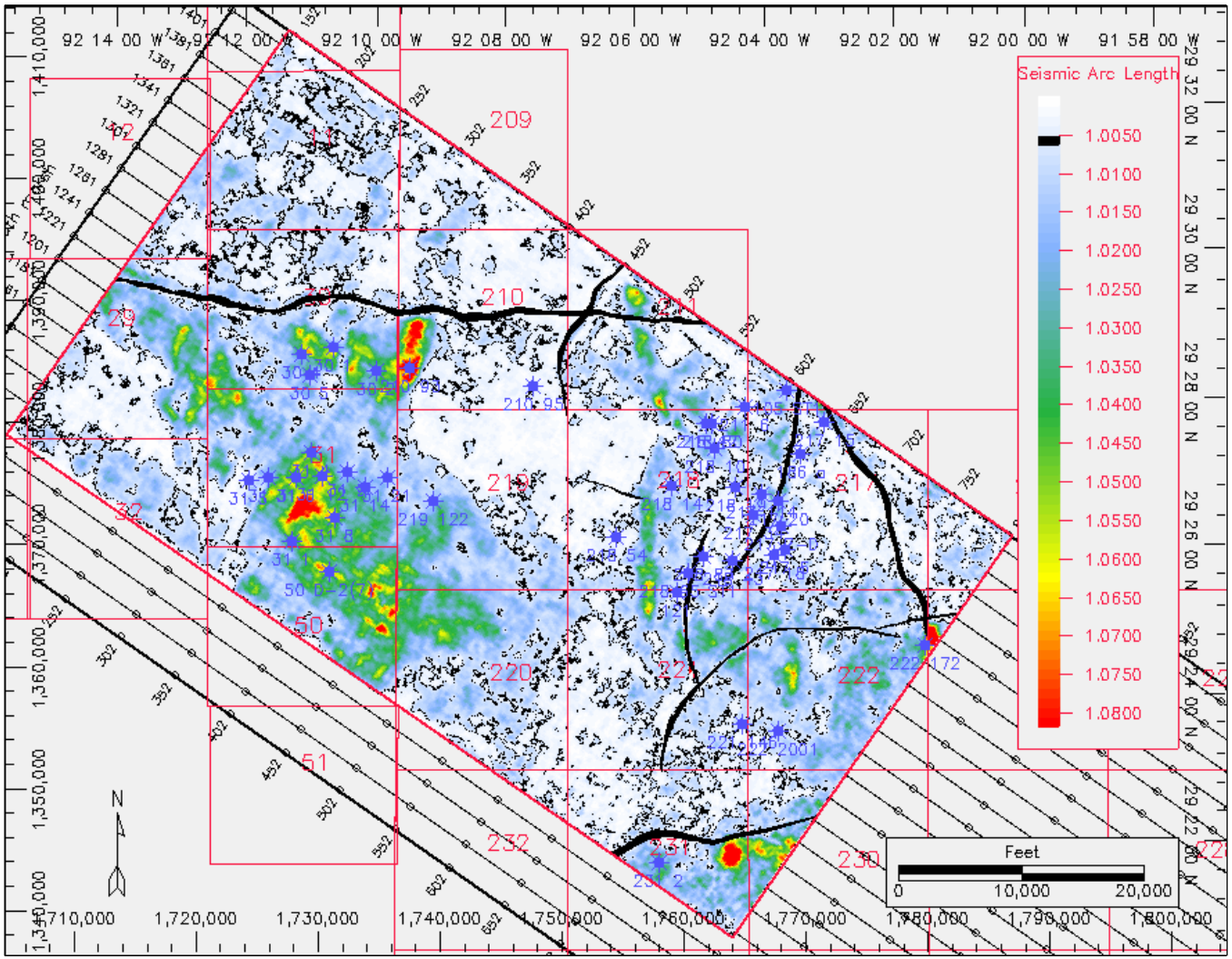

Figure 28. A map presentation of the Arc length seismic attributes, extracted within an interval of 5ms above and below of the two phantom horizons. Anomalies characterized by higher arc length values represent regions with heterogeneous sediment fill deposits.

Table 3. A summary table listing the 18 different extracted seismic attributes and their definitions and common applications. *

Attribute	Definition	Application**
Arc Length	Measure of the trace wiggle's length within the analysis window interval.	A measure of reflection heterogeneity which is used to quantify lateral changes in reflection patterns. Used as a stratigraphic sequence indicator.
Bandwidth Rating (Bias)	Statistical estimation of bandwidth of data within window. A measure of the frequency range in data, computed from the smoothed auto-correlation of the data.	A measure of reflection heterogeneity. It quantifies data similarity. Cyclic and shale sequences are presented by narrow bandwidth; However, widely varying lithologies more likely have a border bandwidth
Bandwidth Rating (Debias)	It is a statistical estimation of bandwidth of data within window. It is similar to Bandwidth Rating (Bias), but corrected for the bias effect of the smoother. This is usually the preferred measure of the bandwidth.	A measure of reflection heterogeneity. Generally more stable than Bandwidth Rating (Bias), unless window is small.
Half Energy	It is the proportion of time required for the "energy" within a window to reach one-half of the total energy within the entire window. It shows the relative distribution of energy in the window interval, where half of the energy is above, and half below.	A lithology and porosity indicator. A measure of reflection heterogeneity. May be used to identify uneven reservoir features along the zone of interest. The attribute may indicate changes in lithology or porosity within a specified zone.
Mean Instantaneous Frequency	It is the mean Instantaneous Frequency within a window. Instantaneous Frequency is the time derivative of Instantaneous Phase, when an analytic seismic trace is decomposed into amplitude and phase components.	Often used to estimate seismic attenuation. A drop in frequency is associated with horizon occurring below oil and gas reservoirs. Also, it helps to measure cyclicity of geological in windowed intervals.
Mean Instantaneous Phase	It is the Mean of Instantaneous Phase component of an analytical seismic trace when decomposed into amplitude and phase components (Hilbert transform technique).	This measure can be use to track events of discontinuities such as pinchouts, angular unconformities, and oil/gas or oil/water contacts along very limited windowed intervals.
Max Amplitude	Maximum value of peak or trough Amplitude values within the analysis window.	A measure of direct hydrocarbon indicators. Used to identify amplitude anomalies of Bright spots due to changes in lithology or hydrocarbon accumulation.
Max Magnitude	Maximum absolute value of Amplitude within the analysis window.	A measure of the strongest direct hydrocarbon indicators within the analysis window.

Mean Amplitude	Average (mean) value of amplitude within the analysis window.	Commonly used for facies and reservoir property mapping. Bright spot indicator, where high sand/shale ratio show higher Amplitude values.
Mean Magnitude	Average absolute value of Amplitude within the analysis window.	This attribute may be used as a direct hydrocarbon indicator in a zone.
Mean Trough Amplitude	Average of the amplitudes of waveform troughs.	Lithology and porosity indicator.
Min Amplitude	Minimum value of Amplitude.	A measure of the negative direct hydrocarbon indicators within the analysis window.
Number of Zero Crossing	The average number of zero crossings within the analysis window.	A measure of horizontal and vertical lithology changes. A high number of zero crossings indicate a great degree of vertical lithology complexity (i.e. a thick sequence of thin beds).
Polarity Ratio	Ratio of number of positive samples to total number of samples.	A main lithology and porosity indicator. Used to detect lateral changes in thickness, and lithology.
RMS Amplitude	A measure of reflectivity within a time window. The square root of the sum of time-domain energy (square of amplitude) within the window interval.	Indicates isolated or extreme amplitude anomalies. Used to track lithologic changes such as deltaic channel and gas sand, and used mainly as a direct hydrocarbon indicator.
Sum of Amplitudes	Sum of Amplitude values within the window interval.	A lithology and porosity indicator. A Large value may indicate a high net-to-sand ratio, or a high porosity interval.
Sum of Magnitudes	Sum of the absolute Amplitude values within the analysis window.	A lithology and porosity indicator. Used to characterize sequences and indicate amplitude anomalies due to changes in lithology or hydrocarbon accumulation.
Sum of Negative Amplitudes	Sum of the negative Amplitude values within the analysis window.	A lithology and porosity indicator. A Large value may indicate a high net-to-sand ratio, or a high porosity interval.

* Summarized from Sukmono, 2001; GeoFrame 4.0 documentation, 2002; Chen and Sidney, 1997.

** Gray shaded attribute indicate a main direct hydrocarbon indicator, whereas white shaded attributes indicate a main a lithology and porosity indicator.

3.5.2 Multivariate statistical analysis of seismic attributes

Multivariate statistics refer to a variety of statistical methods that have been developed to handle conditions in which multiple variables or measures are involved (Marcoulides and Hershberger, 1997). Since each seismic attribute represents a subset of the total information contained within the real earth model (Barnes, 2001), multivariate statistics can be employed to adequately elucidate and understand the multiple relationships among these different seismic attributes.

This study is interested in two types of multivariate statistics; *Principal Component Analysis (PCA) and Principal Factor Analysis (PFA*). Principal Component Analysis and Principal Factor Analysis are employed with an aim to reduce the dimensionality of a data matrix and the noise associated with the extracted attributes. This is achieved by reducing the number of basis vectors that are used to model the data, which might reveal simpler patterns within a complex set of variables. Factor analysis can further reduce the matrix of data to its lowest dimensionality by the use of orthogonal factor space. The results of PCA and PFA are considered as multivariate statistically-generated seismic attributes, which are used later as inputs for the final step of geostatistical log properties mapping.

3.5.2.1 Data preparation

The 18 seismic attribute grids were converted back to seismic horizons. These new horizons were re-sampled and exported in ASCII format; such that every other inline and cross-line reading is reserved (each exported file contains one fourth of the original grid points ~52,220 samples). This process minimized the time and space needed for mathematical computations into one fourth of the original size, without compromising the fundamental feature of spatial coverage of seismic data.

Most of the multivariate statistical techniques are based on the assumption that the data were generated from a multivariate normal distribution (Johnson and Wichern, 1998). The central limit theorem states that given a distribution with a mean μ and variance σ^2, the sampling distribution of the mean approaches a normal distribution with

a mean (μ) and a variance σ^2/N as N, the sample size, increases. Accordingly the central limit theorem allows relaxing the prerequisite of normality in a case of a large sample size (Johnson and Wichern, 1998; Marcoulides and Hershberger, 1997). However, it is recommended to assess the assumption of normality for all multivariate distributions. Usually, it is sufficient to investigate the univariate and bivariate distributions of each variable (Marcoulides and Hershberger, 1997).

The assumption of normality was checked by investigating univariate density plots and Q-Q plots for each extracted seismic attributes. Additionally, bivariate plots were investigated to also examine bivariate normality. If the samples were generated from a multivariate normal distribution, each bivariate distribution should also be normal (Marcoulides and Hershberger, 1997). This implies that the contours of a bivariate distribution would be ellipses, and any plot should conform to this structure by exhibiting a pattern that is approximately elliptical in shape. Some of these plots showed some skewness in their distribution, which were transformed into normal distribution by applying appropriate transformations.

Only six attributes proved to be slightly skewed. The natural log transformation was applied to the mean magnitude, mean instantaneous frequency and maximum magnitude attributes, meanwhile the square transformation was applied to the root mean square (RMS) amplitude, max amplitude and sum of magnitudes attributes. Figure 29 shows an example of normal density distribution plots of bandwidth rating (debais), maximum magnitude seismic attributes. In this example, maximum magnitude was transformed to normality by using the natural log transformation.

The final step in data preparation was to standardize all the extracted seismic attributes. This step is very crucial due to the fact that multivariate statistics are not scale invariant especially in the case that the original variables have different ranges and different units.

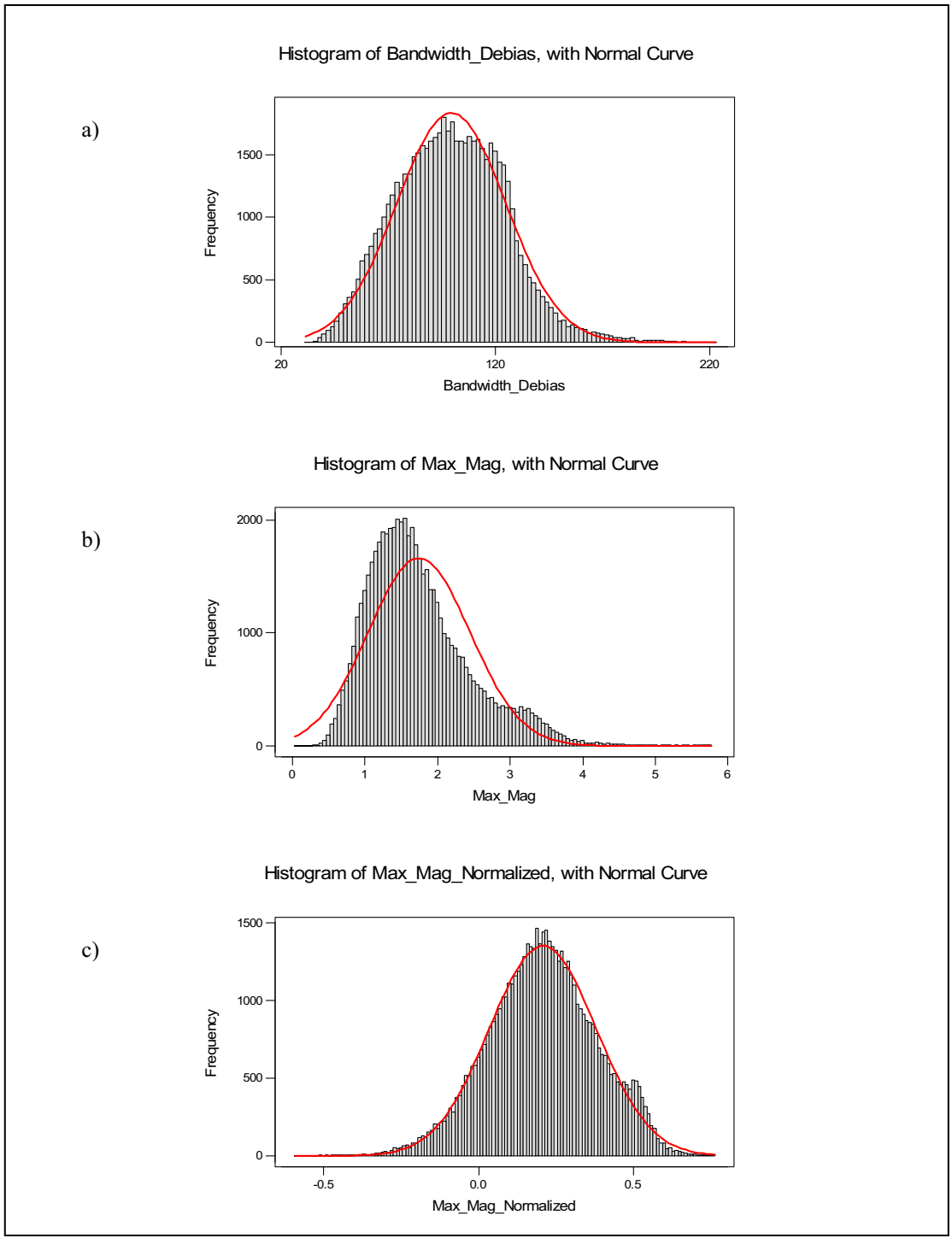

Figure 29. Normal density distribution plots showing (a) Bandwidth rating (debias) attribute; (b) Maximum magnitude attribute; and (c) Maximum magnitude after natural log transformation. Bandwidth debias attribute shows a clear normal distribution pattern, meanwhile maximum magnitude is positively skewed distribution, which is transformed into normality by using a natural log transformation.

The standardized transformation is used to standardize the normalized seismic attributes (Marcoulides and Hershberger, 1997). It causes all the different scales to be converted into a single standard distribution, which has a mean (μ) of zero and a standard deviation (σ) of 1. Assuming that the condition of normality is met, the final standard normal distribution can be visualized as the single reference distribution for comparing a wide variety of otherwise not comparable statistics.

3.5.2.2 Principal component analysis (PCA)

Principal component analysis (PCA) is concerned with explaining the variance-covariance structure of a data set of observed variables through a few linear combinations of these variables (Johnson and Wichern, 1998). This method is probably the most frequently used one in applied multivariate statistics (Reyment and Savazzi, 1999). Its general objectives are (Johnson and Wichern, 1998):

- Data reduction: The variability contained in the original data set, consisting of (p) variables, can often be accounted for by a smaller number (k) of principal components. Although the original data set consists of (p) variables, there is almost as much information in the (k) components as there is in the original (p) variables. The original data set consisting of (n) observations on p variables can be reduced to one consisting of (n) observations on (k) principal components.
- Interpretation: PCA can reveal obscure relationships that were not previously suspected, allowing for possible interpretations that would not typically result.

PCA can summarize the variation in a correlated multivariate data with a set of uncorrelated components, each of which is a particular linear combination of the original variables. Geometrically, these linear combinations represent a new coordinate system obtained by rotating the original coordinate system, such that the first principal component (PC1) is the axis of closest fit to the n observation. Equivalently, the second principal component (PC2) is orthogonal to the first principal component and is an axis of closest fit to the residuals from the first principal component (Dunteman, 1989; Johnson and Wichern, 1998).

The resulting PCs are extracted in a decreasing order of importance so that the first PC accounts for as much of the variation as possible and each successive component accounts for less.

Let the random vector $\boldsymbol{X} = (X_1, X2, \ldots, X_p)$ have the correlation matrix $\boldsymbol{R}$. Let **R** have the eigenvalue-eigenvector pairs $(\lambda_1, \boldsymbol{e}_1)$, $(\lambda_2, \boldsymbol{e}_2)$, ..., $(\lambda_p, \boldsymbol{e}_p)$ where $\lambda_1 \geq \lambda_2 \geq \ldots \geq \lambda_p \geq 0$. Then the *ith* Principal Component can be defined as (Johnson and Wichern, 1998):

$$\text{PC}i = \mathbf{e}_i' \mathbf{X} = e_{i1}x_1 + e_{i2}x_2 + \ldots + e_{ip}x_p, \quad i=1, 2, \ldots, p$$

such that, for each principal component of (i), Var($\mathbf{e}_i' \mathbf{X}$) is maximized, $\mathbf{e}_i' \mathbf{e} = 1$ and Cov($\mathbf{e}_i' \mathbf{X}, \mathbf{e}_{i+1} \mathbf{X}$)=0.

The percent of the total variance explained by each principal component is defined accordingly:

$$\%\text{Variance (PC}_i\text{)} = \left(\lambda_i \cdot 100\right) / \sum_{i=1}^{p} \lambda_i$$

where λ_i is the ith eigenvalue of the correlation matrix (**R**), so that $\sum_{i=1}^{p} \lambda_i$ equals to (p).

Unfortunately, it is not possible to tell exactly how many principal components or factors are needed to adequately describe the total variance of the observed variables. However, several different methods have been proposed to answer this question (Dunteman, 1989; Marcoulides and Hershberger, 1997; Johnson and Wichern, 1998):

1. Retain only those PCs whose eigenvalues of (**R**) are greater than unity.
2. Retain all PCs, such that their cumulative variance is greater than a certain threshold (i.e. 80-90%).
3. Scree plot test, where the eigenvalues of (**R**) are plotted against their ordinal number, then retain all PCs before the curve becomes nearly horizontal.

In general, PCs can be extracted by using the covariance matrix or the correlation matrix of the observed variables. The use of the correlation matrix is preferred when dealing with variables with diverse units and different ranges. However, for large size samples, the results obtained by either method should be very similar (Dunteman, 1989).

The correlation matrix, shown in Figure 30, indicates that some of the extracted seismic attributes are possibly correlated. Therefore, PCA was applied to the extracted and seismic attributes, aiming to reduce the dimensionality of the whole data set by reducing redundancy between any similar attributes. In this study, the correlation matrix method was used for principal components extraction. The final results were gridded and used as inputs in subsequent geostatistical reservoir log property mapping.

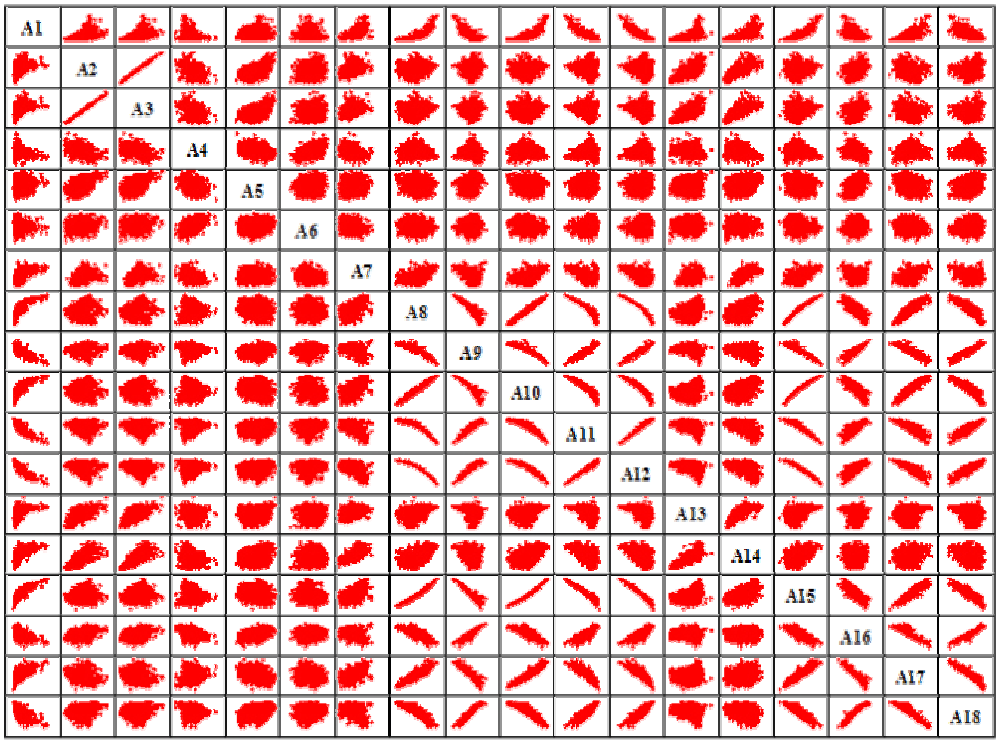

A1 = Arc Length
A2 = Bandwidth Rating (Bias)
A3 = Bandwidth Rating (Debias)
A4 = Half Energy
A5 = Mean Instantaneous Frequency
A6 = Mean Instantaneous Phase
A7 = Max Amplitude
A8 = Max Magnitude
A9 = Mean Amplitude
A10 = Mean Magnitude
A11 = Mean Trough Amplitude
A12= Min Amplitude
A13 = Number of Zero Crossing
A14 = Polarity Ratio
A15 = Root mean square (RMS) Amplitude
A16 = Sum of Amplitudes
A17 = Sum of Magnitudes
A18 = Sum of Negative Amplitudes

Figure 30. Correlation matrix for the 18 extracted attributes. The degree of correlation between some attributes indicates that applying principal component analysis would be beneficial to reduce the dimensionality of the data base.

3.5.2.3 Principal factor analysis (PFA)

Factor Analysis (PFA) can be considered as an extension of PCA. Although the two methods have the common aim of reducing the dimensionality of a data set there are clear differences between them with regard to their goal of the analysis and, therefore, their methods for estimation (Dunteman, 1989; Johnson and Wichern, 1998).

A basic dissimilarity between PFA and PCA is that there is a model underlying factor analysis but no such model exists in PCA (Jolliffe, 1986). Thus, PFA attempts to describe the covariance or correlation relationships among many variables in terms of few underlying, unobserved, random quantities named as factors.

The factor analysis assumes that it is possible to assign the different observed variables into different groups based on their correlations, such that all variables within a given group are highly correlated among themselves, but have relatively small correlations with variables in different groups. Then it is probable that each group of variables correspond to a single underlying factor that is responsible for the observed correlation (Johnson and Wichern, 1998). Accordingly, PFA uses a reduced form of the correlation matrix aiming to explain the common variance, which is the amount of variance shared with other variables. On the other hand, PCA tries to explain the total variance between observed variables.

Let the random vector $\boldsymbol{X} = (X_1, X2, \ldots, X_p)$ have the correlation matrix (**R**). Then the factor analysis model can be defined as (Johnson and Wichern, 1998):

$$\mathbf{X}=\mathbf{LF}+\boldsymbol{\varepsilon}$$

where each (**L**) represent the matrix of factor loadings, (**F**) is the matrix of underlying common factors, and ($\boldsymbol{\varepsilon}$) is a matrix of error of measurements, known as specific factors. Then the *i*th observed variable can be decomposed into a smaller number of common factors (m) as follows:

$$X_i = l_{i1}F_1+l_{i2}F_2+\ldots+l_{im}F_m+\varepsilon_i$$

In factor analysis, the portion of variance of the *i*th variable contributed by the (m) common factors is called the *i*th *communality* (h_i^2), and the portion of $\mathrm{Var}(X_i)=\sigma_{ii}$

due to the specific factor is called the *specific variance*, or *uniqueness* (ψ_i), which is the unexplained or random variance for a variable (Johnson and Wichern, 1998), as follows:

$$\sigma_{ii} = h_i^2 + \psi_i$$

where the *i*th communality is the sum of the squares of the loadings of the *i*th variable on the reduced (m) factors (i.e. $h_i^2 = l_{i1}^2 + l_{i2}^2 + ... + l_{im}^2$).

The estimation of (**L**) and (**ψ**) is the core procedure in factor analysis. It can be achieved by using any of these two popular methods: the Principal factor method and the Maximum likelihood method (Johnson and Wichern, 1998). The results of principal factor analysis are presented in this study. However, initial results using both procedures proved to be very consistent.

In principal factor analysis, PCA is used to generate a set of initial factors from which to start an iterative procedure that continues until the factor loading matrices converge (i.e. until further gains in the communality explained are negligible). This procedure is very useful in exploring the structure of the data set when no particular underlying model in the data set is in mind (Dunteman, 1989).

Once the loadings and specific variances are estimated, factors are identified and factor scores are estimated. Factor scores are estimates of values for unobserved random factor vectors (Johnson and Wichern, 1998). It is very common to impose some constraints when estimating the score factors, such that loading values below certain threshold, (i.e. 0.3-0.4), can be considered as unimportant and, eventually, can be discarded (Johnson and Wichern, 1998).

The final step in PFA is to interpret its results. In order to simplify the interpretation of factor analysis, a priori step may involve rotating the loading victors aiming to reveal useful factor patterns. Moreover, estimated loadings may be constrained, such that loading values below certain threshold can be considered as not important and eventually may be discarded. Further discussion concerning the methods

of PFA estimation, and factor rotation can be found in Johnson and Wichern (1998) and Marcoulides and Hershberger (1997).

In this study, PFA is employed to achieve a number of goals. The first is to understand the underlying structure giving rise to the different extracted seismic attributes. The second one is to reduce the dimensionality of the whole data set by reducing the redundancy between similar attributes. The last goal is to generate a new set of attributes, so that the resulting factor scores are able to describe most of the common variance, to be used as inputs for subsequent geostatistical reservoir log property mapping.

The following points summarize the different criteria used in this study:

- Following the same criteria used in retaining the appropriate number of PCs (Marcoulides and Hershberger 1997), 3 orthogonal factors are used to explain the common variance, such that their eigenvalues were greater than unity.
- Varimax rotation of factors is applied. This rotation results in maximizing the variance between orthogonal factor loadings and tends to simplify the interpretation of each factor (Marcoulides and Hershberger 1997).
- Loadings less than 0.3 are considered unimportant and are discarded from factor score computation.

3.6 Well log analyses

3.6.1 Multi-well normalization

The wireline log data used in this study were collected over a long period of exploration and production from the fields of Tiger Shoal and Vermilion 50. Experience had shown that about 50 percent of all logs are expected to need some normalization to correct for discrepancy in field calibrations of logging tools (Hunt et al., 1996). In such case, multi-well normalization is an essential prerequisite to ensure accurate, consistent and comparative results from multi-well log analysis (Aly et al., 1997).

Histogram normalization is used to correct log data for errors resulting from inaccurate field tool calibrations (Aly et al., 1997). This process involves three steps: First, a multi-well histogram of all the data is generated, and the data of wells closer in agreement were used to construct a standard histogram representing the correctly calibrated well logs for the interval. Second, an individual histogram is generated for each well not complying with the standard histogram. Finally, each individual histogram is correlated to the standard histogram and shifted accordingly to achieve proper correlation.

Figure 31 shows an example of standard histogram used to normalize neutron porosity log data. Initial investigation of neutron porosity log (NPHI) showed that the wells 30-1, 30-4, 210-93, 31-4, and 31-12 are highly correlated to each other; thus, they were used to construct an initial standard histogram. A good correlation is demonstrated between well 31_12 (named as target data) and the standard histogram (named as key data). Thus, no normalization is needed and well 31-12 is combined with the standard histogram and used to normalize the other well log data. An example of normalized log data is shown in Figure 32, displaying an example from well 31-5 before and after normalization.

Aly and others (1997) mentioned that 50 percent of density logs and 40-50 percent of neutron density logs may require some normalization; accordingly, this

process was applied to the bulk density, neutron porosity and density porosity log data. The results are used in subsequent steps of petrophysical analysis.

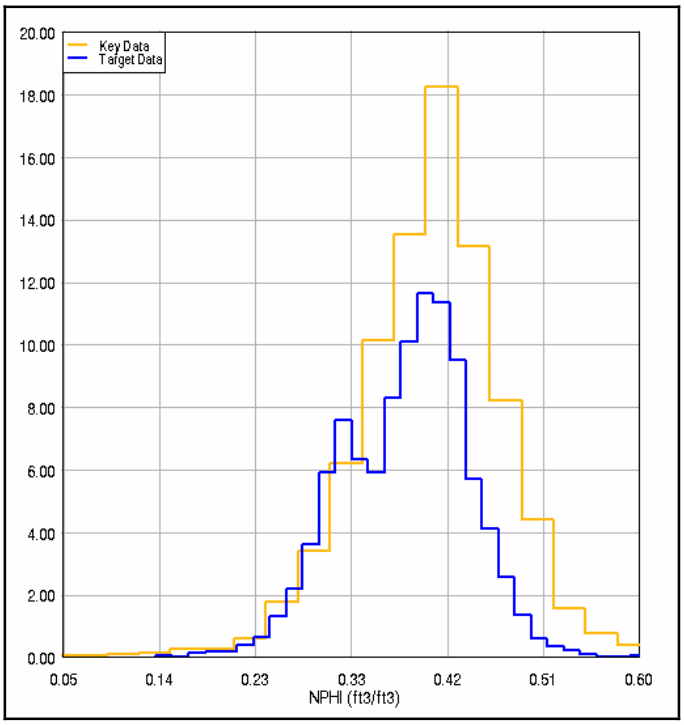

Figure 31. Neutron porosity log histogram. The standard histogram is correlated well log data. Key data represent data of the following wells: 30_1, 30_4, 210_93 and 31_4. The target data is from well 31_12. Notice that no normalization is needed in such case. Frequency is plotted on the vertical axis.

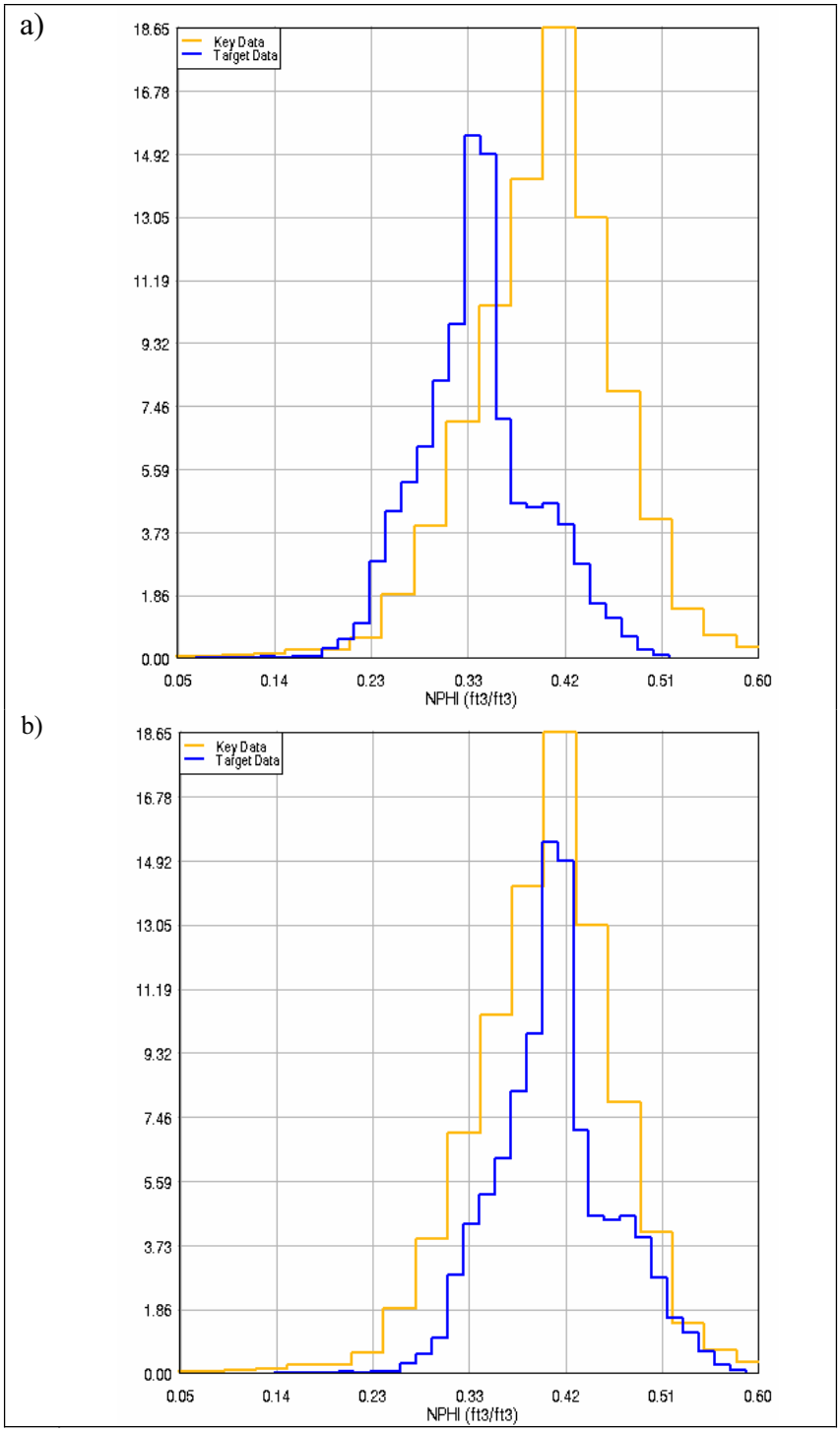

Figure 32. Neutron porosity log data of well 31_5 before normalization (A), and after normalization (B).

3.6.2 Petrophysical analysis

Certain petrophysical and reservoir properties are estimated in this study. The results of this analysis are summed and averaged over the N-sand interval. Petroview Plus, a product of Schlumberger, is used assuming a *ShalySand model* (Asquith, 1990).

3.6.2.1 Shale volume (V_{sh}) estimation

Shale volume is defined as the ratio of the volume of shale to the bulk volume of the rock. The V_{sh} can be estimated using the logs of gamma ray, SP and neutron porosity. However, the neutron porosity technique was avoided due to the fact that the N-sand interval is a gas-charged sandstone deposits, as shown in Figure 33. Gamma ray and Sp logs were used to estimate the volume of shale content. Following the approach outlined by Asquith (1990), the minimum estimate between the two logs was retained to provide a best estimate of clay volume when both curves are available. Shale volume, known as shale index, was estimated using the following equations:

$$V_{sh}=(GR_{log}-GR_{clean})/(GR_{shale}-GR_{clean})$$

$$V_{sh}=(SP_{log}-SP_{clean})/(SP_{shale}-SP_{clean})$$

N-sand interval deposits were deposited during the Miocene, which are considered as unconsolidated sediments. Figure 34 shows that unconsolidated rocks tend to show overestimated shale volumes (Asquith, 1990). Accordingly the V_{sh} estimates were corrected for this effect using the Larionov nonlinear model of Tertiary-rocks, as follows (Asquith, 1990):

$$V_{sh.unconsolidated}=0.0834(2^{3.7*Vsh}-1)$$

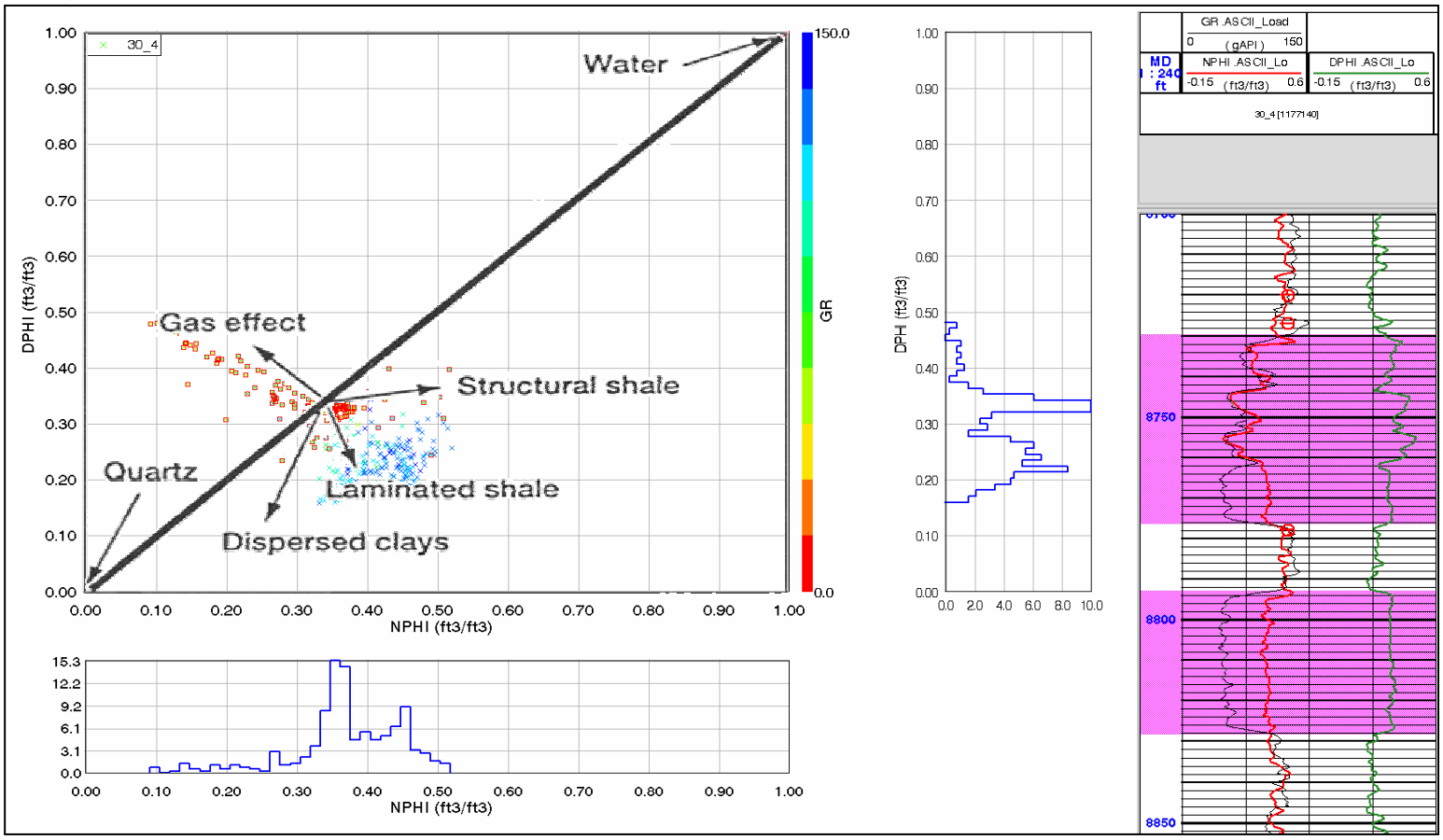

Figure 33. Density porosity-neutron porosity crossplot of well 30-4. Gas effect tends to shift the sample points up the 45º line, thus lowering the neutron porosity values. Shale free and water-filled samples fall on the 45ºline. The effect of shaliness tends to displace the sample points below the line, depending on the type of clay present, thus increasing the neutron porosity values. Highlighted points in red are those shown in the adjacent strip log presentation. (Overlay is modified after Hunt and Pursell, 1997).

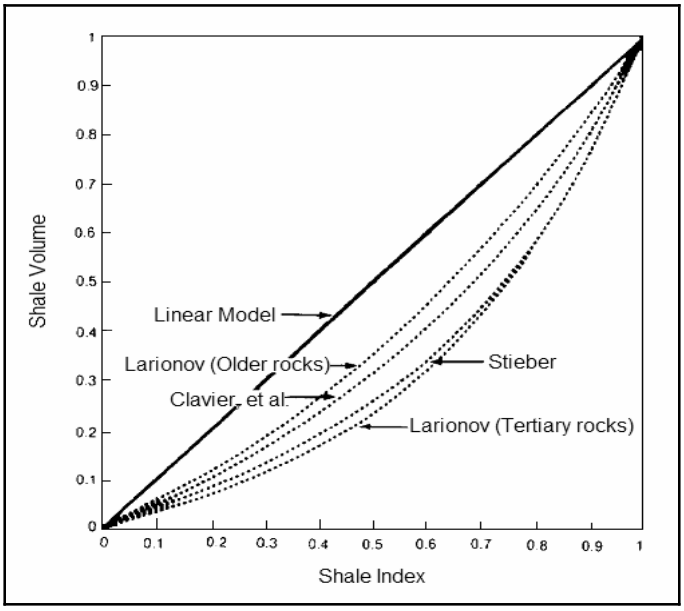

Figure 34. Nonlinear shale volume chart (after Alberty, 1992).

3.6.2.2 Porosity estimation

In general, the presence of shale causes all porosity logs to read higher values of porosity (Asquith, 1990). On the other hand, the presence of hydrocarbons adversely affects neutron, density and acoustic log responses.

Figure 35 shows a correlation between shale-free core porosity and the logs of neutron and density porosity of wells 30-2 and 30-4. Due to the presence of gas, porosities derived from neutron logs are underestimated. Meanwhile, density porosity logs demonstrate a more accurate estimate of porosity (Figure 36).

Accordingly, the volume of porosity was calculated using normalized bulk density logs (RHOB). Aiming to estimate the effective porosity, the density porosity was also corrected for shale content, as follows (Asquith, 1990):

$$\phi_e = \frac{\rho_{ma} - \left[\rho_b + V_{sh}(\rho_{ma} - \rho_{sh})\right]}{\rho_{ma} - \rho_f}$$

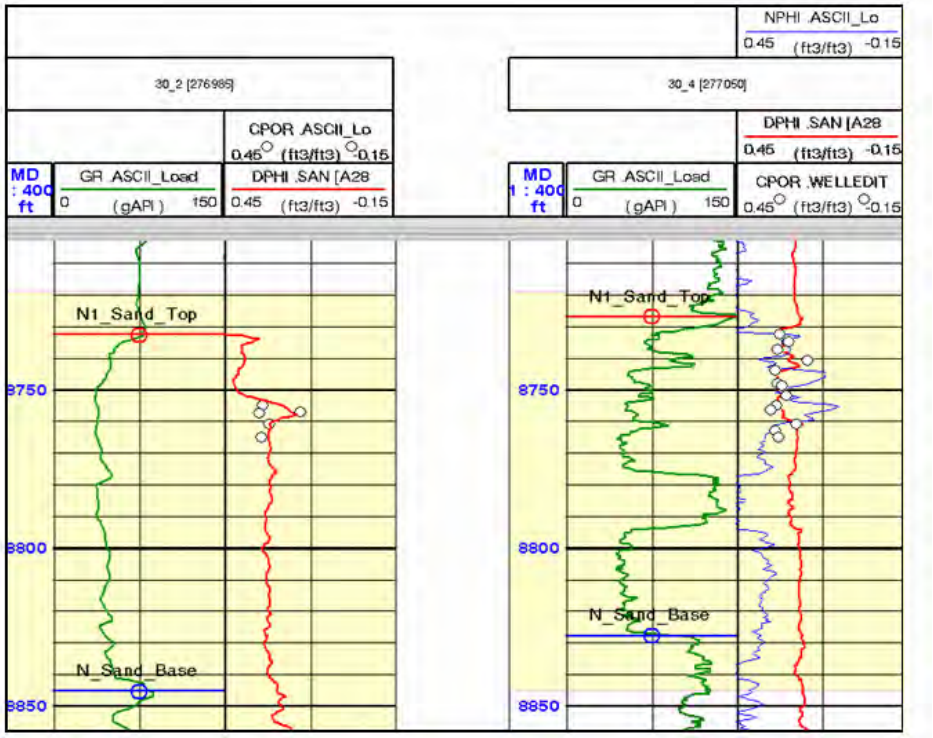

Figure 35. Strip log presentation of wells 30-2 and 30-4 indicating a good correlation is observed between core porosity and density porosity logs. Core-to-log scatter plot is shown in Figure 36.

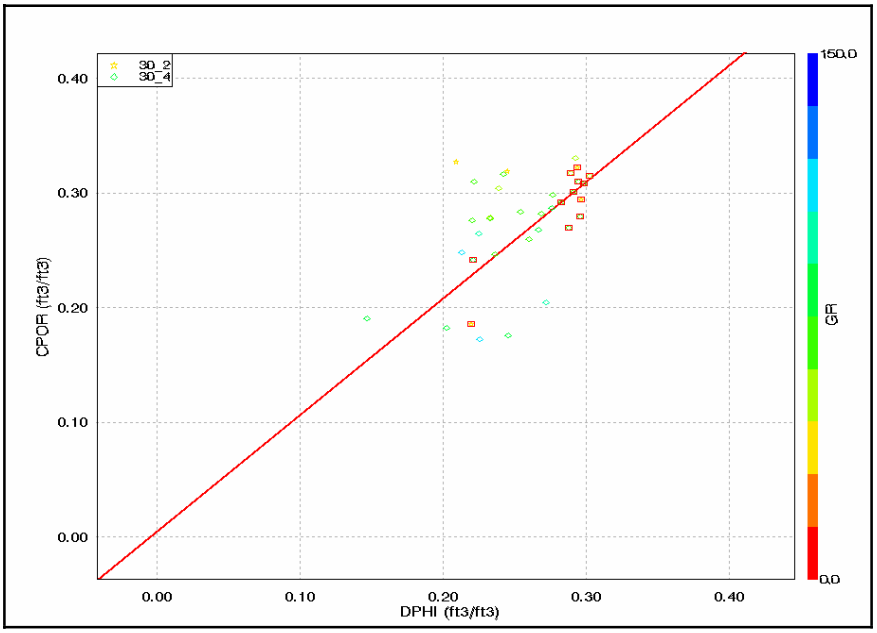

Figure 36. Core-to-log scatter plot illustrating the correlation between core porosity of wells 30_2 and 30_4 and density porosity logs. The highlighted points represent shale-free samples within the N-sand interval. Fitting is produced by reduced major axis regression technique.

3.6.2.3 Water saturation estimation (Sw)

The empirical equation of Archie's (1942) represents the keystone model for the estimation of pore water saturation in a shale-free environment. A shaly-sandstone reservoir is described as a difficult lithology (Hashmy and Alberty, 1992). The presence of shale causes the resistivity logs to read lower values, leading to overestimate of the volume of water saturation.

A number of methods were developed to provide an accurate estimate of water saturation in a shaly sandstone medium. Most of these methods are extensions of the very basic equation of Archie's (1942), thus, at zero shale content, these equations collapse to the Archie equation. For small amounts of shale content, most of these models provide comparable results. Further discussion regarding these models can be found in Schlumberger (1999).

Among many, the models of the Waxman and Smits (Waxman and Smits, 1968) and the Dual Water (Clavier, et al., 1977) are commonly used to estimate the volume of water saturation in the presence of shaliness (Hunt, 1997). Both models can be used in all water salinity environments and they can handle moderate amounts of dispersed clays (Hashmy and Alberty, 1992). However, the shale content of the N-sand interval is mostly present in the form of laminated shale; dispersed shale does not exist (Figure 34). Accordingly, any of these methods can be used to give an estimate of water saturation of the N-sand interval.

Hunt (1997) proposed an empirical methodology for model selection. It is based on the contrast between the value of the equivalent water resistivity (R_{we}) of a shaly sands and the equivalent water resistivity ($R_{we} = R_w$) of a clean sand medium. Multi-well Pickett plot is generated using clean data points (V_{sh}=0-10%), and the resistivity value obtained from this plot represents the formation water resistivity value (R_w). Another plot is generated using shaly sand points (V_{sh} =10-20%), and the value of the equivalent water resistivity (R_{we}) is estimated. If the data points shift down due to the effect of shale, then (R_{we}) is lower than (R_w), and the Waxman and Smits model is used in water

saturation calculations. The other scenario will cause the data points to shift up, the (R_{we}) is greater than (R_w), and as a result, the Dual Water model is the correct model to use.

Figure 37 shows a comparison between two Pickett plots generated using data from the wells 30-1, 30-2, 30-4, 30-6, 31-4, 31-5, 31-6, 31-8 and 50-D-2(7). Based on Hunt's criterion, the Dual Water model is used to give an accurate estimate for water saturation for the N-sand interval. The Dual Water model can be written as follows (Schlumberger, 1999):

$$\frac{1}{R_t} = \frac{\phi_t^m s_{wt}^n}{a}\left[\left(\frac{s_{wt} - s_{wb}}{s_{wt}}\right)\frac{1}{R_w} + \left(\frac{s_{wb}}{s_{wt}}\right)\frac{1}{R_{wb}}\right]$$

where ϕ_t is total porosity, S_{wt} is water saturation of the noninvaded zone, S_{wb} is the bound water saturation and equals the fraction of the total pore volume occupied by bound water, a is an empirically determined constant known as the tortuosity factor, m is the cementation factor, n is the saturation exponent, R_t is the resistivity of the noninvaded zone, R_w is the resistivity of formation water, R_{wb} is the resistivity of bound water.

The different parameters used to estimate the volume of water saturation of the N-sand interval, using the Dual Water model, are summarized as follows: a, m, and n factors are assumed to be equal to 1, 2 and 2, respectively, R_w is estimated from Pickett plots of clean sand sample points, V_{sh}<10%, for each well, the deep induction log is used for R_t, R_{wb} is estimated from the resistivity of adjacent shale samples, and finally, S_{wb} equals to the difference between the total porosity and the effective porosity divided by the total porosity, which was estimated in the earlier. Figure 38 represents an example of the final results of well log analyses of well 30-4.

Unfortunately, some of the well logs used in this study lack their header information. Additionally, no special core analyses were available to this study. Subsequently, fundamental information to saturation analysis such as, measured saturation exponent (n), cementation exponent (m), surface and bottom-hole temperatures, formation water resistivity and resistivity of mud filtrate, are missing. This fact imposes some degree of uncertainty, especially when it comes to the estimation of water saturation.

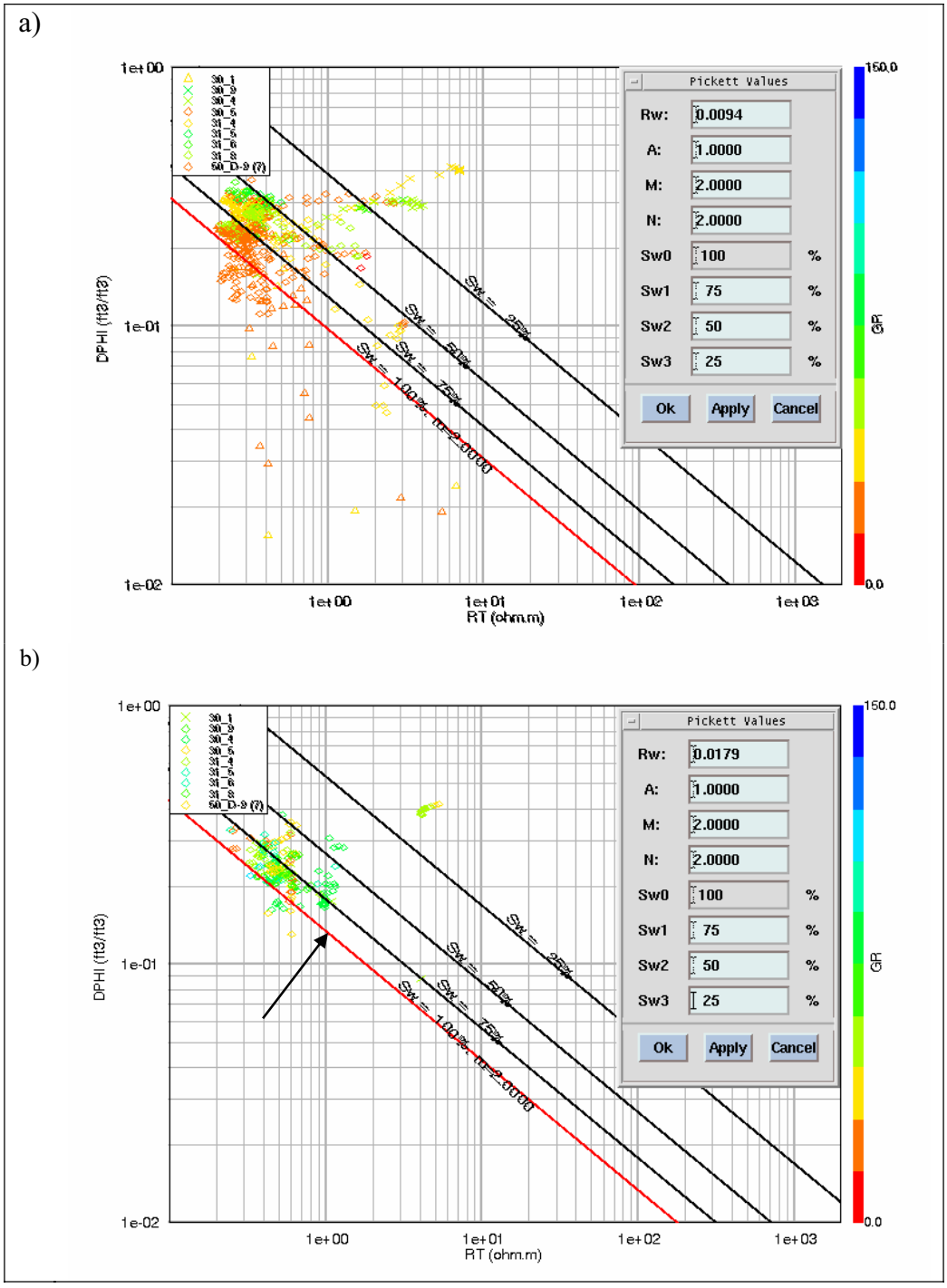

Figure 37. A multi-well pickett plot comparison between a clean sand model with V_{sh} < 5% (A), and shaly-sand model with V_{sh}=15-20% (B). In the clean sand case R_w=0.01 ohm-m, while in the shaly-sand model R_{we}=0.018 ohm-m. Accordingly, the dual water motor is the correct model to calculate water saturation (Hunt, 1997).

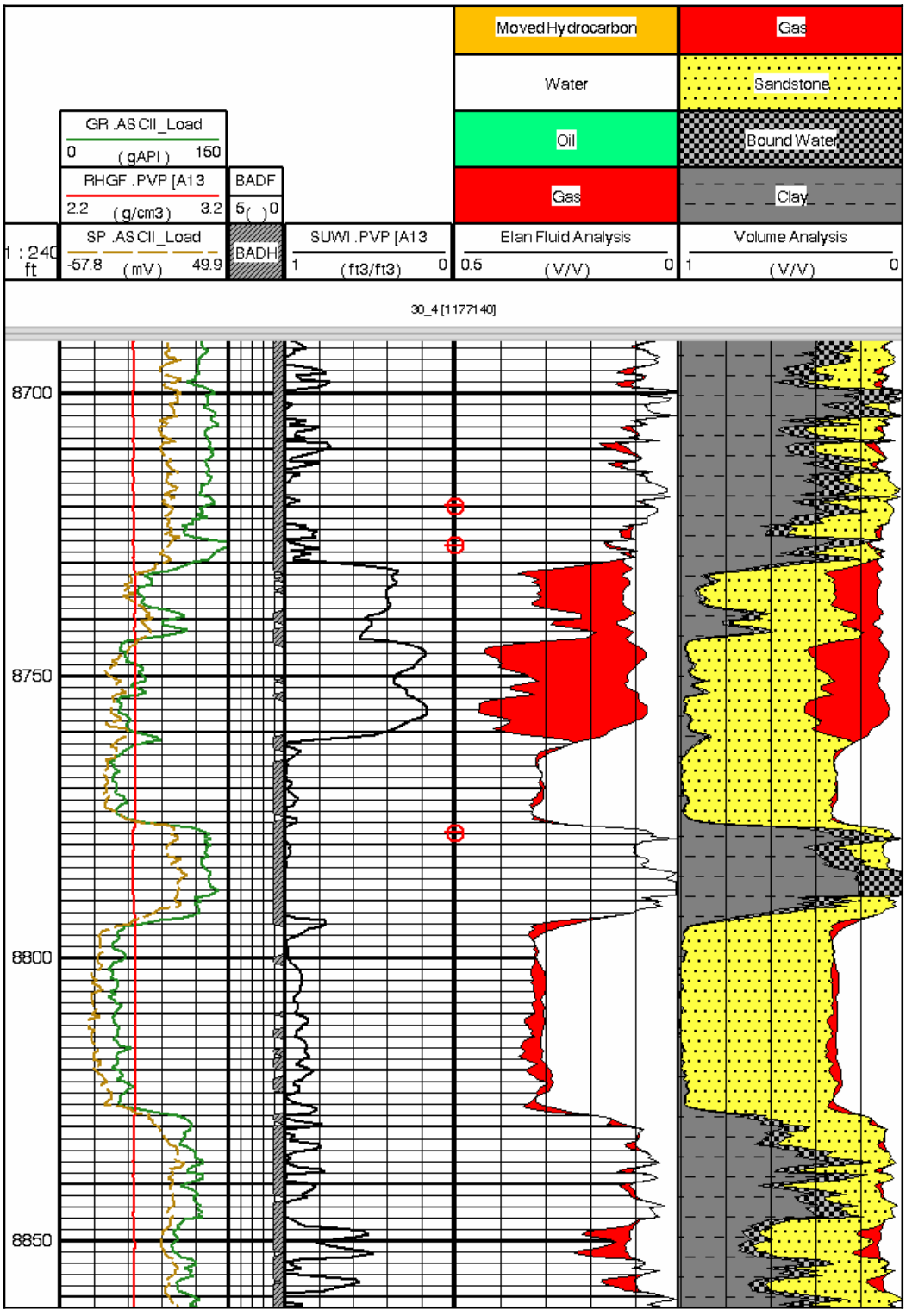

Figure 38. Strip log final presentation of well log analyses results of well 30_4.

3.6.3 Reservoir property summation

The results of the well log analyses are stored in the data base as log curves. These logs are averaged over the vertical depths of the N-sand interval, using a sample interval of 1ft interval. The final reservoir properties are estimated over the N-sand interval using ResSum/GeoQuest, GeoFrame 4.0. Table 4 lists the different estimated properties and their descriptions.

Aiming to evaluate the response of multivariate seismic attribute to net reservoir properties, the product of net reservoir porosity thickness was estimates by imposing two main constraints; 1) Shale volume must be lower that 25% and 2) average porosity is not lower that 15%. Failing to meet any of these two conditions indicates a non-reservoir interval.

Table 4. The different reservoir properties estimated over the N-sand interval and their descriptions.

Reservoir Property	. Description[1]
Gross thickness	The thickness of the interval equals to the difference between the top and base of the interval
Average gross effective porosity	Thickness-weighted arithmetic mean of porosity over the gross thickness.
Net thickness	Total thickness of the non-shales in the interval.
Sand volume fraction	The fraction of the non-shale material in the interval, it is equal to the *net-to-gross ratio*.
Net reservoir water saturation[2]	The average water saturation in the net reservoir zone interval.
Net reservoir porosity-thickness[3]	The sum of the product of the thickness and the porosity logs.

1. ResSum user guide, GeoFrame 4.0.
2. Maximum cutoff of 25% of V_{sh} is applied.
3. Minimum cutoff of 15% of porosity is applied, in addition to the net level cutoff of maximum 25% of V_{sh} is allowed.

3.7 Geostatistical reservoir property estimation

The principal objective of reservoir characterization is to develop a spatial understanding of inter-well heterogeneity that is associated with each reservoir property. Reservoir characterization can be defined as a systematic process for the quantitative description of reservoir properties and for the recognition of geological information and uncertainties in spatial variability (Lake and Carroll, 1986). It involves the integration of multidisciplinary geologic information for an enhanced recovery of hydrocarbons.

This process can be seen as a continued course of integrating and interpreting geological, geophysical, petrophysical, fluid and performance data to form an accurate description of a reservoir. A number of methods have been proposed to attain the premise of integration. Among the many methods, this study is interested in investigating the use of geostatistics as a tool to provide accurate log reservoir property maps. In the following sections, an attempt will be made to shed some light on background of geostatistics. A proposed workflow is presented in Figure 13, and is outlined in later section.

3.7.1 Background

Earth science derived data are characterized by a fundamental feature of spatial variability (Isaaks and Srivastava, 1989). Spatial variability includes scales of continuity, or heterogeneity and directionality within the data (Chambers et al., 2000a). Accordingly, these data types are not purely random, they are a product of natural geological processes, and they have a component of spatial continuity, correlated over some distance, which is often called *regionalized variables* (Wackernagel, 2003).

Unlike other random variables, regionalized variables are distributed in space (and/or time) with location information attached to each measurement. Each measurement is related to nearby observations as a consequent of the physical process or the multiple processes that generated them. None of the known classical statistical methods, such as regression methods, are adequately able to address the spatial feature associated with regionalized variables (Isaaks and Srivastava, 1989).

Geostatistics, which can be defined as a collection of tools which are used to quantify and model spatial variability (Chambers et al., 2000a), are often used to estimate the spatial variability in geological properties and other earth sciences' related properties. Among its different applications, geostatistics is being increasingly used to develop accurate models in petroleum reservoir studies (Deutsch, 2002).

The strength of geostatistics tools lies in their ability to respect the intrinsic spatial information associated with the regionalized variables. Deutsch (2002) stated that geostatistics is distinct from known statistics in three aspects: (1) focus on the geological origin of the data, (2) provide definite modeling and treatment of spatial correlations between data, and (3) ability to handle data at different levels of volumes, scales and levels of precisions.

An infinite sampling scenario is not a plausible reality, such that to sample every location ($\boldsymbol{x}$) within a given domain. Accordingly, geostatistics adopts a probabilistic approach to model the uncertainty about the unsampled, $z(x_i)$, true values produced by a random variable function $Z(\boldsymbol{x})$ (Deutsch, 2002; Wackernagel, 2003).

In a probabilistic model, a regionalize variable $z(\mathbf{x})$ is seen as a realization of a random function $Z(\mathbf{x})$, that is, an infinite family of random variables constructed at all points of ($\mathbf{x}$) of a given region (Isaaks and Srivastava, 1989; Wackernagel, 2003). In other words, the limited volume of sampled data, i.e. $z(\mathbf{x})$, is considered as a subset or a particular realization of infinite probable observations or realizations governed by a general random function $Z(\mathbf{x})$.

This approach allows simplifying the formulations needed to model regionalized variables by modeling their random function $Z(\mathbf{x})$. This is assuming that the statistics of a regionalize variable are spatially invariant (i.e. stationary). Accordingly, stationarity is a decision that is usually imposed; assuming that the probability of a random function does not depend on the location within the study area, but it depends only on the separation vector ($\mathbf{h}$) between paired observations or values (Isaaks and Srivastava, 1989).

This form of stationarity is known as strict stationarity. Due to evaluation challenges, strict stationarity is rarely assumed. However, a second-order stationarity exists if the first two moments (mean and variance) of the random function are independent on location, but dependent on separation (i.e. lag) (Wackernagel, 2003).

Subsequently, the prime interest of geostatistics is focused on understanding the spatial relationship or correlation between all pairs of measurements, ($Z(x_i)$, $Z(x_i+\mathrm{h})$; i=1, 2, 3,…, n), separated by (**h)** vector within the study area. A number of different spatial estimators are developed, such as covariance $C(\mathbf{h})$, correlogram or correlation function $C(0)$, and semivariogram $\gamma(\mathbf{h})$ (Isaaks and Srivastava, 1989; Deutsch, 2002; Wackernagel, 2003). However, under the decision of stationarity, all these measures tend to be equivalent (Deutsch, 2002).

3.7.2 Spatial analysis

The semivariogram, commonly referred to by variogram, is the most commonly used measure of spatial variability (Deutsch, 2002). A variogram function $\gamma(\mathbf{h})$ is a spatial estimator statistic tool. It characterizes the spatial correlation between paired samples by computing the squared differences between their values, as follows:

$$\gamma(\mathbf{h}) = \frac{1}{2N(\mathbf{h})} \sum_{i=1}^{N(h)} [z(x_i) - z(x_{i+\mathbf{h}})]^2$$

where ($\mathbf{h}$) is a lag vector, between sample $z(x_i)$ and sample $z(x_{i+\mathbf{h}})$, and N is the number of data. Thus, a variogram can be described as a measure of dissimilarity or increasing variance as a function of distance, between pairs of measured values.

An estimate of a variogram is named the experimental variogram, where the estimated values are plotted against the lag separation ($\mathbf{h}$). Spatial analysis is considered as the first step to modeling the regionalized variables by using the different methods of spatial interpolation or modeling, such as kriging or cokriging. A number of alternative measures for spatial analysis can be investigated, if the variogram plot does not result in an interpretable spatial relationship. These measures might include: the correlogram, covarigram, and several types of relative variograms. A comprehensive description of

these functions can be found in Isaaks and Srivastava (1989), Goovaerts (1997), and Deutsch (2002).

However, spatial analysis usually includes two main steps (Chambers et al., 2000a): (1) computing experimental variogram, accounting anisotropy and azimuthal directions; and (2) modeling experimental variograms with continuous functions. An example of an experimental variogram and its variogram model is shown in Figure 39.

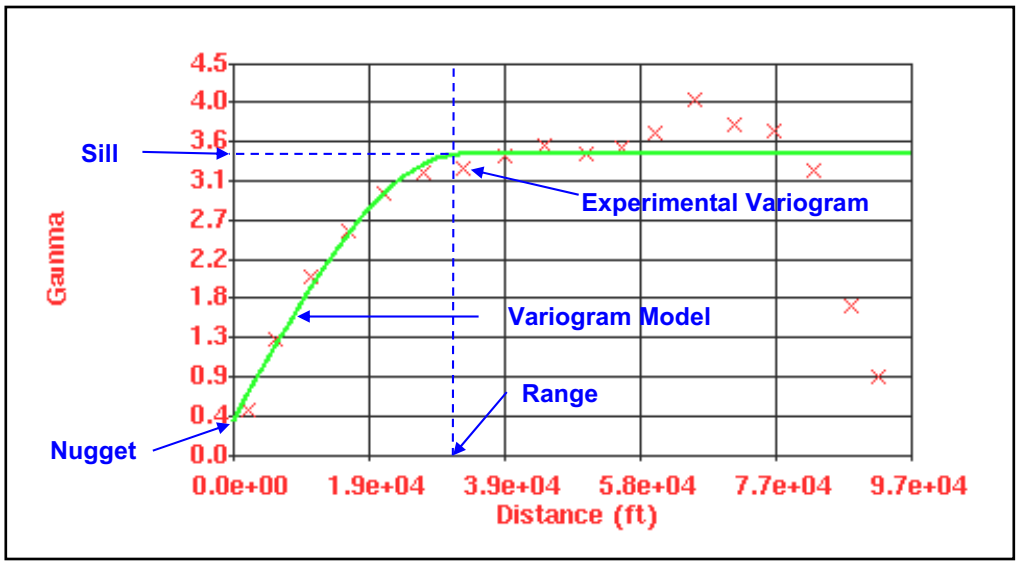

Figure 39. A typical plot of an experimental variogram and the fitted variogram model. Range (R), the nugget (C0) or the nugget effect and the sill (C) are known as variogram attributes.

The need to model the experimental variogram requires to define a variogram surface function, which is defined over all possible distances and directions, whereas, the experimental variogram estimates spatial correlation for a specific distances and directions. In addition, the variogram model needs to honor the condition of positive definiteness (Deutsch, 2002). A positive definite variogram model ensures the existence of a unique solution for the kriging equations and that the variance of any linear combination of the data values will be positive (Kupfersberger and Deutsch, 1999).

The number of theoretical variogram models that can be described as positive and definite models is very limited. The commonly used ones are the spherical, exponential, and Gaussian models (Isaaks and Srivastava, 1989; Goovaerts, 1997).

Nested forms of variogram models, which make use of multiple variogram structures, are often used to model the spatial variations in complex settings. As an example, the spherical variogram model is defined as (Deutsch, 2002):

$$\gamma(\mathbf{h}) = C0 + C\begin{cases} \dfrac{1.5h}{R} - 0.5\left(\dfrac{h}{R}\right)^3 & \text{..... if } h \le R \\ 1 & \text{..... otherwise} \end{cases}$$

where R, $C0$, and C are known as the attributes of a variogram, and they are named as the range, the nugget or the nugget effect and the sill, respectively. The relationship between these three attributes and their variogram model is shown in Figure 40.

The range is the distance where the variogram reaches the sill or zero spatial correlation. No spatial correlation exists between data points farther apart than the range. The plateau of $\gamma(\mathbf{h})$ values that a variogram reaches at the range is called the sill. The sill is the variance where the variogram reaches its range, and it is equal to the theoretical variance of the sample variance. The nugget effect causes the variogram to be discontinuous at the origin. It is related to a combination of effects that are mainly attributed to random noise, short scale variability, and measurement errors (Chambers et al., 2000a).

3.7.3 Spatial anisotropy

Earth deposits are rarely spatially isotropic. Horizontal spatial continuity depends on the direction of deposition and on any subsequent digenetic alterations (Deutsch, 2002). The effect of anisotropy can be revealed from the behavior of the experimental variogram estimated in different directions. However, some prior information can suggest the existence of possible directions of maximum and minimum continuity that urges to explore the pattern of anisotropy with various directional variograms (Isaaks and Srivastava, 1989).

Regional anisotropy and zonal anisotropy are the two basic types of anisotropies distinguished in geostatistics. Regional anisotropy is the typical type of anisotropy associated with directional continuity (Deutsch, 2002). It refers to the case where the different directional variograms have a constant sill value, but demonstrate variant range

values. Zonal anisotropy is another case of anisotropy, which tends to show variant values of sills and ranges of various directional variograms.

The anisotropy ratio for spatial data is defined as the ratio of the range in the greatest and least continuity directions (Kupfersberger and Deutsch, 1999). The major axis will represent the trend of maximum spatial continuity. Perpendicular to this trend will be the minor axis of anisotropy, representing the axis of minimum spatial continuity. The anisotropy ratio is needs to be defined in order to correct for its effect in subsequent modeling steps.

Additional to previous knowledge, a number of different methods are used to assess the effect of anisotropy within a spatial data. Variogram maps plotted as a function of lag vector can show the major and minor axes of continuity. Another frequently used technique involves fitting an ellipse to the range values estimated from various directional variograms (Isaaks and Srivastava, 1989). Figure 40 shows an example of anisotropy analysis by fitting an ellipse to range values estimated every 15º.

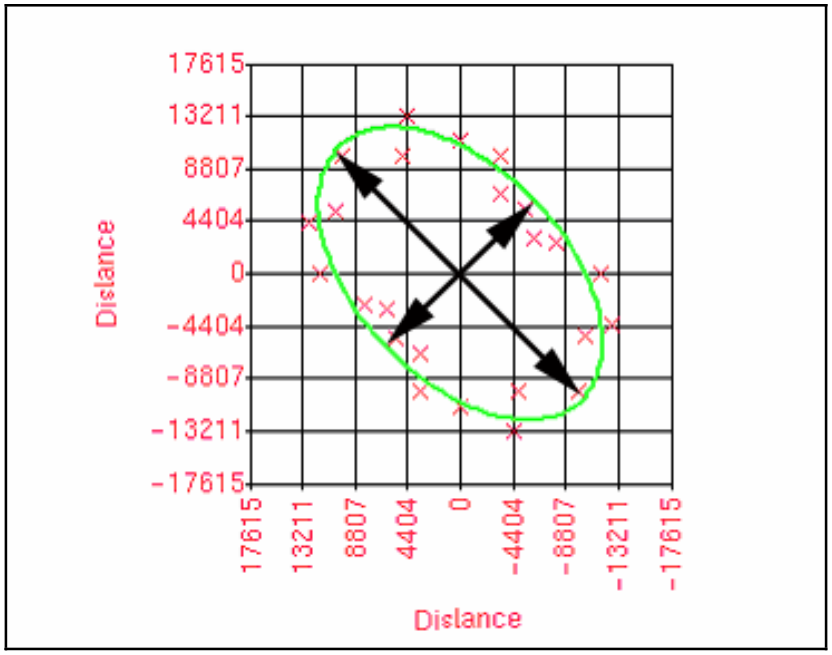

Figure 40. An example of ellipse fitting case of 12 different directional variograms. A major axis represents the direction of maximum continuity. The minor axis represents the trend of minimum continuity.

3.7.4 Spatial mapping using kriging and cokriging methods

The diversity shown among the different interpolation methods diminishes with respect to their common goal, which is to fill gaps of unsampled locations within spatial data sets. These methods might include (Isaaks and Srivastava, 1989): inverse distance, nearest neighborhood, least square polynomial fit, etc.

Kriging is developed, as a collection of geostatistical tools, to address the same problem of estimating a regionalized variable at unsampled location. It is considered as a method of interpolation, but it is different in some fundamental aspects. Kriging uses adjacent sampled location, but it strictly honors the spatial variability of the regionalized variogram model and it minimizes the error variance (Isaaks and Srivastava, 1989). Accordingly, kriging is not a typical linear regression algorithm.

The basic kriging estimator, $Z^*(x_0)$, can be seen as a weighted average of an unsampled location, (X_0), and the adjacent sampled values, $Z(x_i)$, which is defined as (for all i=1, …,n):

$$Z^*(x_0) = \sum_{i=1}^{n} \lambda_i Z(x_i)$$

where (λ_i) are a set of weights. The kriging weights are determined by minimizing the estimated variance, $\mathrm{Var}\left(Z^*(x_0) - \sum_{i=1}^{n} \lambda_i Z(x_i) \right)$, while ensuring the unbiasedness of the estimator, E[Z^*(**x**)-Z(**x**)]=0. Minimizing the variance of estimation involves solving a set of linear regression equations:

$$\sum_{j=1}^{n} \lambda_j C(x_i, x_j) = C(x_i, x_0),\ i=1, \ldots,\ n$$

where $C(x_i, x_j)$ is the covariance between adjacent sampled points, and $C(x_i, x_0)$ is the covariance between unsampled and sampled adjacent location. The covariance function will depend only on the distance between any two locations and not on their values.

A prerequisite for solving for these weights entails the choice of the best model of covariance that describes the exact spatial continuity within the data. The decision of

stationarity allows relating the modeled variogram to its covariance function. $\gamma(\boldsymbol{h})=C(0)-C(\boldsymbol{h})$, where $C(0)$ is the sill or covariance at zero lag (Chambers et al., 2000a). Accordingly, the details of the variogram model will be included in the kriging process in terms of its covariance function. This fact enables the kriging algorithm to capture the details of any possible spatial anisotropy shown by prior variogram analysis.

The preceding linear system produces n equations and n unknown kriging weights. To solve for the weights, the unbiasedness condition is imposed, such that, for a given unsampled location, the sum of all weights should equal unity, and simultaneously should minimize the error variance (Isaaks and Srivastava, 1989). Finally, a number of $n+1$ equations will be formulated, which can be solved for their n unknown kriging weights. The solutions will represent a set of weights that is used to relate the value of a given unsampled location $Z^*(x_0)$ to the known values of adjacent sample points $Z(x_i)$.

The multivariate extension of kriging is known as cokriging. It is typically used to account for the spatial information shared between a primary and a secondary spatial variable. Cokriging improves the reliability of estimation by exploiting the spatial cross-correlation between the primary variable of interest and a spatially denser secondary variable, or covariate (Isaaks and Srivastava, 1989). Each of the primary and the secondary spatial variables exhibits its own statistical character and its own spatial continuity structure, but they may exhibit a degree of spatial correlation between them. Therefore, cokriging seeks to honor the spatial relations contained within the variograms for each variable and the cross-variogram function between both.

The cross-variogram can be seen as an expansion to the classical definition of the semivariogram itself. Contrary to the variogram function, having only positive and null values, the cross-variogram can take a negative value, where the two variables have the tendency to vary oppositely. Assuming an example of two spatial variables $Z(x_i)$ and $Y(x_i)$, a cross-variogram function ($\gamma_{Z,Y}(\mathbf{h})$) can be defined as (Deutsh, 2002):

$$\gamma_{Z,Y}(\mathbf{h}) = \frac{1}{2N(\mathbf{h})}\sum_{i=1}^{N(h)}[z(\mathbf{x}_i)-z(\mathbf{x}_{i+\mathbf{h}})][y(\mathbf{x}_i)-y(\mathbf{x}_{i+\mathbf{h}})]$$

The basic form of a cokriging, $Z_{cokriging}{}^{*}(x_0)$, can be seen as a multivariate weighted average of an unsampled location, (x_0), and the adjacent sampled values of $Z(x_i)$ and $Y(x_j)$. For all i=1, …,n, and j=1, …,m, the cokriging estimator can be defined as (Goovaerts, 1997):

$$Z^{*}_{cokriging}(x_0) = \sum_{i=1}^{n} \lambda_i Z(x_i) + \sum_{j=1}^{m} \lambda_j Y(x_j)$$

where $Z^{*}_{cokriging}(x_0)$ is the simple cokriging estimator of the under-sampled primary variable at location (x_0). A system of linear regression equations is produced, by minimizing the variance of estimation, to solve for the different cokriging weights. This set of equations can be written as (Goovaerts, 1997):

$$\sum_{k=1}^{n} \lambda_k C_{11}(a_i, a_k) + \sum_{l=1}^{m} \lambda_l C_{12}(a_i, b_l) = C_{11}(x_0, a_i),\ i=1,\ldots,n.$$

$$\sum_{k=1}^{n} \lambda_k C_{12}(a_j, b_k) + \sum_{l=1}^{m} \lambda_l C_{22}(b_j, b_l) = C_{21}(x_0, b_j),\ j=1,\ldots,m.$$

where $C_{11}(a_i, a_k)$ is the covariance of the primary variable estimated between the sample point located in location (i) and the sample point located in location (k), $C_{22}(b_j, b_l)$ is the covariance of the secondary variable estimated between the sample point located in location (j) and the sample point located in location (l), and $C_{12}(a_i, b_j)$ is the cross-covariance between the primary and the secondary sample points, located in (i) and (j), respectively. Similar to the kriging case, these equations are constrained by $\Sigma\lambda_i=1$, and $\Sigma\lambda_j=0$, to ensure the condition of unbiasedness (Isaaks and Srivastava, 1989).

In a dense secondary variable case, i.e. seismic attributes, a full cokriging process is very demanding as it requires the complete knowledge of all covariance functions. Xu et al., (1992) outlined the main problems associated with a full cokriging approach. The extreme proximity and the large correlation between adjacent samples of a secondary spatial variable, e.g. seismic data, as opposed to more sparse primary data points, e.g. well data, create unstable cokriging matrices. Additionally, proximal sample points of a secondary spatial variable tend to screen the influence of distal sample points.

Collocated cokriging is a reduced form of cokriging. It retains the secondary data closest to the location where the primary variable is to be estimated. The procedure requires the secondary data to be available at every node where the primary variable is being estimated. It demands less computational resources.

Since collocated cokriging accounts for the values of secondary data that exclusively exists at the grid nodes, its estimator is defined as (Xu et al., 1992):

$$Z^*_{collcated-cokriging}(x_0) = \sum_{i=1}^{n} \lambda_i Z(x_i) + \lambda_2 Y(x)$$

The location (x) of the secondary variable is the same location of the unknown sample point (x_0), where the primary variable needed to be estimated for. The different weights are obtained by solving the following system of linear equations (Xu et al., 1992):

$$\sum_{k=1}^{n} \lambda_k C_{11}(a_i, a_k) + \lambda_2 C_{12}(a_i, b) = C_{11}(x_0, a_i)\,,\ i=1,\ldots,n.$$

$$\sum_{k=1}^{n} \lambda_k C_{12}(a_k, b) + \lambda_2 C_{22}(0) = C_{21}(0)$$

where $C_{11}(a_i, a_k)$ is the covariance of the primary variable estimated between the sample point located in location (i) and the sample point located in location (k), $C_{22}(0)$ is the variance of the secondary variable, $C_{21}(0)$ is the cross-variance between the primary and the secondary variable estimated at zero displacement, and $C_{12}(a_i, b)$ is the cross-covariance between the primary sample located in (i) and the secondary sample point.

Typically, the cross-covariance model is often approximated by using the Markov hypothesis (Xu et al., 1992), which eliminates the need to compute for the computation of the cross-covariance function. The Markov model provides a cross-covariance function as a rescaled form of the primary covariance function, as follows:

$$C_{12}(\mathbf{h}) = B \cdot C_{11}(\mathbf{h})\,, \text{ and}$$

$$B = (C_{22}(0) / C_{11}(0))^{0.5} \cdot \rho_{12}(0)$$

where $C_1(\mathbf{h})$ is the covariance of the primary spatial data, $C_1(0)$ and $C_2(0)$ are the variances of primary and secondary spatial data, respectively, and $\rho_{12}(0)$ is the linear

correlation coefficient between primary and secondary data. The application of Markov based model of collocated cokriging simplifies considerably the covariance modeling and is therefore the most used form of cokriging.

As described earlier, kriging and cokriging are developed, as a collection of geostatistical tools. Further details can be found in Isaaks and Srivastava (1989), Deutsch (2002) and Goovaerts (1997).

3.7.5 Spatial mapping workflow

The general workflow proposed in this study is presented in Figure 12. Log property mapping software (LPM) of GeoQuest was used in this study. Collected cokriging approach was used as a geostatic tool to map the different reservoir log properties.

The essential components of the proposed workflow are summarized in the following steps:

1. The statistical inference for the correlation between a given log properties and the extracted and/or the statistically computed seismic attributes is investigated. Seismic attribute indicating an acceptable degree of correlation is selected as a secondary data and used as a predictor for the log property of interest in subsequent collocated cokriging mapping algorithm.
2. Omnidirectional experimental variograms are investigated. If a spatial pattern of correlation is suspected, the effect of anisotropy is tested by using directional variogram ellipse fitting method. The results of anisotropy analysis are investigated against our previous knowledge related to the geology of the investigated interval and adjusted accordingly.
3. Appropriate positive and definite models are used to model experimental variograms. Variogram attributes are iteratively refined to achieve a good fit. If using nested variogram structures, the principle of parsimony is maintained by using the simplest and the minimum number of models consistent with the experimental variogram.
4. The cross-variogram model is estimated, and run into the collocated cokriging algorithm. The aerial distribution for the log property of interest is produced.

These maps are verified against the geological model developed for the interval of interest.

3.8 Summary

The two primary sources of data reservoir characterization are well and seismic data. Geostatistics provide the tools to integrate sparse well data and seismic attributes. It has helped to reduce the uncertainty associated with spatial predictions of reservoir properties derived from well logs (Chawatté et al., 1997).

The methodology proposed in this study is based on a balanced equation of three main components. First is an accurate geological model, where the final results of integration need to be geologically significant (Hart, 1999). Second are accurate representative integration inputs. The frequency difference between seismic and well log measurements imposes a main concern regarding the validity of the outcomes of integration procedure. The additional non-uniqueness (Table 3) and vague relationships between extracted seismic attributes and geology have tempted to understand the multivariate statistics of these attributes. Principal components analysis has the ability to summarize the data by means of linear combinations of the original inputs, mean while factor analysis results can explain the common variance shared between them. Accordingly, multivariate statistics are used in this study to provide greater insight into the extracted seismic attributes by understanding their hidden structure that can be related to the geology of the interval of interest. The applied integration method is the third main component.

This study investigates the use of collocated cokriging as a method of integration to achieve accurate reservoir characterization results. Collocated cokriging maximizes both the well control and seismic data to create accurate reservoir property maps for targeted infill future drilling activities.

CHAPTER IV

RESULTS AND DISCUSSION

This chapter presents and discusses the results compiled during the course of this research to develop a consistent reservoir characterization study of the N-sand interval. It is comprised of four major sections. The first section develops a proposed geological model for the interval of interest. The second section details the various multivariate statistical results, principal component and principal factor analyses, which were targeted for their potential advantages to reduce redundancy and to generate additional seismic attributes of multivariate statistics.

The third section of this chapter introduces the results of the well log analyses, which reports the results of various log properties of the N-sand interval. This is followed by the fourth section, which presents and discusses the results of geostatistics, i.e. collocated cokriging algorithm, to produce accurate reservoir property maps. Finally, the last section concludes the earlier sections and suggests potential location for future infill drilling activates.

4.1 Structure and stratigraphy of the N-sand interval

The top of the N-sand interval is associated with a major marine flooding event, *Cibicides carstensi* (10.85 Ma), defining the boundary between the middle and upper Miocene.

According to Fillon and Lawless (2000), this boundary represents a maximum expression of a major second order lowstand that was coincident with the development of an East Antarctic ice sheet. During this period, slope-margin prograding wedges shifted northeastward forming a major sand-rich depocenter in southern Louisiana and most of the Mississippi lease area. Additionally, significant seaward displacement of the progradational shelf edge suggests shelf sand bypass and continued fan deposition in deep waters.

4.1.1 Structural framework

The structure map of the top of the N-sand interval (Figure 41) area reveals a general gentle regional structural dip of limited faulting activity, and minimal distortion due to salt movement. Depth conversion of the time structure map of the N-sand interval is achieved by using collocated cokriging geostatistical approach.

Salt related structures are deeply buried only in the eastern side of the study area. Deep-seated salt structure gave raise to the development of a structural high that defines the structural closure for Tiger Shoal field (Figure 41). Meanwhile, the western region of the Vermilion 50 field represent a major rollover structure formed against a regional growth fault system (Figure 42).

The Maximum apparent vertical offsets of faults A and B are ~90 and ~150ft, respectively. Vertical offsets of secondary faults range from ~40 to 110 ft. The spatial distribution of the faults and their vertical offset suggest a strong structural-trapping component within the two fields.

4.1.2 Stratigraphic framework

Hentz and Zeng (2003) divided the stratigraphic section of the study area into proximal, medial and distal third-order sequences representing upper, middle and upper lower Miocene. The N-sand interval belongs to upper middle Miocene medial third-order sequence that was deposited in inner-outer shelf settings (Hentz and Zeng, 2003).

This sequence is composed of two aggradational third-order lowstand incised valleys that are overlain by a section of thick upward-fining, retrogradational transgressive marine shale and a succession of progradational highstand systems tracts that is composed of thick shale and sandstones (Figure 43).

The N-sand interval represents the uppermost unit of third-order lowstand systems tracts. It is characterized by sharp erosional contacts that are overlain by sharp-based aggradational sandstone units and underlain by thick transgressive marine shales (Figure 43).

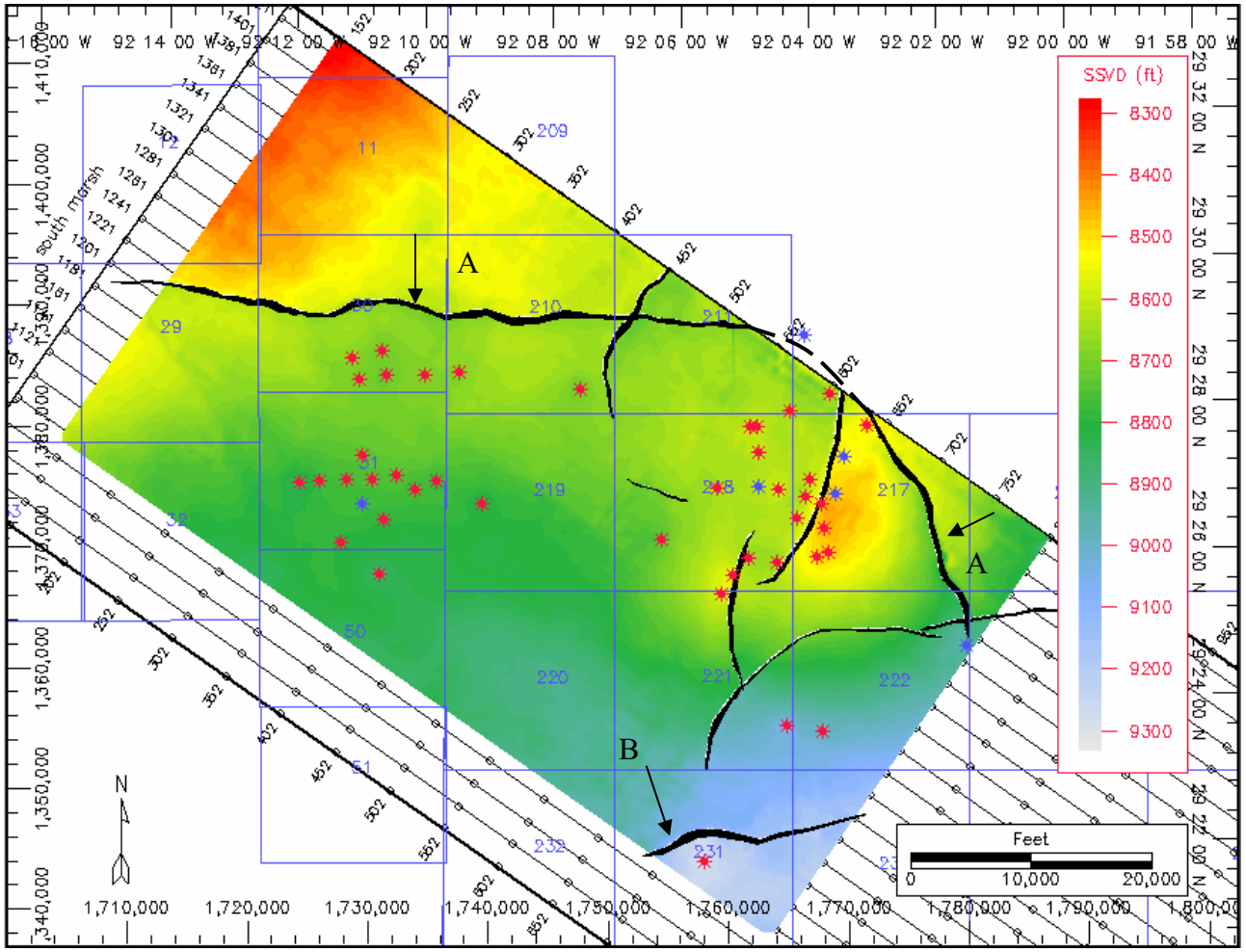

Figure 41. Structure map of the top of N-sand interval. Major growth faults are highlighted by black arrows. Time-to-depth conversion was achieved by using collocated cokriging approach. Wells shown in red were used in the time-to-depth conversion.

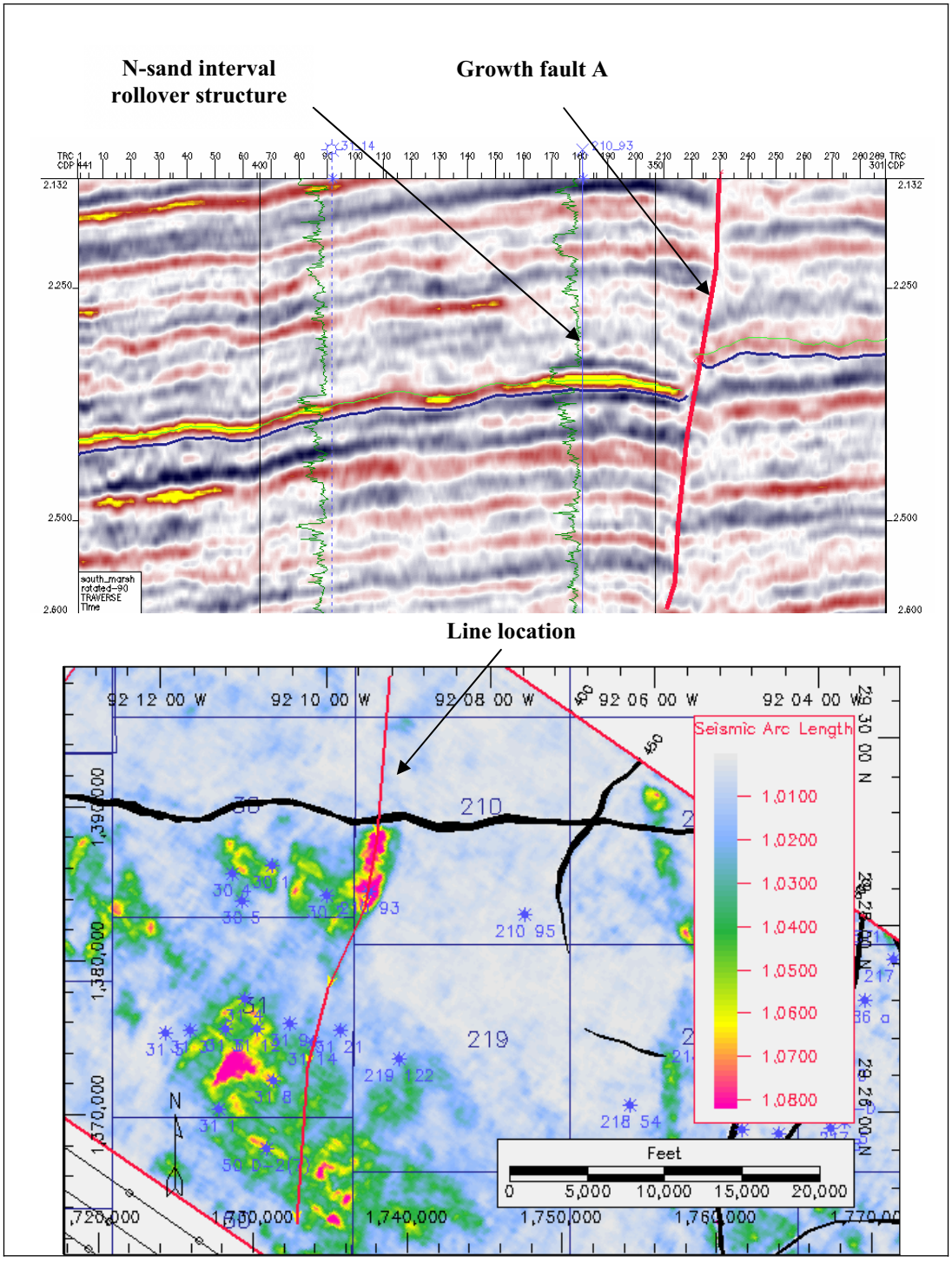

Figure 42. Dip-oriented seismic section across fault A illustrating a gentle rollover structure of the of Vermilion 50 field. The distance between the posted wells equals to 1.96 miles. Troughs appear as hot colors.

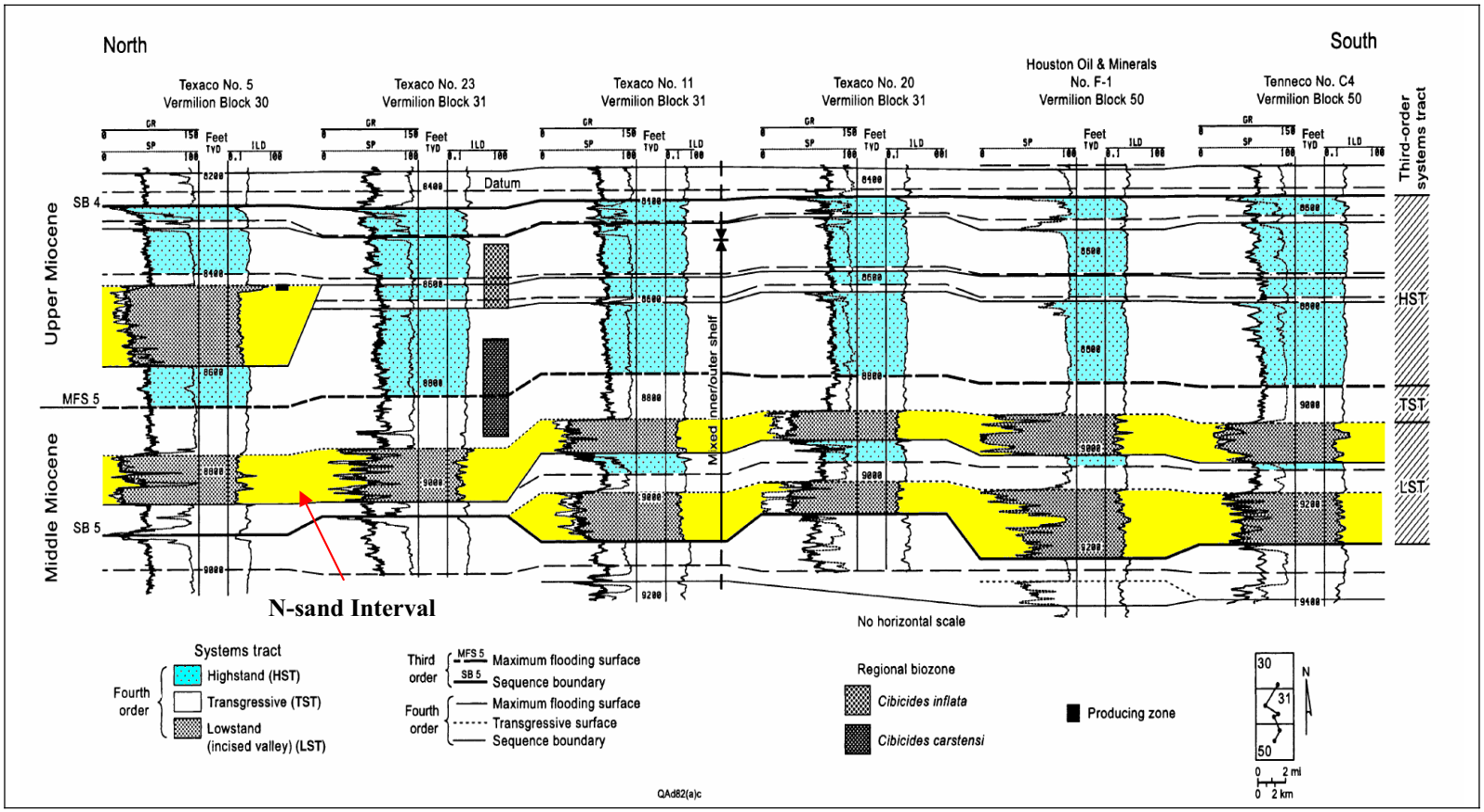

Figure 43. Dip-oriented cross section illustrating the forth medial third-order sequence composed of lowstand, transgressive and highstand system tracts. The N-sand interval represents the uppermost lowstand system tract incised valley unit. (after Hentz and Zeng, 2003).

The measured average gross thickness of the N-sand interval ranges from 70 to 115ft. Seismic data allow distinguishing two distinct vertical events if they are separated by more than quarter wavelength (Sheriff, 1991). The average N-sand velocity equals to 7500ft/s and the seismic dominant frequency equals to 25Hz. The resolution limit of the seismic data is 74.5ft (i.e. $\lambda/4=7500/(25*4)=298ft/4$). Therefore, the resolution of our seismic data and any seismic-derived attributes are able to detect the limits of the N-sand interval.

An incised valley is defined as an entrenched fluvial system that extends its channels basinward and eroding into underlying strata in response to a relative fall in sea level. This leaves the formerly active flood plains abandoned and serving as interfluve exposed areas. These valley systems extend over the subaerially exposed shelf to the outer shelf/upper slope regions and start deposition at the lowstand shorelines (Van Wagoner et al., 1990). During a later phase, deposition within the valleys occurs in response to a relative rise in sea level during the late lowstand or transgressive systems tracts (Van Wagoner et al., 1990).

An incised valley fills represent a wide spectrum of sediment types comprising various depositional environments. The proximal parts of an incised valley contain estuarine and braided-stream sandstones, fluvial sandstones with significant tidal reworking, or coastal-plain sandstones, mudstones or coals, while distal reaches include lowstand-delta and tidal-flat sandstones and mudstones and beach and estuarine sandstones (Van Wagoner et al., 1990).

Figure 44 shows a quality factor map produced across the N-sand interval. This attribute map provides a measure of the similarity between adjacent wavelets of a defined interval. The western side of the study area, containing the Vermilion 50 field, demonstrates the existence of a major incised valley system. Thick incised valley sandstone deposits produce highly correlated seismic wavelets, meanwhile, thin transgressive and highstand systems tracts, underlying the N-sand deposits (Figure 43), produce heterogeneous seismic wavelets that are poorly correlated.

The upper part of the valley is associated with a second-order channel system feeding the eastern main channel of the incised valley is located over the exposed marine shelf to the east of this valley (Figure 44). The presence of numerous minor tributary channels that developed on adjacent abundant flood plan and run orthogonal to the major trunk of the incised valley is a typical characteristic of incision (Posametier, 2001).

Compared to the Tiger Shoal field located to the eastern side of the study area, Vermilion 50 field was highly accentuated by conditions of regional subarial shelf exposure, sediment bypass and incision activities that led to the build up of a substantial incised valley system. In a shelf marginal setting, the presence of growth faulting controls the stratigraphy and sediment dispersal across subaerially exposed shelves during a lowstand eustatic sea drop (Van Heijst et al., 2002).

Growth faulting within the western region played a major role in focusing sediment pathways leading to the accumulation of thick sedimentary deposits. The major trunk of the western incised valley channel is located within the area of maximum offset across fault (A) which is located down dip of the curvilinear arch segments of the growth fault (Figure 45). Focused loading across growth fault (A) onto unstable shelf areas caused the region to subside faster than the adjacent shelf regions. The effect of subsidence is manifested in upper horizons above the N-sand interval (Figure 45).

Draping quality factor map (Figure 46) over the 3D time surface structure of the N-sand interval shows that both western and eastern regions were characterized by sediment bypass across the fault systems indicating a probable syndepositional fault control within the western and central regions of the study area.(Figure 46).

The effect of localized growth faulting is mostly seen in the southern part of the study area (across fault B in Figure 41). The pronounced growth in stratigraphy of the N-sand (Figure 47) is due to the relative increase in accommodation space, due to extension and subsidence, across growth fault (B).

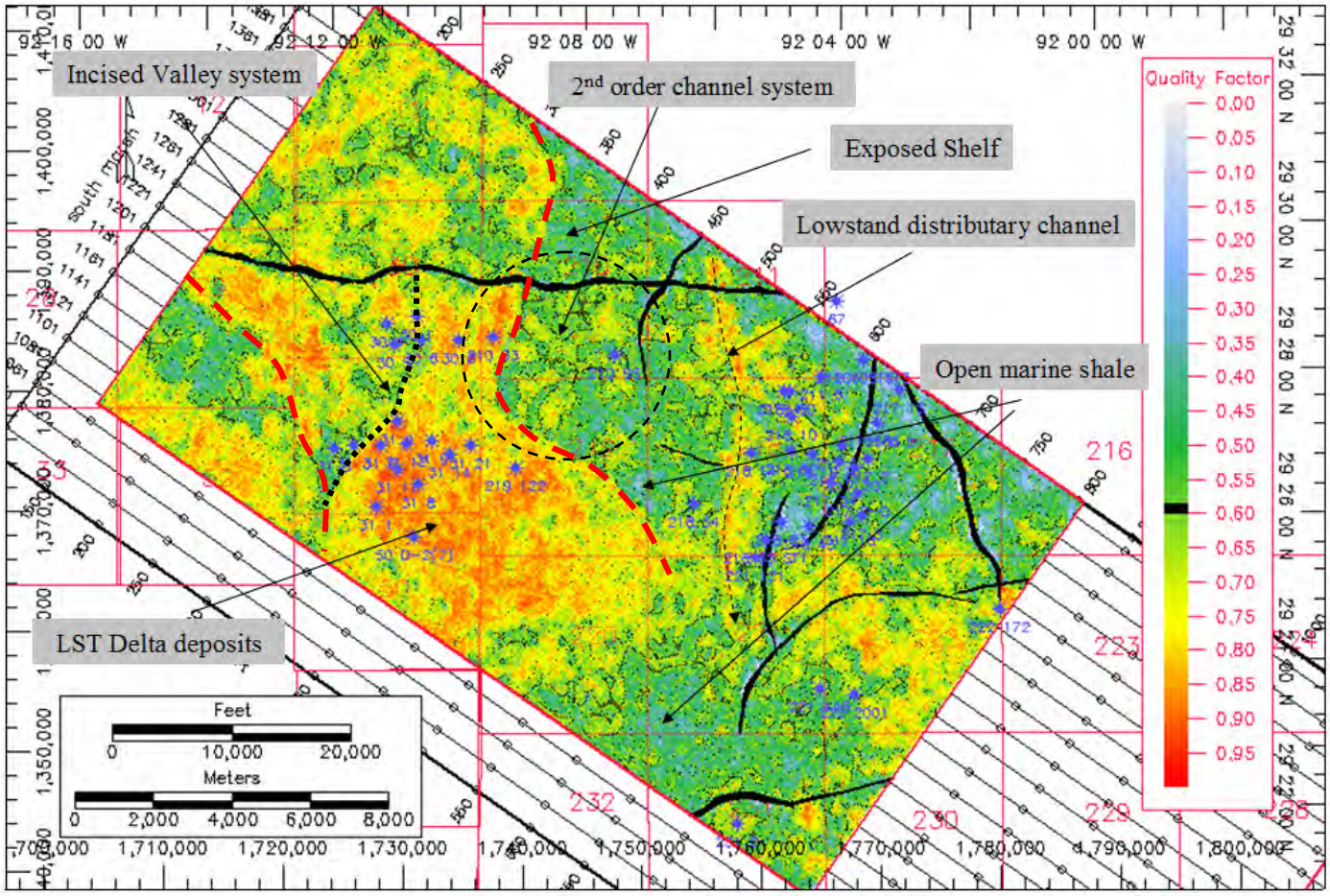

Figure 44. Quality factor map of the N-sand interval showing the general depositional setting of the interval. Vermilion 50 field is associated with a major incised valley system developed in the western side of the study area. The boundaries of the incised valley are shown with dashed red line segments. The eastern side of the valley defines a main channel system developed into a lowstand deltaic system. The area delimited by dashed circle identifies a second-order fluvial channel system feeding the major trunk of the valley. The Tiger Shoal field is slightly affected by incision, but reflects a general sediment bypass activity.

In general, the western region of the study area was able to accommodate more sediment than the eastern region. On the other hand, the major domal structure associated with the Tiger Shoal field acted as barrier and prevented the passage of distributary channels to the far-east footwall blocks (Figure 46).

It is expected that the central region of the study area represents a major remnant flood plain which was subaerially exposure and remained structurally higher than adjacent incised regions. According to Figure 48, this interfluve region divides the study area into two different systems of valley incision; the major western incised valley of the Vermilion 50 field and the eastern incised valley of the Tiger Shoal field which indicates that each of these systems were fed by distinct distributaries systems (Figure 48).

Figure 49 shows a comparison between the mean values of the different well log-derived reservoir properties of Vermilion 50 and Tiger Shoal fields. Both fields show comparable gross thicknesses, but net thickness, gross effective porosity, net sand volume (net-to-gross ratio) and porosity thickness product present different mean estimates. The high mean sand volume (net-to-gross ratio) of Vermilion 50 sands (85%) relative to Tiger Shoal sands (55%) indicates that fluvial incision and reworking in the western region of the study area created cleaner sand deposits than on the eastern side.

In a passive marginal setting, incised valley systems vary in response to the amplitude of sea level fluctuations relative to the elevation of the shelf/slope break and rate of sediment supply (Bowen et al., 1993), who described four end-member variants of passive margin valley systems developed within the Cenozoic of the GOM (Figure 50). In general, the northern GOM is characterized by the models (c and d) that are characterized by high sediment supply identity (Bowen et al., 1993, Seni, 1997).

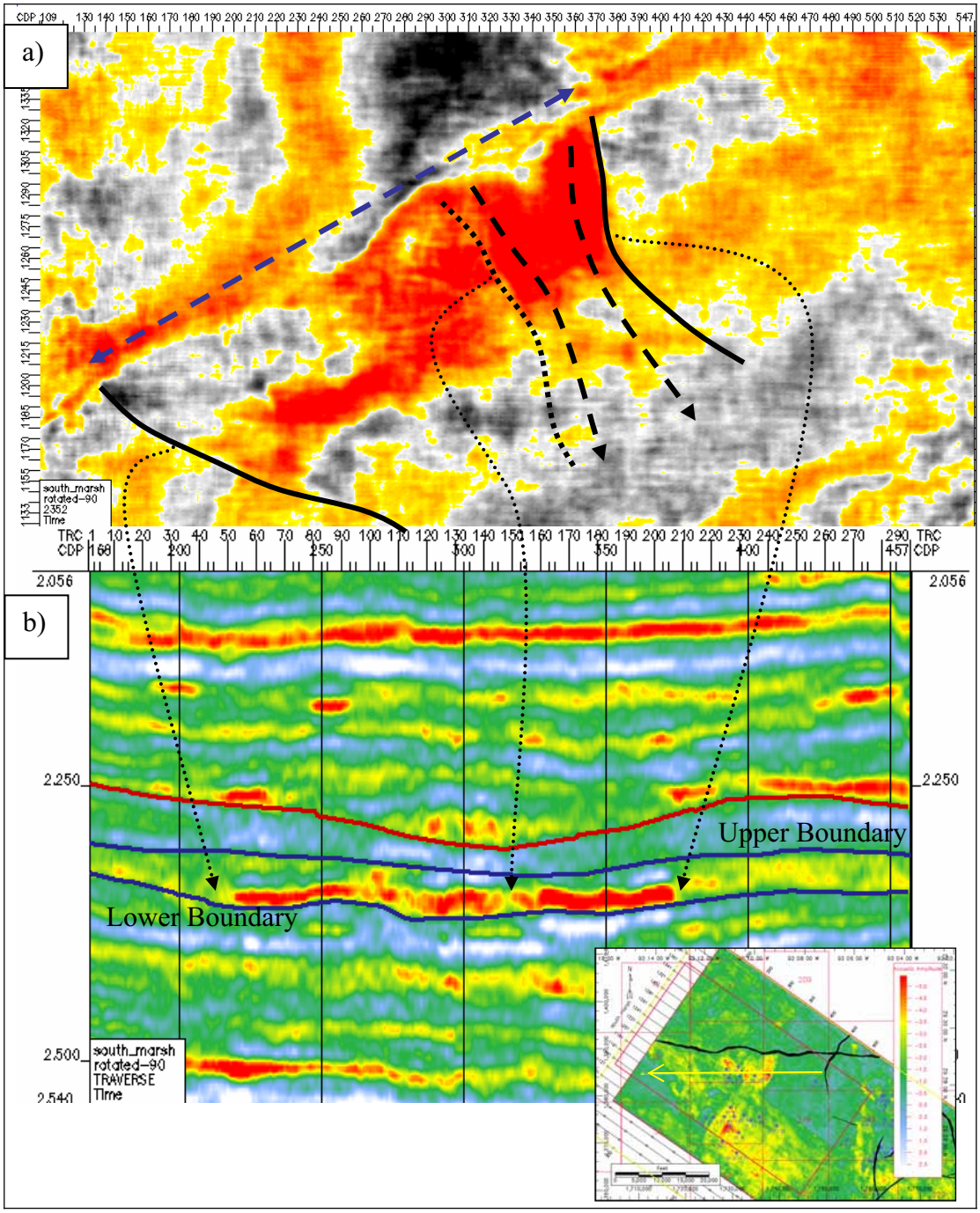

Figure 45.Seismic amplitude map on the right corner shows clear anomalies of higher negative amplitude. These anomalies are associated with regions of maximum offset across the growth fault suggesting sediment focused accumulations and subsidence activity. The effect of subsidence is manifested in higher zones above the N-sand Interval. A and B illustrates the spatial (time-slice 2353ms) and lateral distribution of the major trunk region of the incised valley, respectively. The orientation of the seismic section is shown with yellow trace across the seismic amplitude map.

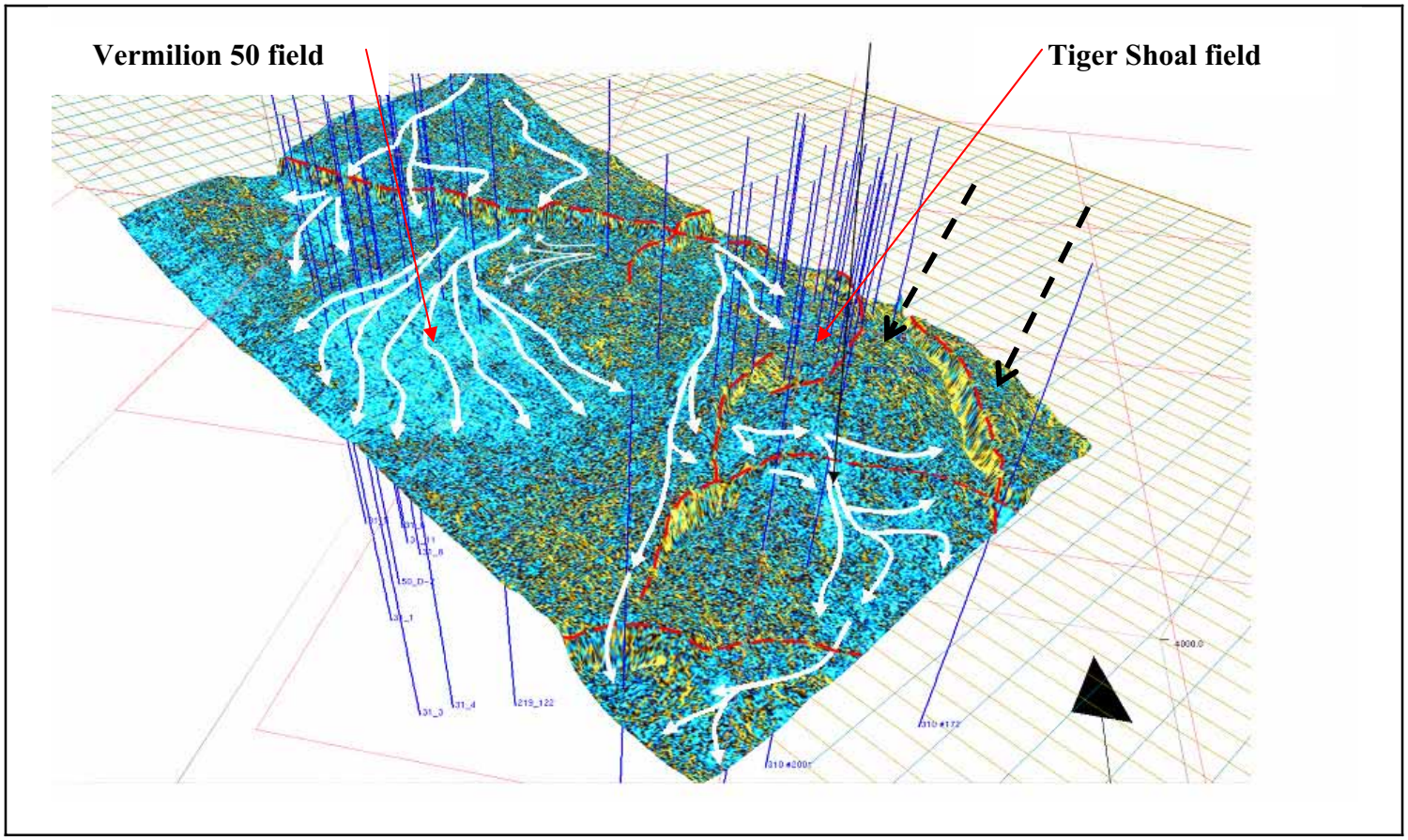

Figure 46. Quality factor map draped over 3D time surface structure of the N-sand interval. Postulated sediment dispersal pathways across the western and the eastern regions are shown with white colored traces. Distribution patterns indicate a general sediment bypass behavior across syndepositional fault systems, which is a typical pattern of lowstand systems tracts. The western region was able to attain more sediment compared to the eastern region. The major domal structure associated with the Tiger Shoal field prevented the far-east footwall blocks (highlighted by dashed black arrows) from receiving sediments representing remnant marine shale flood plains. Fault traces are high lighted in dashed red color. Sediments pathways are highlighted with white color.

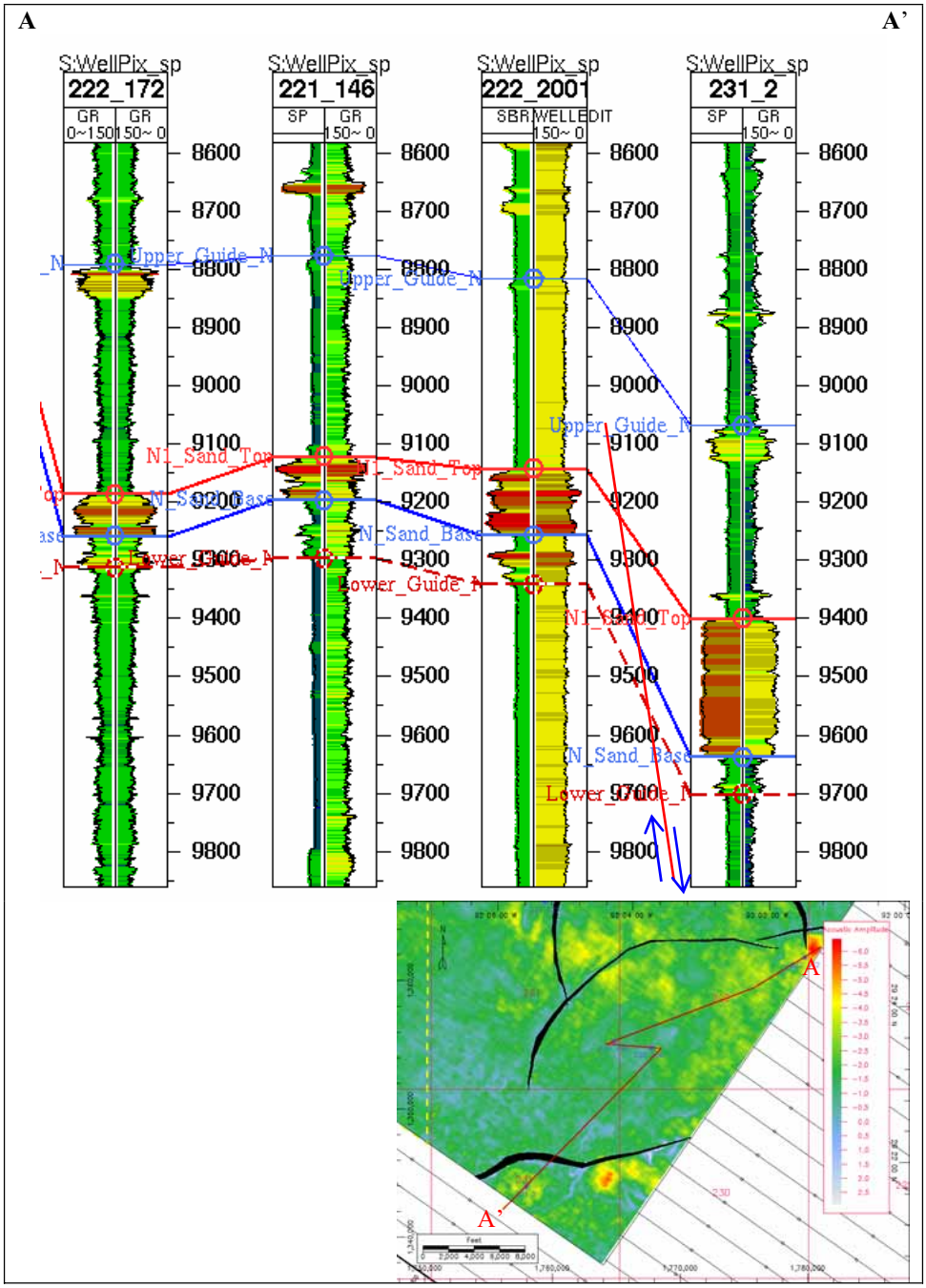

Figure 47. A structural cross-section across fault (B) indicated a pronounced localized growth stratigraphy of N-sand interval in relation to syndepositional growth faulting activities (well 231-2).

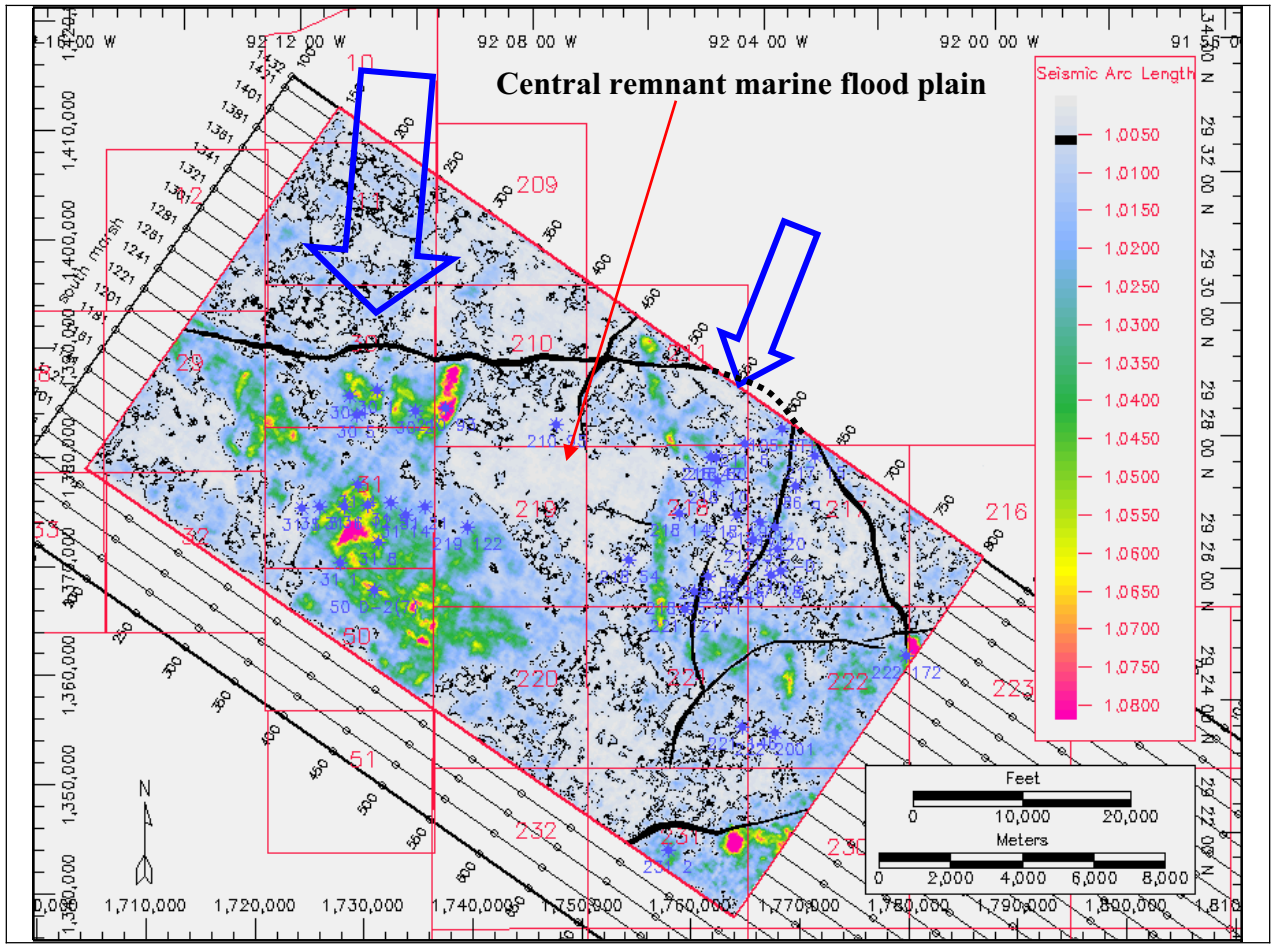

Figure 48. Seismic arc length attribute map showing exposed remnant marine flood plains. A major interfluve plain located in the center of the study area suggests that the western major incised valley and the eastern region were fed by separate distributaries. Black arrows represent probable trend of the distributary systems feeding the western and eastern incised valleys. The orientation of the axis of distributary feeders was concluded based on subsidence signatures across seismic section parallel to the main growth fault. Unfortunately, the lack of seismic coverage from the eastern side imposes limitation on this interpretation.

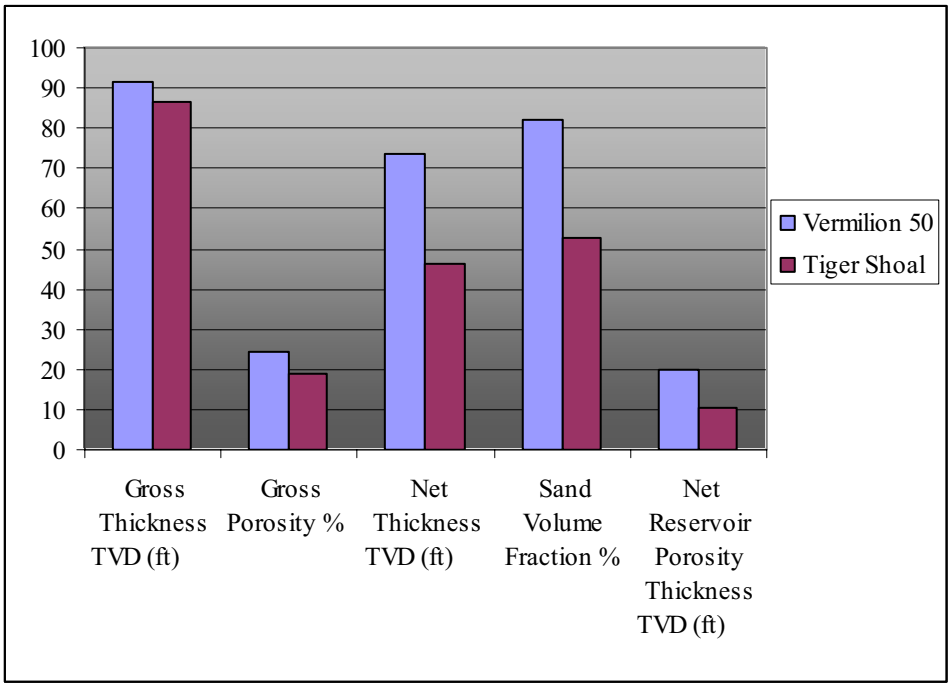

Figure 49. Comparison between the mean values of the different well log-derived reservoir properties of Vermilion 50 (n=19) and Tiger Shoal (n=19) fields, indicates that the western and the eastern regions of the study area have different depositional properties.

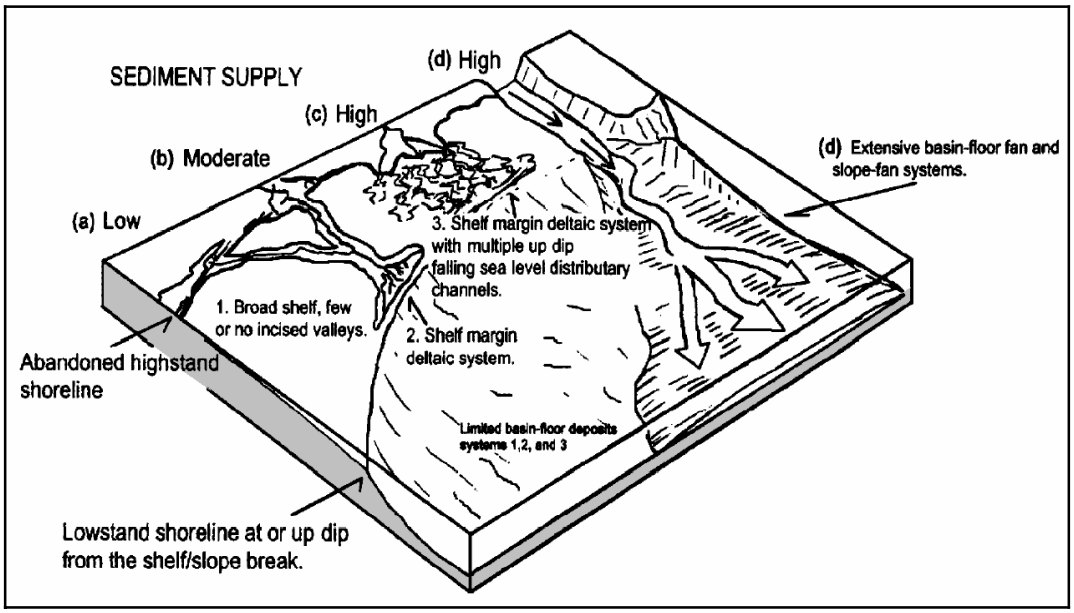

Figure 50. Passive margin incised valley systems of the Cenozoic of the GOM, cab be classified into 4 major end-members, based on the interaction between the amplitude of sea level fluctuations relative to the elevation of the shelf/slope break and rate of sediment supply. (after Bowen, et al., 1993).

The low sediment supply and low amplitude relative sea level fluctuations characterize model (a). These condition results in a small number of incised valleys that are essentially mud filled. In model (b), moderate sediment supply and moderate relative sea level drop results in simple incised valley pattern and development of shelf margin deltaic systems. Model (c) is a product of high sediment supply and moderate amplitude of sea level drop. If the sea level fails to drop to the shelf/slope break, significant shelf margin deltaic systems will develop marking the position of the lowstand shore lines. On the other hand, a major incised valley will breach the shelf margin area (model-d, Figure 50), if the shore line drops below the shelf/slope break, (Bowen et al., 1993).

The western region of the study area can be designated as a (c) model depositional environment (Figure 42). This region is characterized by strong valley incision activities that resulted in the formation of an extensive lowstand deltaic system. The fact that dip oriented seismic sections across this region are distinguished by their gentle slope morphologies (Figure 42) makes model (d) inapplicable in this setting. However, the effects of local subsidence need to be incorporated in this model to full elucidate the different geological and depositional factors controlling this region.

The eastern region of the study area is a combination of (c) and (b) models. This area demonstrates less active valley incision than the western region. The moderate sediment supply (b) is feasible due to the fact that the Tiger Shoal field was structurally higher than adjacent areas. Therefore, the resultant shelf margin delta is restricted compared to the extended shelf margin delta produced in the western region. The longitudinal offshoot shown in Figures (46 and 48) that is located to the west of Tiger Shoal field is interpreted as a lowstand incised distributary channel. Longitudinal incised channels are typical for (b) as shown in Figure 50.

Figure 51 shows a quality factor maps generated across the N-sand interval relative to the base of this interval summarizes the full history of progressive incision taking place across the shelf area. It is evident that valley incision in western region was more active than in eastern region.

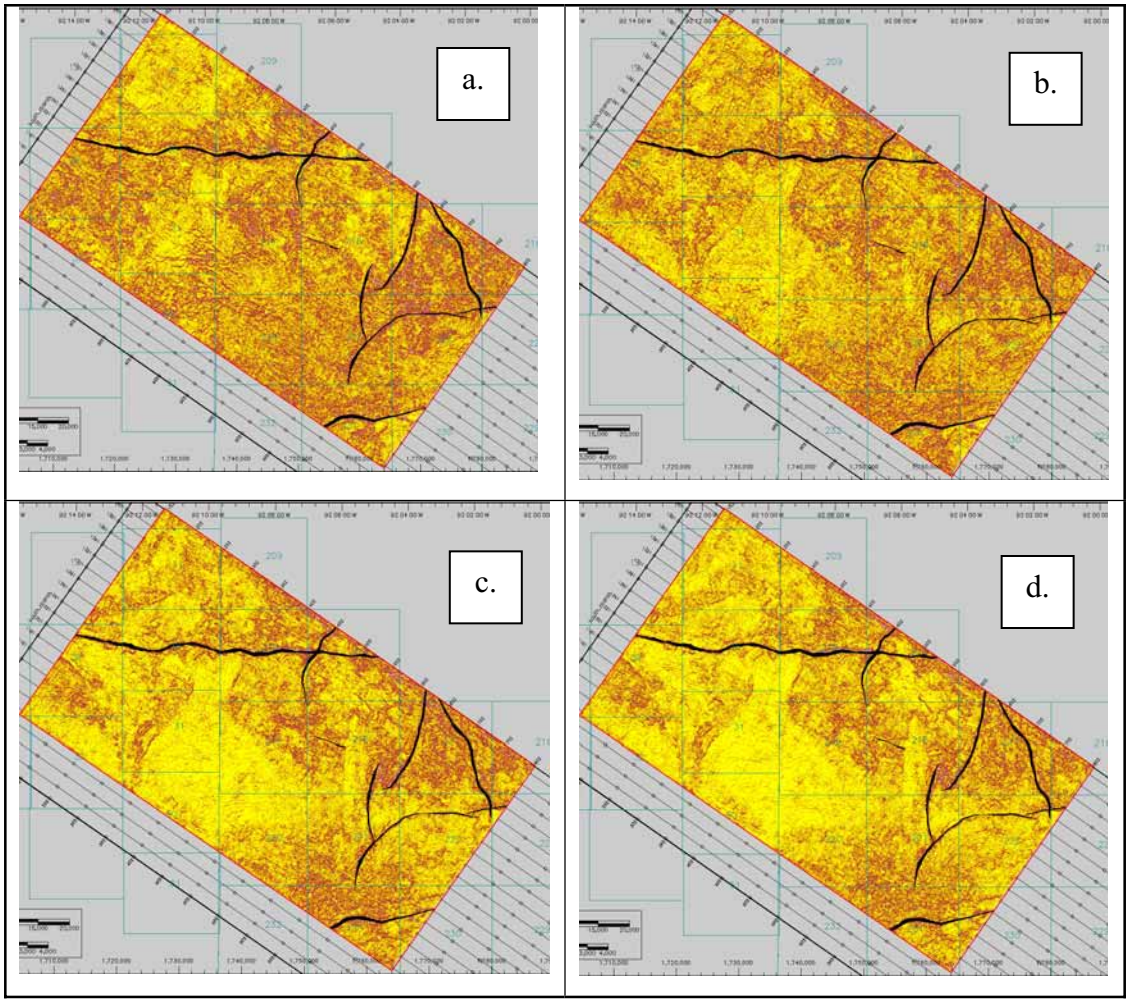

Figure 51. A set of quality factor seismic attribute maps generated relative to the lower boundary of the N-sand interval using a 5ms sample interval. These maps represent the history of progressive incision and deposition taking place across an exposed shelf during a major lowstand conditions. The oldest phase is presented in map (A) and the final phase is presented in map (j) which culminates the lowstand period by a wide marine transgression episode defining the middle section of the 4th medial third order sequence (Hentz and Zeng, 2003), shown in Figure 44.

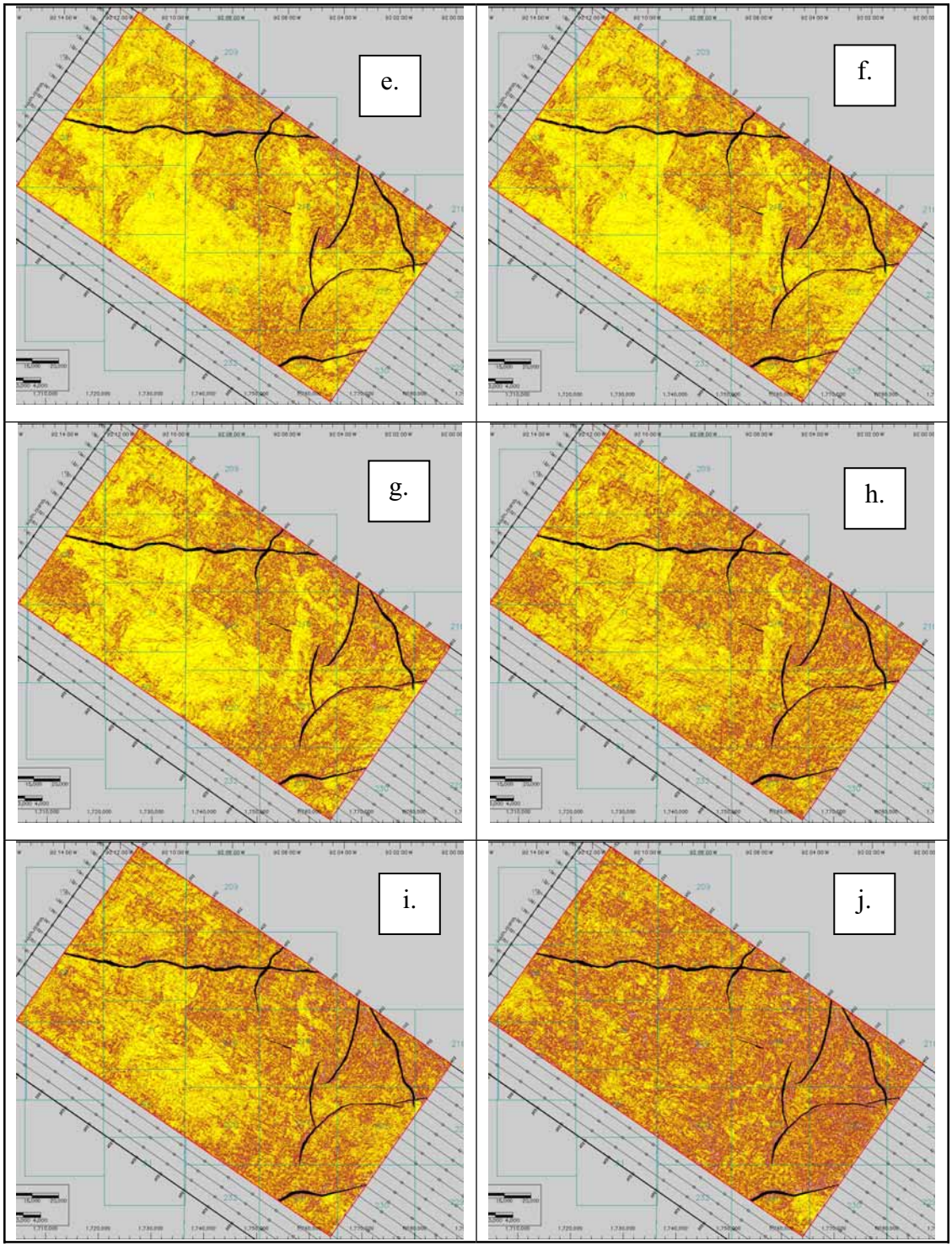

Figure 51. Continued.

These map intervals belong to the medial section of the upper middle Miocene lowstand third-order sequence (Hentz and Zeng, 2003) shown in Figure 43. Map interval is 5ms. The first map represents phase (A) located immediately below the N-sand interval and the last map is phase (j) represents the culmination of the lowstand interval. This succession f events conforms with the results of experimental analogy flume studies to model the control of syndepositional faulting on systems tracts evolution across growth faulted shelf margins (Van Heijst et al., 2002)

4.1.3 Subconclusions

- Structural elements present are related to growth faults, normal non-growth faults and fault-bounded salt-induced localized structures. These elements are similar to the general structural framework of the northern Gulf of Mexico. Although a strong structural-trapping component is present in the fields, the stratigraphic controls on reservoir explain much of the resource-distribution patterns within the study area.
- The western and the eastern regions of the study area were deposited during a major sea level lowstand. Shelf subaerial exposure and sediment bypass were active in the two areas.
- Syndepositional growth faulting played a major role in focusing sediment pathways and in inducing local subsidence features.
- A modified extension of model (c in Figure 50) incorporating the effect of syndepositional growth faulting is proposed as a general geological model for the western region of the study area. Local subsidence across growth fault A supported the formation the western incised valley system. This valley system served as a main conduit for sediment supply to deeper water and fed a lowstand marginal delta at the toe of the valley (Van Heijst et al., 2002).

- On the other hand, the eastern region of the study area was topographically higher than the western region, due to a deep seated salt structure beneath the Tiger Shoal field. Valley incision appears to have been less intense within this area. This area is a typical (c) model (Figure 50) characterized by shelf margin deltaic system with multiple distributary channels.
- Figure 52 shows acoustic amplitude map of the N-sand interval overlain by the time structure contour map. The contour interval is 5ms. The boundaries of the valley are shown by an orange dashed boundary. The main channel contained within the valley is shown by dashed red boundary lines which developed into shelf margin deltaic systems. The boundaries of the incised valley and the channel conform to the time structure counter map.
- Accordingly, both western and the eastern regions of the study area are not perfectly identical. In order to achieve accurate estimate for the log reservoir properties listed in Figure 49, it is of prime importance that the grand study area be partitioned into separate areas. Failing to do so will increase uncertainties in the results estimates.

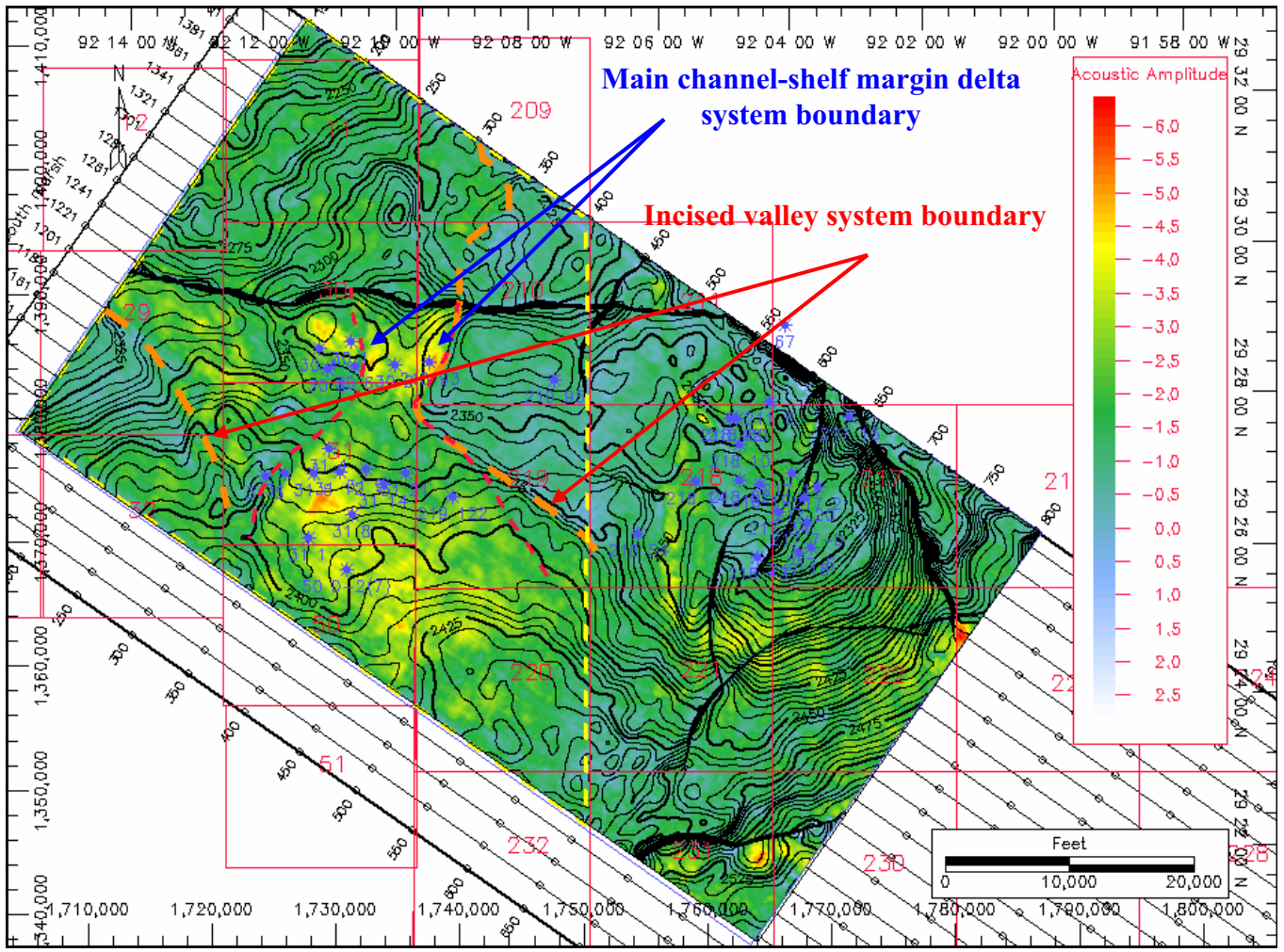

Figure 52. Acoustic amplitude map of the N-sand interval overlain by time structure contour map. Note that the boundaries of the incised valley confirm to the time structure contour line.

4.2 Seismic attributes multivariate statistical analysis

Eighteen different seismic attributes are extracted and averaged across the N-sand interval. Figure 53, shows degree of correlations between extracted original attributes. Most attributes correlate to some degree with one or more of the attributes. This indicates that these attributes are related and share a lot of information in between.

Principal component analysis (PCA) and principal factor analysis (PFA) were applied to these attributes in order to enhance the degree of correlation between seismic attributes and well log-derived reservoir properties.

The application of PCA and PFA should increase uniqueness of the attribute by reducing the dimensionality and redundancy between the original seismic attributes. This in turn will assist in identification of new meaningful multivariate seismic attributes that can be used to map reservoir properties into interwell areas.

4.2.1 Principal components analysis results

PCA decomposes the variance of a data matrix into uncorrelated or independent orthogonal principal components (PC's), which are linear combinations of the original variables. Interpretation of a PC's is made possible by examination of the sign and magnitude of the loading in loading plots.

The PCA loadings (i.e. weights) are the coefficients of the principal components transformation. They provide a convenient summary of the influence of the original seismic attributes on the PC's and a useful basis for interpretation. A large absolute coefficient corresponds to high loadings while coefficients near zero have no loading.

In order to increase the interpretability of the result of PCA and PFA, a certain loading cutoff may be applied to help in pinpointing the most important attributes that are significantly contributing to each PC (Johnson and Wichern, 1998). In this study a cutoff value of (0.3) is used to help highlighting the most significant attributes loader for each PC.

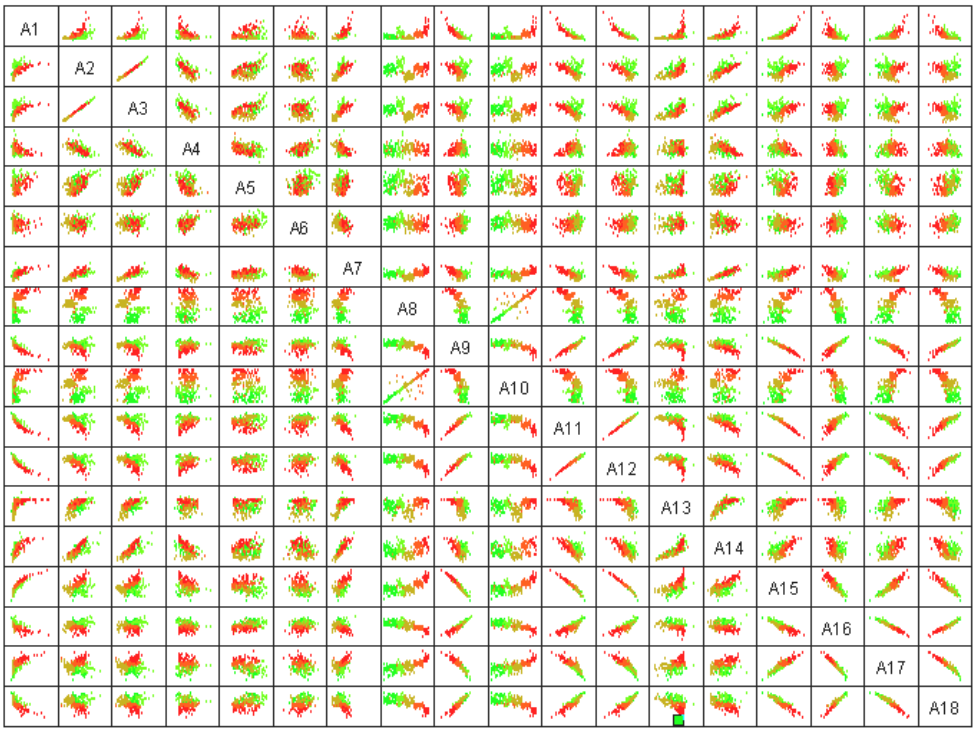

A1 = Arc Length
A2 = Bandwidth Rating (Bias)
A3 = Bandwidth Rating (Debias)
A4 = Half Energy
A5 = Mean Instantaneous Frequency
A6 = Mean Instantaneous Phase
A7 = Max Amplitude
A8 = Max Magnitude
A9 = Mean Amplitude
A10 = Mean Magnitude
A11 = Mean Trough Amplitude
A12= Min Amplitude
A13 = Number of Zero Crossing
A14 = Polarity Ratio
A15 = Root Mean Square (RMS) Amplitude
A16 = Sum of Amplitudes
A17 = Sum of Magnitudes
A18 = Sum of Negative Amplitudes

Figure 53. Correlation matrix plot illustrating the degree of correlation between extracted seismic attributes. Correlated attributes share information between them which can mask the level of correlation between them and well log reservoir properties. Red color denotes clean sand deposits and green color represent shaly deposits.

PCA results indicate that the first three principal components of the correlation matrix accounted for ~89% of the total variance of the original dataset (Figure 54). Table 5 shows the eigenvalues of the 18 principal components and the proportion of variance explained by each. The individual loadings or eigenvectors are listed in Table 6. The main principal component loaders of the first five PC's are shown graphically in Figure 55.

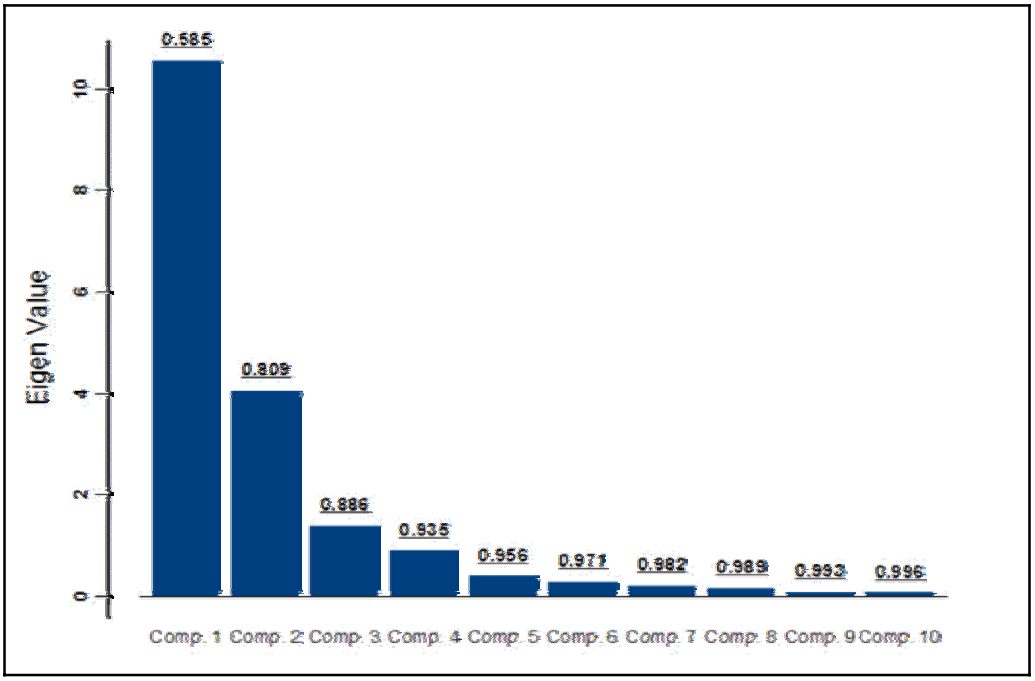

Figure 54. Scree plot presentation of the results of the first 10 PC's. The first 3 PC's represent 0.89 of the total variance in the original 18 seismic attributes. Values posted above bars represent the cumulative variance value (Table 5). Seismic attribute grid map contains 56715 samples and 2505 missing values. Correlation matrix was used in the analysis.

Table 5. Results of the eigenvalues and the proportion of variance explained by each principal component.

Principal component	Eigen Value	Proportion of Total Variance	Cumulative Variance
PC1	**10.532**	**0.585**	**0.585**
PC2	**4.039**	**0.224**	**0.809**
PC3	**1.372**	**0.076**	**0.886**
PC4	0.881	0.049	0.935
PC5	0.382	0.021	0.956
PC6	0.279	0.016	0.971
PC7	0.185	0.010	0.982
PC8	0.136	0.008	0.989
PC9	0.064	0.004	0.993
PC10	0.055	0.003	0.996
PC11	0.048	0.003	0.998
PC 12	0.010	0.001	0.999
PC 13	0.007	0.000	0.999
PC 14	0.005	0.000	1.000
PC 15	0.003	0.000	1.000
PC 16	0.002	0.000	1.000
PC 17	0.001	0.000	1.000
PC 18	0.000	0.000	1.000

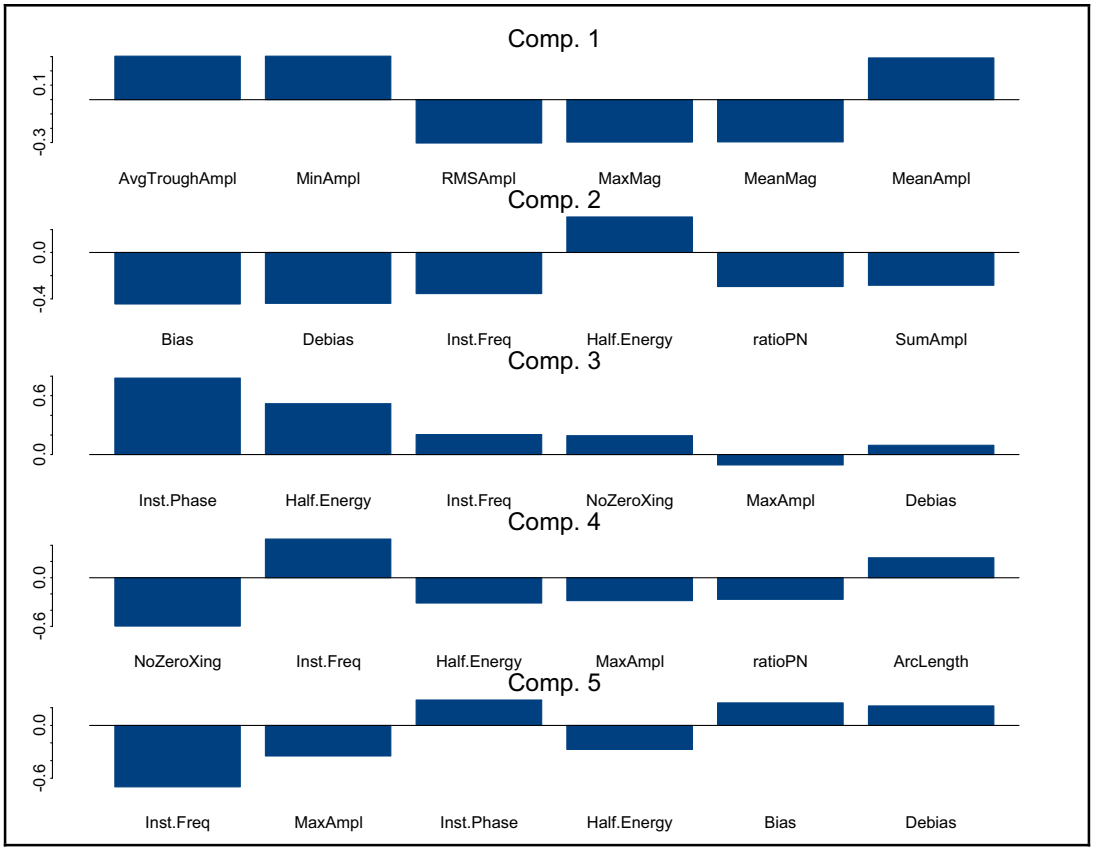

Figure 55. Principal components loading plot illustrating the main seismic attributes imposing significant load on each transformed PC. Note that the first three represent 0.89 of the total variance. The full loading values are listed in Table 6.

The first principal component (PC-1) 1 represents 59% of the total variance. It is mainly loaded by seismic amplitude-based attributes (A8, A9, A10, A11, A12 and A15 in Figure 55 and Table 6). The fact that they are highly correlated (Figure 53) is shown in their equal loading value ~0.3. These attributes are hydrocarbon indicators (Table 3) which are able to detect changes related to geology or hydrocarbon accumulation within the analysis window. Figure 56 shows a comparison between PC-1 and mean trough amplitude. Mean trough amplitude has the highest loading value (0.304).

The second PC represents 22.4% of the total variance. The highest loadings for PC-2 are (A2, A3, A4, A5 and A14 in Figure 55 and Table 6). These attributes are strongly sensitive to existing heterogeneities within a given analysis window. For example, bandwidth rating seismic attribute (A2) response to cyclic and shaly sequences

is represented by narrow bandwidth whereas widely varying lithology layering has a border bandwidth (Table 3). PC-3 represents 8% of the total variance. The highest loadings for PC-3 are mainly associated with half energy and mean instantaneous phase (Figure 55 and Table 6). These attributes are used to detect uneven reflection surface heterogeneities of pinchouts, unconformities and changes within internal lithology or porosity. PC-2 and PC-3 are shown in Figure 57.

The fact that a seismic attribute can indicate reservoir fluid content and lithology is an important observation. The greater the number of seismic attributes used in multiattribute study, the greater the likelihood of false correlation (Kalkomey, 1997). However, the mutual independence of PC's minimizes the risk of misleading relationships (Scheevel and Payrazyan, 1999).

PCA can estimate a number of components equal to the number of input variables (18 PC's in this study). However, 3 components are sufficient to describe the correlation matrix of the 18 original seismic attributes of the studied interval. Other dimensions tend to screen noise and redundant information shared between original attributes but they may contain valuable information. The estimated PC's are considered multivariate seismic attributes since they are derived from multiple seismic attributes (Taner, 2001),

Dunteman (1989) outlined that the number of retained PC's depends on the goals of analysis. If PC's are used as predictors of a dependent variable, then it is important to consider their correlations with the dependent variable as well. Subsequently, aiming to push the limits of our extracted attributes, the resulted 18 PC's were retained and assessed for proper use to estimate well-log derived reservoir properties.

Table 6. Principal components loadings for 18 extracted seismic attributes representing the N-sand interval.

	A1	A2	A3	A4	A5	A6	A7	A8	A9	A10	A11	A12	A13	A14	A15	A16	A17	A18
PC1	-0.274	-0.114	-0.116	0.098	0.042	0.083	-0.225	-0.297	0.291	-0.296	0.304	0.303	-0.186	-0.215	-0.303	0.247	-0.274	0.277
PC2	-0.122	-0.445	-0.440	0.308	-0.356	-0.007	-0.221	0.067	-0.123	0.098	-0.028	-0.035	-0.210	-0.293	0.062	-0.282	0.196	-0.202
PC3	-0.062	-0.076	-0.095	-0.520	-0.203	-0.780	0.106	-0.038	0.037	-0.018	-0.012	0.032	-0.192	-0.056	-0.022	0.057	-0.041	-0.006
PC4	-0.245	-0.025	0.024	0.313	-0.478	-0.172	0.282	-0.059	0.177	-0.106	0.067	0.114	0.594	0.266	-0.108	-0.009	0.001	-0.065
PC5	-0.004	0.255	0.220	-0.274	-0.698	0.287	-0.348	0.136	-0.049	0.030	-0.063	-0.104	-0.040	-0.098	0.066	0.120	-0.213	0.094
PC6	0.141	-0.090	-0.124	0.037	-0.268	0.278	0.651	-0.033	0.110	0.007	-0.008	-0.011	-0.522	0.222	0.016	0.204	0.015	0.076
PC7	-0.020	0.374	0.452	0.284	-0.083	-0.163	0.215	-0.002	0.078	-0.004	0.168	0.059	-0.207	-0.532	-0.049	-0.163	0.319	-0.022
PC8	-0.720	0.048	0.033	-0.065	0.140	0.053	0.012	0.435	0.172	0.376	0.089	0.065	-0.130	0.142	0.162	0.073	0.091	0.059
PC9	0.026	0.119	0.135	0.008	-0.103	-0.050	-0.334	-0.294	-0.095	0.040	0.230	0.220	-0.279	0.598	-0.075	-0.255	0.371	0.013
PC10	-0.447	0.062	0.054	-0.328	0.048	0.274	0.209	-0.337	-0.219	-0.254	-0.149	0.009	-0.031	-0.072	-0.096	-0.302	-0.090	-0.449
PC11	0.130	-0.101	-0.166	-0.425	-0.049	0.255	0.160	-0.151	-0.053	0.316	0.376	0.304	0.336	-0.248	0.069	-0.013	0.329	0.158
PC12	0.182	-0.056	-0.017	-0.214	0.019	0.118	-0.127	0.260	0.617	-0.270	0.212	-0.140	0.010	0.036	-0.076	0.022	0.235	-0.488
PC13	0.167	0.062	0.064	0.135	-0.001	-0.055	-0.046	-0.041	-0.035	0.405	0.027	0.498	-0.067	-0.012	0.024	0.253	-0.336	-0.585
PC14	-0.048	-0.061	0.064	-0.039	-0.009	0.052	-0.111	-0.187	0.243	0.067	-0.738	0.237	0.036	-0.070	-0.113	0.265	0.425	0.058
PC15	0.159	0.039	-0.039	-0.077	-0.002	0.047	0.069	0.194	0.350	0.098	-0.228	0.343	-0.031	0.013	-0.111	-0.682	-0.310	0.214
PC16	0.044	-0.167	0.119	-0.064	-0.006	0.034	0.050	0.559	-0.435	-0.292	-0.001	0.344	-0.007	0.029	-0.464	0.094	0.134	0.008
PC17	0.001	-0.270	0.251	-0.037	-0.002	0.021	0.012	-0.117	0.055	0.485	0.049	-0.406	0.004	0.004	-0.660	-0.042	-0.075	-0.017
PC18	0.007	-0.652	0.616	-0.034	-0.002	0.014	0.003	-0.052	0.044	-0.103	0.035	0.094	-0.015	0.005	0.397	-0.050	-0.081	0.044

A1 = Arc Length
A2 = Bandwidth Rating (Bias)
A3 = Bandwidth Rating (Debias)
A4 = Half Energy
A5 = Mean Instantaneous Frequency
A6 = Mean Instantaneous Phase
A7 = Max Amplitude
A8 = Max Magnitude
A9 = Mean Amplitude
A10 = Mean Magnitude
A11 = Mean Trough Amplitude
A12= Min Amplitude
A13 = Number of Zero Crossing
A14 = Polarity Ratio
A15 = Root Mean Square (RMS) Amplitude
A16 = Sum of Amplitudes
A17 = Sum of Magnitudes
A18 = Sum of Negative Amplitudes

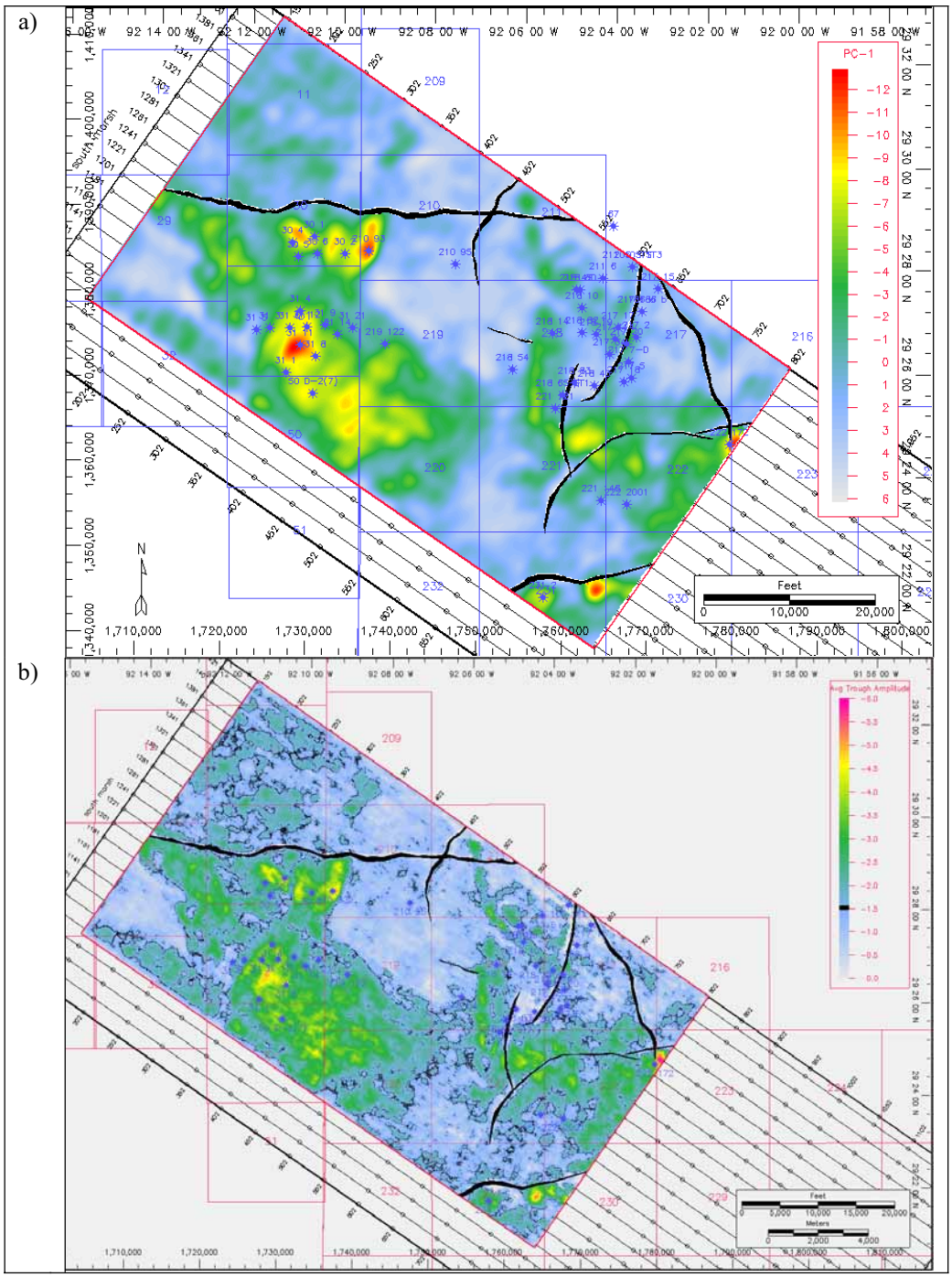

Figure 56. Comparison between the PC-1 (a) and the mean trough amplitude attribute (b). Note that PC-1 was able to reduce noise and to highlight a set of anomalies which are related to changes in lithology or hydrocarbon bearing deposits.

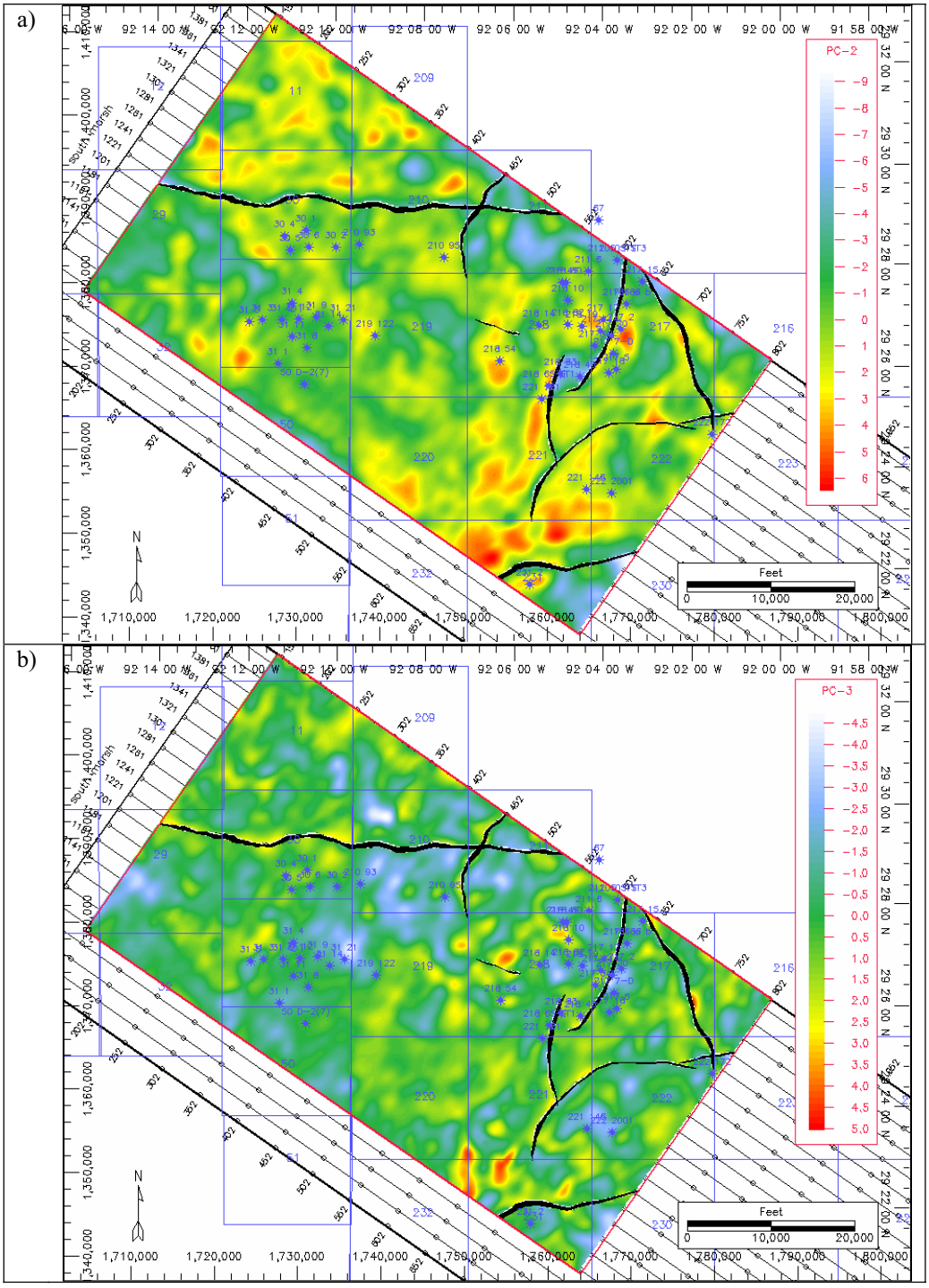

Figure 57. Principal components two (a) and three (b). Compared to PC-1 which is more sensitive to hydrocarbon accumulation and related lithology changes, PC-2 and PC-3 more sensitive to internal heterogeneities and cyclicity within the time window.

4.2.2 Principal factor analysis results

The results of principal factor analysis (PFA) indicate that three factors are sufficient to explain the common variance shared between the original seismic attributes. These factors account for 89% of the reduced original correlation matrix. The reduced correlation matrix equals to the original correlation matrix minus the diagonal matrix of the unique variances. For each attribute, the unique variance is the amount of variance that has nothing in common with the remaining attributes and the communality is the amount of variance shared with the remaining attributes (Dunteman, 1989).

The results of PFA were subjected to Varimax rotation which maximizes the sum of the variances of the squared loadings within each column of the loading matrix (in upper section of Table 7) (Dunteman, 1989). The new loading matrix results are shown in lower section of Table 7. Varimax rotation reduces the number of factors on which the variables under investigation have high loadings and make simplifies interpretation.

Figure 58 shows a comparison between the initial loadings matrix of PFA (a), and the loading matrix after applying Varimax rotation and sorting (c). Although the quest in PFA is concerned with explaining common variance and not the total variance, comparing the results of PFA (Figure 58) with the results of PCA (Figure 55) indicates comparable results. This is due to the size of the original seismic attribute (Dunteman, 1989). In order to interpret the results of PFA, Johnson and Wichern (1998) proposed to drop out the variables shared between two and more factors. Accordingly, the first principal factor (PF-1) is loaded by amplitude-based attributes; sum of negative amplitude, sum of magnitude, mean amplitude, mean magnitude, RMS Amplitude, amplitude sum, maximum magnitude, minimum amplitude and average trough amplitude (Figure 58, c). These attributes are mainly described as direct hydrocarbon indicators (Table 3).

PF-1 is contrast between negative and positively valued attributes. It behaves as a tool to screen out any possible noise samples extracted within a time window and are not representative of the N-sand deposits, which is associated with the trough portion of the seismic data (Figures 15 and 19).

Table 7. Principal component factor analysis of the correlation matrix. The upper table shows the unrotated factor loadings and communalities. The lower table represents the final results of PFA loadings after Varimax rotation and sorting. Loadings less than 0.3 were considered not important. The communality of each attribute is the portion of the total variance shared with the remaining attributes (Dunteman, 1989).

Unrotated Factor Loadings and Communalities				
Seismic attribute	**Factor1**	**Factor2**	**Factor3**	**Communality**
Arc Length	0.74	0.548	-0.101	0.858
Bandwidth Bias	0.022	0.967	-0.096	0.944
Bandwidth Debias	0.033	0.964	-0.075	0.936
Half Energy	-0.009	-0.564	0.732	0.854
Inst. Freq.	-0.369	0.654	0.153	0.588
Inst. Phase	-0.17	0.09	0.933	0.908
Max Ampl.	0.5	0.639	-0.296	0.746
Max Mag.	0.945	0.22	-0.085	0.949
Mean Ampl.	-0.969	-0.11	0.067	0.955
Mean Mag.	0.962	0.156	-0.099	0.96
Avg. Trough Ampl.	-0.931	-0.287	0.158	0.974
Min Ampl.	-0.939	-0.284	0.105	0.973
No-ZeroXing	0.424	0.639	0.067	0.592
P/N ratio	0.435	0.796	-0.127	0.839
RMS Ampl.	0.957	0.232	-0.108	0.982
Sum Ampl.	-0.955	0.229	-0.022	0.966
Sum Mag.	0.971	-0.044	-0.034	0.946
Sum Neg. Ampl.	-0.981	0.062	0.088	0.973
Sorted Rotated Factor Loadings and Communalities using Varimax rotation method				
Seismic Attribute	**Factor1**	**Factor2**	**Factor3**	**Communality**
Sum Neg Ampl.	-0.981	0	0	0.973
Sum Mag.	0.971	0	0	0.946
Mean Ampl.	-0.969	0	0	0.955
Mean Mag.	0.962	0	0	0.96
RMS Ampl.	0.957	0	0	0.982
Sum Ampl.	-0.955	0	0	0.966
Max Mag.	0.945	0	0	0.949
Min Ampl.	-0.939	0	0	0.973
Avg. Trough Ampl.	-0.931	0	0	0.974
Arc Length	0.74	0.548	0	0.858
Bandwidth Bias	0	0.967	0	0.944
Bandwidth Debias	0	0.964	0	0.936
P/N ratio	0.435	0.796	0	0.839
Inst. Freq.	-0.369	0.654	0	0.588
No-ZeroXing	0.424	0.639	0	0.592
Max Ampl.	0.5	0.639	0	0.746
Inst. Phase	0	0	0.933	0.908
Half Energy	0	-0.564	0.732	0.854

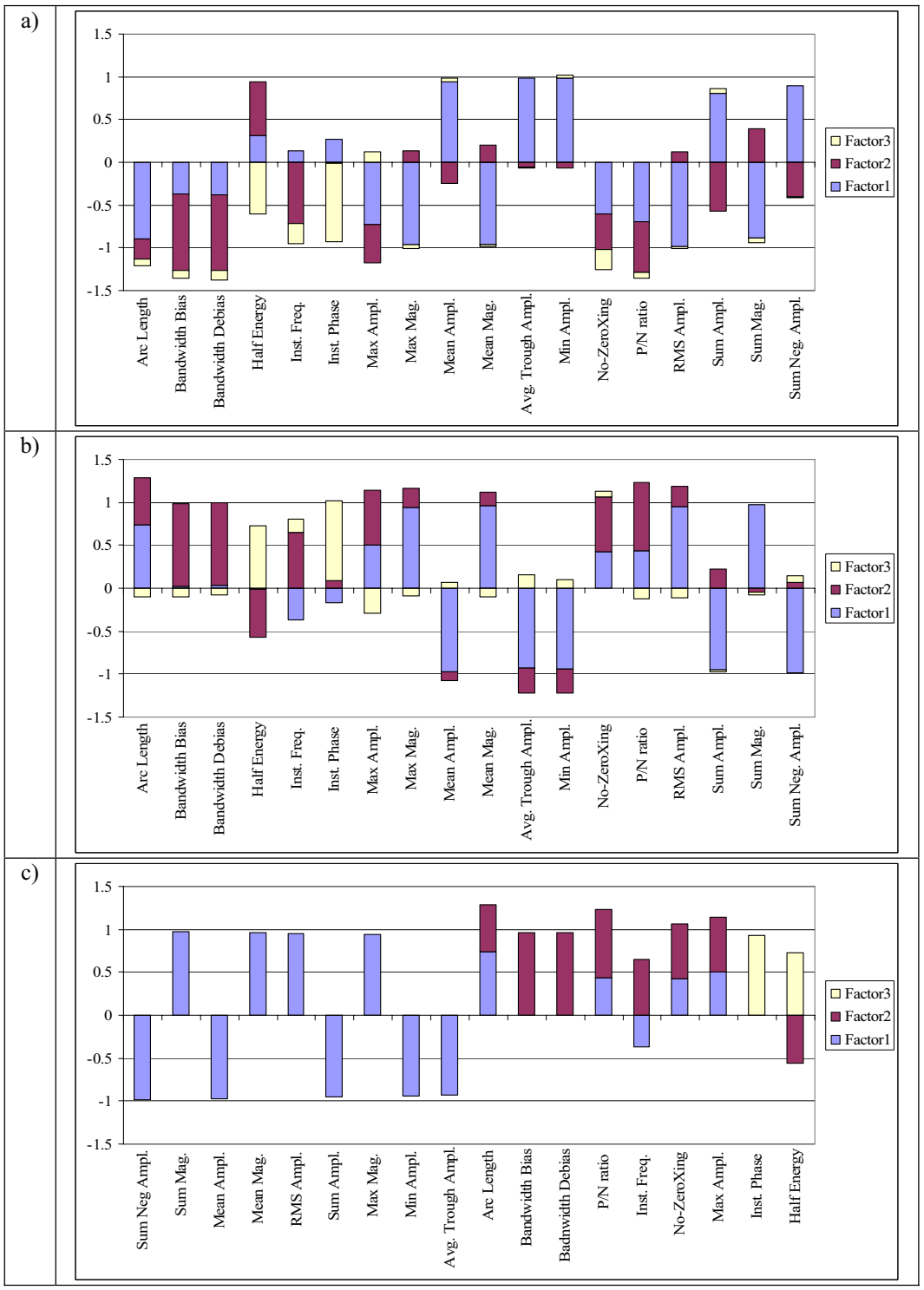

Figure 58. PFA loadings matrix comparison between unrotated loading (a) rotated loadings using Varimax (b) and rotated and sorted loading with a cutoff value of (0.3). Plot (c) is much easier to interpret and indicates that the results of PFA were comparable to the PCA.

For example, in noisy regions, maximum magnitude can extract positive samples from adjacent peak portion above or below the N-sand interval. According to synthetic seismogram modeling, these positive samples belong to bounding shaly deposits enveloping the N-sand interval. Subsequently, it is expected that PF-1 is more representative to the N-sand interval.

Figure 59 shows a map presentation of PF-1. It suggests that the upper region of the major incised valley system in the western side of the study area is mainly composed of 3 main distributary channels. Moreover, it is possible that the western channel was active during the early lowstand period which might be abandoned due to stepwise migration of the main axes of distributary channels. The 30-1 and 30-6 wells received marginal sand deposits during the upper section the N-sand interval (Figure 59).

PF-2 is loaded by bandwidth rating attributes (Figure 58, c) in addition to arc length and the ratio of positive to negative seismic attributes. The later two attributes were discarded since they are shared by PF-1. However, these attributes are sensitive to heterogeneities within the extracted time window (Table 3). Accordingly, PF-2 (upper map in Figure 60) can be described as measure of heterogeneities related to possible lithologic cyclicity. PF-3 is loaded mainly by the instantaneous phase seismic attribute. This factor can be described as measure of lateral continuity across the N-sand interval (lower map in Figure 60).

Based on the results of PFA, it is possible to derive linear combinations of the original standardized attributes (Johnson and Wichern, 1998). This is achieved by adding the original standardized seismic attributes that demonstrate a higher loading on each PF. It is possible that these new linear combinations might reveal subtle features were smeared off in other PF's or original attribute. Figure 61 shows two linear combination maps based on the loading results of PF-1 and PF-2, (LFSC-1 and LFSC-2) respectively.

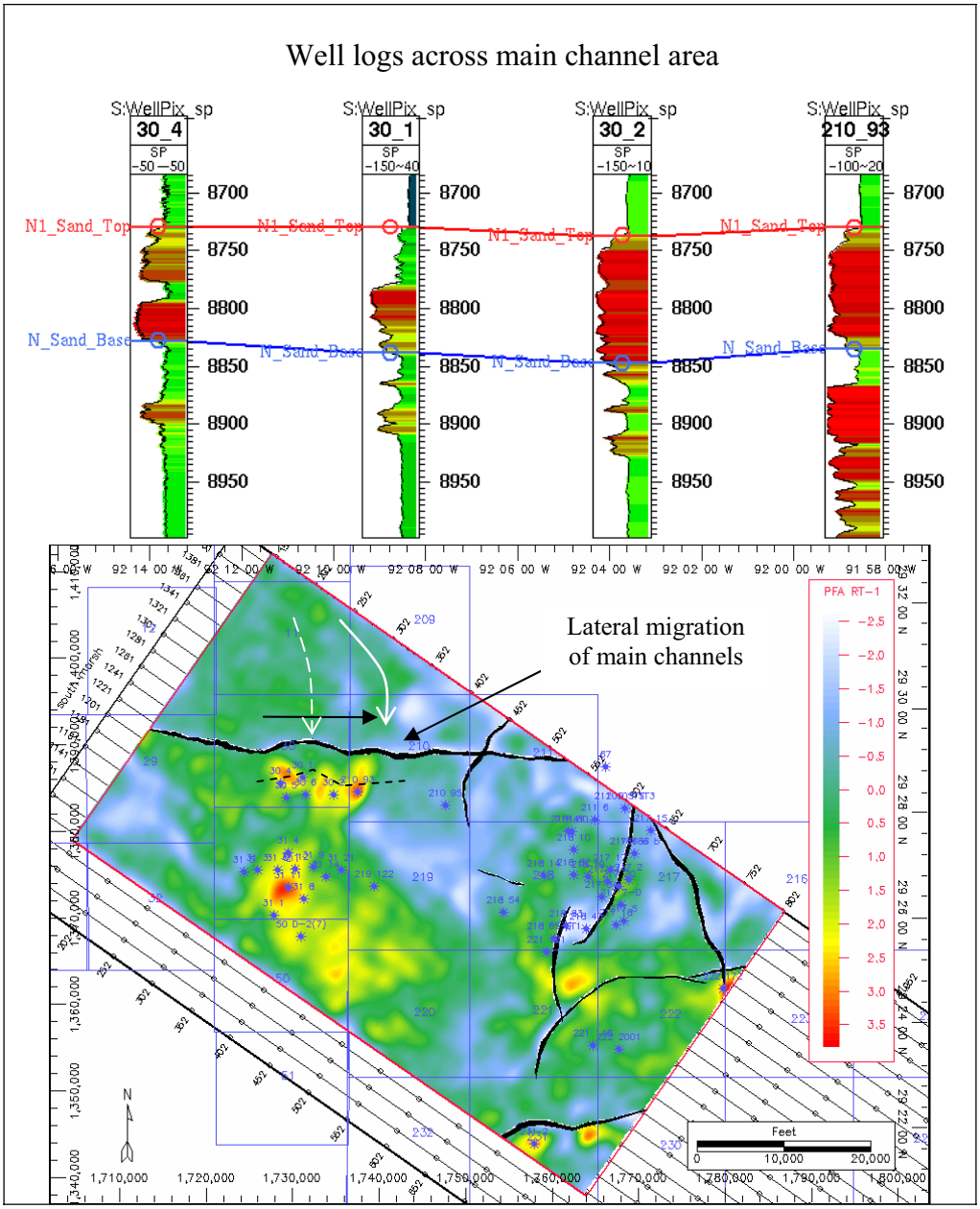

Figure 59. PF-RT-1 is the first rotated principal factor after Varimax rotation. The upper channel region of the incised valley shows a possible lateral migration of the axis of distributary channels. The upper section of the of well 30-1 and 30-6, not shown in section, received marginal sand deposits compared to adjacent wells located with eastern channels gorge.

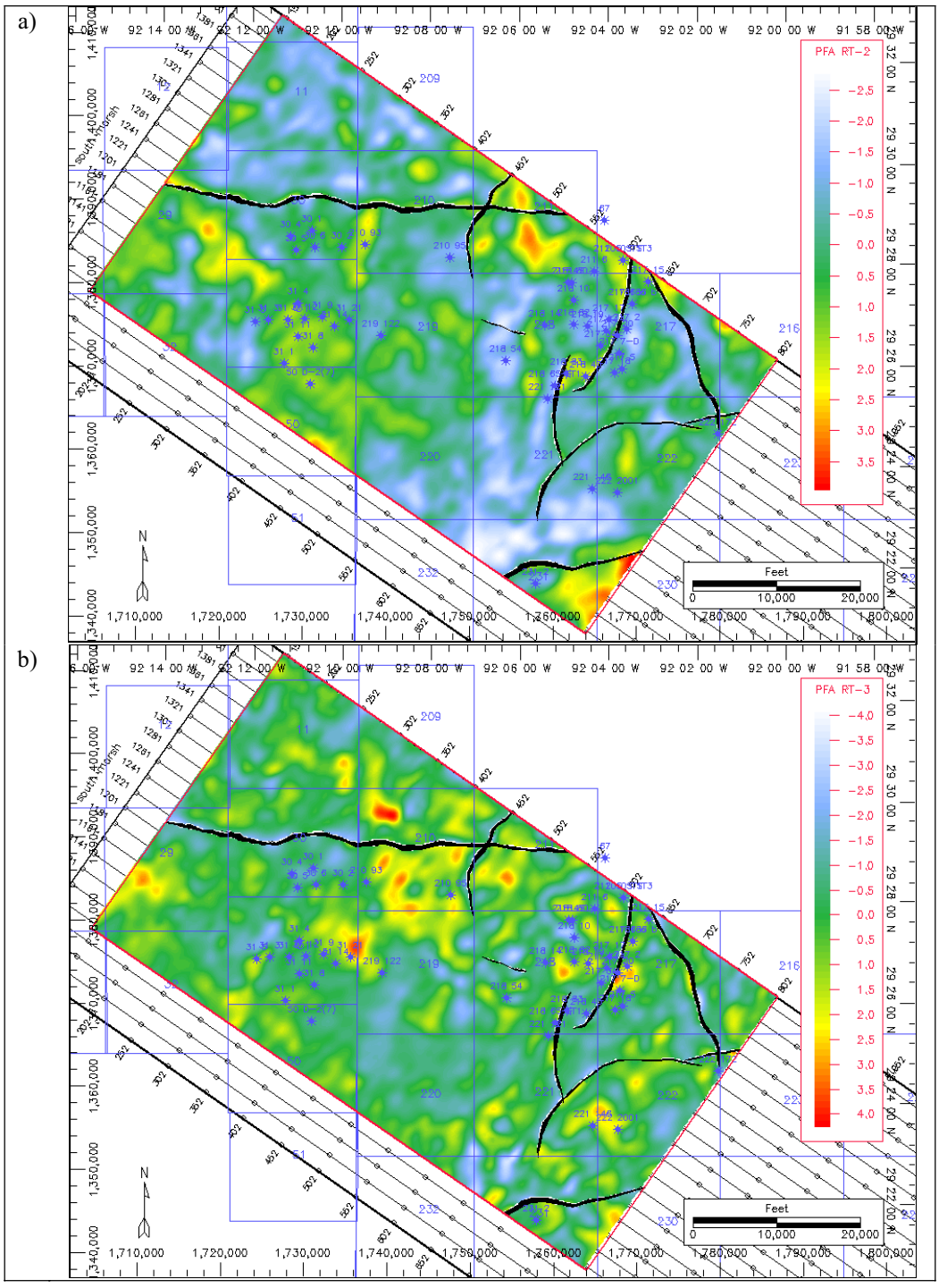

Figure 60. PF-2 (A) and PF-3 (B) map presentation with Varimax rotation applied. These PF's reflect possible heterogeneities similar to PC-2 and PC-3, but they show fewer variations due to tighter scale.

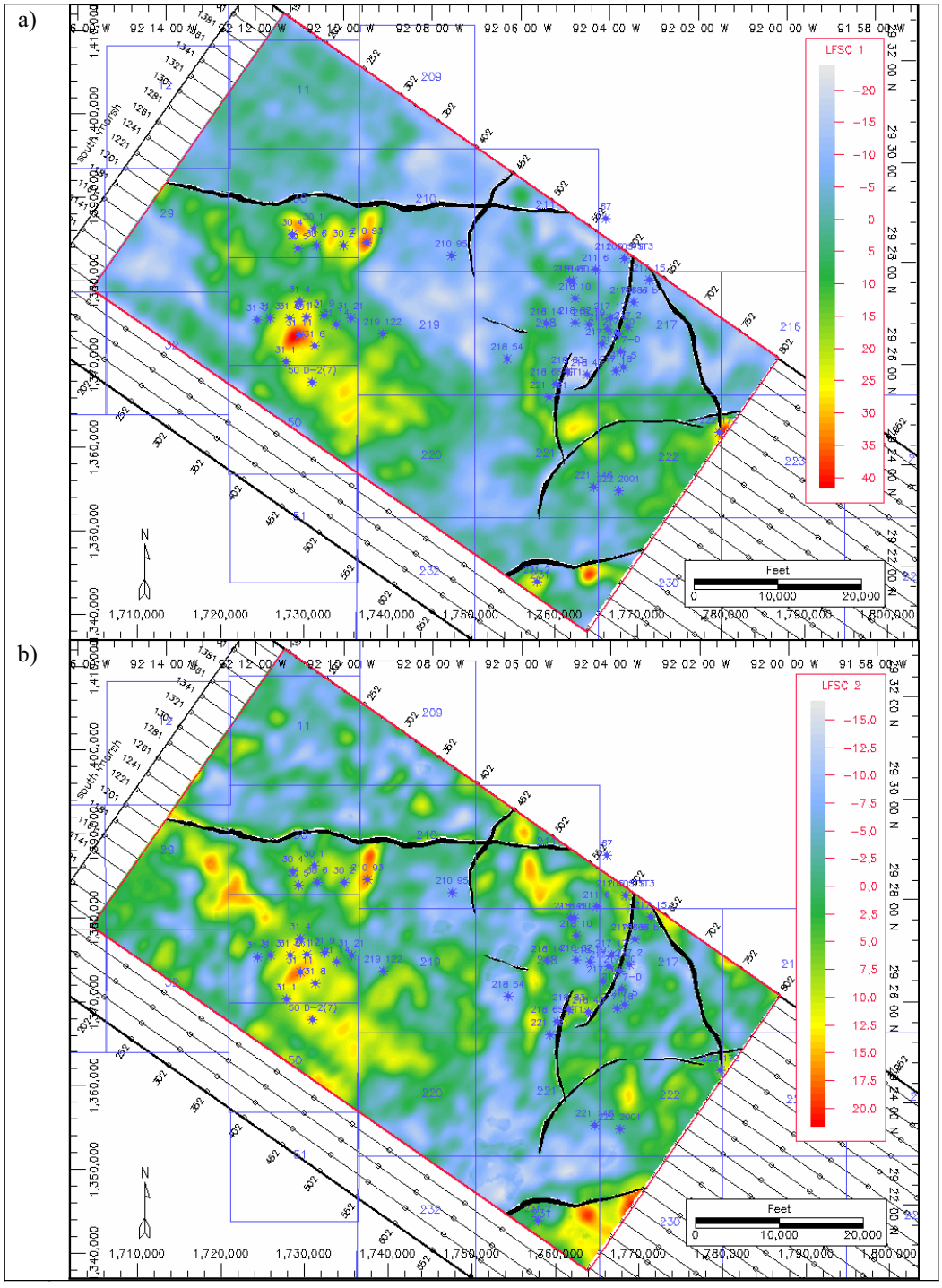

Figure 61. LFSC-1 is the linear factor score combinations of the main loaders of PF-1 (upper) and LFSC-2 is the linear factor score combinations of the main loaders of PF-2 (lower).

In summary, PCA and PFA were used to reduce the dimensionality of the data set, produce orthogonal multivariate seismic attributes and to provide a mean to understand associations existing between the various attributes. The resulted multivariate seismic attributes are relatively comparable due to the size of the data set. Correlating these multivariate attributes with reservoir properties, in the next step of this study, will give a definite meaning and asses the feasibility of these attributes.

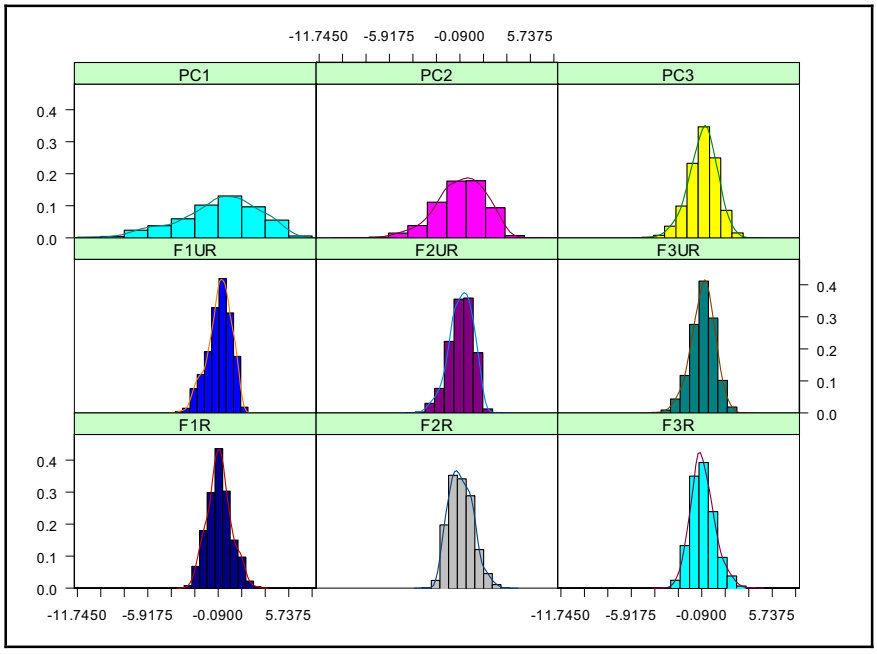

Figure 62. Normal density plots of the multivariate seismic attributes. PC's tend to have wider ranges compared to PF's.

Each PC attribute map provides wider range than its corresponding PF (Figure 62). This is mainly attributes to the fact that PFA tends to blur the relationship between clusters because it assumes that factor scores are normally distributed, meanwhile PCA tends to maintain the representation of widely separated clusters in a reduced space but also minimizes the distances between groups that are not widely separated (Rohlf, 1970).

4.3 Well log analysis

Forty two wells were available for this study. The N-sand interval is primarily sand-shale sequences located between ~8460 and ~9490ft. Partially penetrating wells are discarded from the study. Older well logs contain limited arrays of log curves, mainly belonging to the Tiger Shoal field, were used for shale volume assessment only.

The shale volume is determined mainly from the minimum of gamma ray and spontaneous potential logs. The total porosity is based on the density log, which showed good correlation with estimated core porosity measured from the wells 30-4 and 30-2. Available caliper logs showed good wellbore conditions in the zone of interest. Table 8 lists the various log measured properties for the wells of Vermilion 50 and Tiger Shoal. The results of water saturation were dropped out of the study due to the noisy results and the lack of proper core control.

Table 8. Summary of N-sand interval well log properties of Vermilion 50 and Tiger Shoal wells.

Borehole Name	Top MD (ft)	Bottom MD (ft)	Gross Thickness TVD (ft)	Gross effective porosity TVD (ft3/ft3)	Net Thickness TVD (ft)	Sand Volume Fraction TVD (ft3/ft3)	Net Reservoir Porosity Thickness TVD (ft)	Net Reservoir Water Saturation TVD (ft3/ft3)
Vermilion 50 wells								
210-93	8732.55	8824.98	92.43	0.34	91.93	0.99	31.12	0.64
210-95	8795.00	8897.34	102.34	0.13	47.50	0.46	6.70	0.71
30-1	8730.41	8841.99	111.58	0.16	55.00	0.60	8.94	0.89
30-2	8739.37	8846.20	106.82	0.30	106.82	1.00	31.82	0.72
30-4	8730.11	8828.61	98.49	0.25	66.00	0.67	19.31	0.68
30-5	8763.62	8869.89	106.27	0.26	94.00	0.88	24.87	0.96
30-6	8750.13	8855.91	105.77	0.17	52.00	0.49	13.00	-
31-1	8846.28	8922.29	76.01	0.29	75.01	0.99	22.01	0.91
31-12	8826.96	8931.30	104.34	0.25	97.00	0.93	24.90	0.82
31-14	8852.36	8930.26	77.88	0.26	71.89	0.92	19.23	0.86
31-21	8882.60	8966.34	83.75	0.24	74.00	0.88	18.95	-
31-3	8860.67	8949.19	88.52	0.27	86.00	0.97	23.23	0.89
31-4	8788.96	8875.98	87.03	0.29	83.00	0.95	24.08	0.94
31-5	8892.70	8974.07	81.38	0.27	67.00	0.82	19.14	0.87
31-6	8824.54	8906.08	81.54	0.22	56.00	0.69	13.66	-
31-8	8861.11	8944.74	83.63	0.27	82.00	0.98	21.89	-
31-9	8835.89	8923.95	88.07	0.18	39.50	0.45	11.05	-
50-D-2 (7)	8958.36	9042.17	83.81	0.26	82.50	0.98	21.35	0.79
219-122	8889.16	8967.53	78.38	0.25	74.00	0.94	18.21	0.91
Tiger Shoal wells								
211-6	8840.70	8969.26	128.57	0.29	119.57	0.93	35.78	-
212-105	8704.04	8790.01	85.91	0.17	46.97	0.55	9.75	0.90

Table 8. Continued.

217-114	8695.77	8786.08	90.31	0.19	54.00	0.60	11.18	0.68
217-15	8494.19	8574.11	79.92	0.22	44.42	0.56	13.38	0.66
217-17	8664.56	8730.45	65.89	0.27	45.00	0.68	14.11	0.87
217-18	8505.57	8589.06	83.49	0.15	33.00	0.40	7.16	0.38
217-20	8459.85	8540.06	80.21	0.15	38.00	0.47	8.19	0.41
217-34	8656.27	8730.18	73.91	0.17	33.00	0.45	8.50	0.35
217-5	8501.98	8585.17	83.19	0.18	36.00	0.43	8.07	0.43
217-7-D	8470.56	8548.99	78.43	0.18	46.00	0.59	6.61	0.79
218- 14	8648.82	8713.43	64.62	0.22	34.00	0.53	7.48	-
218-10	8593.13	8700.31	107.18	0.22	51.00	0.48	11.22	-
218-19	8602.91	8693.20	90.29	0.11	42.00	0.47	4.42	0.79
218-42	8625.16	8730.41	105.25	0.12	46.00	0.44	5.19	0.65
218-43	8707.89	8785.75	77.86	0.17	31.00	0.40	7.66	0.86
218-54	8805.12	8889.54	84.42	0.26	55.00	0.65	16.95	0.87
218-65	8572.50	8658.87	85.94	0.15	20.88	0.24	3.62	-
218-80	8606.92	8706.50	99.58	0.17	52.00	0.52	7.60	-
218-83	8724.09	8806.63	82.53	0.18	51.00	0.62	9.54	0.87
221-121	8634.28	8698.36	61.02	0.19	39.03	0.64	8.88	-
221-146	9124.13	9198.58	74.45	0.22	39.00	0.52	10.55	0.95
222-2001	9143.99	9257.21	113.22	0.32	99.00	0.87	33.50	0.66
231-2	9401.22	9638.38	237.16	0.31	235.00	0.99	72.68	0.93
Borehole Name	**Top MD (ft)**	**Bottom MD (ft)**	**Gross Thickness TVD (ft)**	**Gross effective porosity TVD (ft3/ft3)**	**Net Thickness TVD (ft)**	**Sand Volume Fraction TVD (ft3/ft3)**	**Net Reservoir Porosity Thickness TVD (ft)**	**Net Reservoir Water Saturation TVD (ft3/ft3)**

4.4 Log-derived reservoir properties estimation using collocated cokriging

The main goal of this study is to obtain accurate estimates of key log-derived reservoir properties of the N-sand interval measured Vermilion 50 and Tiger Shoal fields. These key properties include; gross thickness, gross effective porosity, net thickness, net reservoir porosity thickness product, sand volume fraction (net-to-gross ratio), and water saturation. Unfortunately, water saturation was dropped out of the study due to the noisy results and the lack of proper core control.

The use of collocated cokriging allows the integration between sparse primary well data and a more spatially dense secondary seismic attributes data inputs. This algorithm tends to screen the influence of further away secondary data (Xu, et al., 1992). A prerequisite of accurate estimates is good correlation between primary well data and secondary seismic attributes data. The higher the correlation coefficient between these inputs, the minimum the amount of collocated cokriging variance estimate and the greater the reliability. However, in collocated cokriging integration study a value of as low as 0.4 of correlation coefficient can enhance the results of estimated reservoir properties (Chambers et al., 1994)

Figure 63 illustrates the cokriging estimation variance as a function of the coefficient of correlation for different values of the kriging variance. The plot can be used to assess how high the correlation coefficient has to be for cokriging to significantly reduce the expected estimation error compared to kriging. In order to enhance the kriging estimates, the kriging variance should decrease and eventually a higher coefficient of correlation is required to reduce the estimation variance by the same amount (Doyen, et al., 1996). If the correlation coefficient between primary and secondary data equals to 0.0, then the contribution of the secondary data is ignored (Xu et al., 1992). The value of the correlation coefficient is used to provide a cross-covariance function relating primary to secondary data by using the Markov hypothesis (Xu et al., 1992). A number of seismic attribute were investigated to establish an accurate integration scheme between a reservoir properties by selecting highly correlated seismic attribute. The following sections will present and discuss the Vermilion 50 field.

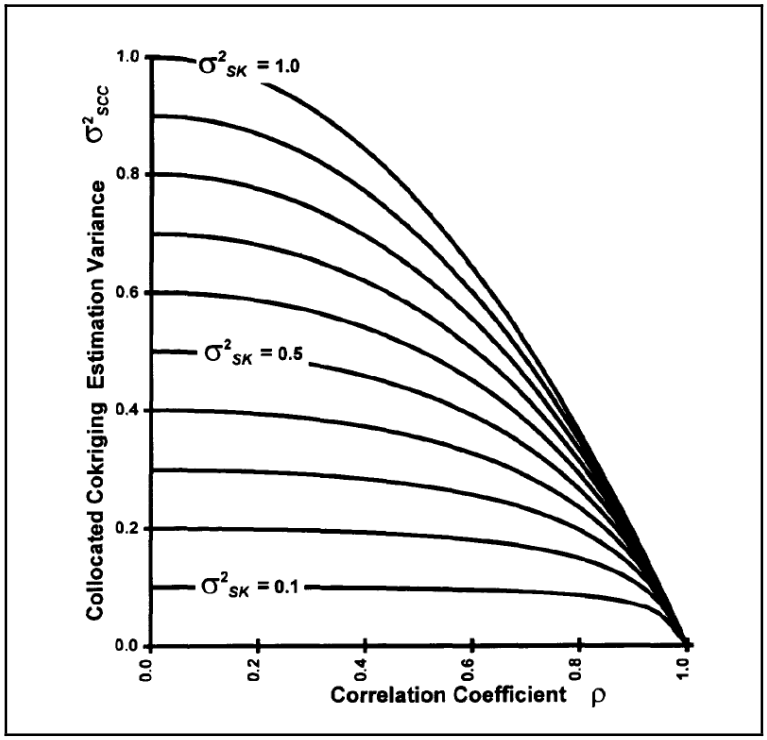

Figure 63. Collocated cokriging variance as a function of the coefficient of correlation, assuming normalized primary and secondary variable inputs. An increase in correlation coefficient between primary and secondary data will minimize the amount of variance associated with collocated cokriging. Note that collocated cokriging will fall to a simple kriging case, when the correlation coefficient equals to 0.0. Hence, secondary data contribution is ignored. (after Doyen et al., 1996). σ^2_{SK} is simple kriging estimation variance.

Although, the main objective of this study is to investigate the use of multivariate seismic attributes to obtain better reservoir property estimates of the N-sand interval of Tiger Shoal and Vermilion 50 wells, this study reports the results from the field of Vermilion 50 only. Unfortunately, the aerial distribution of wells across the field did not allow building a spatial model by the use of experimental semivariograms. Moreover, seismic events located above the N-sand interval shows low frequency contents due to gas saturated stacked sediments which are characterized by sagging and tuning effects (Figure 64), which weaken the correlation with reservoir log properties.

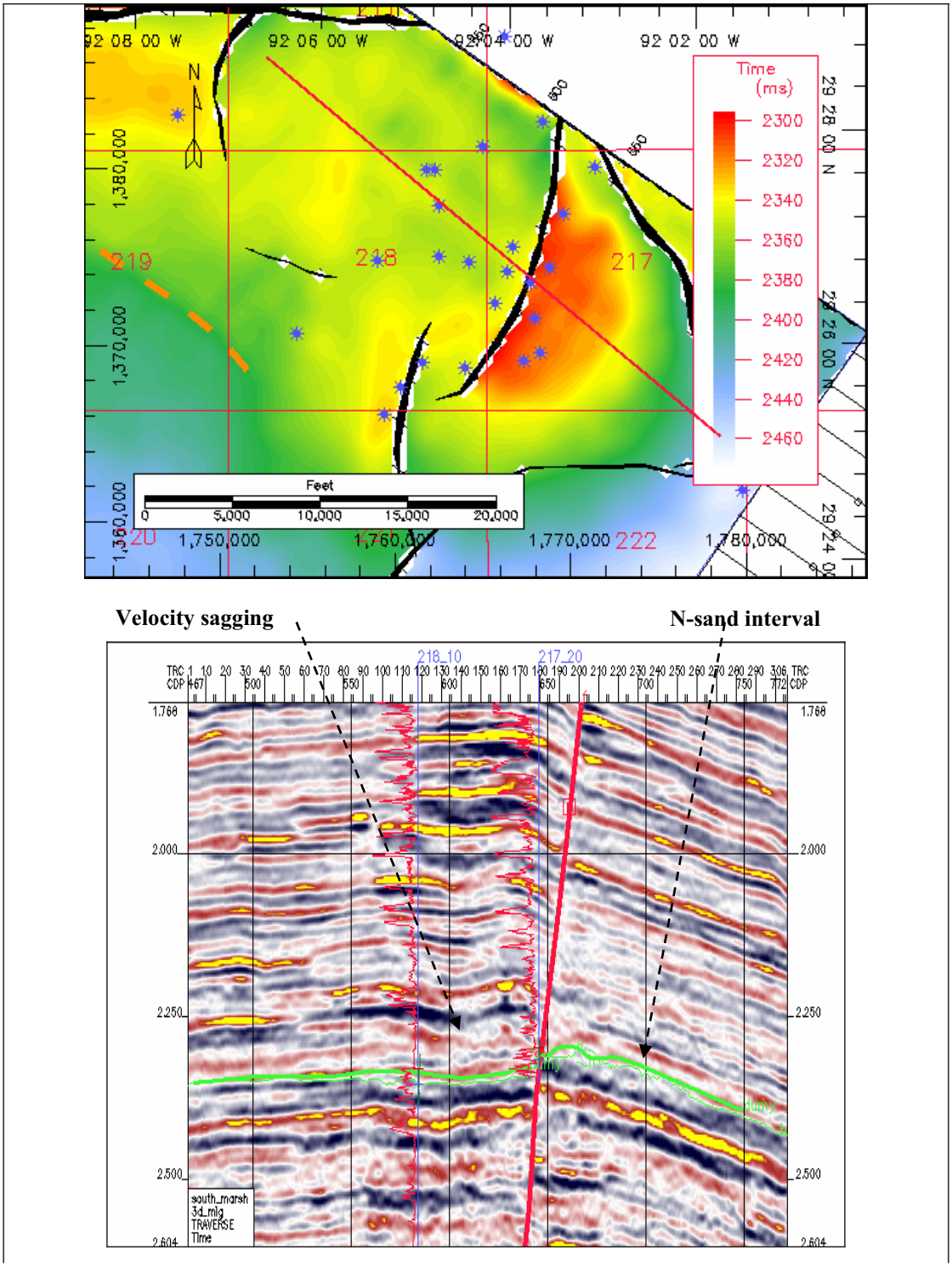

Figure 64. Dip- oriented seismic section across Tiger Shoal field. N-sand interval shows a sagging effect due to overlaying stacked gas saturated sediments. Additionally, the proximity of the wells to the fault plain produces low correlative relationship with reservoir log properties. SP logs are posted in red.

Nineteen wells are located within the field of Vermilion 50, (Figure 65). However, well 210-95 is located to the eastern side of the incised valley containing the Vermilion 50 field. Previous geological interpretation showed that this region represents a major marine flood plain with minimum sediment bypass with minimal incision activities. Texaco scout records indicate that this well did not have commercial production and was plugged and abandoned. Accordingly, it was discarded from the group of wells used in the study.

4.4.1 Gross thickness mapping

The gross thickness represents the true vertical thickness difference between the upper and the lower boundary of N-sand interval. Figure 65 shows the acoustic amplitude map of the N-sand interval across the western area of the study area. The bubble plot overlay represents the spatial distribution of gross thickness property. The maximum gross thickness of N-sand interval is associated with the maximum accommodation space produced by growth faulting. Gross thickness is about 111ft in the landward side of incised valley system. It thins basinward and towards the eastern and western margins of the valley system. The minimum thickness is recorded at well 31-1 of about 76ft.

This behavior suggests that N-sand interval represent atypical wedge model of incised valley fill fan deposits. This behavior is predictable and might proposes the possibility of using the time structure map of the N-sand interval as a secondary data to provide a collocated cokriging map for the distribution of gross thickness. Cross-plotting gross thickness values vs. time (TWT) shows a highly correlated relationship (r=0.78 in Figure 66). However the resulted map will be very smooth and will not show the roughness related to the real geology of the N-sand deposits.

The first step in geostatistical mapping is defining a representative spatial model that is able to capture the spatial details of the property investigated. The spatial model for the distribution of the gross thickness values was estimated by the use of an experimental semivariogram. The best spatial model was achieved by using a lag interval of about 1190ft. Examination of directional experimental semivariograms

(n=12) revealed anisotropic behavior for the spatial distribution of gross thickness property.

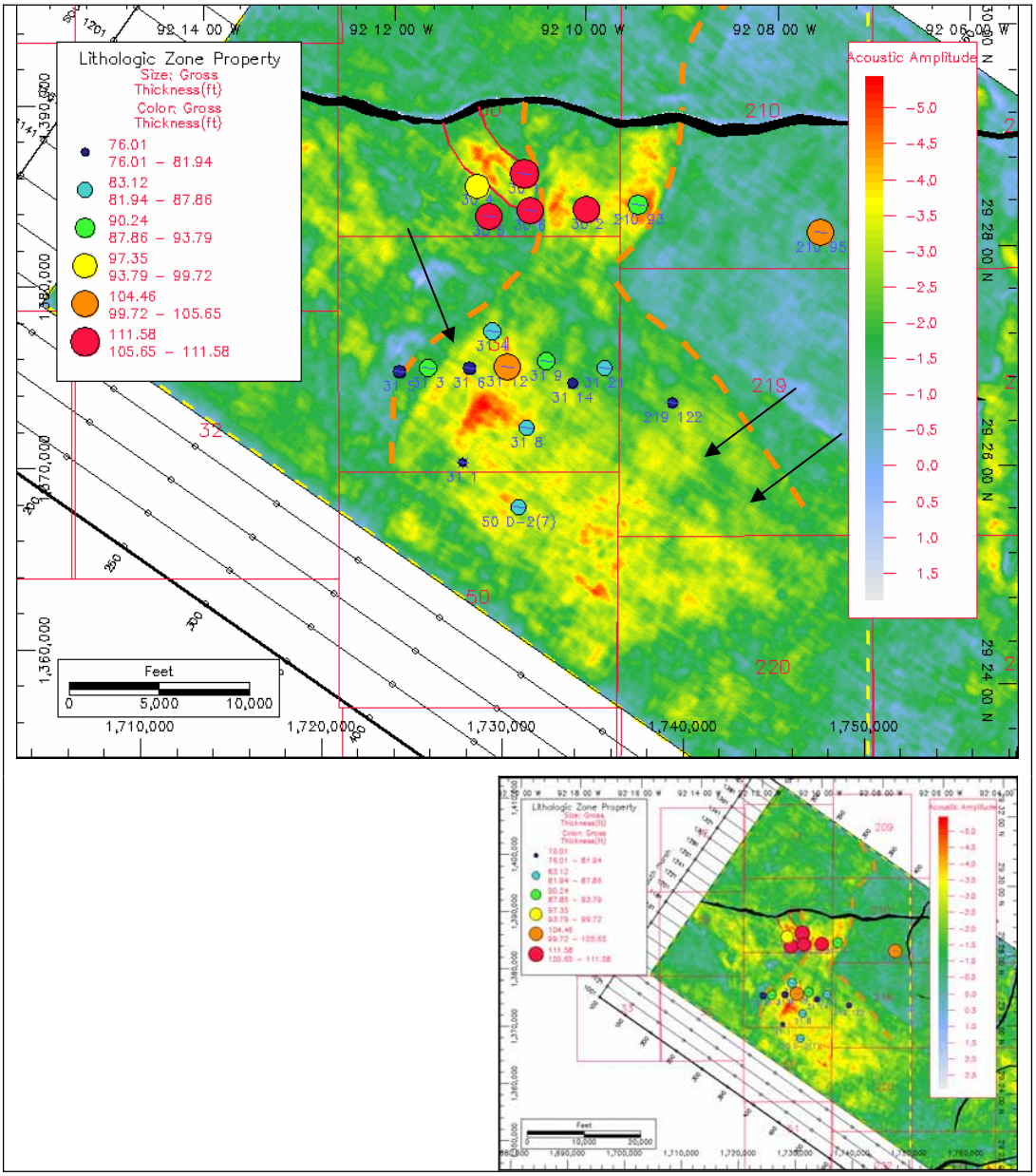

Figure 65. Seismic amplitude map of the western region of the study area. In general, wells located up dip of the incised valley have higher gross sand thicknesses. The postulated boundaries of the main incised channel are shown with dashed orange line. A subsidiary distributary system is shown to the west of the major trunk of the incised valley. Well 210-95 is located off the incised valley and was discarded from spatial analysis studies. The lower map shows the whole western region which is defined by the dashed yellow border. Black arrows indicate possible incised valley boundaries due to successive eastward accretion activities.

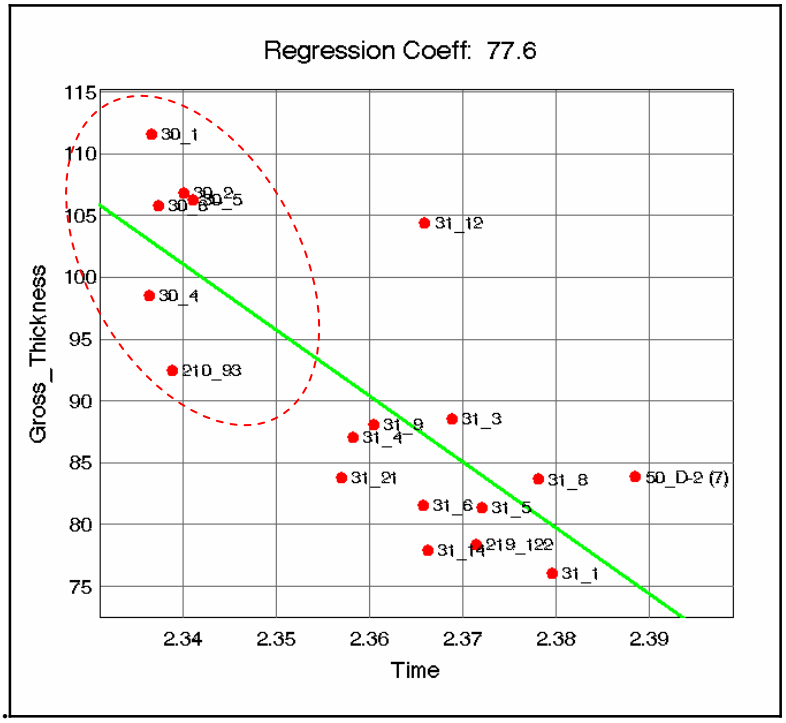

Figure 66. Crossplot between the gross thickness (ft) and TWT Time (s). Updip wells, highlighted by the dashed ellipse, are characterized by higher gross thickness measures while down dip wells show a general decrease in gross thickness.

The ellipse plot of anisotropy showed that the maximum direction of continuity is parallel to the regional strike of the study area, azimuth angle of major axis of anisotropy equals to 95°. The properties of the spatial model are shown in Figure 67.

Figure 68 shows a summary plot of correlations between gross thickness and the various seismic attributes. The first eighteen seismic attributes are the original attributes extracted across the N-sand interval. The remainder attributes are the multivariate attributes produced by PCA and PFA.

The correlation between gross thickness values and original seismic attributes (n=18) showed that only the instantaneous phase seismic attribute correlates well with gross thickness (r=-0.65). Figure 69 shows instantaneous phase seismic attribute map and a cross-plot presentation of instantaneous phase vs. gross thickness. The sum of amplitudes and magnitudes came in the second stage in correlation to gross thickness (Figure 68).

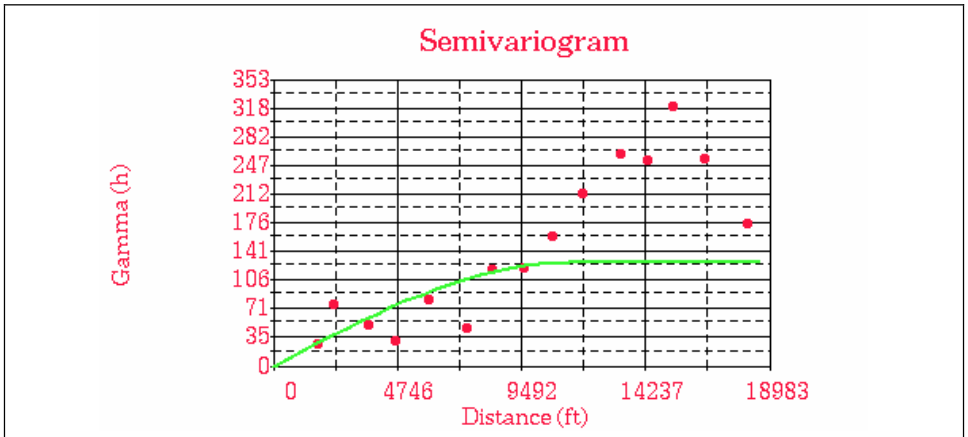

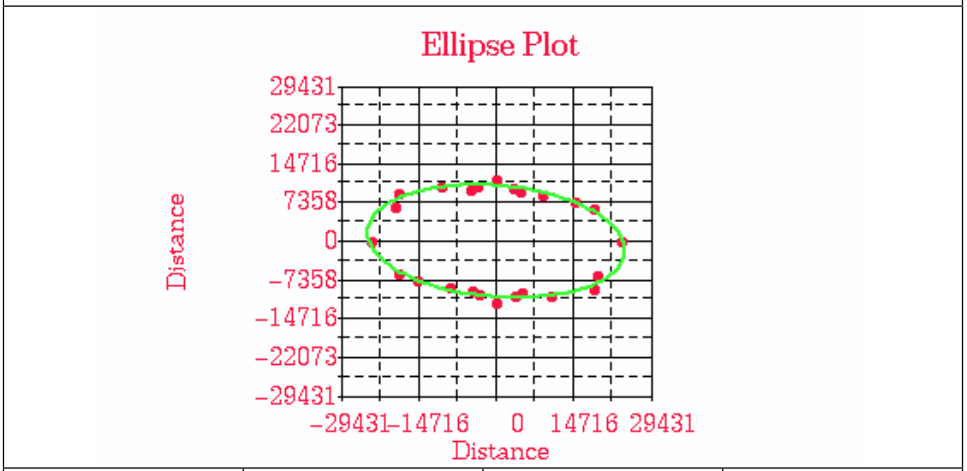

Lag Interval (h)	1189.78ft	**Sill**	127.1147
Max. Lag	20,000ft	**Nugget**	0
Model	Spherical	**Anisotropy Angle**	95°
Range	11200.584ft	**Anisotropy ratio**	0.45

Figure 67. Spatial analysis parameters of gross thickness property of Vermilion 50 wells. The direction of maximum continuity is parallel to the regional strike of the region which is correlated to the local depositional strike orientation.

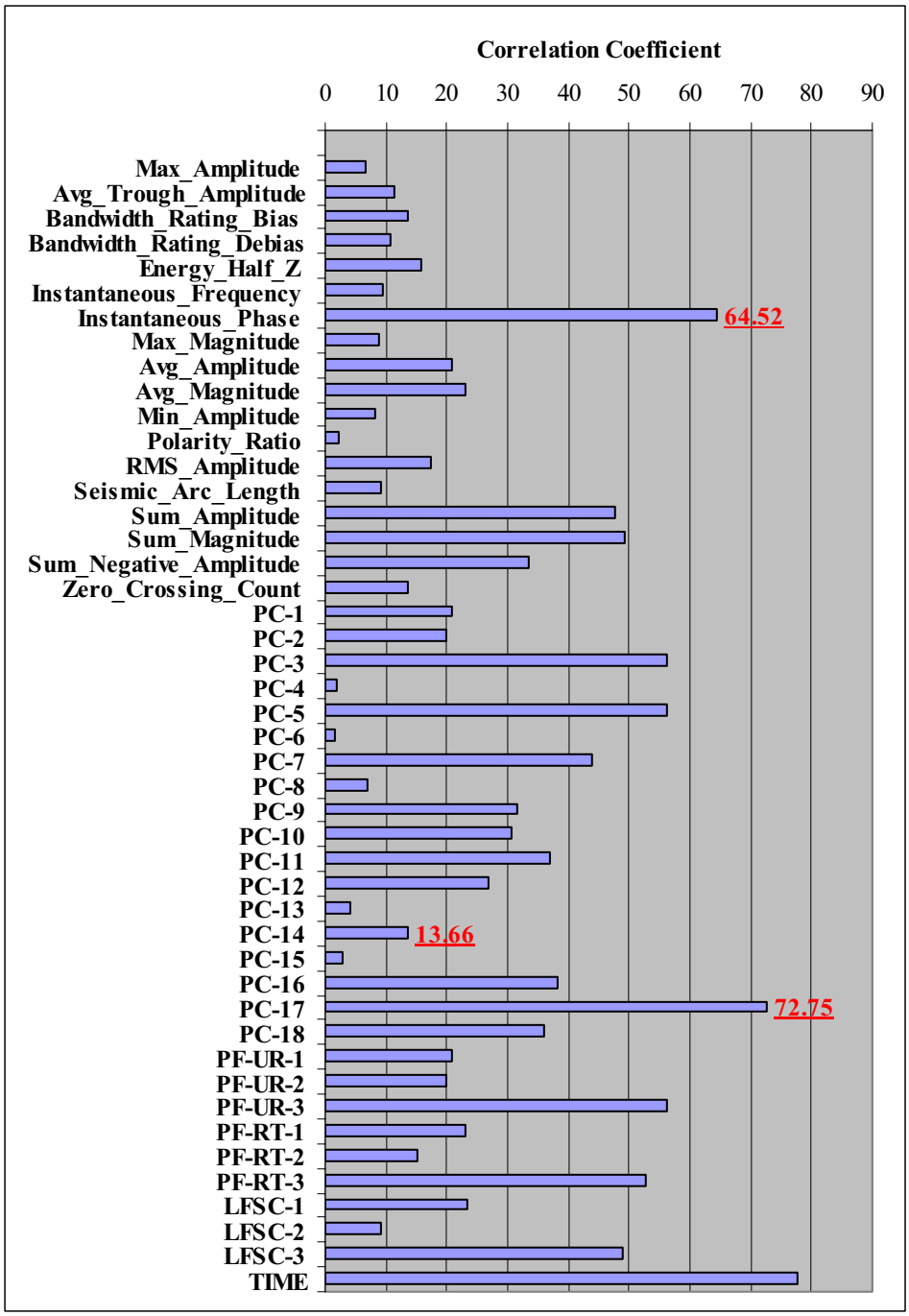

Figure 68. Correlation coefficient plot of the absolute value of the correlation coefficient (r) between gross thicknesses inferred from wells and seismic attributes. Gross thickness property showed good correlations with instantaneous phase (r=0.65) and PC-17 (r=0.73). Note that original seismic attributes were standardized by subtracting the mean and division by the standard deviation value. LFSC-1 is a linear factor score combination of PF-RT-1.

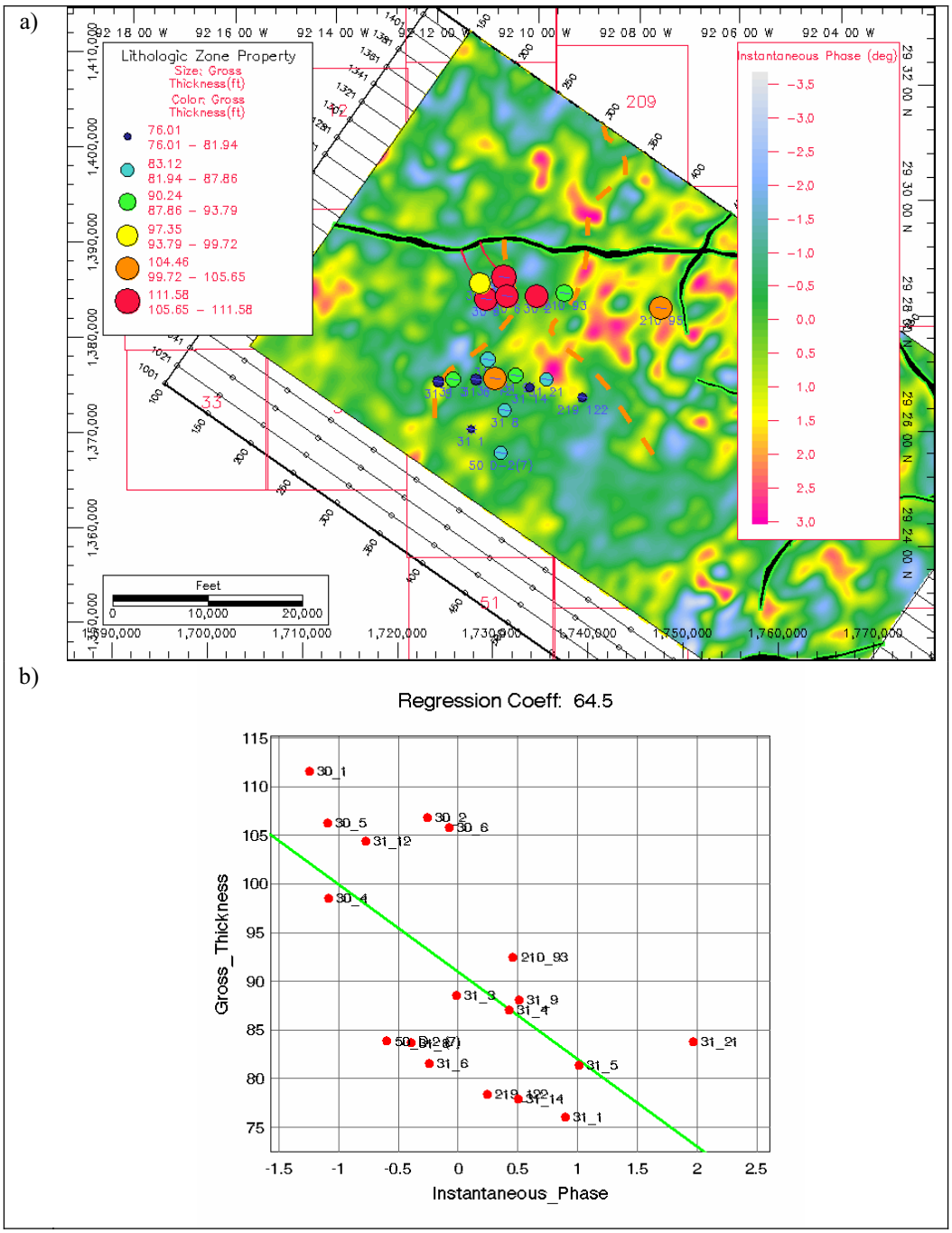

Figure 69. Instantaneous phase in Vermilion 50 area of the study area (a) showed good correlation with well-log derived gross thickness (b). The correlation coefficient value seen in the plot is -0.65.

In general, multivariate seismic attributes correlate better with gross thickness than original seismic attributes. The number of multivariate seismic attributes showing relative correlation to gross thickness is higher than original attributes. However, PC-17 showed the highest correlation with gross thickness measurements (r=-0.73 in Figure 68).

In comparison to instantaneous phase map (Figure 69), the spatial distribution of PC-17 shows an increasing behavior in the basinward of the incised valley (Figure 70). Accordingly, the inverse relationship between PC-17 and gross thickness (Figure 70) will produce better results from a geological point of view, since deltaic deposits across growth fault systems tend to decrease in gross thicknesses in the basinward direction (Coleman and Prior, 1980; Van Heijst et al., 2002).

The scatter-plots of Figures 69 and 70 shows that PC-17 has less dispersion of points around the regression line than that for instantaneous phase. This behavior is best shown in the down dip wells.

The results of multivariate statistical analysis indicated that PC-17 is mainly a weighted linear combination of mean magnitude, minimum amplitude and RMS amplitude (Figure 71 and Table 6). Note that the contribution from instantaneous phase to PC-17 is negligible. This indicates that the response of instantaneous phase attribute may be simultaneously associated with other properties rather than the gross thickness. Therefore, the loading plot (Figure 71) drops the contribution from instantaneous phase to PC-17 and highlights attributes that contribute highly to PC-17 in response to gross thickness property.

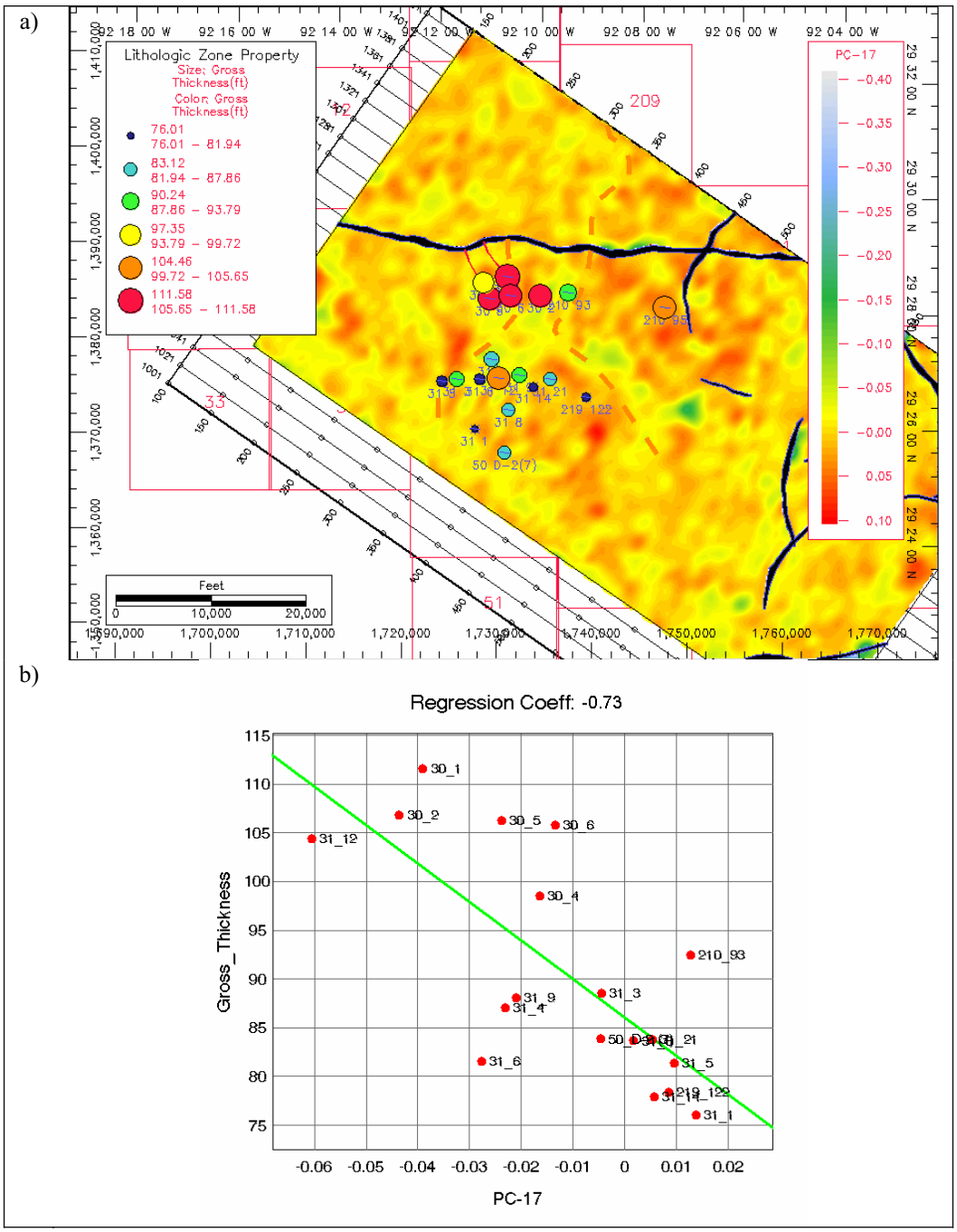

Figure 70. The multivariate seismic attribute PC-17 of the western region of the study area (a) correlate better with gross thickness well-log derived gross thickness (b). Compared to the cross-pot shown in Figure 69, Figure 70 showed less spread for the down dip wells where there is more well control.

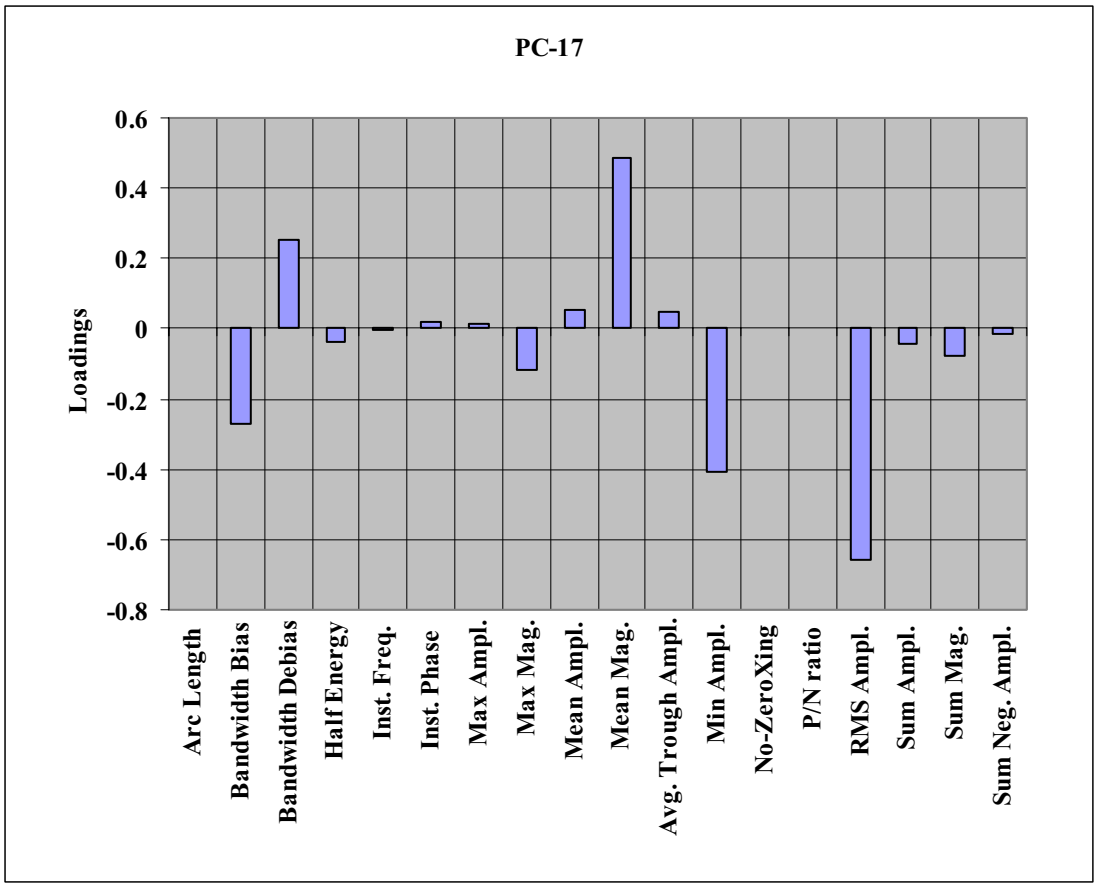

Figure 71. Bar chart illustrating relative contributions (loading) of seismic attributes in PC-17. PC-17 is mainly a weighted linear combination of mean magnitude, minimum amplitude and RMS amplitude. Note that the relative contribution for instantaneous phase to PC-17 is negligible.

The spatial model presented in Figure 67 is used in give an estimate for the spatial distribution of gross thickness property by the use of a collocated cokriging geostatistical method (Isaaks and Srivastava, 1989). For comparison, the results of gross thickness estimations by the use of instantaneous phase and PC-17 are presented in the Figures (72-74).

In contrast to the PC-17 based gross thickness estimate, (Figure 74), instantaneous phase-derived gross thickness map shows higher estimates in the down dip sections of the incised valley (Figure 73). This behavior denoted by instantaneous phase based estimate may be associated with the fact that instantaneous phase was responding to other effects taking place in the lower reaches of the incised valley.

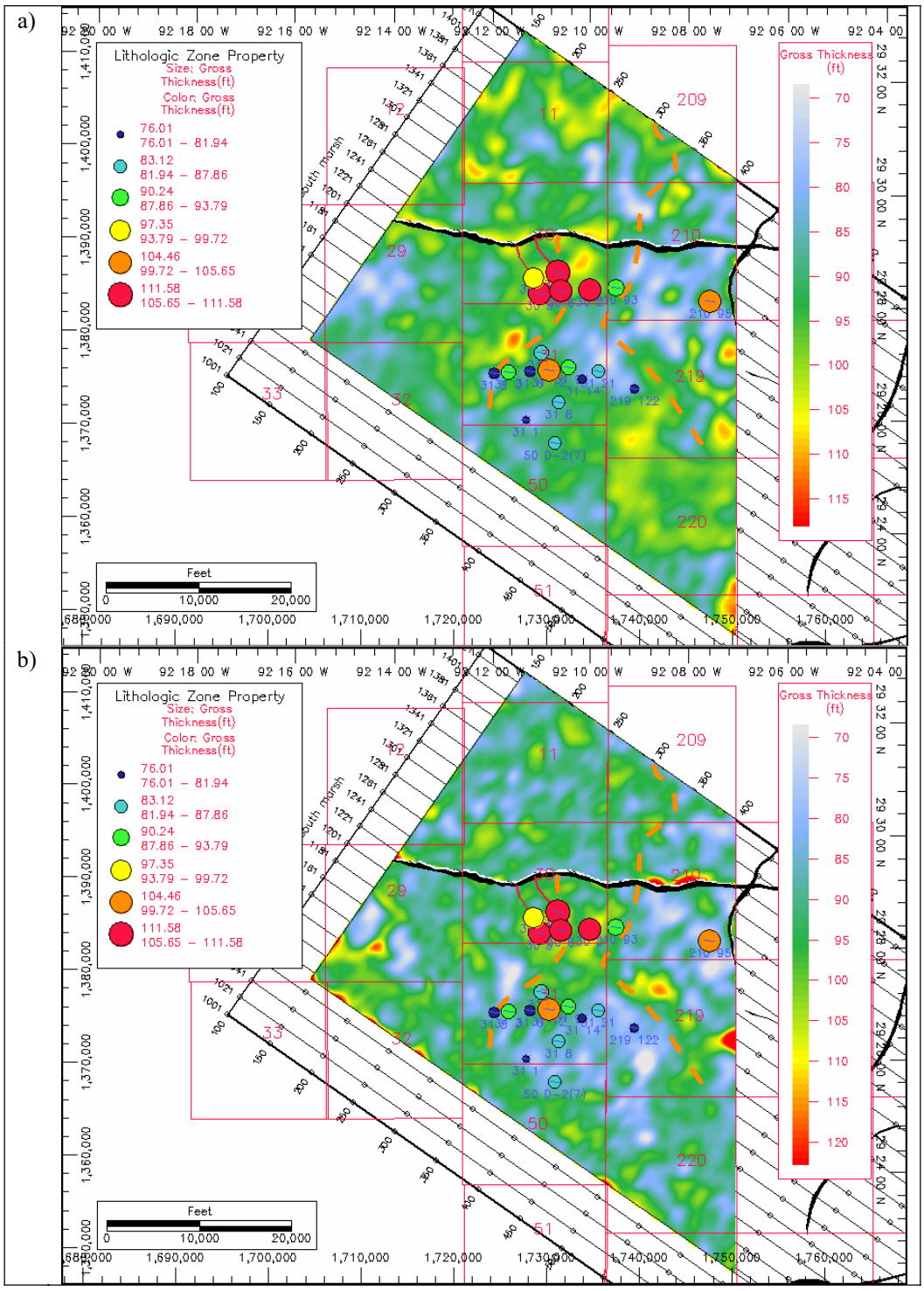

Figure 72. Comparison between gross thickness estimates produced by using instantaneous phase attribute (a) and gross thickness estimates produced by using PC-17 (b). Blow-ups of these maps are shown in Figures 73 and 74, respectively. Note that gross thickness estimates at footwall region showed higher values in (a) than that of (b).

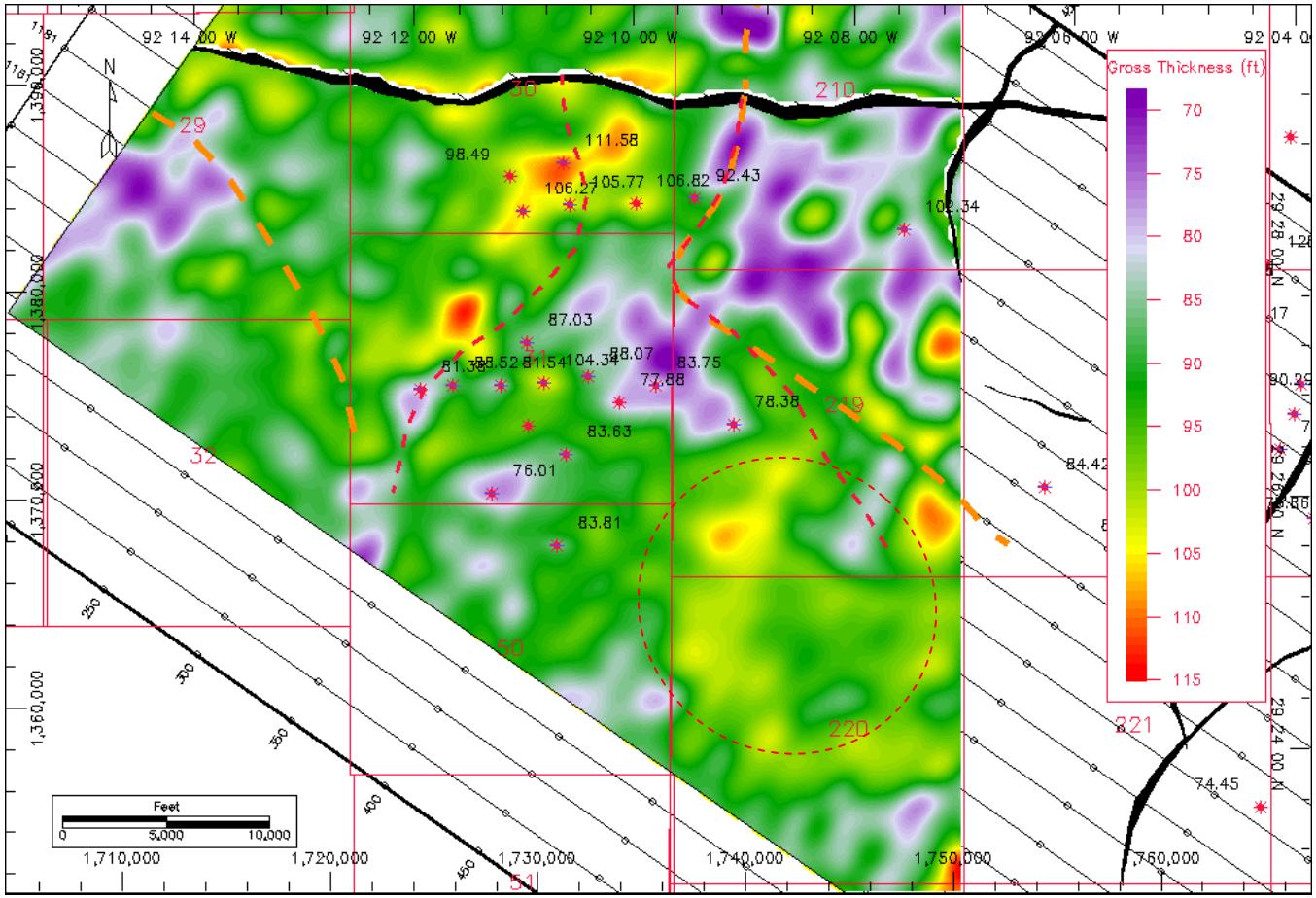

Figure 73. Gross thickness estimate of the N-sand interval from instantaneous phase attribute. Areas highlighted by dashed circles showed high estimates for gross thickness compared to PC-17 estimate of gross thickness (Figure 72).

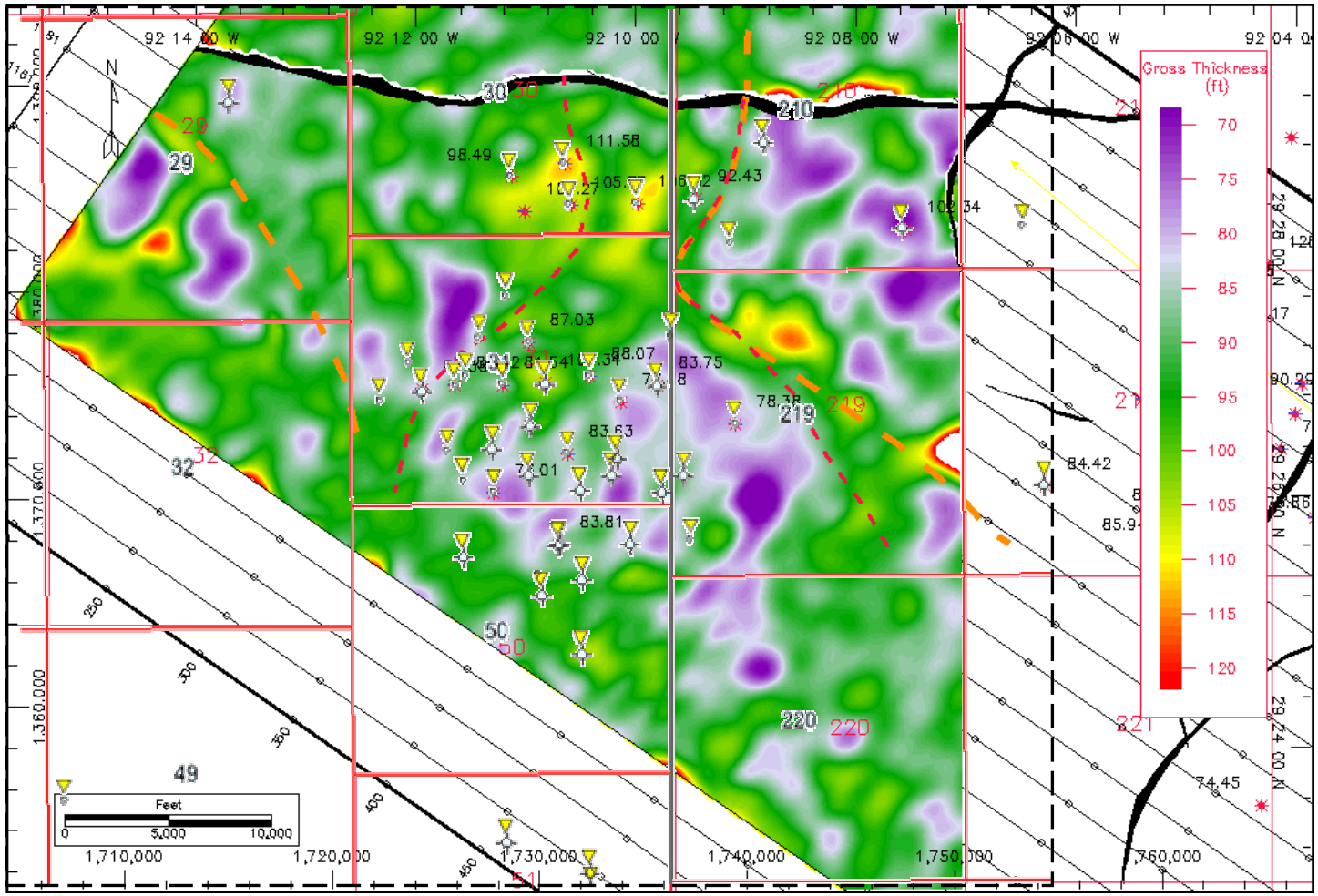

Figure 74.Gross thickness estimate of the N-sand interval from PC-17 showing south-trending linear channel belts of maximum gross thickness which are separated by interchannel areas. These linear trends are strongly correlated with the distribution of historic drilling activates within the area. Figure 75 shows an enlarged version of the central delta deposits. Wells highlighted with yellow triangles represent historic drilling activity within the study area (www.A2D.com, 2003). Wells shown in red stars are these available to this study.

It is expected that the lower and eastern sides of the valley are characterized by more shale intercalations and reworked deposits due the general eastward accretion as shown in Figure 63. Elevated instantaneous phase values may thus be a consequence of internal lithologic heterogeneities rather than in response to increased gross thickness effect.

On the other hand, PC-17-based gross thickness spatial map distribution is geologically reasonable. The region defining the footwall of the N-sand interval and the southern reaches of the incised valley gave lower gross thickness values (Figure 72, 73 and 74) than those produced by instantaneous phase approach.

Gross thickness results of PC-17 showed a distinctive spatial distribution pattern of maximum gross thickness of south-trending linear channel belts which are separated by interchannel areas in which gross thickness is thinner than 80 ft (Figures 74 and 75). These linear trends are strongly correlated with the distribution of historic drilling activates within the area. These results validate the geological model assumed which represents a shelf margin deltaic system. Linear trends represent slightly sinuous gullies of distributary channel crosscutting through the delta plan and delta front sediments.

Figure 76 shows the correlation between measured values of gross thickness and collocated cokriging estimates of gross thickness produced by instantaneous phase attribute (a) and PC-17 (b). Although, the same spatial model is used, estimates produced by PC-17 show slightly less spread around the regression line shown in Figure 76. Correlation coefficient values of PC-17 ($r=0.98$) and instantaneous phase ($r=0.96$) estimated gross thicknesses are equal but PC-17 shows better fit for wells characterized by higher gross thickness estimates.

According to the results shown in Figure 74, it is possible to conclude that PC-17 was able to produce better results compared to the original instantaneous seismic attribute. These results reflect a clear geological control on the gross thickness values, rather than general smooth pattern produced by instantaneous phase attribute (Figure 73).

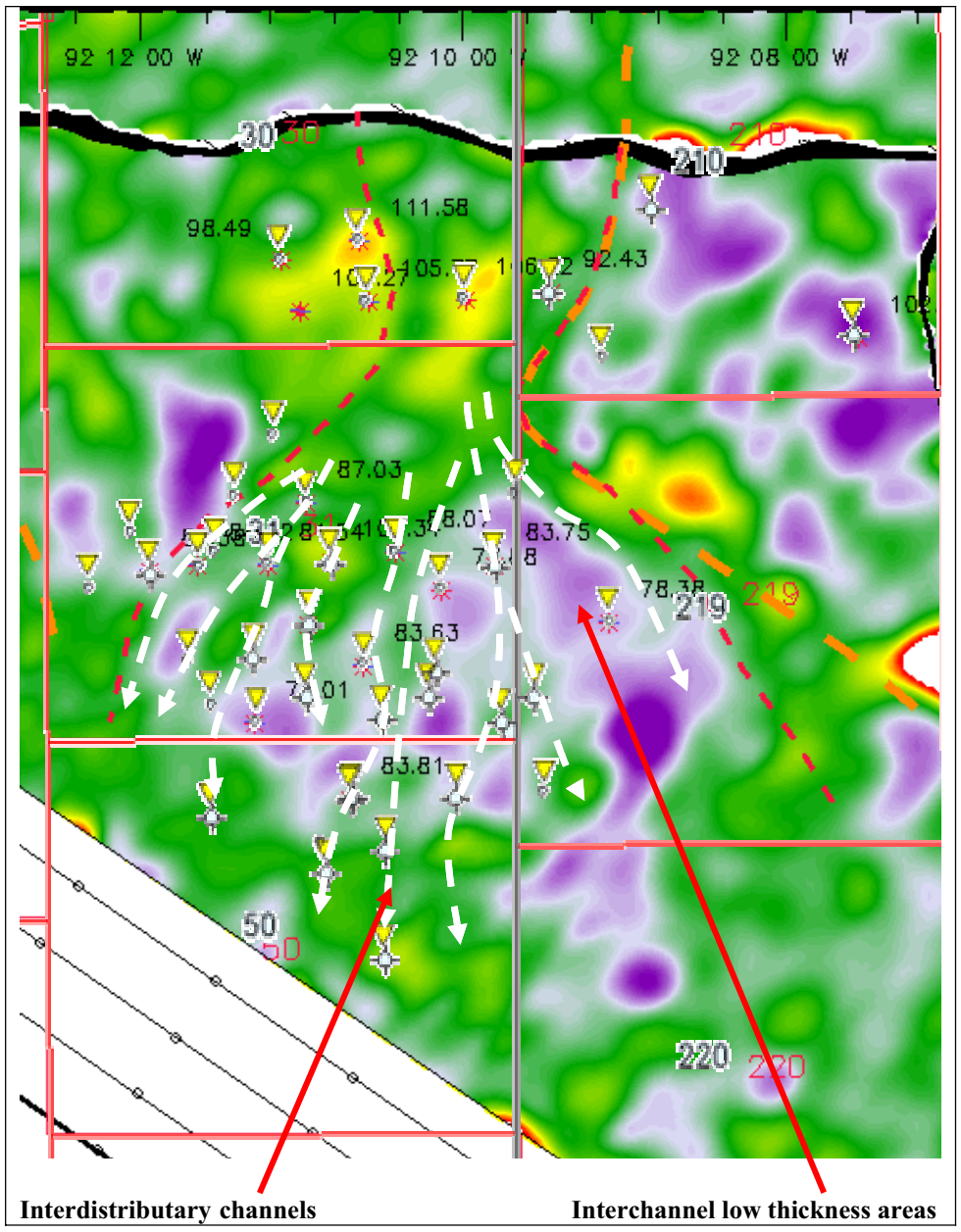

Figure 75. An enlarged plot of the central area of Figure 74. It is possible to distinguish linear trends of high gross thickness values (Figure 74). These trends are interpreted as distributary channels of lowstand deltaic deposits of the valley fill which are strongly correlated with the aerial distribution of historic drilling activates within the area.

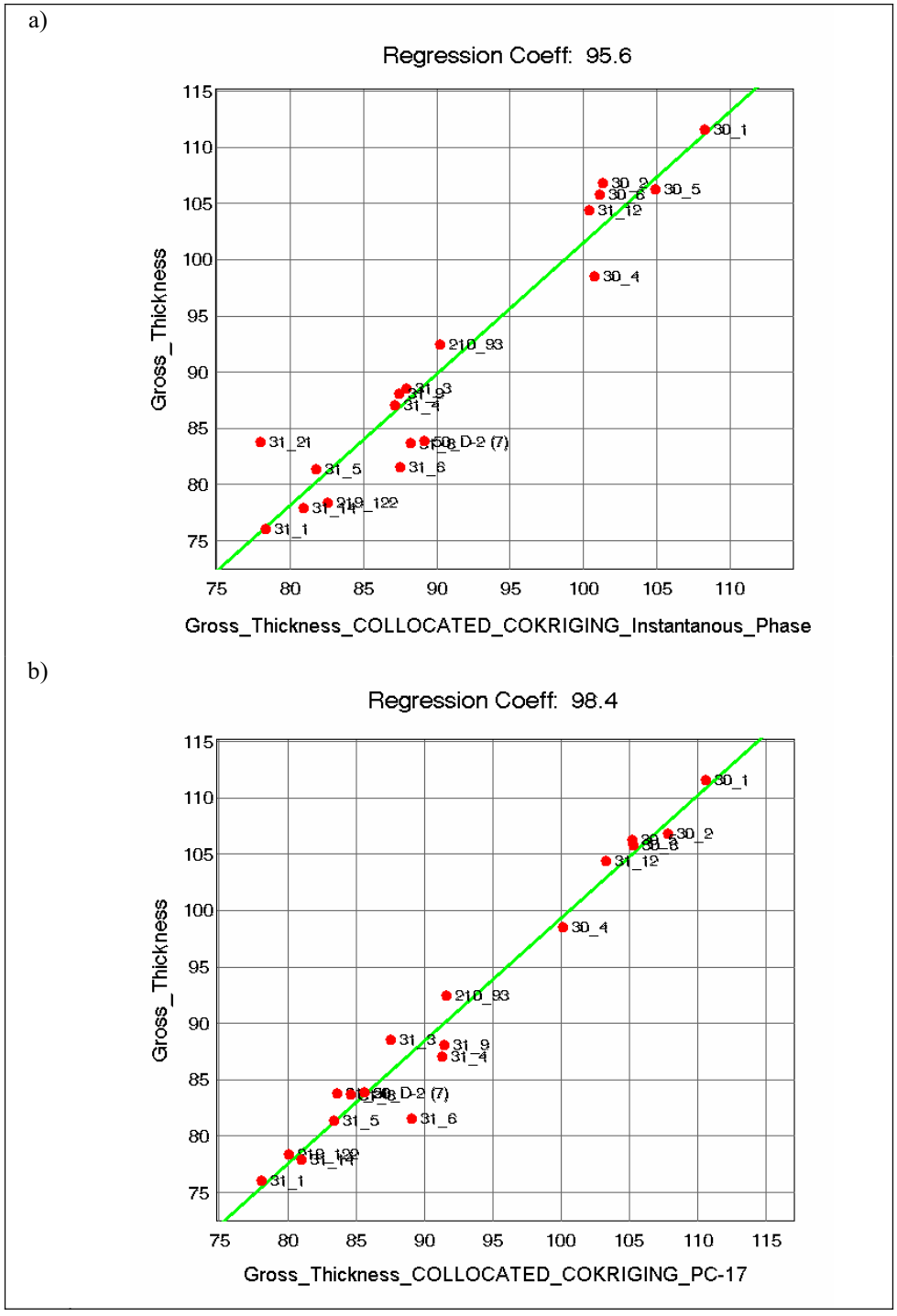

Figure 76. Correlation between measured values of gross thickness and collocated cokriging estimates of gross thickness produced by instantaneous phase attribute (a) and PC-17 (b). Although the same spatial model is used estimates produced by PC-17 showed less spread and a slightly higher correlation coefficient value (r=0.98 vs. 0.96) compared to the original seismic attribute.

4.4.2 Net thickness mapping

The spatial distribution of the log-derived net thickness is presented in Figure 77. The maximum net thickness of N-sand interval is located on the upper and western regions of the incised valley. The maximum measured net thickness value is shown at well 30-2 of about 107ft. The central incised valley showed higher variability than the upper dip reaches of the valley due to variability existing within a deltaic depositional environment which showed a minimum value of 39ft at well 31-9 and a maximum of 97 at well 31-12.

A representative experimental spatial semivariogram able to capture the details of the spatial distribution of the net thickness values was achieved by using a lag interval of 1380ft and a spherical model of 14669ft range and 383.7ft sill values. Net thickness spatial distribution showed a general anisotropic spatial pattern. Directional experimental semivariograms revealed an anisotropic behavior. The maximum axis of continuity azimuthal angle is 80 degrees with an anisotropy ratio of 0.48. The ellipse plot of anisotropy showed similar result to the gross thickness property (Figure 67). The properties of the spatial model are shown in Figure 78.

Figure 79 shows a summary for the absolute values of the correlation coefficient estimates between net thickness property and the various seismic attributes. The first eighteen seismic attributes are the original attributes extracted across the N-sand interval. The rest of the attributes are multivariate attributes produced by from the results of PCA and PFA.

In contrast to gross thickness (Figure 68) the original seismic attributes overall correlate better with net thickness (Figure 79). This indicates that the investigated seismic attributes tend to respond to the net dominant properties existing within the existing interval rather than gross properties such gross thickness (Figure 68).

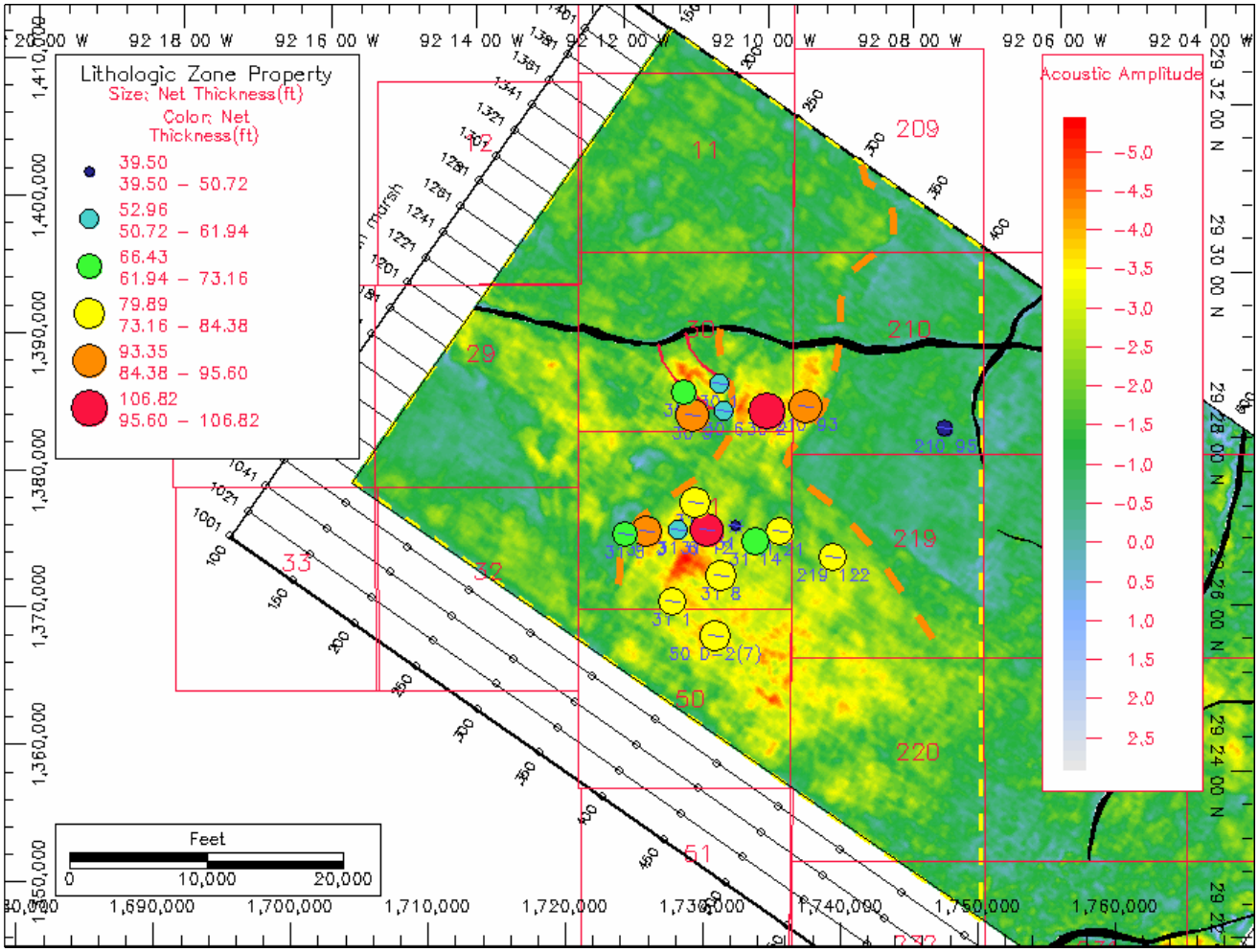

Figure 77. Seismic amplitude map of the western region of the study area overlain by a bubble layout presenting the spatial distribution of well-log derived of net thickness values of N-sand interval. The up dip and western side wells of the incised valley have higher net thicknesses. Postulated boundaries of the incised channel to delta are shown with dashed orange line.

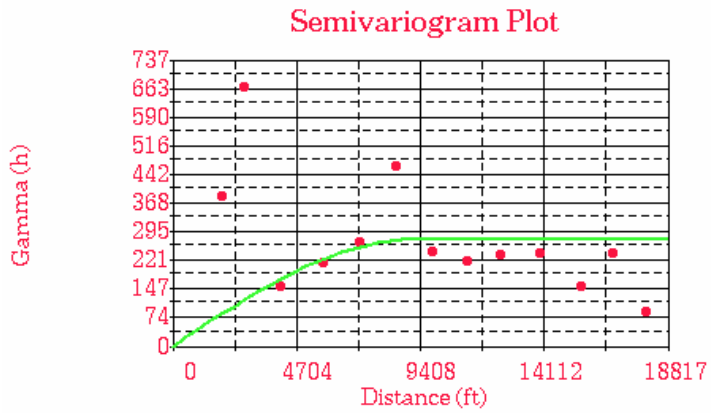

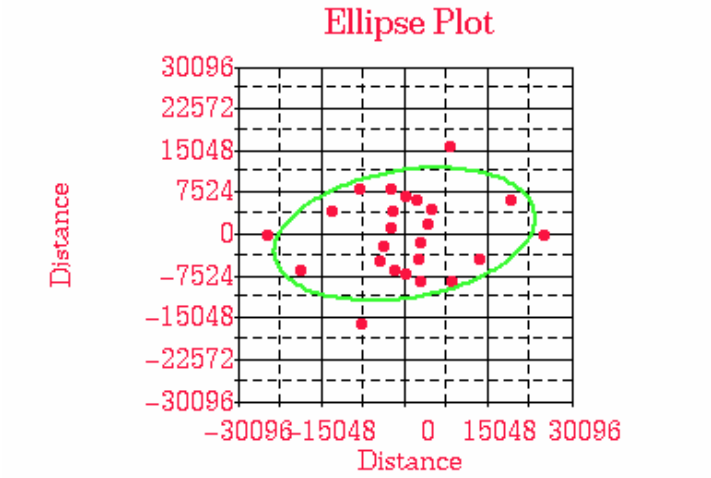

Lag Interval (h)	1395ft	**Sill**	276
Max. Lag	30,000ft	**Nugget**	0
Model	Spherical	**Anisotropy Angle**	89°
Range	9169.2ft	**Anisotropy ratio**	0.48

Figure 78. Spatial analysis parameters of net thickness property of Vermilion 50 wells.

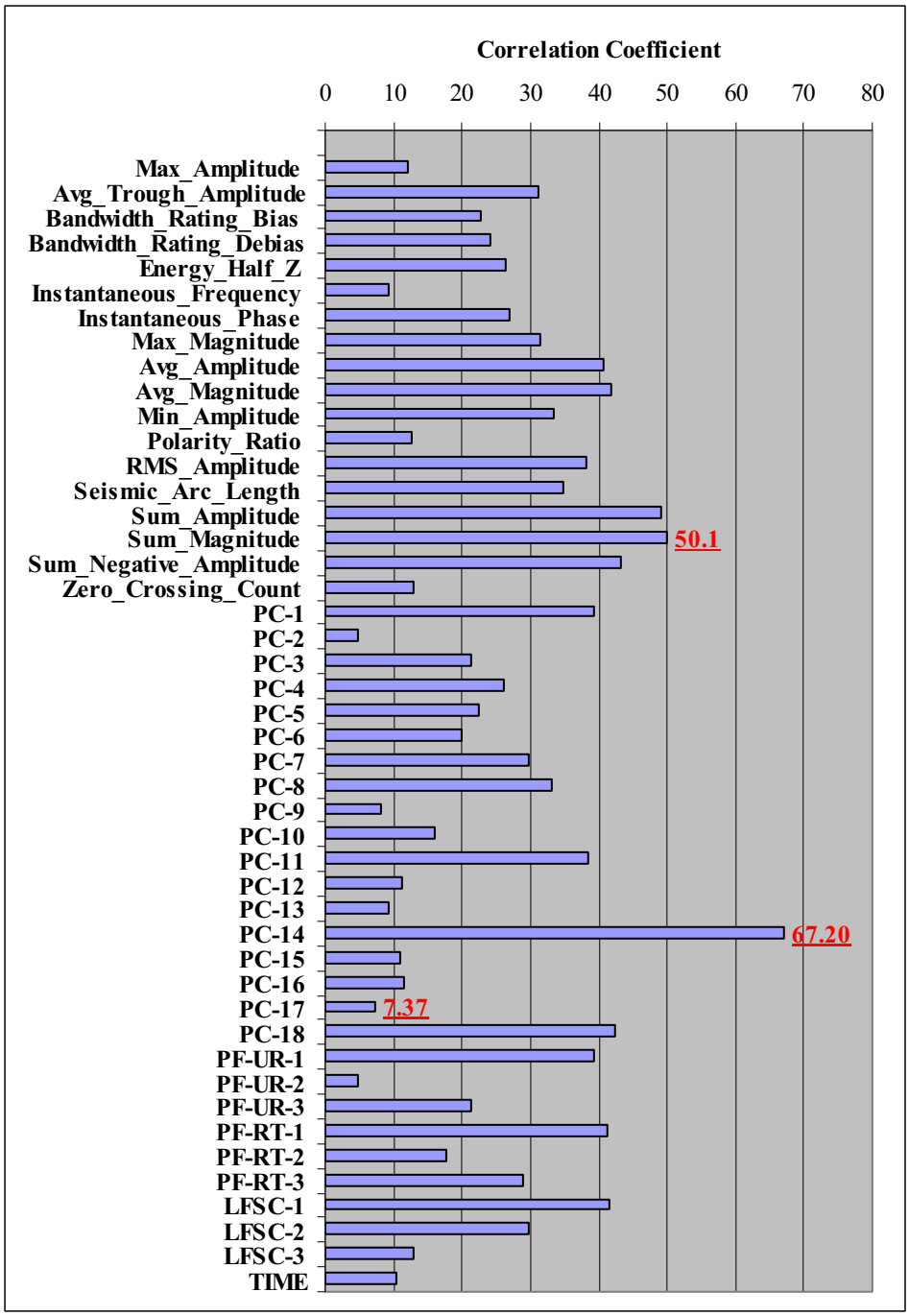

Figure 79. Correlation coefficient plot of the absolute value of the correlation coefficient (r) between net thickness and the various seismic attributes for the wells located within the incised valley (n=18). Net thickness property showed a good correlation with the sum of magnitude (r=0.50) and the PC-14 (r=-0.67). Note that the original seismic attributes are normalized by subtracting the mean and division by the standard deviation value.

The highest correlation coefficient between net thickness values and original seismic attributes (r=0.50) is shown by the sum of magnitude seismic attribute (Figures 79 and 80) which represents the sum the absolute values of reflectivity within a time window (Table 3). On the other hand, PC-14 showed the highest correlation coefficient estimate among the whole set of attributes (r=-0.67) with net thickness property (Figures 79 and 81).

The scatterplot between sum of magnitude and net thickness shows wide variability (Figure 80). This marked variability suggests that the sum of magnitude is also responding to another property. Figure 68 shows that the sum of magnitudes was second (r=49) after the instantaneous phase (r= -0.64) in correlation with gross thickness property. Accordingly, it is anticipated that within clean sand deposits the response of sum of magnitudes attribute will be identical to gross and net thickness properties, meanwhile it is the net thickness property which is contributing to the estimate of correlation coefficient in a shaly-intercalated sand successions.

Among the multivariate seismic attributes, PC-17 showed the highest correlation with gross thickness property (r=-0.73) while PC-14, showed a minimal correlation (r=-0.14) (Figure 68). In net thickness analysis (Figure 79) PC-17 showed minimal correlation to net thickness property (r=-0.07) while PC-14 showed better correlation (r=-0.67).

PC-14 is a weighted linear combination of sum of magnitude and average trough amplitude properties (Figure 82 and Table 6). The higher relative contribution of the average trough amplitude compared to the sum of magnitude attribute suggests that this multivariate attribute is trying to enforce the amount of the seismic information coming mainly from the trough region of the seismic signal. Synthetic seismogram modeling indicated that N-sand interval is associated with seismic trough portion. This PC performs as a tool to correct for possible errors encountered during the extraction of the original seismic attribute. Such errors are expected in regions of poor or unresolved reservoir boundaries that are related to low signal-to-noise ratio or signal tuning effects.

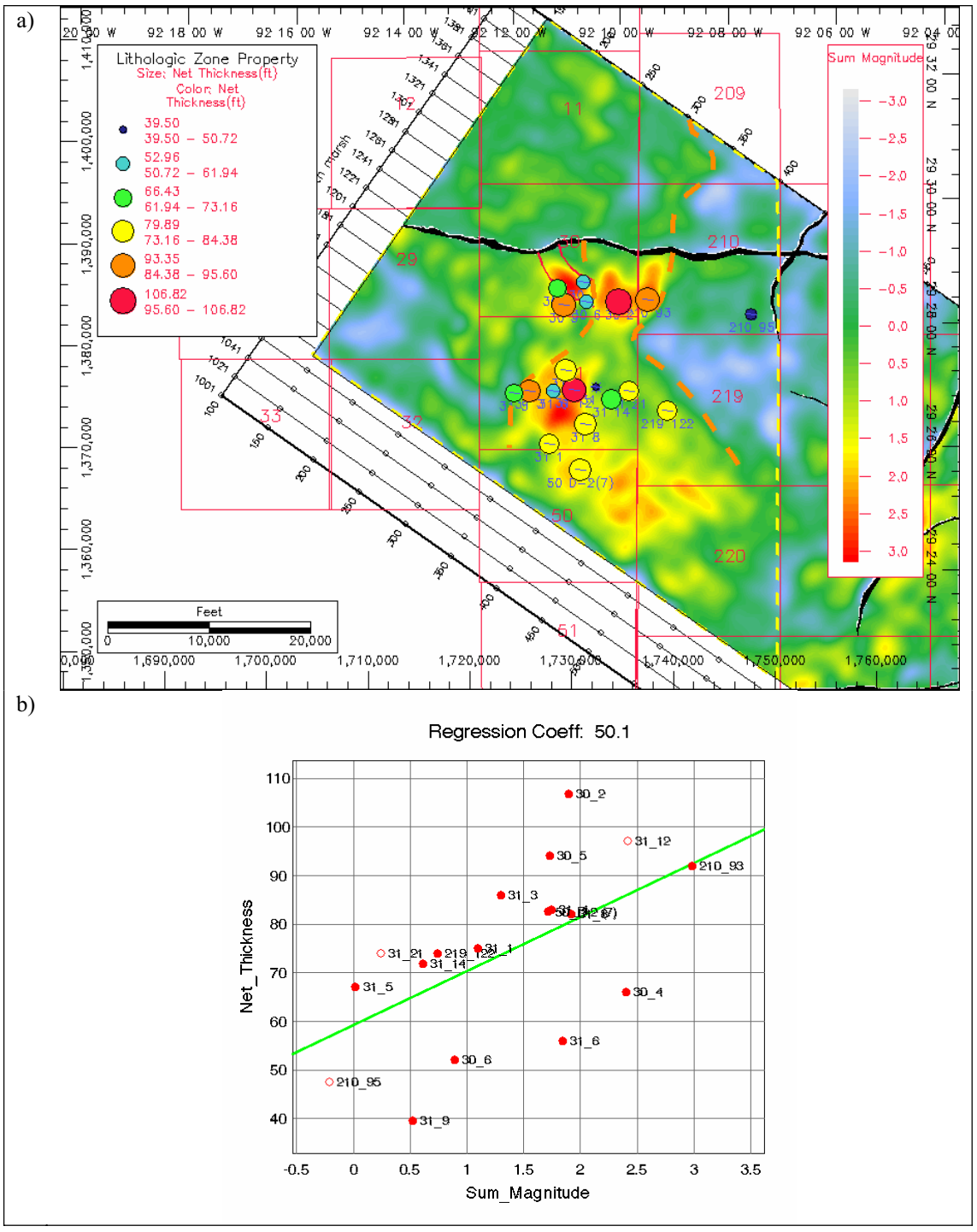

Figure 80. Standardized sum of magnitude seismic attribute of the western area of the study area (a) showed the best correlation with net thickness well-log derived gross thickness (b). The correlation coefficient value seen in the scatterplot is the absolute value of r=0.50.

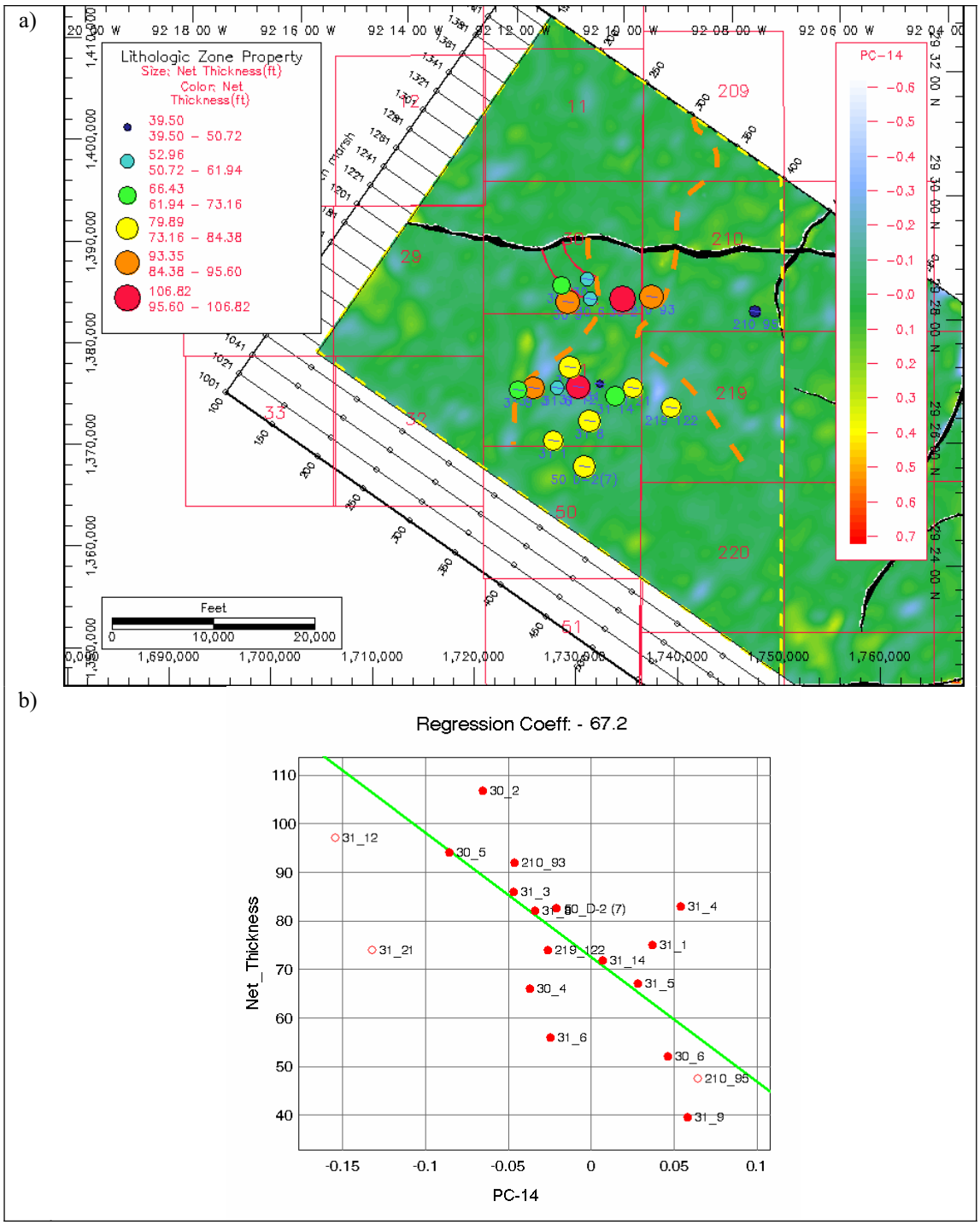

Figure 81. Multivariate seismic attribute PC-14 of the western region of the study area (a) shows better correlation with net thickness (b). Compared to the scatterplot shown in Figure 79, Figure 80 showed less variability around the regression line. Note that well 210-95 is located out side the incised valley system. The wells 31-12 and 31-21 were turned off because they are highly deviated from the general trend shown by the rest wells.

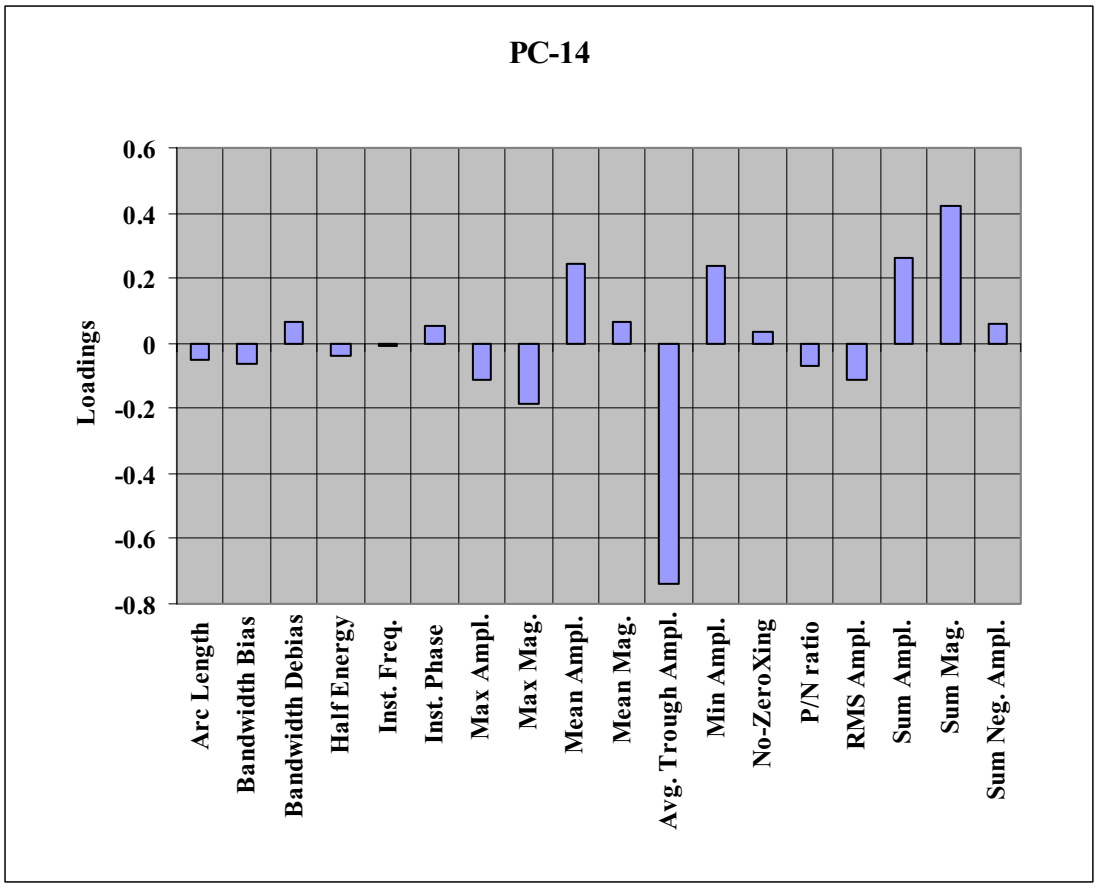

Figure 82. Bar chart illustrating the relative contribution of each seismic attributes in PC-14. Largely, PC-14 is a weighted linear combination of average trough amplitude and sum of magnitude. The higher relative contribution of the average trough amplitude compared to the sum of magnitude attribute suggests that this multivariate attribute is trying to enforce the amount of the seismic information coming mainly from the trough region of the seismic signal. Synthetic seismogram modeling indicated that N-sand interval is associated with seismic trough portion.

Where sharp reservoir boundaries are composed of clean sands, PC-14 and PC-17 show similar behavior, but they tend to separate in regions of poor boundaries due to tuning by thin sand-shale successions (Figure 83). The general inverse relationship between PC-14 and PC-17 and thickness measures (Figures 68 and 79), will ensure that thickness estimates of PC-14 will be lower than those resulted from PC-17 which represent net and gross thicknesses, respectively. This final conclusion supports the earlier one that PC-17 will not be associated with net thickness property.

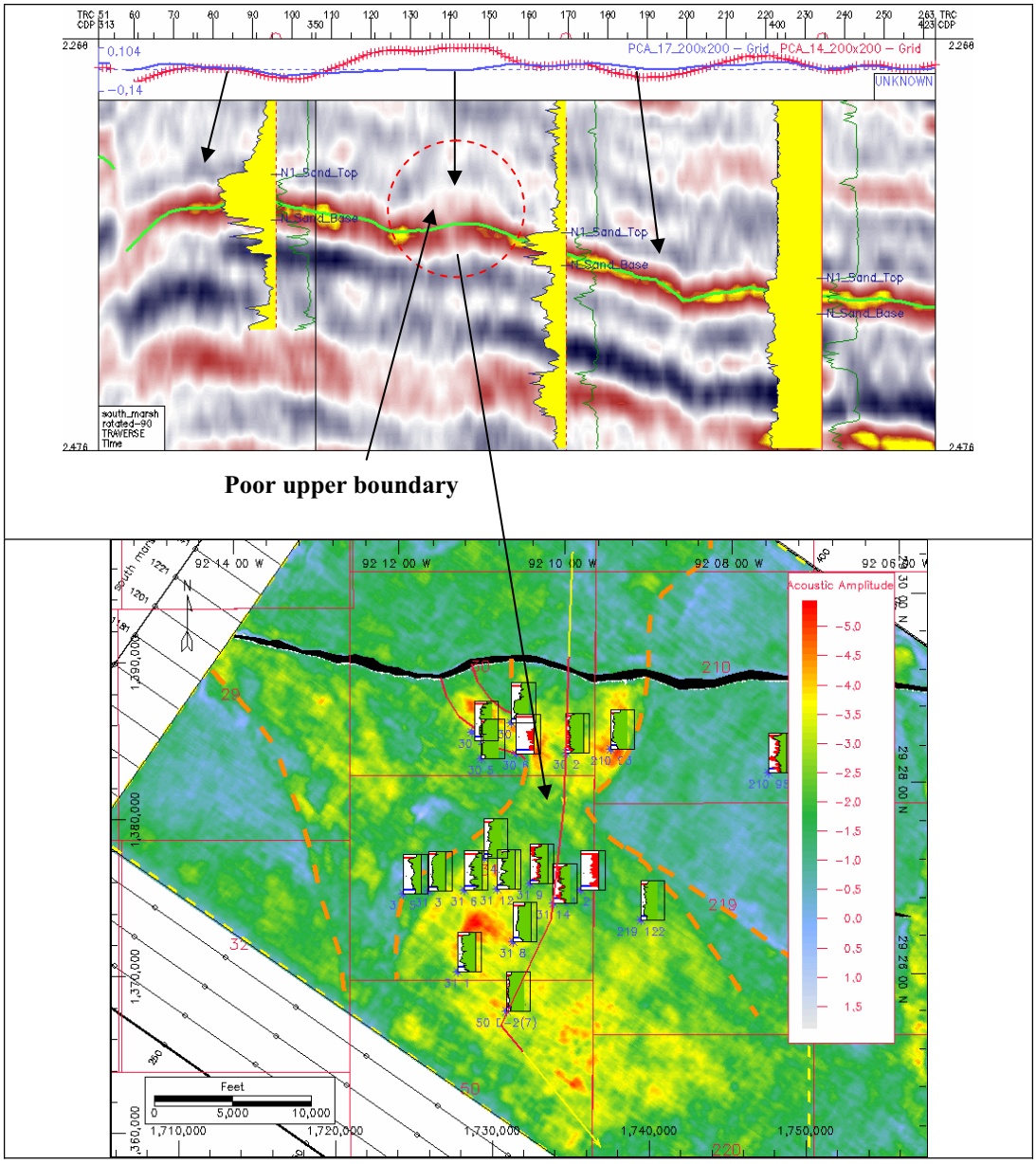

Figure 83. PC-14 and PC-17 have similar response within sharp boundary clean sand deposits. The inverse relationship shown between PC-14 and net thickness ensures that PC-14 will correct for possible errors encountered during attribute extraction in poor boundary deposits due to sampling events from the upper peak. Thus, PC-14 will respond to the net thickness rather than the gross thickness which is fully accounted for by PC-17 and partially by the sum of magnitude attribute. Note the separation seen between PC-14 and PC-17 in poor upper boundary in the center of the upper scale bar, and minimal separation at sharp boundary regions. Well logs are SP log and the right boundary does not reflect the shale baseline.

Figure 78 shows the spatial model used to estimate the spatial distribution of net thickness property. The results of collocated cokriging estimates of net thickness using sum of magnitude and PC-14 are presented in the Figures (84-86).

The sum of magnitude-based estimates of net thicknesses within the lower parts of the main incised valley shows higher values than that those predicted by PC-14 (Figures 84 and 85). The same situation was encountered in gross thickness estimation by the use of instantaneous phase (Figure 73). Chen and Sidney (1997) indicated that the sum of magnitude attribute can highlight amplitude anomalies due to changing lithology or hydrocarbons, meanwhile instantaneous phase attribute can indicate lithological variability within the continuity of seismic events and local hydrocarbon phasing signatures. Due to the lack of well control in this region at region, it is not easy to explain these anomalies. However, a vertical seismic section across these anomalies shows possible bright spot signatures which suggest that the overestimated gross and net thickness in the lower reaches of the incised valley are due to gas saturated sediments (Figure 87).

It is noticeable that the effects of these amplitude anomalies did not bias the estimates of the net thickness produced by PC-14 and gross thickness produced by PC-17. The correlated behavior between PC-17 and PC-14 over this region (upper a scale bar) indicates that the estimated values of gross and net thicknesses produced by using PC-17 and PC-14, respectively, should be equal over this region. The results of Figures 74 and 86 support this conclusion.

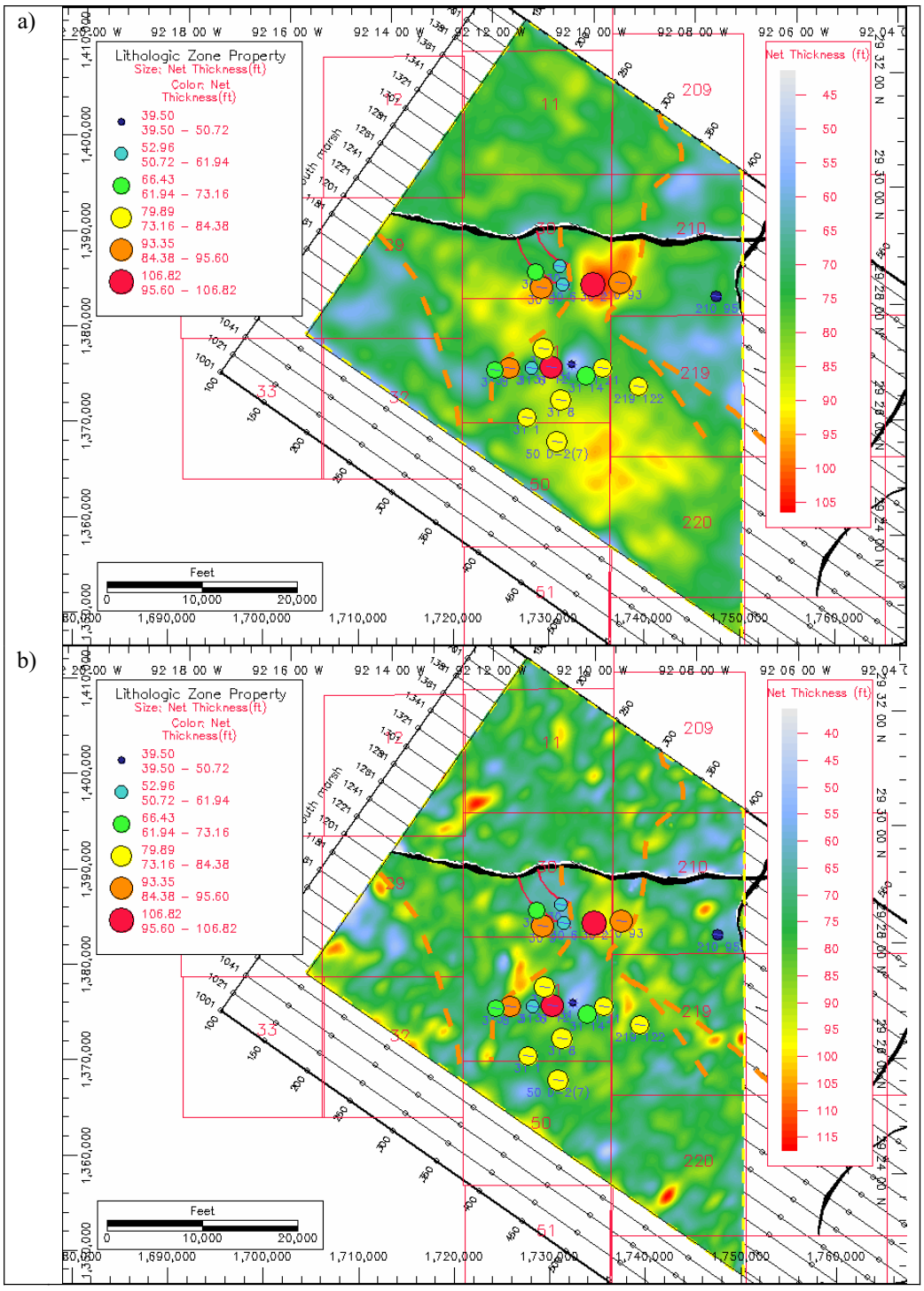

Figure 84. Comparison between net thickness estimates produced by sum of magnitude (a) and net thickness estimates produced by using PC-14 (b). Figures 84 and 85 shows enlarged versions of map (A) and map (B), respectively. Note that net thickness estimates showed smoother behavior in (a) than that of (b).

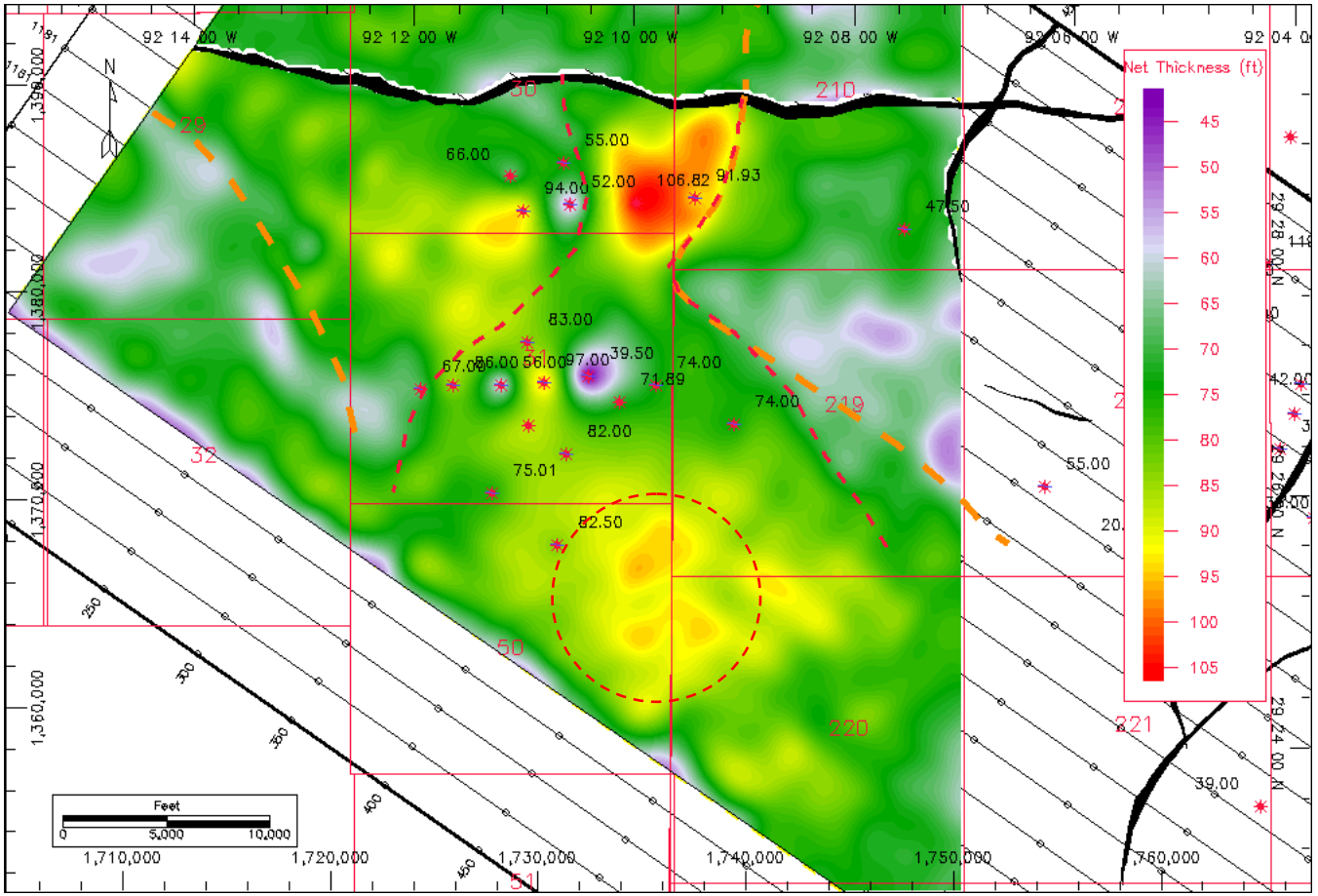

Figure 85. Net thickness estimate of the N-sand interval produced by sum of magnitude attribute as a secondary data. The highlighted area by the dashed-line circle shows high estimates for net thickness compared Figure 84.

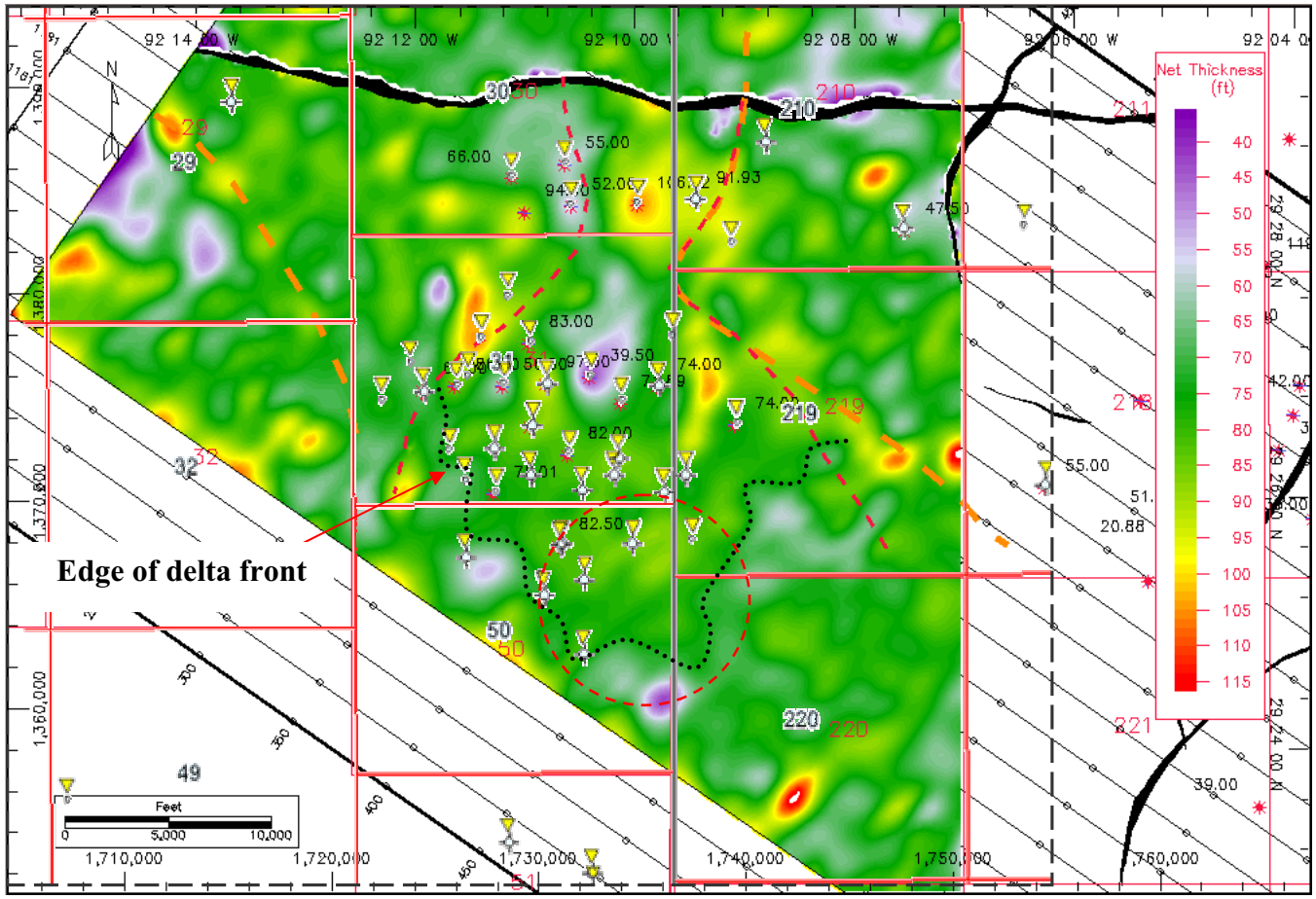

Figure 86. Net thickness estimate of the N-sand interval produced by using PC-14. Net thickness of PC-14 maintains the anticipated roughness associated with the lithology and depositional systems existing within the incised valley and correlates will with historic drilling activities of the study area. The black dashed line highlights a possible boundary defining the edge of delta front deposits of the incised valley fill. Note that the anomalous region shown by the net thickness estimates of the sum of magnitude is not evident in the results of PC-14, shown in red dashed circle.

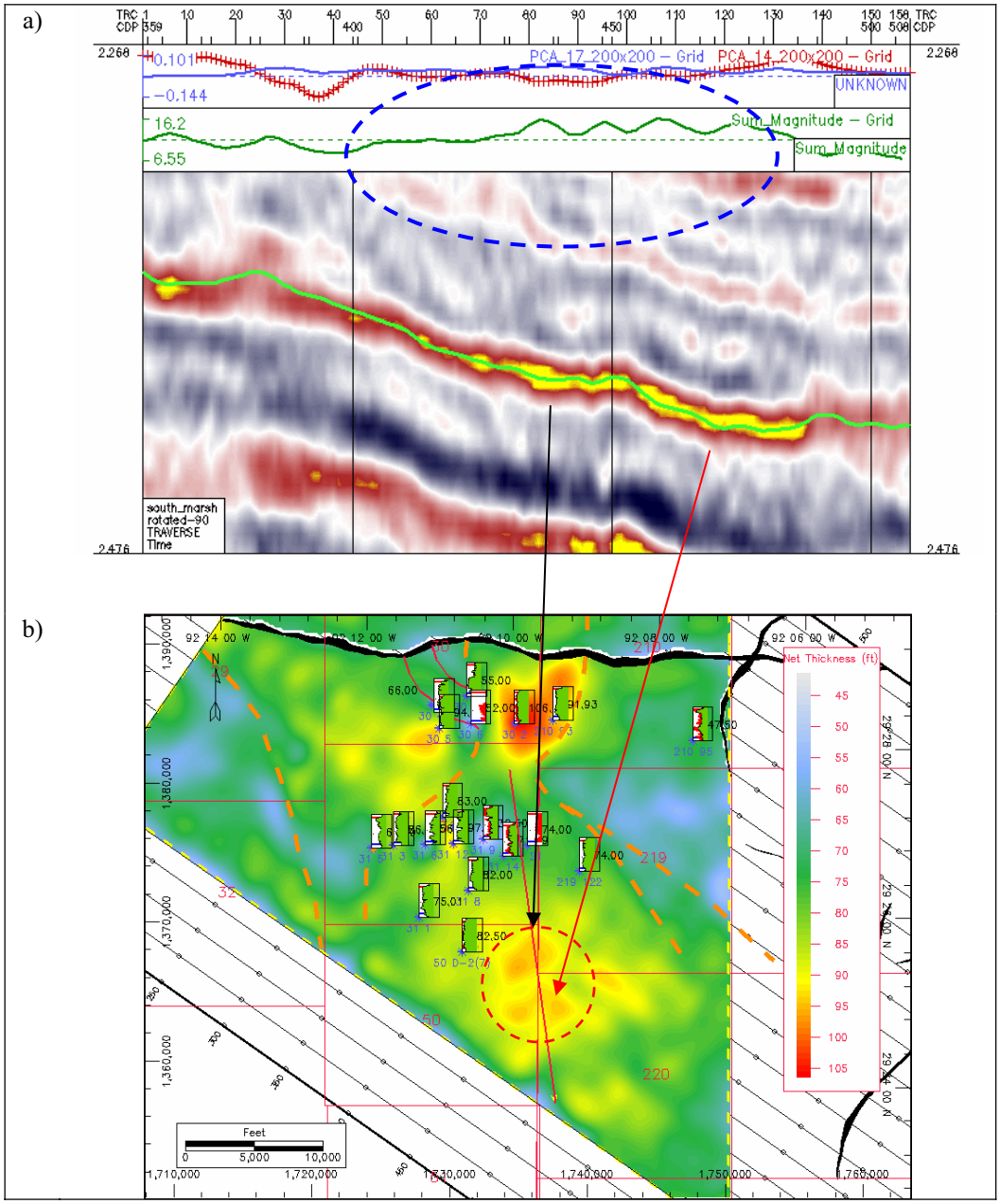

Figure 87. Arbitrary dip-oriented seismic section (a) and the net thickness map produced by sum of magnitudes (b). The highlighted anomalies existing within the southern part of the incised valley are mainly related to possible hydrocarbon saturated sediments. The marked bright spot signature on the vertical seismic section supports this conclusion. The correlated behavior between PC-17 and PC-14 over this region, note scale bar in (a), indicates that estimates of gross and net thicknesses produced by using PC-17 and PC-14 should be equal. The results of Figures 73 and 85 support this conclusion.

Figure 86 indicates that the net thicknesses of PC-14 shows the anticipated roughness associated with the lithology and depositional systems. On the other hand, the sum of magnitude approach to estimate net thickness spatial distribution shows smooth spatial distribution for the net thickness estimates (Figure 85).

The footwall region of the N-sand interval showed lower net thickness values of the PC-14 than those produced by the sum of magnitude (Figure 84) and they are in conformity with the results of the gross thickness estimates across the footwall plain (72).

The eastern region of the main incised valley showed a possible local drainage system associated with net thickness values (Figure 86), whereas the results of the sum of magnitudes showed a smoothed spatial distribution (Figure 85).

Figure 88 shows a correlation between the measured values of net thickness and the collocated cokriging estimates of net thicknesses produced by sum of magnitude attribute (a) and PC-14 (b). Both approaches showed similar scatter plots in terms of regression and variability. Also, they provided accurate estimates for the net thickness of wells 31-12 and 31-21 which were left out of the analysis.

Cross-plotting the results of well 210-95 located outside the valley system showed overestimated results. The estimated net thickness values away from the well control region are less reliable, especially if they represent sediments different that these deposited within the incised valley system. However, estimates produced by PC-14 showed higher correlation coefficient value ($r=0.98$) compared to the sum of magnitude seismic attribute ($r=0.94$). Although, the limited well control imposes significant limitations about the results of net thickness, it is possible to conclude that PC-14 was able to produce better results compared to the original sum of magnitude seismic attribute.

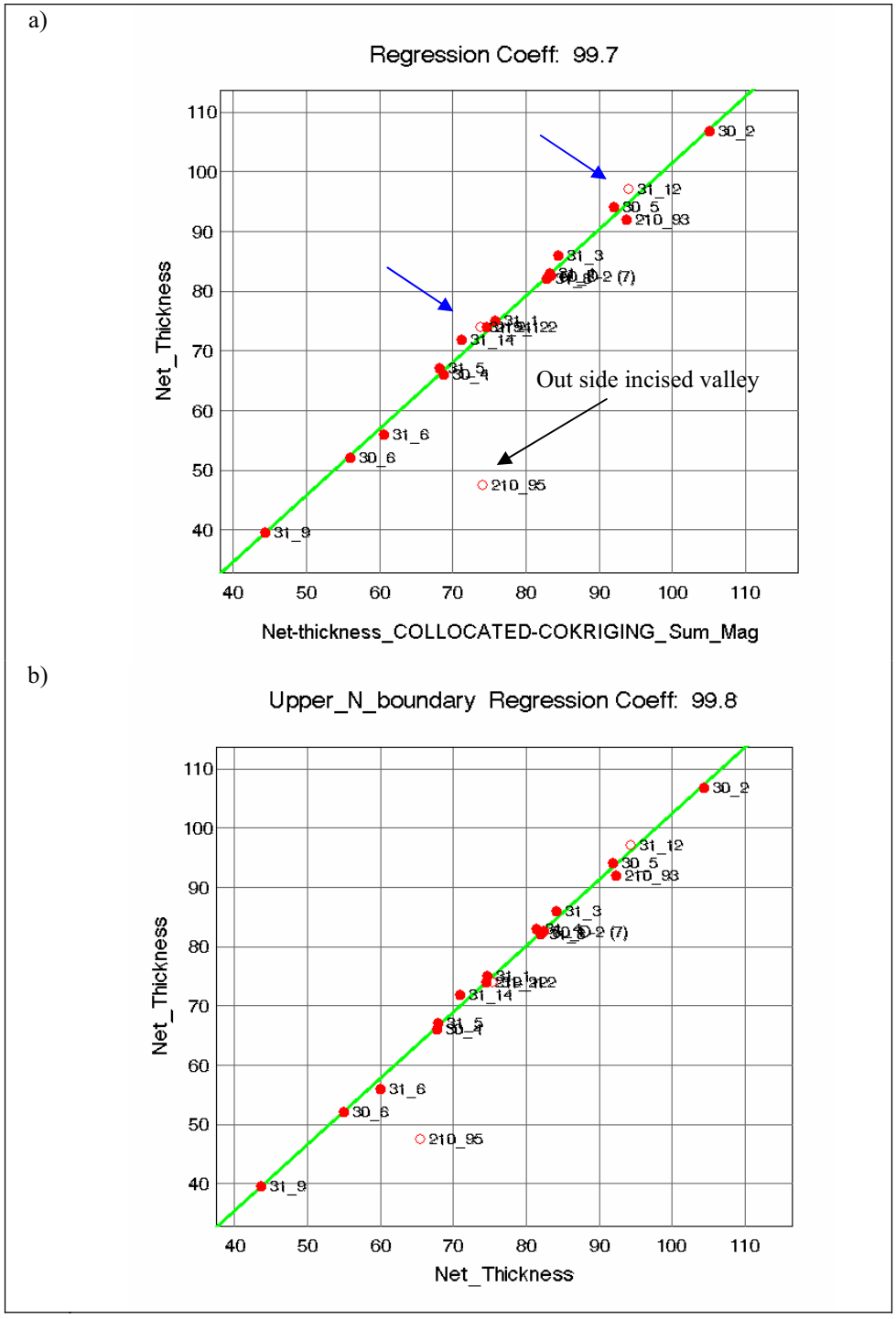

Figure 88. Correlation between measured values of net thickness and collocated cokriging estimates of net thickness produced by sum of magnitude attribute (a) and PC-14 (b). Note that both approaches gave similar results for the wells located within the incised valley. As for the region located out side the valley, the sum of magnitude approach highly overestimated net thickness at well 210-95. Note also that both approaches gave accurate estimates for net thicknesses at the wells 31-12 and 31-21 which were turned off (b in Figure 80).

4.4.3 Average gross effective porosity mapping

Table 8 shows a list of well-log derived gross effective porosity (ϕ_{eff}) estimates for each well of the fields of Vermilion and Tiger Shoal. Effective porosities are corrected porosity estimates for the effect of shaliness; $\phi_{eff} = \phi(1-V_{sh})$ (Asquith, 1982).

Unlike the case of gross and net thicknesses, the validation of the accuracy of porosity estimates represented a major hurdle due to the limited core analysis results. For the field of Vermilion 50, there were two reports available and they cover a limited interval of the investigated window. Studying the relationship between the estimated values of ϕ_{eff} vs. the maximum porosity of sidewall core samples (ϕ_{max}) gives an idea about the accuracy of the results and help identifying possible outliers.

The equation governing the relation between ϕ_{max} and depth within the study area is defined as (Badescu, 2002): ϕ_{max} = 0.42- 0.00001*Depth (ft). For each well, each depth value equals to the average depth (TVD) of the top and bottom boundaries of the N-sand interval. Finally, the estimated values of ϕ_{max} were corrected for shale effect (Table 8).

The scatterplot between the estimated values of ϕ_{eff} and ϕ_{max}, shown in Figure 89, suggests a direct proportional relationship between the two estimates and provides bases to validate the estimated values of ϕ_{eff}. The wells 50-D-2(7), 218-10 and 118-14 showed an outlier behavior. The standard deviation (SD) value for the rest of the wells equals to 0.061. The estimates of these wells were adjusted by adding one SD to well 50-D-2(7) and by subtracting three SD's from the wells 218-10 and 218-14. The goodness of fit between ϕ_{eff} and ϕ_{max} equals 0.75 after adjusting for these outliers (Figure 89).

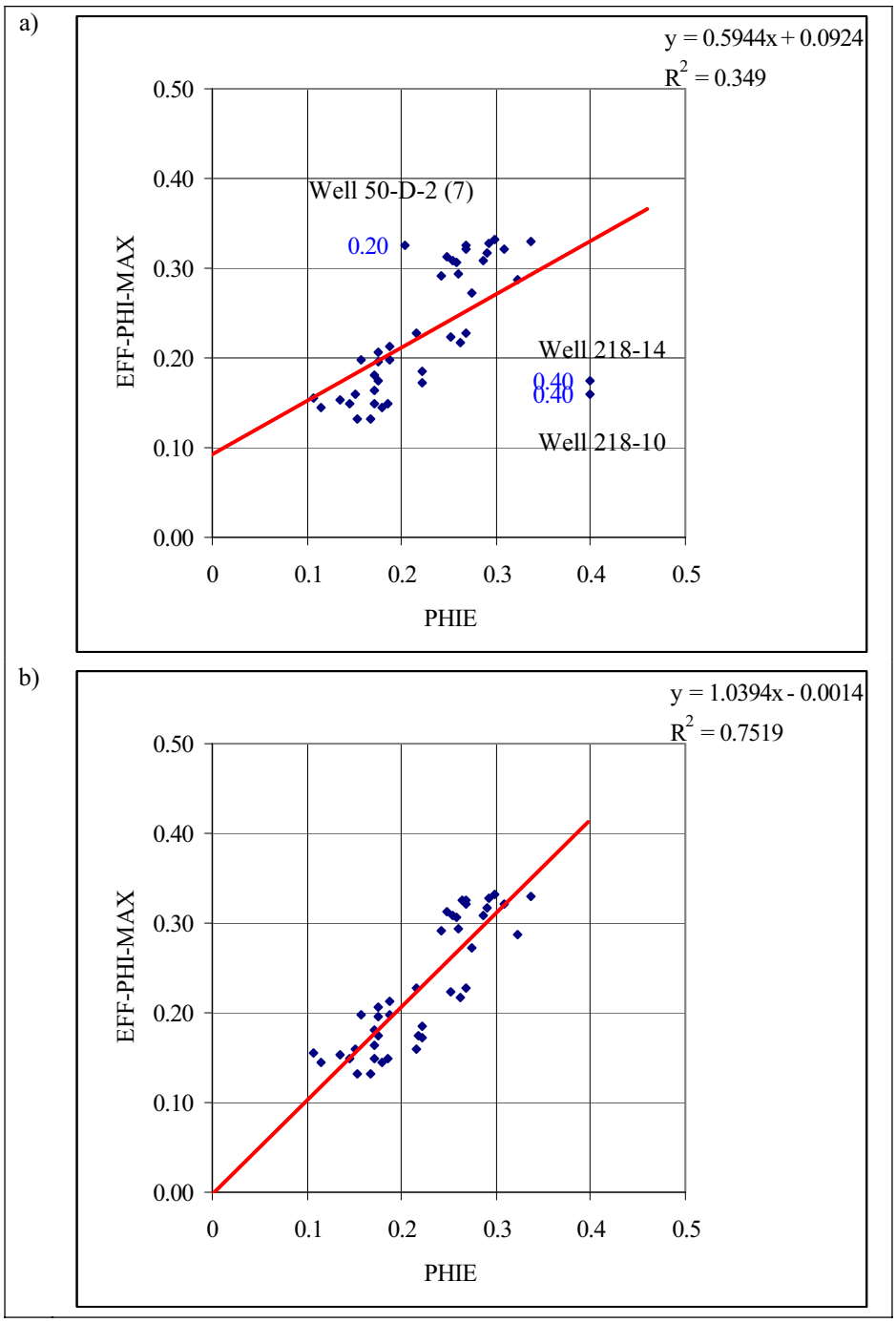

Figure 89. Scatterplot between effective maximum porosity as a function of depth and the well-log derived estimate of effective porosity before (a) and after (b) correction for the outliers: 50-D-2(7), 218-10 and 218-14. B). Note the goodness of fit in (B) equals to 0.75. This scatterplot indicates that the well log estimates of effective porosity are acceptable and considered representative of the N-sand interval.

The spatial distribution of the log-derived ϕ_{eff} values is shown in Figure 90. The maximum ϕ_{eff} of N-sand interval is seen on the upper and western parts of the main channel and the lowstand delta within the incised valley. This spatial pattern can be attributed to a higher energy depositional conditions that were taking place in these regions compared to the distal central and eastern parts of the incised valley. The log signature of the wells of the upper and western wells of high ϕ_{eff} is less seriate and characterized by a general block shape motif with distinct sharp boundaries (Figure 90). The results of gross thickness mapping show a similar spatial pattern which suggests that the deltaic distributary channels shown in Figure 74 are responsible for the spatial distribution of average gross effective porosity.

The spatial details of the distribution of the ϕ_{eff} were achieved by an experimental semivariogram analysis using a lag interval of 820ft. The variogram model is a spherical function with a range of 15888.6ft and a sill of 0.00149 of sill (Figure 91). The ϕ_{eff} spatial distribution map shows a general anisotropic spatial pattern. The maximum continuity axis has an azimuth angle of 164 degrees from the north and an anisotropy ratio of 0.48. The ellipse plot of anisotropy showed a perpendicular trend to the ellipses of gross thickness and net thickness properties (Figures 67 and 78) which indicates that the axis of maximum continuity of ϕ_{eff} of the N-sand interval was trending in the basinward direction and perpendicular to the regional strike direction.

Figure 92 shows a summary of the absolute values of the correlation coefficients between gross ϕ_{eff} and the various seismic attribute grid maps. The first eighteen seismic attributes are the original attributes extracted across the N-sand interval. The rest of the attributes are multivariate attributes produced from the results of PCA and PFA.

In general, all amplitude-based attributes show good correlation with average porosity. Accordingly, PC-1, PF-UR-1 and PF-RT-1 will show high correlations since amplitude-based attributes are the main loaders for these multivariate attributes (Figures 55 and 58).

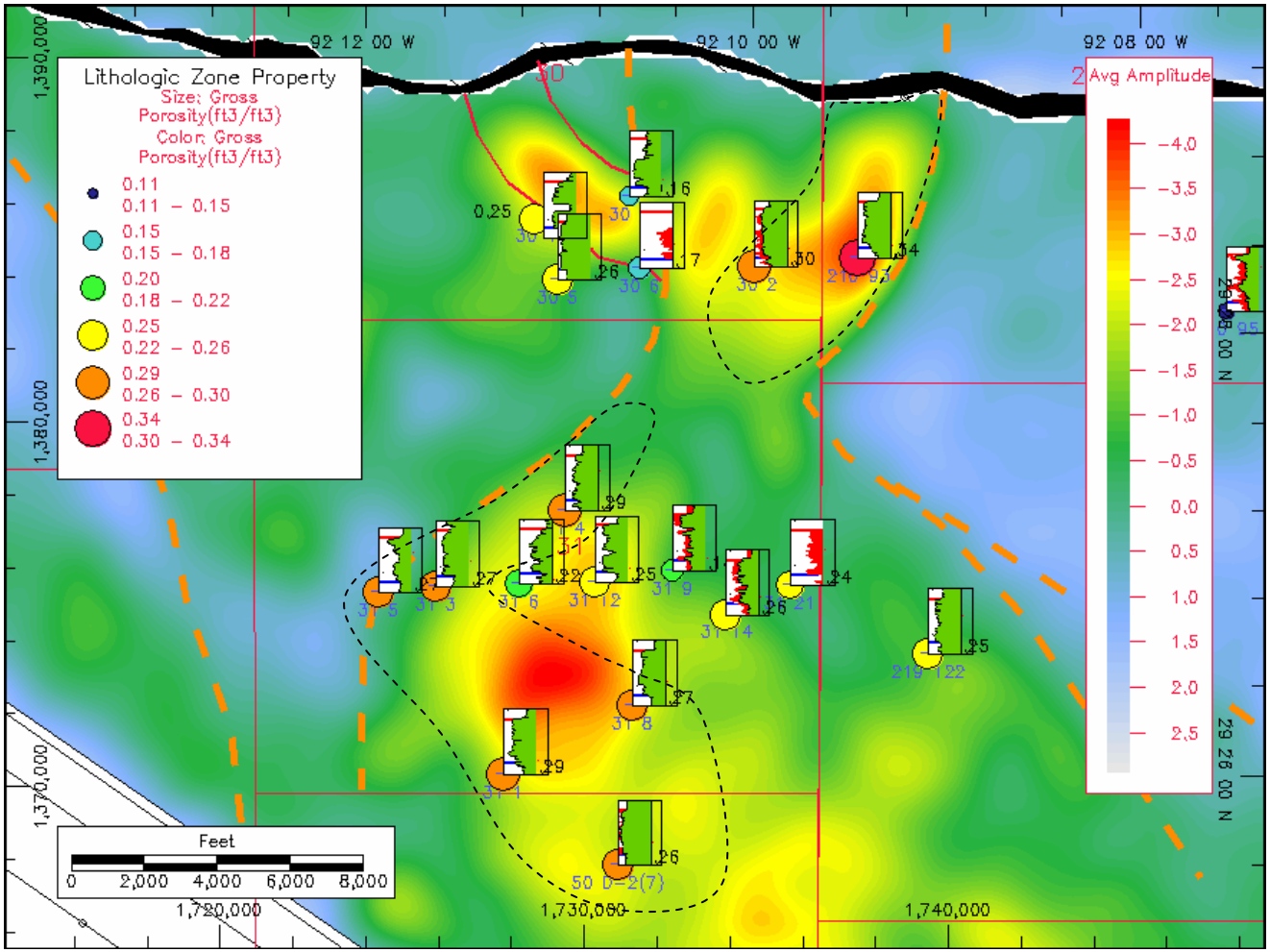

Figure 90. Average amplitude map of Vermilion 50 field overlain by a bubble plot showing the distribution of well-log derived effective porosity estimates of the N-sand interval. The spatial variation between the estimated effective porosity values is minimal but the up dip and western side wells of the major channel within the incised valley have higher ϕ_{eff}. The postulated boundaries of the incised valley are shown with dashed orange line. The shaded area represents a trend of high ϕ_{eff} sediments of high energy depositional conditions.

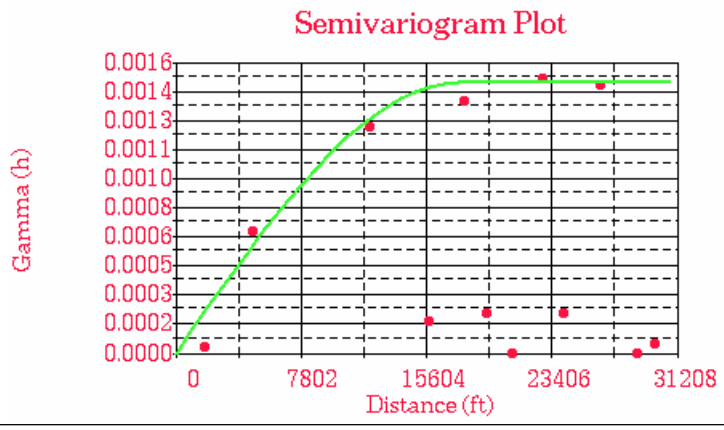

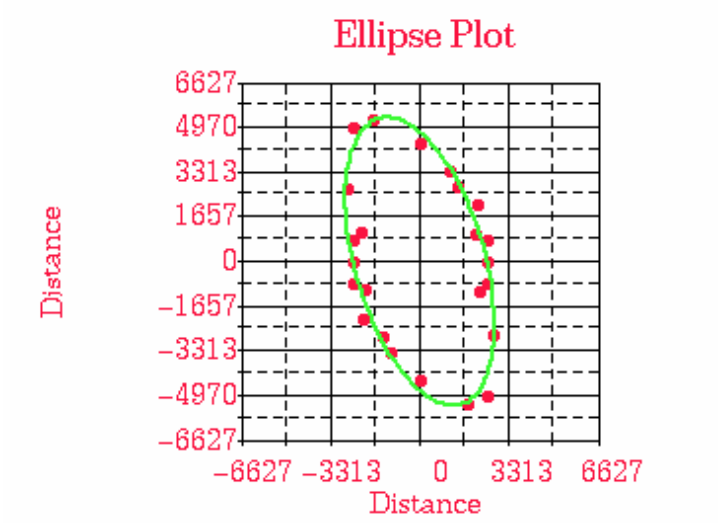

Lag Interval (h)	820ft	**Sill**	0.001486
Max. Lag	30,000ft	**Nugget**	0
Model	Spherical	**Anisotropy Angle**	164°
Range	15888.59ft	**Anisotropy ratio**	0.48

Figure 91. Spatial analysis parameters of gross ϕ_{eff} of Vermilion 50 wells.

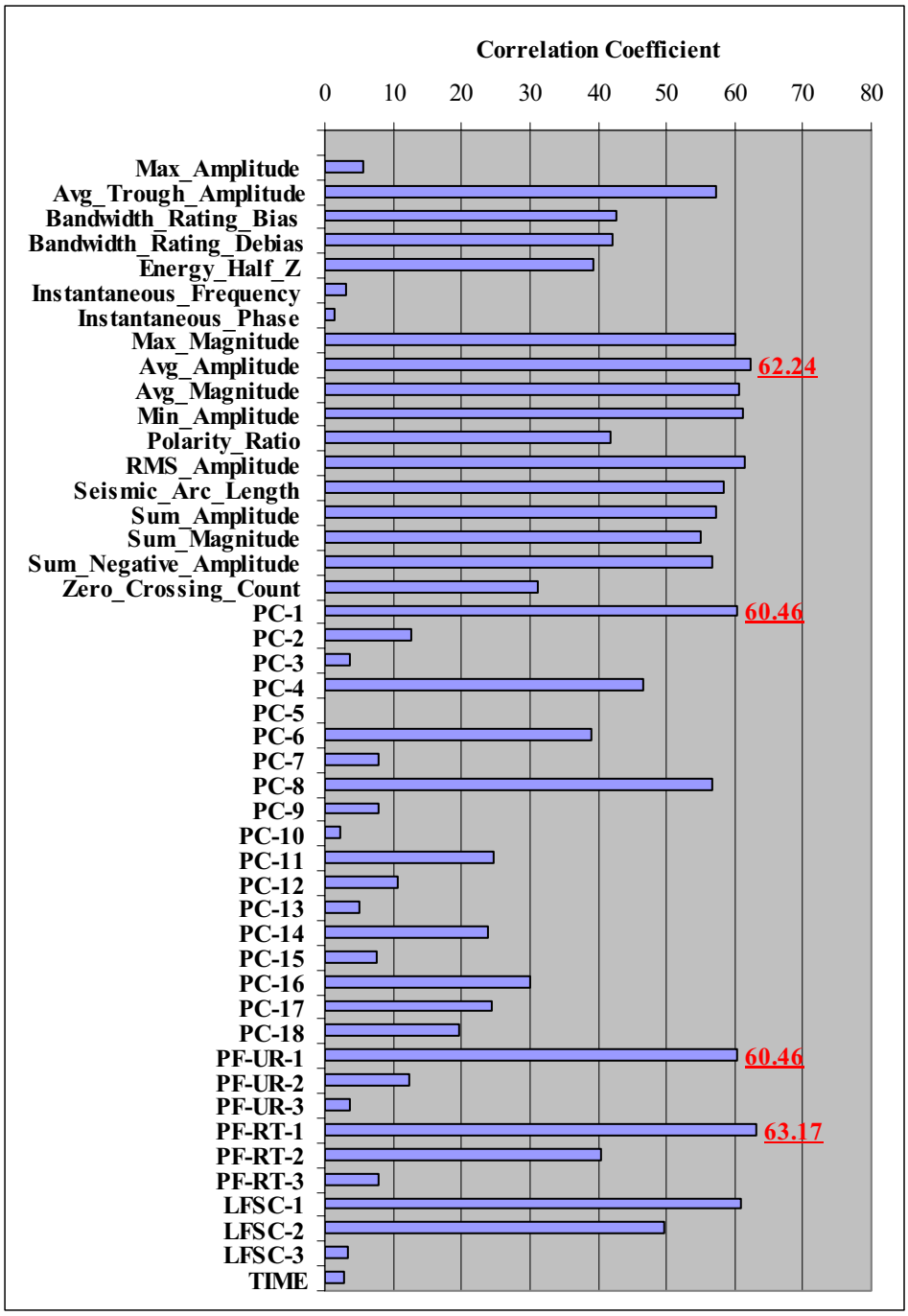

Figure 92. Correlation coefficient plot of the absolute value of correlation coefficients |r| between ϕ_{eff} and the various seismic attributes for the wells located within the incised valley (n=18). In general, all amplitude-based attributes show good correlation with average porosity. Accordingly, PC-1, PF-UR-1 and PF-RT-1 will show high correlations since amplitude-based attributes are the main loaders for these multivariate attributes. The best correlation is shown by the PF-RT-1 (r=-0.72). and the sum of magnitude (r=0.59) original attribute.

The best correlations to ϕ_{eff} were achieved between the various amplitude-based original seismic attributes and the first principal component (PC-1), the first principal factor (PF-UR-1) and the Varimax rotated first principal factor (PF-RT-1). In general, the values of estimated correlation coefficient were much correlated due to the fact that the PC-1 and PF-1 are a function of the same original seismic attributes (Table 6 and Figure 58).

Among the other attributes, seismic arc length showed a nice direct proportional relationship with r=0.58. This association indicates that an increase in the seismic arc length, which is the length of the seismic wavelet across a given interval, will result in a higher value of ϕ_{eff}. The length of the arc length is a measure of vertical heterogeneity or stacking within an interval which may point to settings of high energy depositional systems. Figure 49 shows the arc length spatial distribution of the N-sand interval. The spatial trend of high ϕ_{eff} values denoted in Figure 88 correlates with the anomalies of high arc length attribute suggesting that these anomalies represent stacked sand successions of deltaic distributary channels.

The highest correlation coefficient between ϕ_{eff} and the original seismic attributes is shown by the average amplitude seismic attribute (r=-0.62) (Figures 90 and 93) which represents the average value of the seismic reflectivity within a time window (Table 8). On the other hand, the first principal factor (PF-RT-1) shows the highest correlation coefficient value among the whole set of attributes (r=0.63) (Figures 92 and 93). The difference between the correlation coefficients values is not significant, but it is hoped that the use of the multivariate attribute will enhance the final mapping results of ϕ_{eff}.

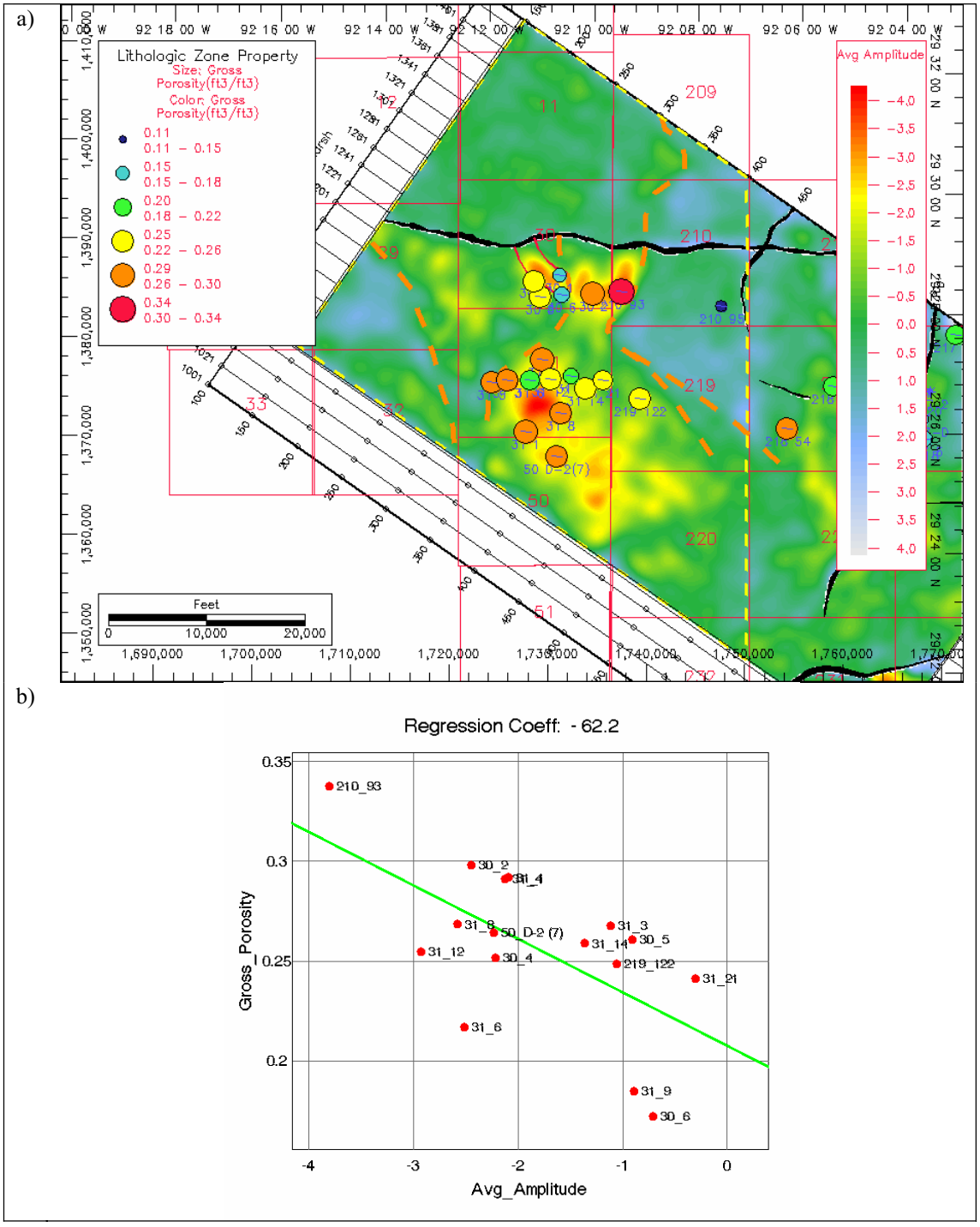

Figure 93. Standardized average amplitude seismic attribute map (a) showed the best correlation with gross effective porosity (b).

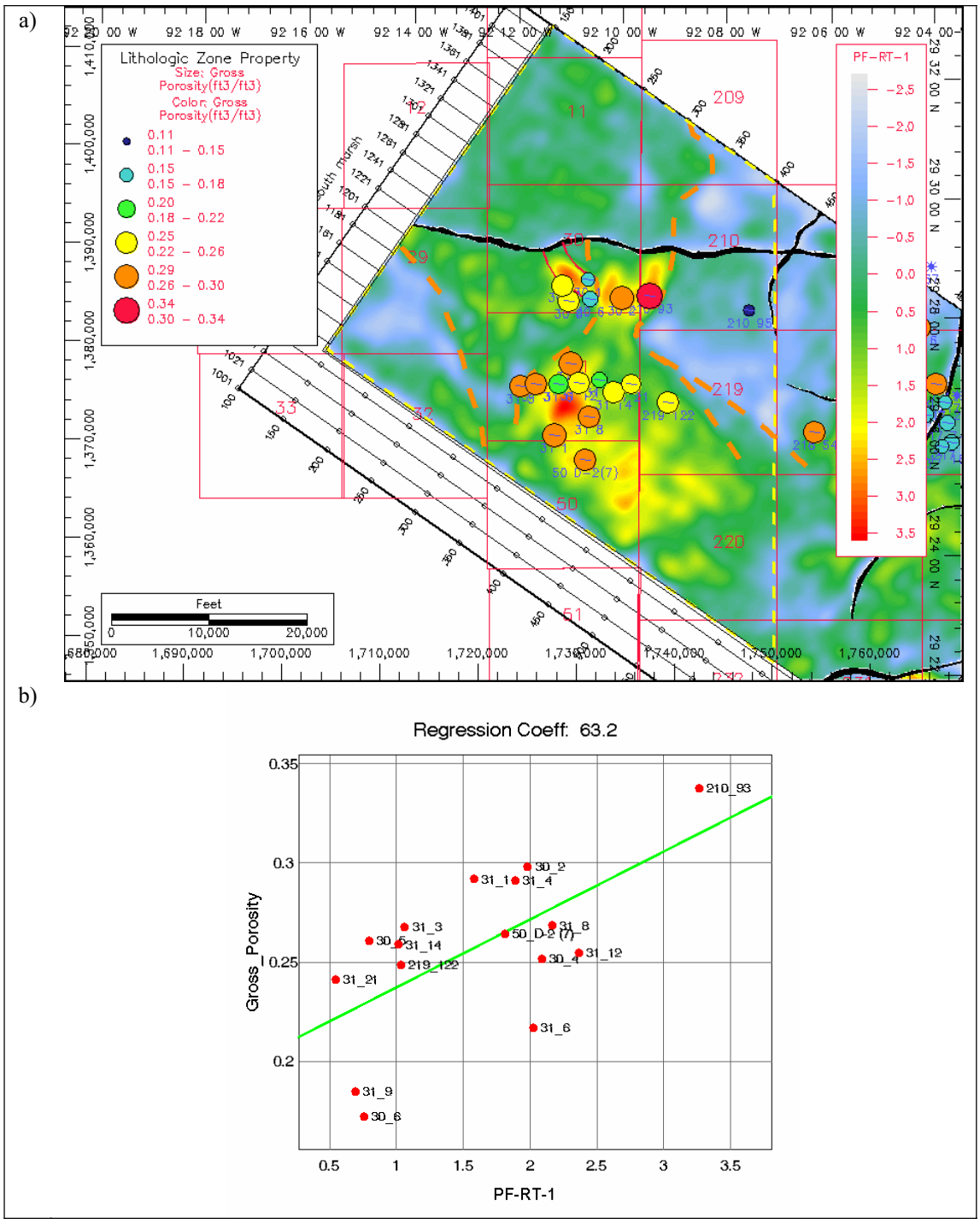

Figure 94. Multivariate seismic attribute PF-RT-1 (a). The correlation coefficient estimate and regression pattern shown in (b) is comparable to that shown by the average amplitude (Figure 92). Compared to spatial map distribution shown in Figure 93, PF-RT-1 enhances the level of contrast between incised valley sediments and adjacent marine shelf sediments and across the footwall region.

The maps of the average amplitude and PF-RT-1 seismic attributes and the scatter plots of these attributes against ϕ_{eff} reveal similar spatial distribution pattern (Figure 93 and 94). However, it can be seen that PF-RT-1 was able to contrast more between the incised valley sediments and the adjacent marine shelf sediment. Additionally, PF-RT-1 was able to increase the variability within the footwall region where average amplitude map tend to smooth out the variability within this region.

PF-RT-1 is a weighted linear combination of the various amplitude-based attributes (Figure 95 and Table 7). In addition to seismic arc length, the number of zero crossing and the ratio of positive to negative seismic attribute provide minor contributions to this factor (PF-RT-1). The later attributes are sensitive to internal stacking heterogeneity within an interval (Table 3) suggesting that this factor is trying to screen those regions characterized by higher gross effective porosity and higher internal heterogeneity.

The results of collocated cokriging estimates of gross effective porosity using average amplitude and PF-RT-1 are presented in the Figure 96. Enlarged versions of these maps are shown in Figures 97 and 98, respectively.

These spatial distributions of gross effective porosity of both approaches showed slightly comparable results. However, the gross effective porosity map of the average amplitude showed two distinct anomalies (Area 1 and Area2) of elevated porosity estimates (Figure 97). On the other hand, porosity map produced by PF-RT-1 is less sensitive to these anomalies, where Area 2 anomaly is mainly present.

Similar anomalies were seen in net thickness results using sum of magnitude seismic attributes (Figure 85). PC-14 did not show these anomalies (Figure 86) and the estimates of net thickness at these areas were overestimated due to the effect of hydrocarbons present at these areas (Figure 85). It is also expected that porosity anomalies exposed by average amplitude attribute to be related to hydrocarbon peering sediments.

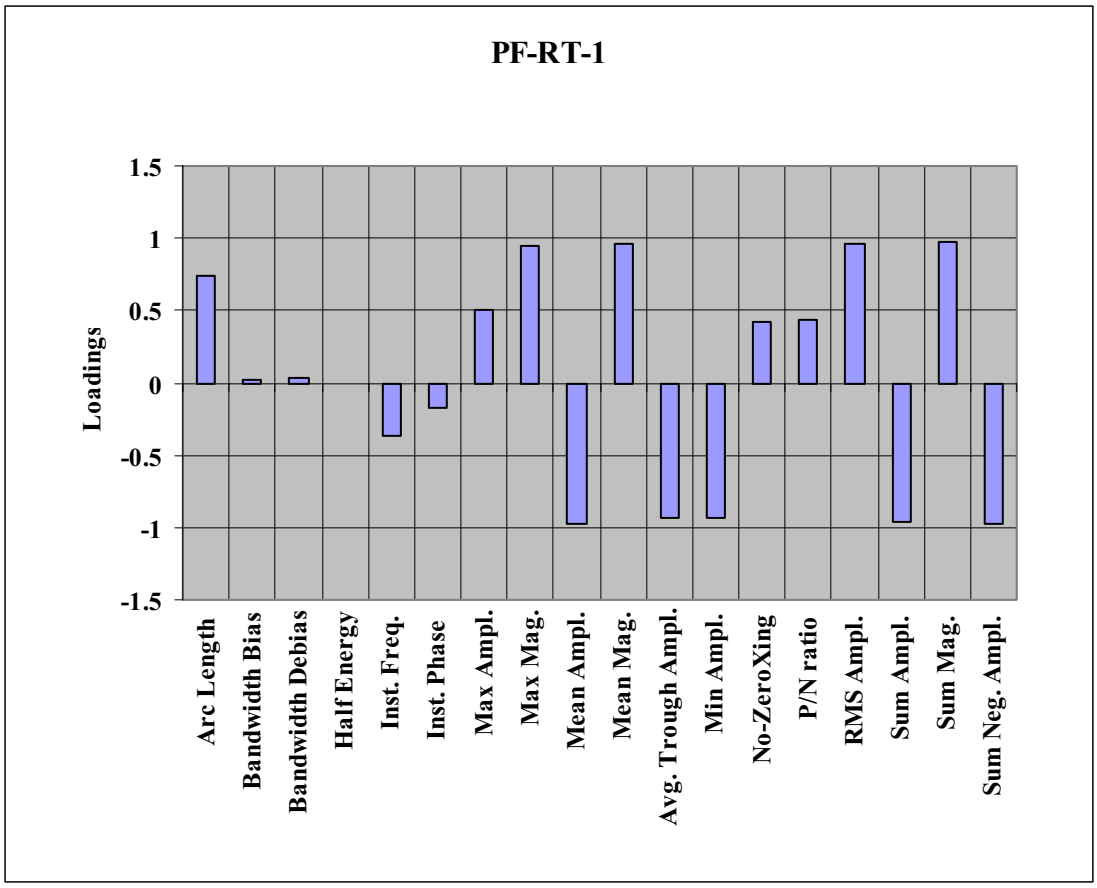

Figure 95. Bar chart illustrating the relative contribution of each seismic attributes in the principal factor PF-RT-1. Amplitude-based seismic attributes represent the highest loaders to PF-RT-1. Minor contributions are offered from seismic arc length, the number of zero crossing and the ratio of positive to negative seismic attributes. These minor attributes are sensitive to internal stacking heterogeneity within an interval (Table 3) suggesting that this factor is trying to screen those regions characterized by higher gross effective porosity and higher internal heterogeneity.

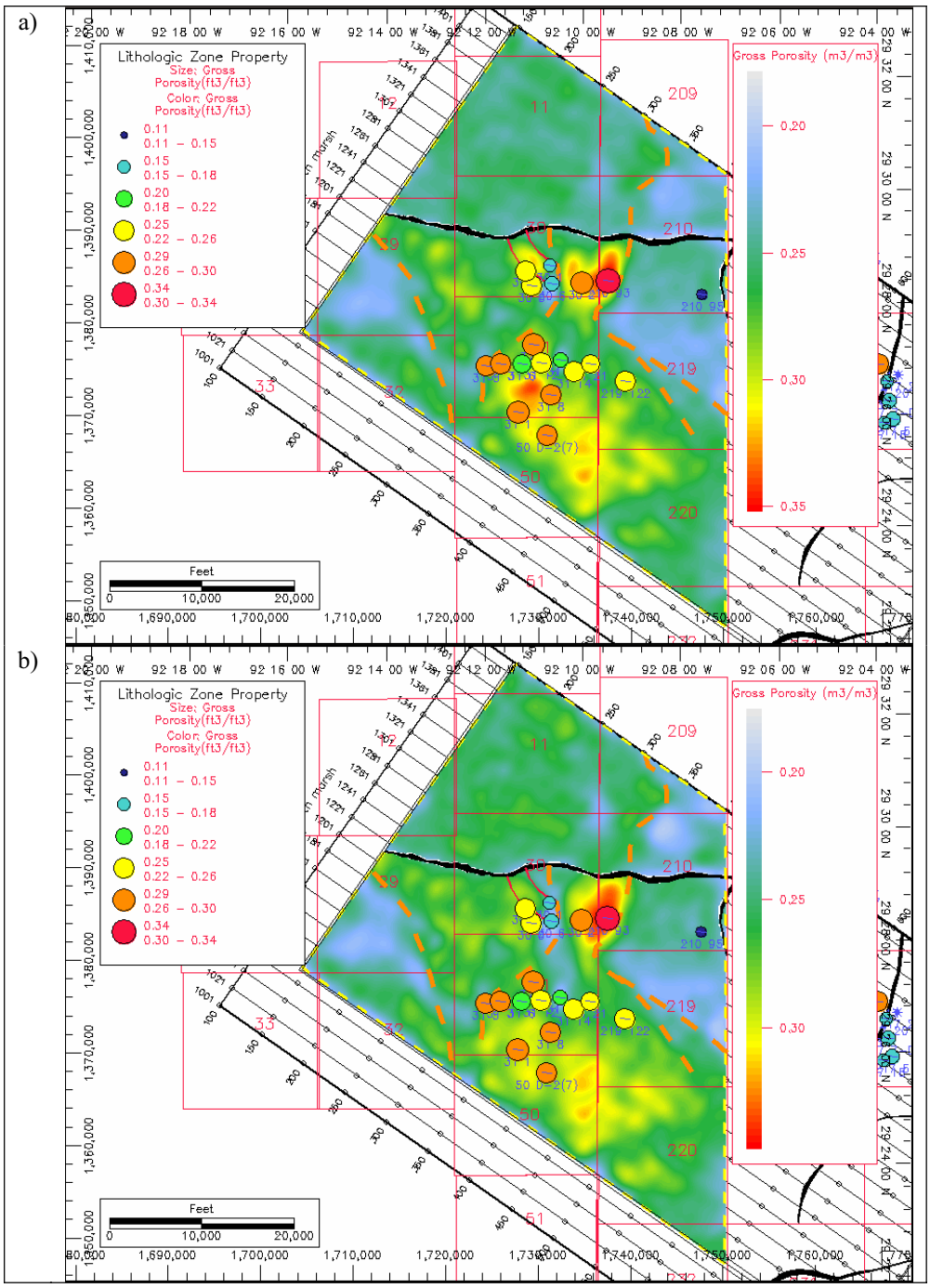

Figure 96. Comparison between gross thickness estimates produced by using instantaneous phase attribute (a) and gross thickness estimates produced by using PC-17 (b). An enlargement of these presentations is shown in Figures 70 and 71, respectively.

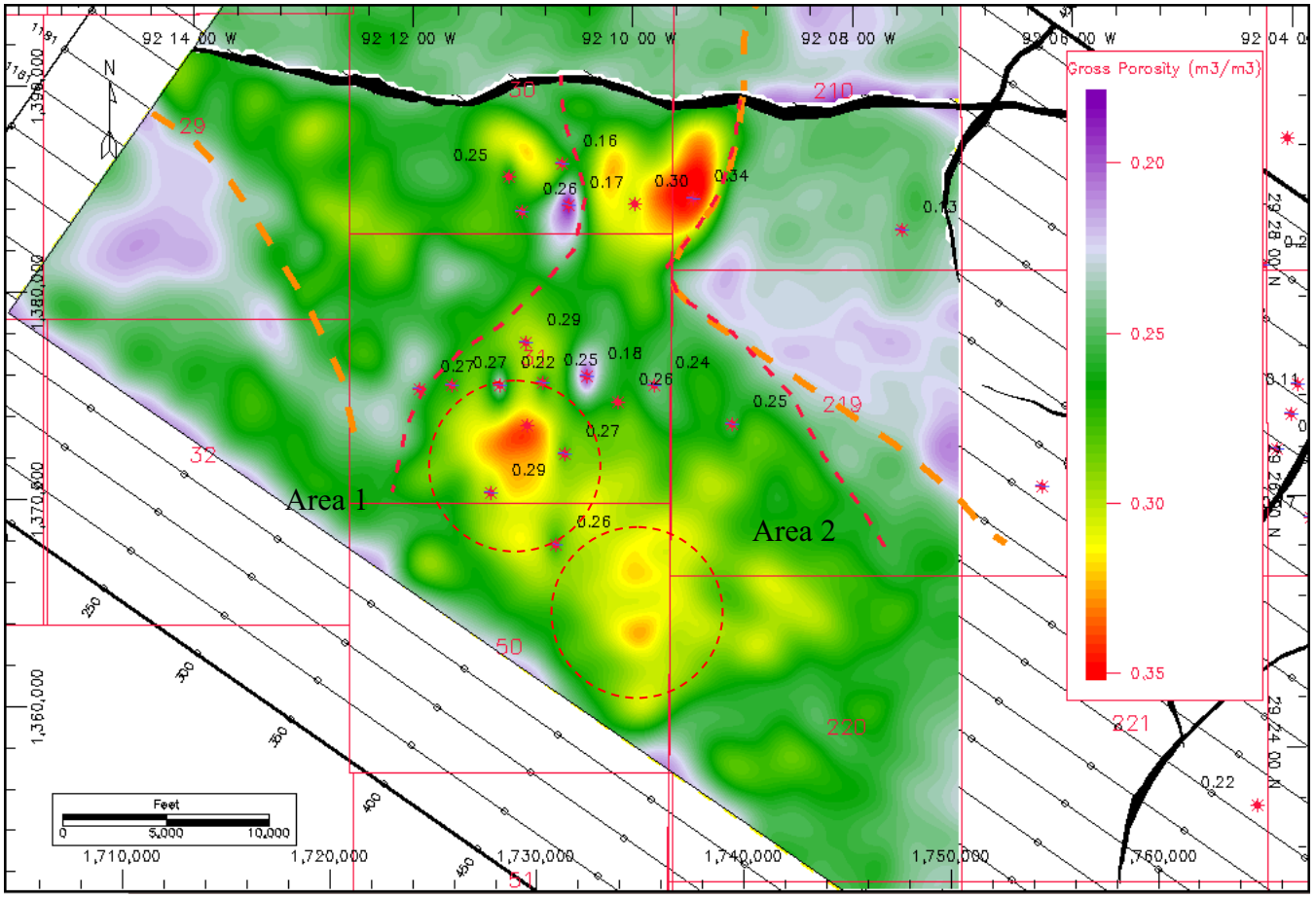

Figure 97. Gross effective porosity estimate of the N-sand interval produced by average amplitude seismic attribute as a secondary data. The elevated estimates of gross effective porosity within Area 1 and 2 are mainly attributed to saturation effect. The Figures 86 and 87 show seismic cross-sections across area 1 and area 2 respectively. It is evident that both areas are defining positive topographic relief that results in closures capable of trapping hydrocarbons. Note the topographic relief and amplitude signature across the both areas.

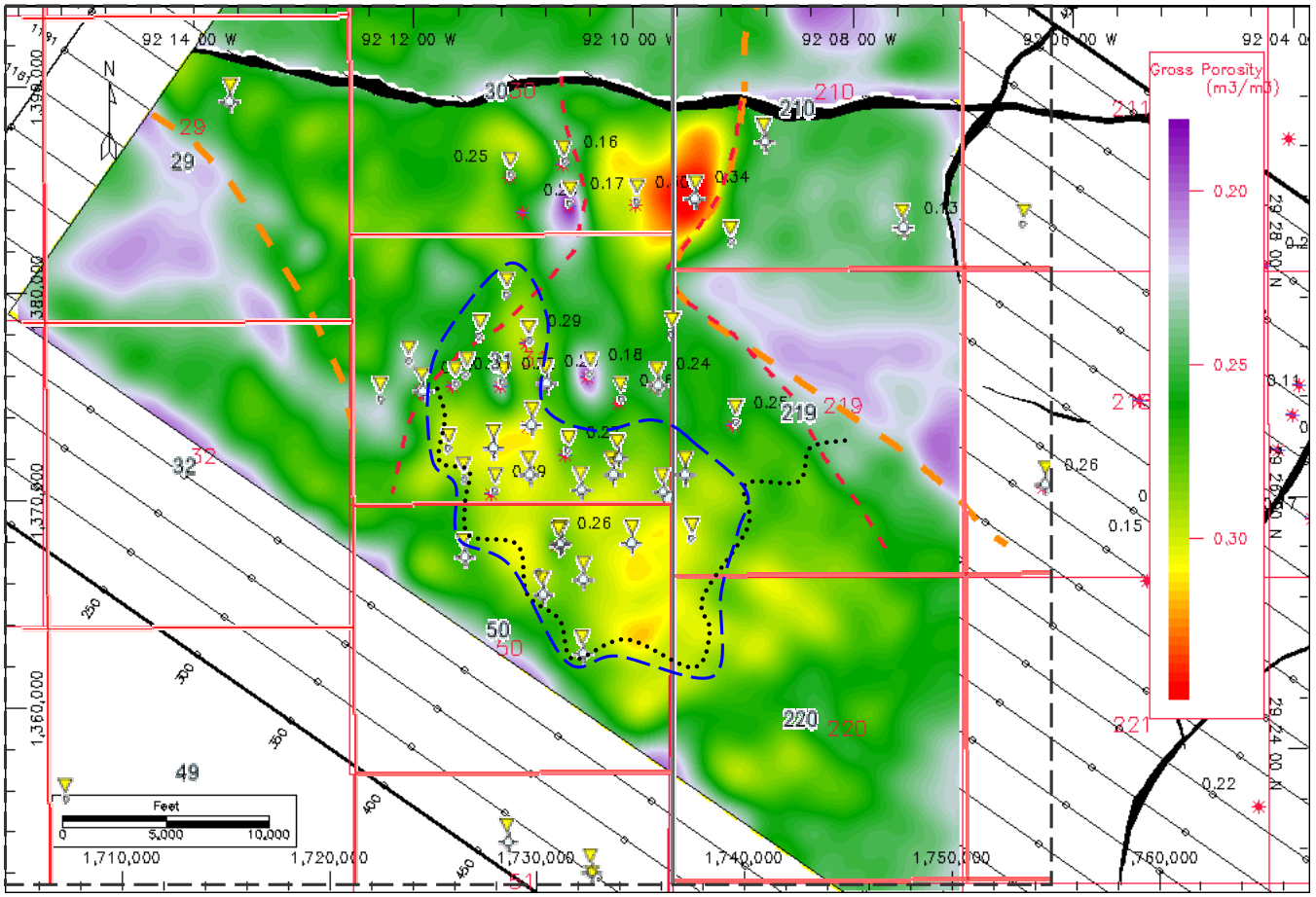

Figure 98. Gross effective porosity estimate of the N-sand interval produced by using PF-RT-1. A trend of high gross effective porosity is seen in the lower and western reaches of the incised valley which correlates with historic drilling activity in the study area (highlighted by the dashed blue line). The anomaly associated with Area 1 is not present and that of Area 2 is less pronounced than that produced by average amplitude (Figure 86). The black dashed line highlights a possible boundary defining the edge of delta front deposits of the incised valley fill (Figure 86).

Figures 99 and 100 show two dip oriented seismic cross-sections across Area 1 and Area 2, respectively. The location maps of these sections represent the spatial estimate of gross effective porosity maps of average amplitude overlain by the time structure contour of the N-sand interval. These sections indicate that the estimates of Area 1 and Area 2 are overestimated due to effect of gas saturation present within a localized positive topographic closure.

Nine of the eighteen original seismic attributes are amplitude-based attributes. These attributes can indicate changes related to hydrocarbon or lithologic changes (Chen and Sidney, 1997). PF-RT-1 is mainly loaded by amplitude-based attributes which causes the estimates of gross porosity to be slightly similar to the results of average amplitude.

A low gross effective porosity trend was shown by the results of average amplitude and PF-RT-1 (Figures 97 and 98). This zone is located within the central upper region of the incised valley. It is bounded by 2 main distributary channels defining the upper dip section of the incised valley (Figure 101). This zone of low gross effective porosity represent of interdistributary bay sediment.

Figure 102 shows a correlation between the measured values of gross effective porosity and the collocated cokriging estimates of gross effective porosity produced by average amplitude seismic attribute (a) and PF-RT-1(b). In terms of regression and variability, both approaches showed similar scatter plots.

During the course of the analysis, well 31-5 was left out because it is located at the western margin of the lowstand delta which tends to bias the estimates of correlation coefficients. Cross-plotting the results of well 31-5 over Figure 102 indicated that PF-RT-1 performed better than average amplitude in predicating the estimates of this well.

It can be concluded that gross effective porosity estimates produced by PF-RT-1 showed higher correlation coefficient value (r=.99) and less dispersion compared to the average amplitude seismic attribute (r=0.97). Moreover, PF-RT-1 was able to produce better results compared to the original average amplitude seismic attributes, especially in regions characterized with high gas saturation.

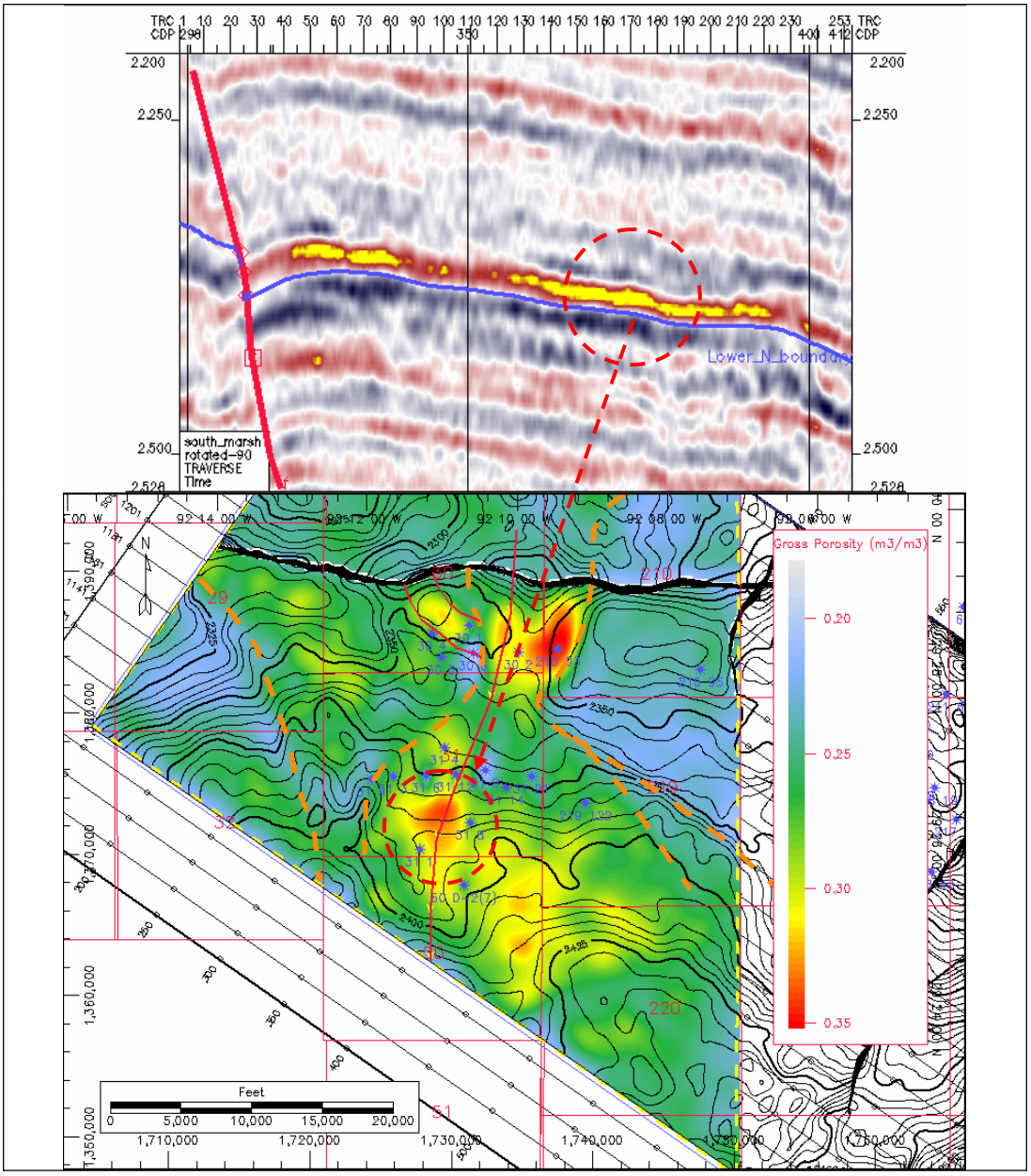

Figure 99. (A) Dip oriented seismic section across Area 1 showing that the elevated estimate of gross effective porosity is a product of gas saturation effect within a localized positive topographic closure. (B) Gross effective porosity estimate of collocated cokriging of average amplitude seismic attribute. The contour lines represent the time structure counter map. The location of the seismic section is shown in red.

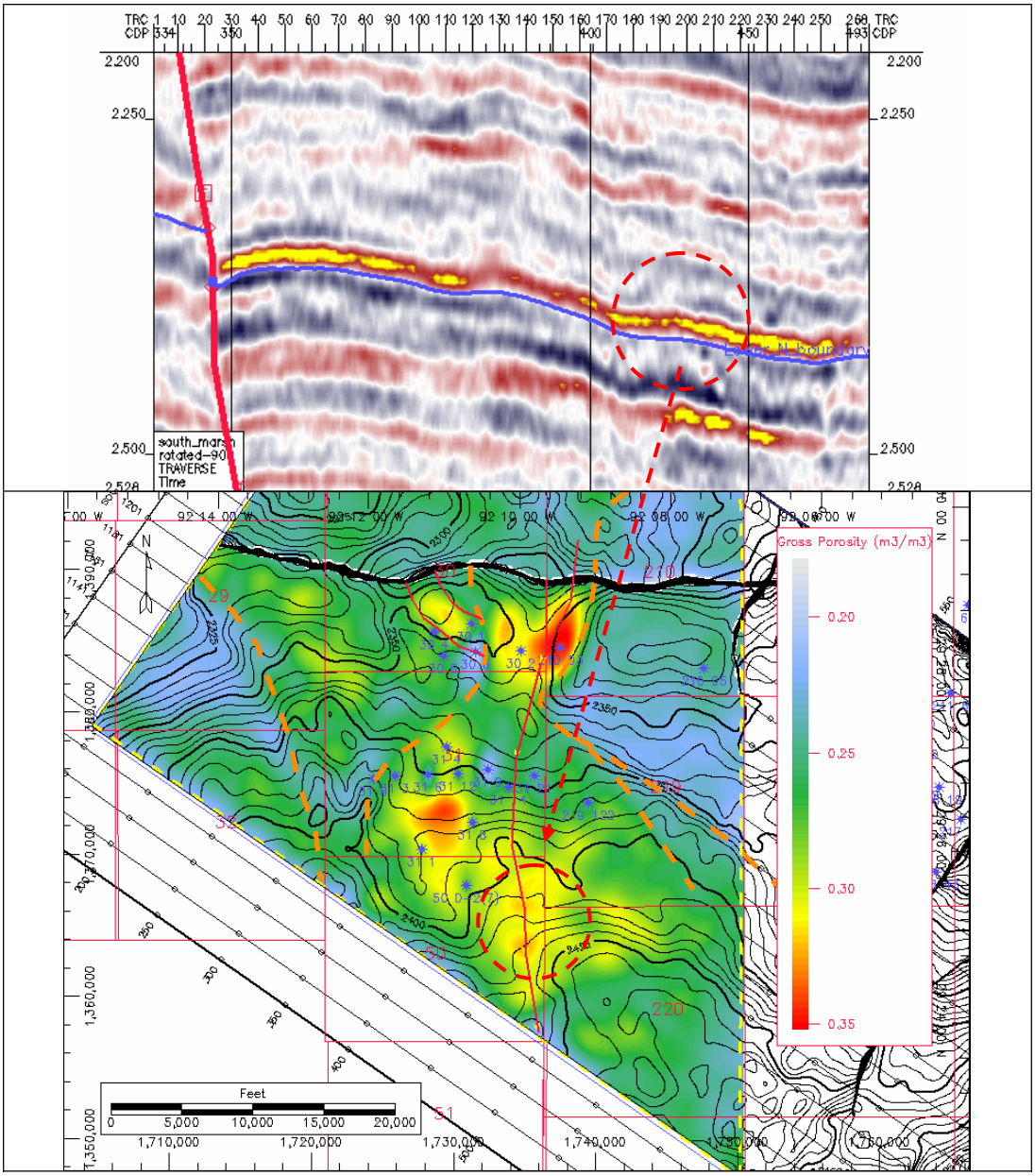

Figure 100. (A) Dip oriented seismic section across Area 2. The elevated estimate of gross effective porosity is related to gas saturation effect within a localized positive topographic closure. (B) Gross effective porosity estimate of collocated cokriging of average amplitude seismic attribute. The contour lines represent the time structure counter map. The location of the seismic section is shown in red.

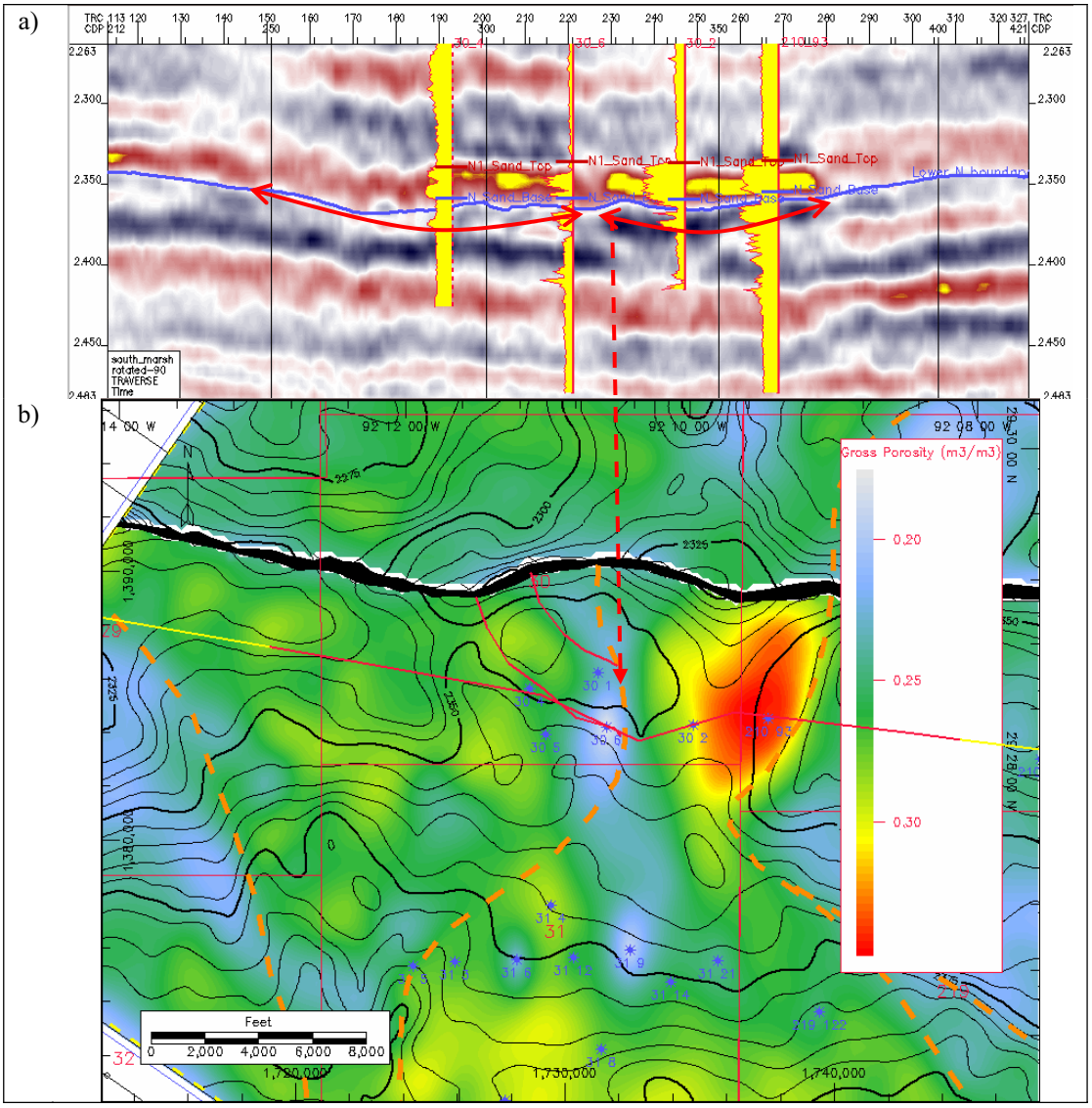

Figure 101. (A) Strike oriented seismic section across the upper region of the incised valley showing the possible location of the trend of low gross effective porosity. The low gross effective porosity trend shown in Figure 85 can be interpreted as interdistributary bays bounded by natural levees deposits. (B) Gross effective porosity distribution overlain by time structure contour map. The location of the seismic section is highlighted inn red.

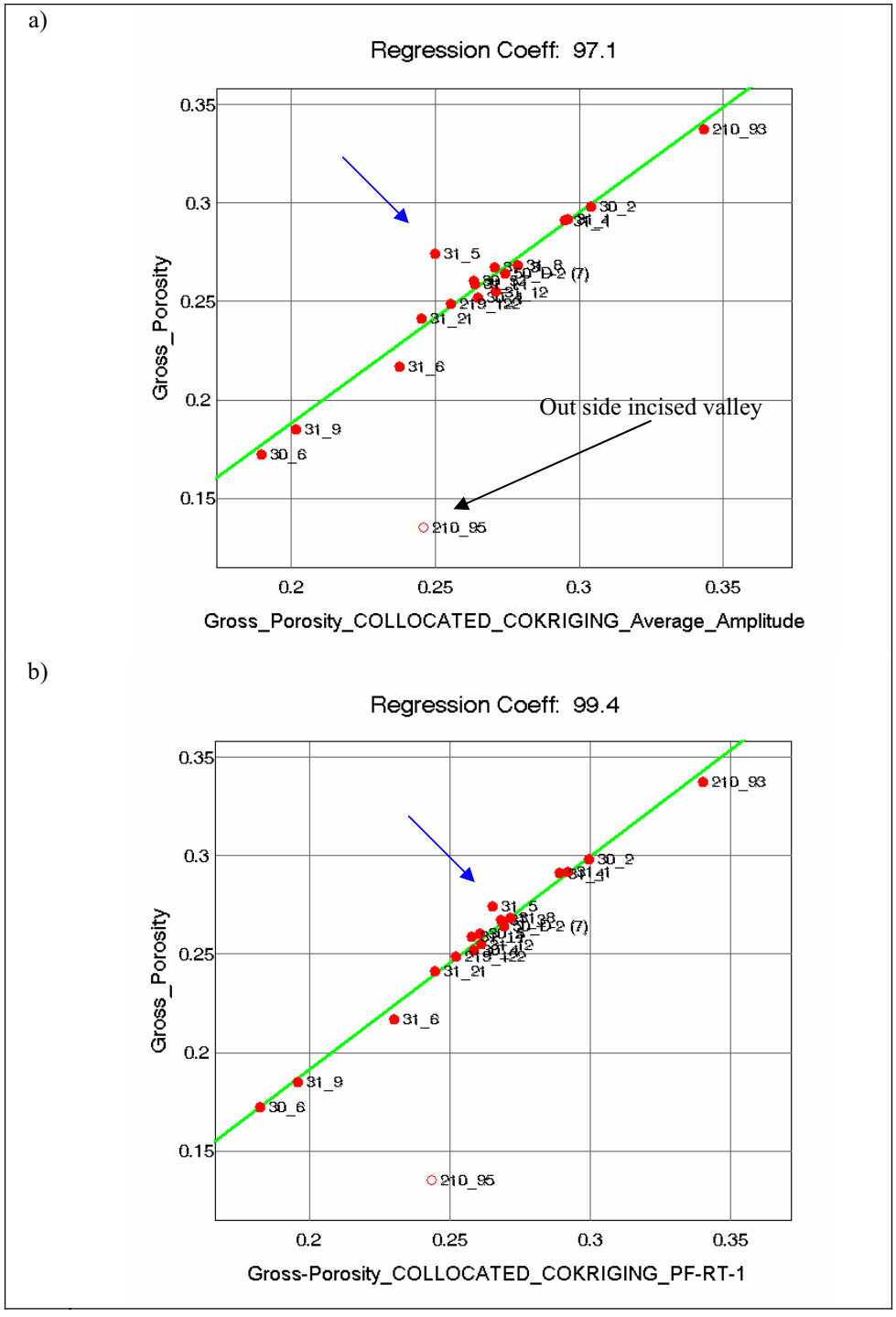

Figure 102. Correlation between measured values of gross effective porosity and collocated cokriging estimates of gross effective porosity of average amplitude attribute (a) and PF-RT-1 (b). Note that both approaches gave similar results for the wells located within the incised valley. However, PF-RT-1 gave accurate estimate for well 31_5 (highlighted with a blue arrow) than the average amplitude attribute. Well 210-95 is located outside the incised valley and is discarded from the study.

4.4.4 Sand volume fraction (net-to-gross N/G ratio) mapping

The net-to-gross (N/G) ratio is another reservoir property which gives an idea about the vertical heterogeneity within an interval of investigation. The spatial distribution of the N/G ratio is shown in Figure 103. N-sand interval within the main channel of the incised valley shows higher N/G ratio than the wells located outside the channel. The higher ratio is mainly related to thick distributary channel sand deposits. The maximum value for N/G ratio of N-sand interval is seen at well 210-93 and the minimum value is shown by well 31-9.

The spatial details of the distribution of the N/G ratio were achieved by an experimental semivariogram analysis using a lag interval of 820ft. The variogram model is a spherical function with a range of 11,060ft and a sill of 0.035796 (Figure 104). The spatial distribution of N/G ratio shows a general anisotropic spatial pattern such that the major axis of continuity is trending in the S21E direction. The anisotropy ratio is equal to 0.44 (Figure 104).

Brown (1999) classified the response of reflectivity of seismic data into two main groups: 1) the bright spot regime and 2) the dim spot regime. In a bright spot regime, such as the GOM basin, it is anticipated that an increase in porosity, N/G ratio and saturation will decrease the reservoir acoustic impedance which will result in higher amplitudes of the reservoir reflections (Brown, 1999). Accordingly, it is expected that N/G ratio will show strong linear relationships with the various original and multivariate amplitude-based seismic attributes.

Figure 105 shows an overall weak correlation behavior between N/G ratio and the various original and multivariate seismic attributes that are investigated in this study. Inspecting these relationships showed that the weak associations are mainly related to the existence of some local trends between N/G ratios and the inspected seismic attribute that tend to divide the wells of the study area into two groups; a high N/G ratio and a low N/G ratio clusters (Figure 106).

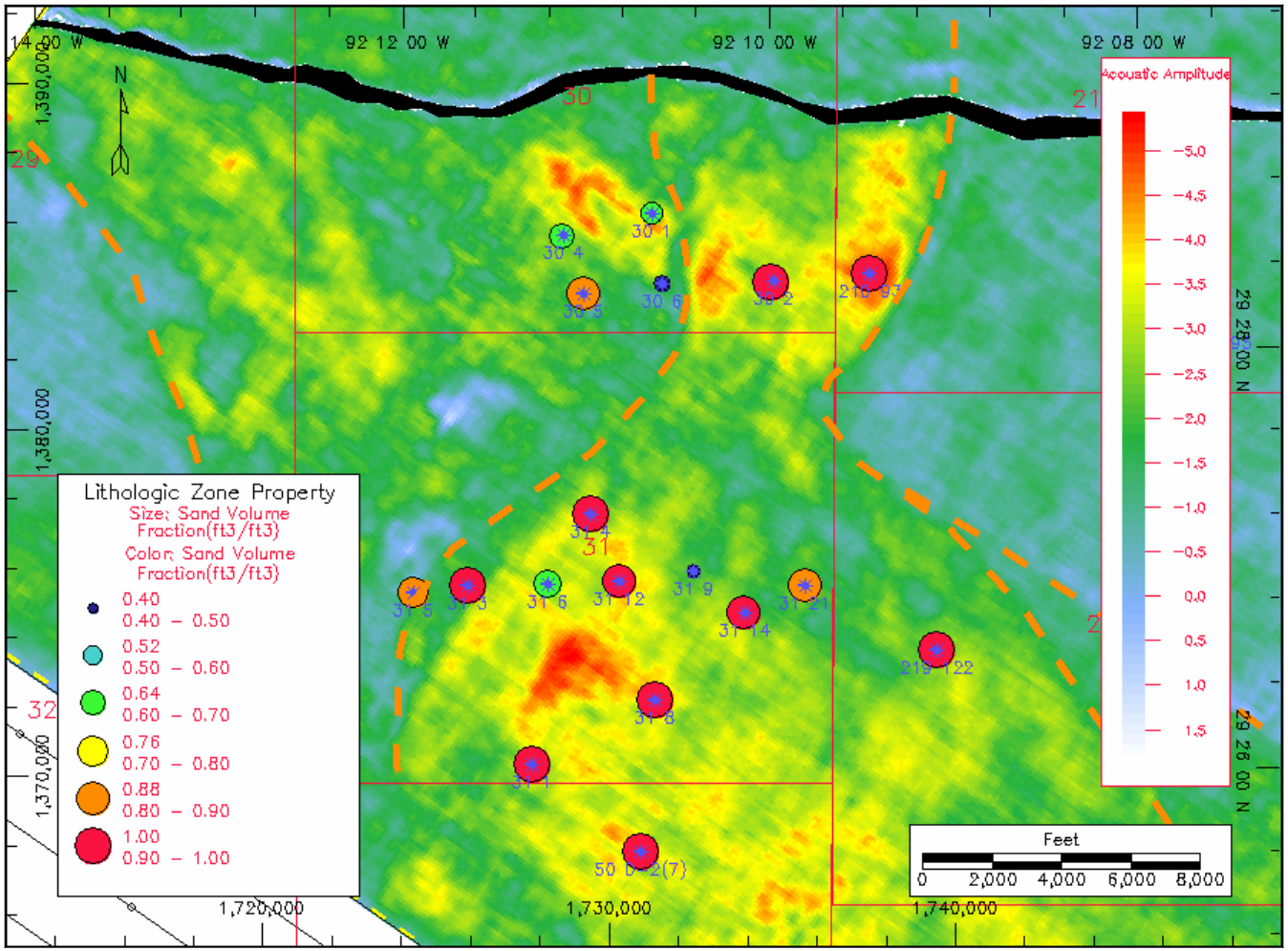

Figure 103. Amplitude map overlain by a bubble layout showing the spatial distribution of net-to-gross ratio of the N-sand interval.

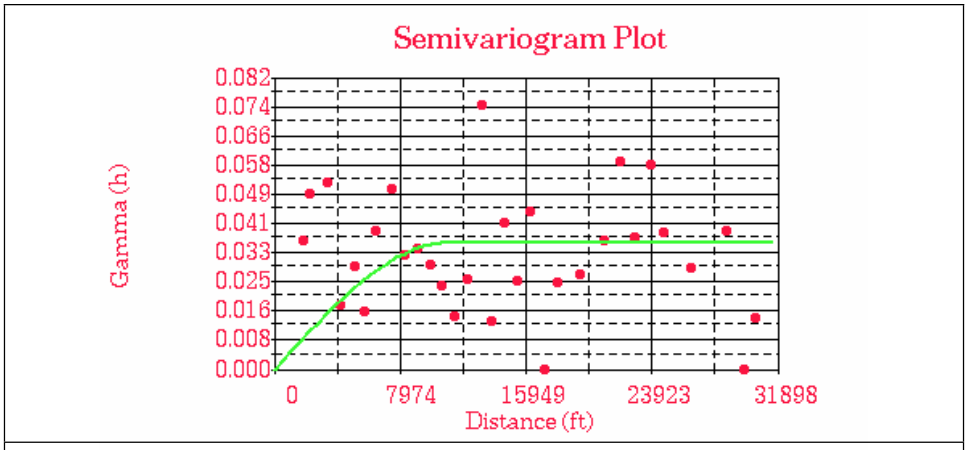

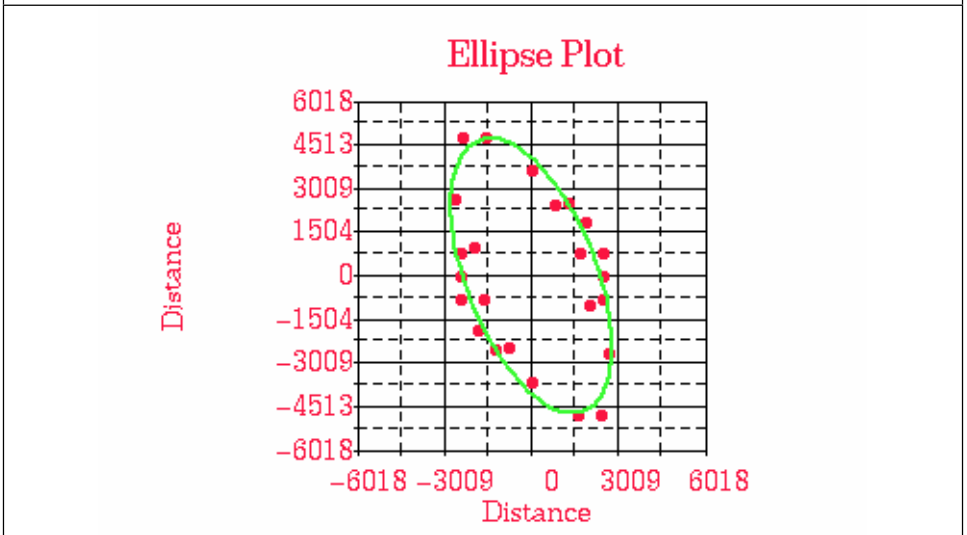

Lag Interval (h)	820ft	**Sill**	0.035796
Max. Lag	30,000ft	**Nugget**	0
Model	Spherical	**Anisotropy Angle**	159°
Range	11,060ft	**Anisotropy ratio**	0.44

Figure 104. Spatial analysis parameters of N/G ratio of Vermilion 50 wells.

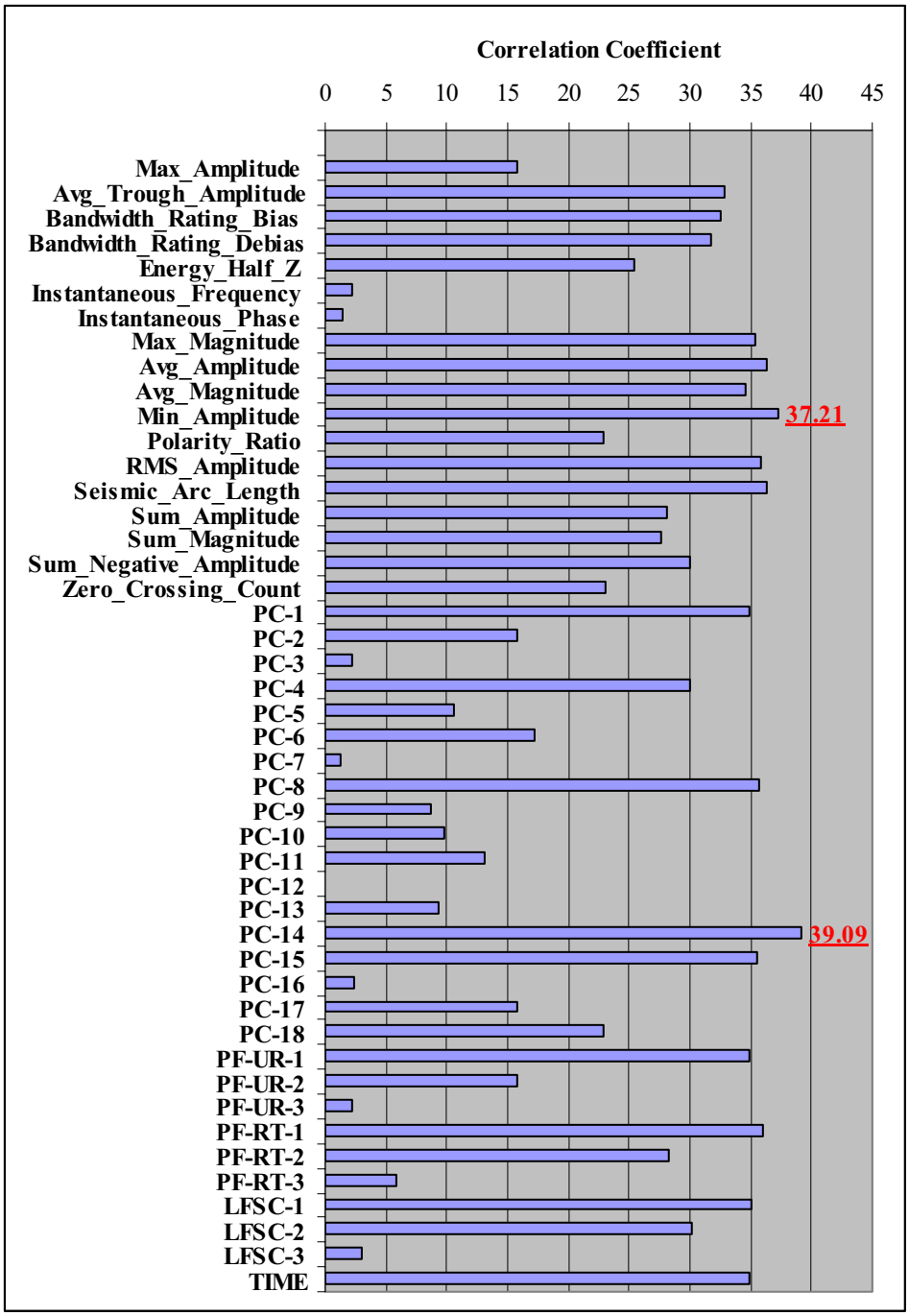

Figure 105. Correlation coefficient plot of the absolute correlation coefficients |r| between N/G ratio and the various seismic attributes for the wells located within the incised valley (n=18). An overall general weak correlation behavior is seen against all available attributes due to the occurrence of separate trends separating high N/G ratio wells from low N/G ratio wells (Figure 106).

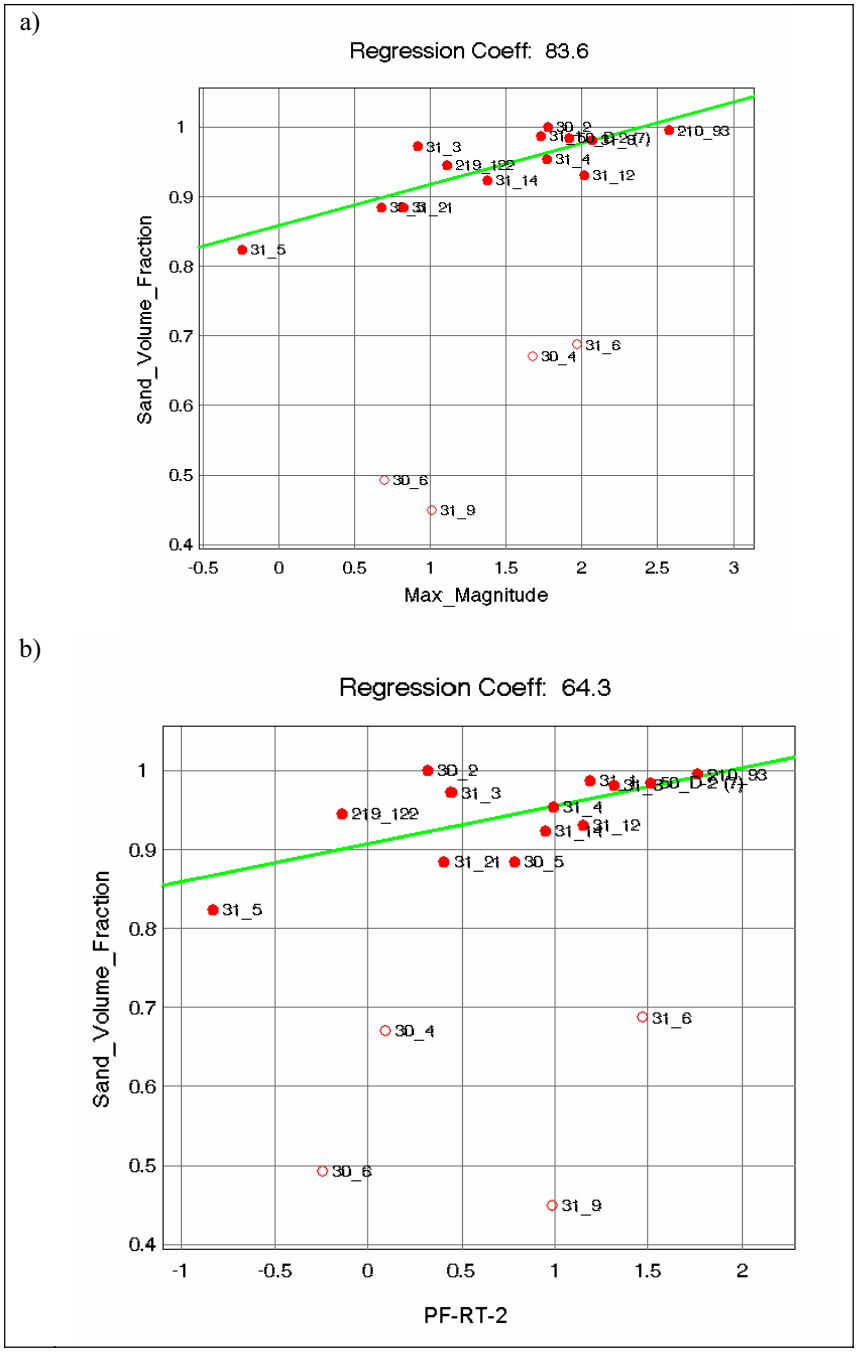

Figure 106. Sand volume fraction (N/G ratio) versus maximum amplitude seismic attribute (a) and PF-RT-2 (b) shows two separate trends that contrast between high N/G ratio wells and low N/G ratio wells. The location of these wells is illustrated on Figure 103.

Figure 106 shows two scatter plots of the N/G ratio against the maximum amplitude seismic attribute and PF-RT-2. These plots divide the dataset into

Figure 106 shows two scatter plots of the N/G ratio against the maximum amplitude seismic attribute and PF-RT-2. It is evident that the anticipated relationship between N/G ratio and amplitude attributes still exists, but due to the limited number of samples this strong relationship is not emphasized.

PF-RT-2 can be described as a measure of heterogeneities that are related lithologic cyclicity (Figure 107). Accordingly, it is expected that the use of PF-RT-2 will provide better estimates of N/G ratio than the original maximum magnitude. Figure 108 shows map presentations of maximum magnitude and PF-RT-2.

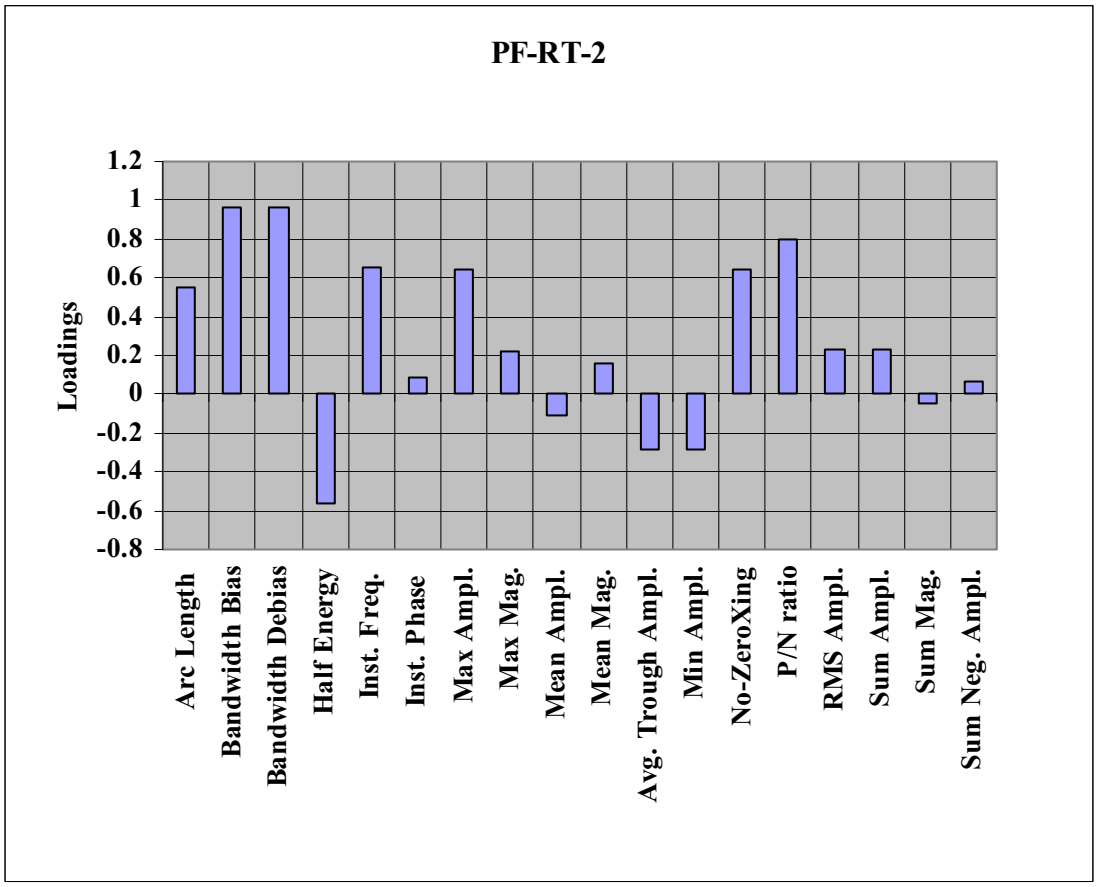

Figure 107. Bar chart presentation of the relative contribution of each attributes to PF-RT-2. These seismic attributes are sensitive to internal heterogeneity of the investigated interval.

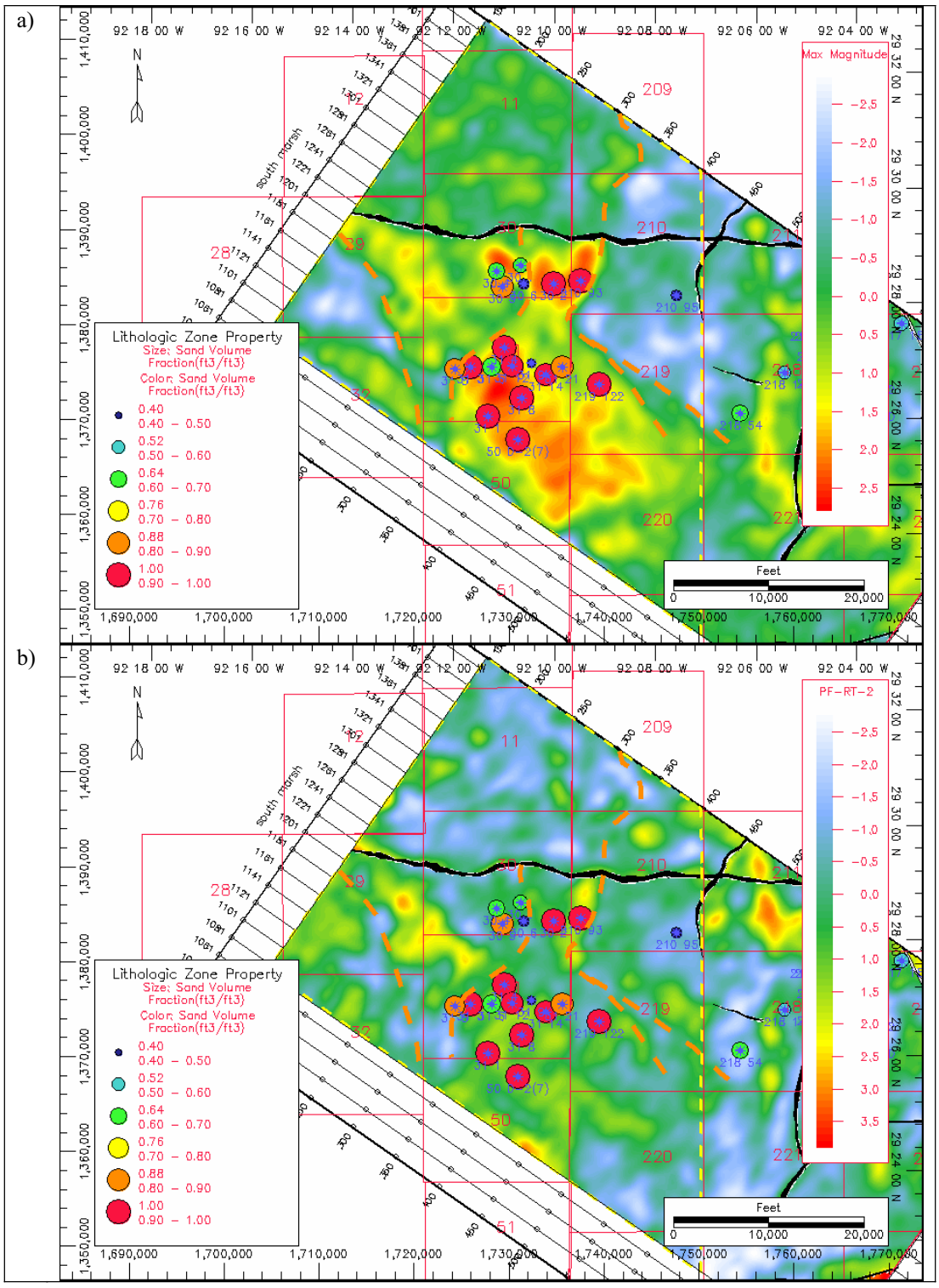

Figure 108. Map presentations of maximum magnitude (a) and PF-RT-2 (b).

The major advantage of the collocated cokriging method is that it relies on the value of the correlation coefficient between primary and secondary data inputs (Xu et al., 1992). The higher the correlation coefficient value the accurate the estimates of the collocated cokriging method.

In order to map N/G ratio, the wells defining a low G/N ratio were left out of the study. This means that 22% of the sample size which represents the low N/G ratio samples will be ignored in favor of the high N/G ratio. Accordingly, it is expected that the final results will be biased and not conclusive. The resulted increased correlation coefficient between the retained well measures of G/N ratio and the used seismic attribute could be a product of another associative relationship (Brown, 1996).

The final reservoir property maps of N/G ratio of maximum magnitude and PF-RT-2 are shown in Figures 109 and 110, respectively. Both maps showed similar spatial distribution patterns within the main channel boundaries of the incised valley (Figure 111).

PF-RT-2 results show a limited basinward extension and present channel shape extensions in the down dip regions (Figure 110). On the other hand, the maximum magnitude results showed smooth front pattern which might indicate poor geological control over the results (Figure 109). Outside the boundaries of the incised valley, the results are not reliable due to the lack of enough well control.

Although, both of the previous approaches yielded accurate estimates for N/G ratio at well location, but their results are not geologically reliable and they lack a reasonable degree of correlation to any of the investigated seismic attributes. The estimates of gross thickness of PC-17 and net thickness of PC-14 were geologically acceptable and were derived using different spatial models which indicate that they possess an identical spatial model. Moreover, PC-17 and PC-14 were clearly correlated with gross thickness and net thickness, respectively (Figures 68 and 79). Accordingly, it will plausible to use their estimates to provide an accurate estimate for N/G ratio or to verify the results obtained by using maximum magnitude seismic attribute and the PF-RT-2 multivariate seismic attribute.

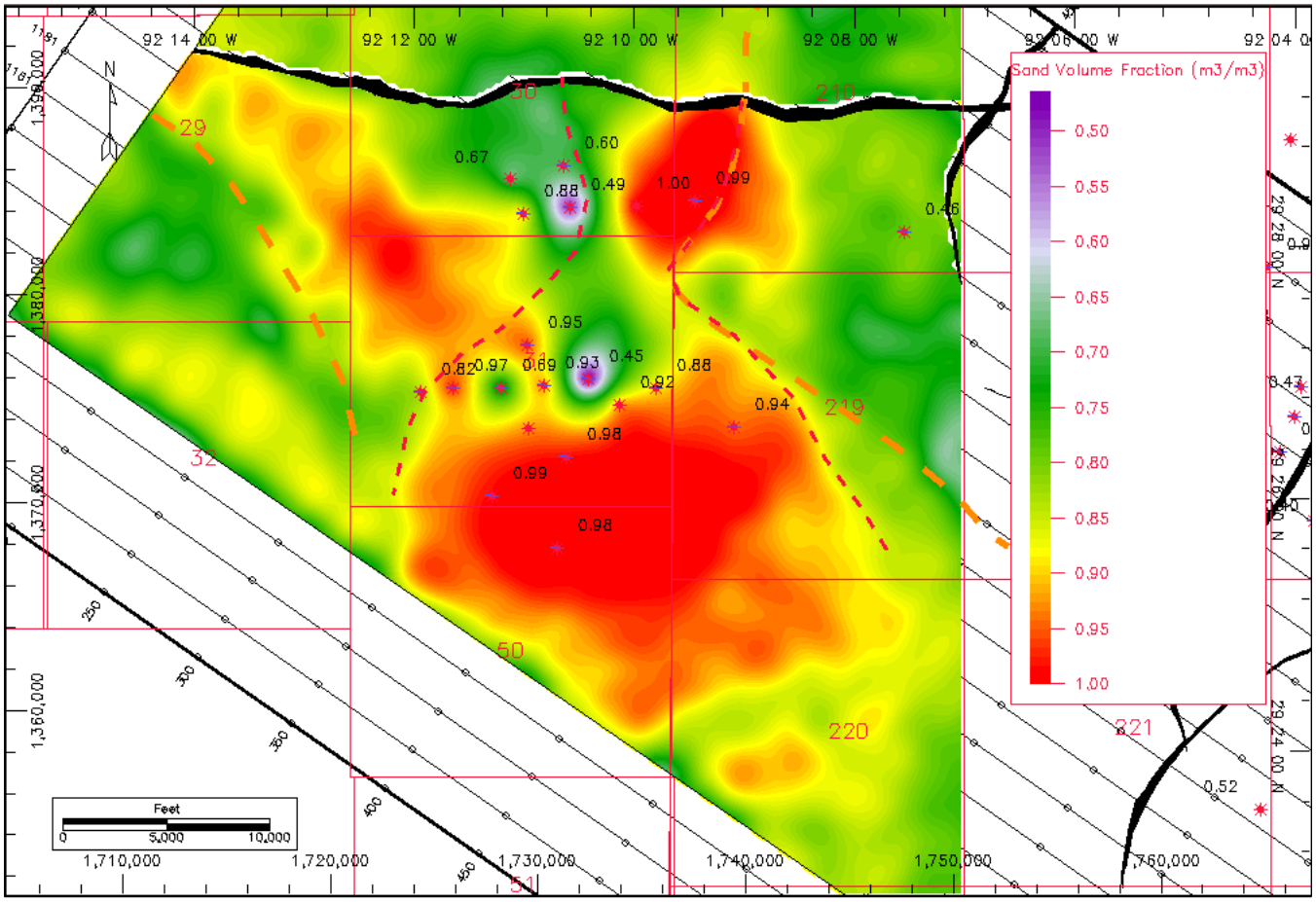

Figure 109. N/G ratio estimates produced by using maximum magnitude seismic attribute. The down dip region of the lowstand delta shows a smooth front pattern.

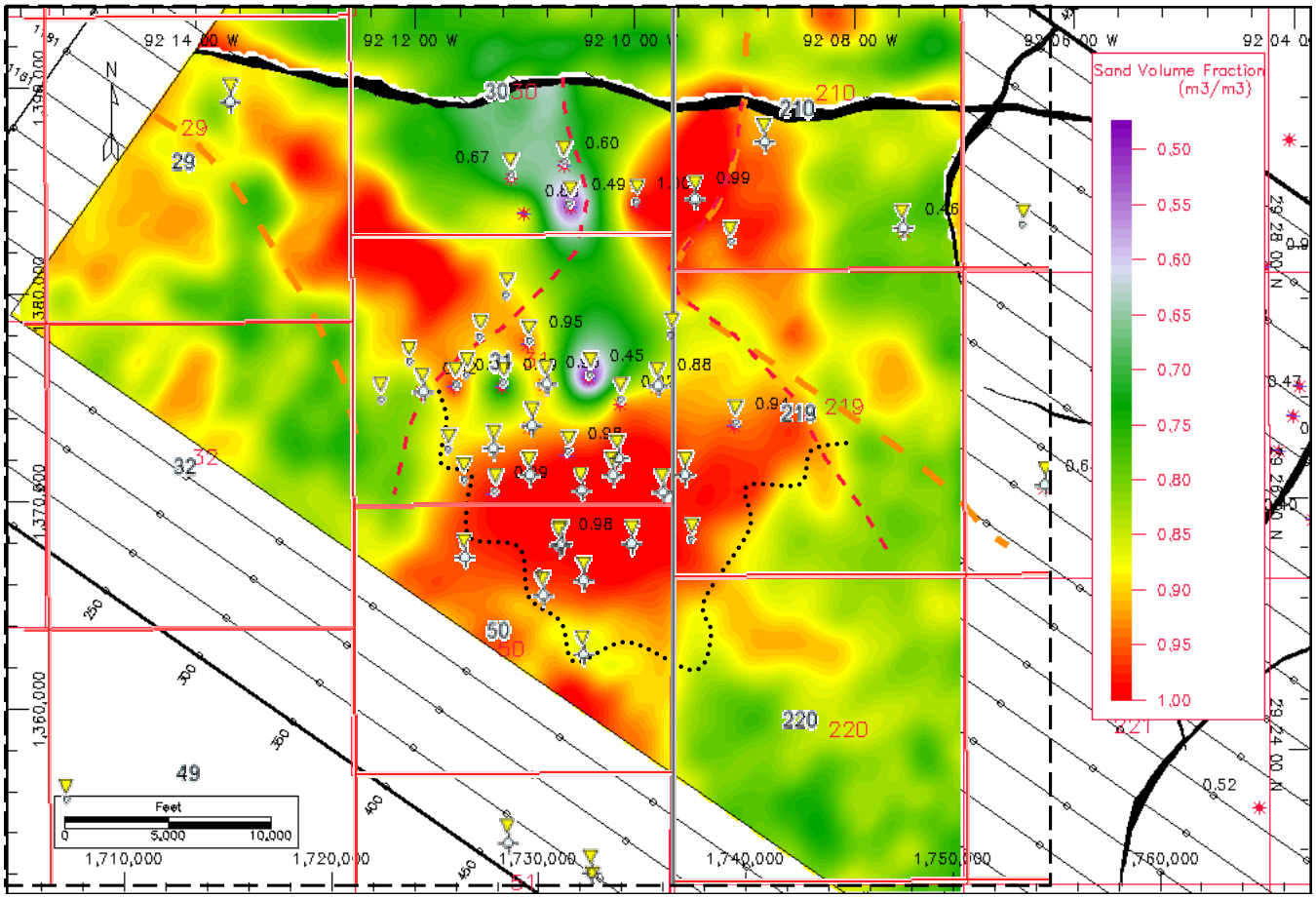

Figure 110. N/G ratio estimates produced by using PF-RT-2 multivariate seismic attribute. The down dip region of the lowstand delta shows the maximum estimates for N/G ratio which is bordered by the interpreted edge of the delta front highlighted by the black dashed line (Figure 86).

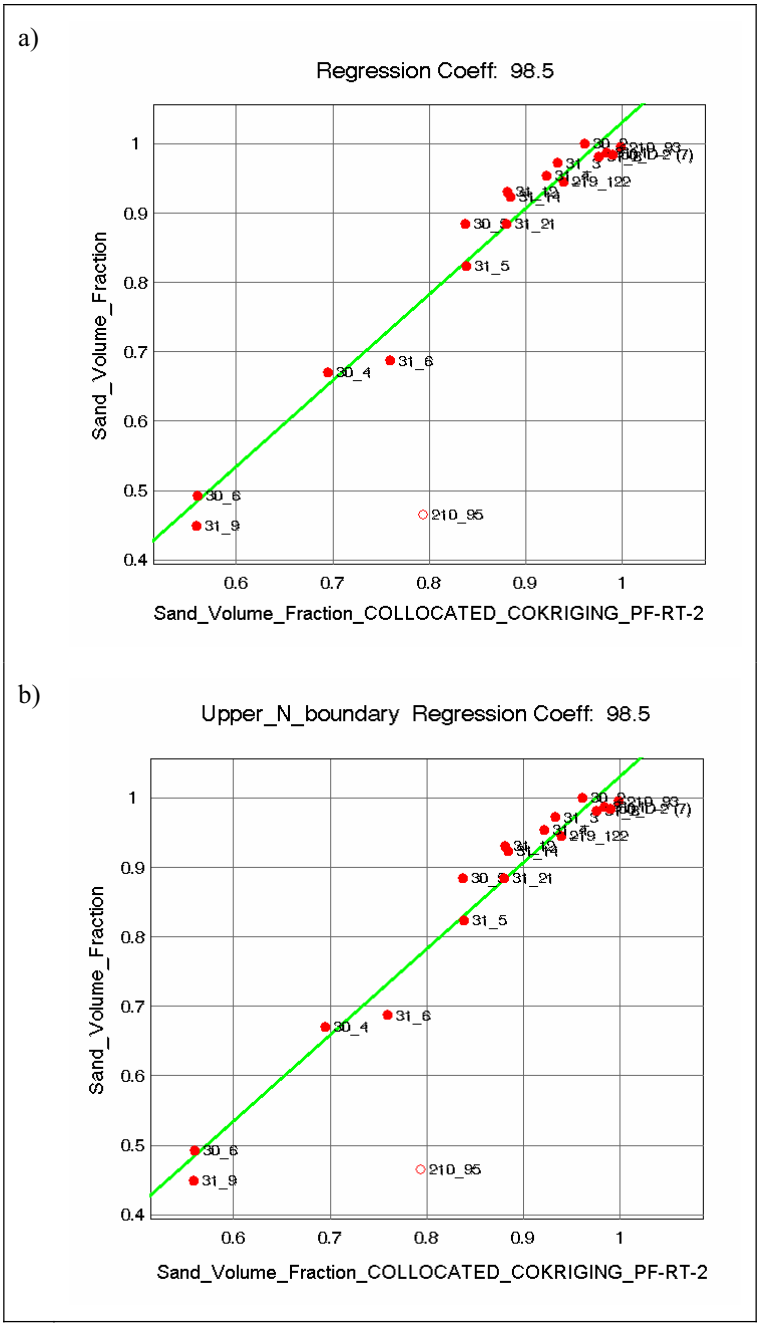

Figure 111. Correlation between measured values of N/G ratio and collocated cokriging estimates of N/G ratio produced by maximum of magnitude attribute (a) and PF-RT-2 (b). Both cases gave similar results for the wells located within the incised valley. As for the region located out side the valley, both methods highly overestimate of N/G ratio (at well 210-95). Note also that both approaches gave accurate estimates for N/G ratio at the wells 30-4, 30-6, 31-6 and 31-9 which were left out of the study (Figure 106).

Figure 112 represents the result of the division of net thickness of PC-14 and gross thickness of PC-17. The resultant estimate of net to gross is a product of two different estimates created using the method of collocated cokriging with different spatial models. However, the final estimate of N/G ratio reflects a strong geological control. The footwall region of the incised valley shows a set of channels running across the exposed shelf and feeding the lower courses of the incised valley system.

Figure 113 shows a scatter plot between the results of Figure 112 against the log derived measurements of N/G ratio at well site, suggesting that the estimates of this approach is acceptable. The fact that net and gross thickness measures showed good correlations with PC-14 and PC-17, it is can be generalized that the result of this approach is more accurate than the biased estimates produced maximum magnitude or PF-RT-2. Additionally, Figure 112 reflects a clear lateral heterogeneity that is not present in the results of maximum magnitude and PF-RT-2 (Figures 109 and 110).

4.4.5 Net reservoir porosity thickness product mapping

The fifth reservoir property is the net reservoir porosity thickness product ($\phi_{eff}h$) or the net reservoir pore footage reservoir. It has a finer vertical scale than the previous ones. The computation of this property was constrained by two restrictions: 1) shale volume should be less than 0.25 and 2) gross effective porosity should not be less than 0.15. These conditions were investigated every 1ft sample interval. A sample interval is discarded if one of these conditions is not met. For this study, these two conditions define what is meant by a net reservoir property.

A comparison between net and reservoir properties of thickness and porosity is shown in Figure 114. Constraining the computation of this property by these conditions will increase the value of average porosity and decrease the thickness of the interval expected to be a reservoir unit.

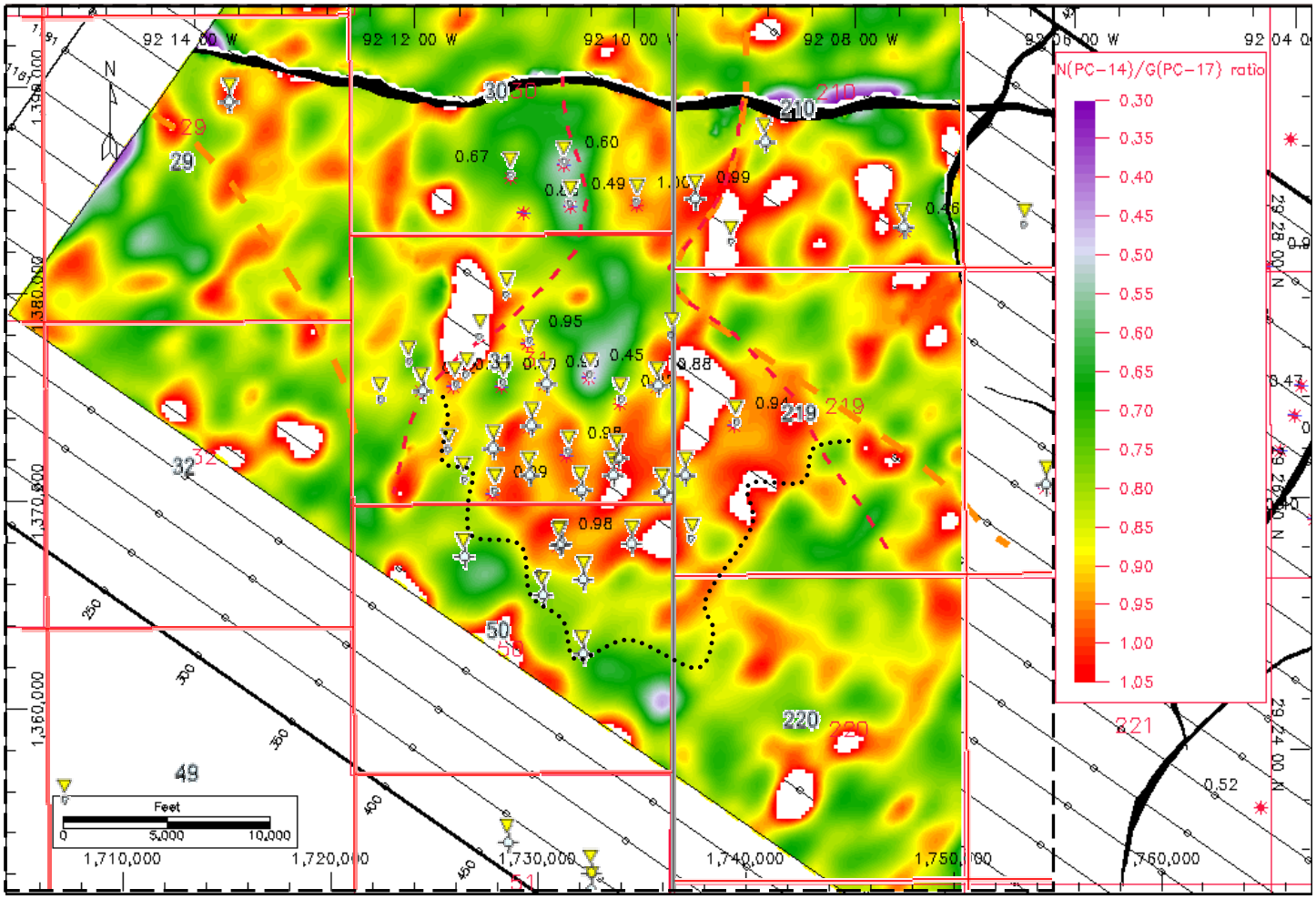

Figure 112. Estimated N/G ratio map produced by dividing the estimates of net thickness of PC-14 by the estimates of gross thickness produced by PC-17 showing similar results to the N/G ratio results of PF-RT-2. The measured values of N/G ratio are shown in black along well location. White gaps represents region of overestimates values of N/G ratio due to overestimates net thickness or underestimates gross thickness values.

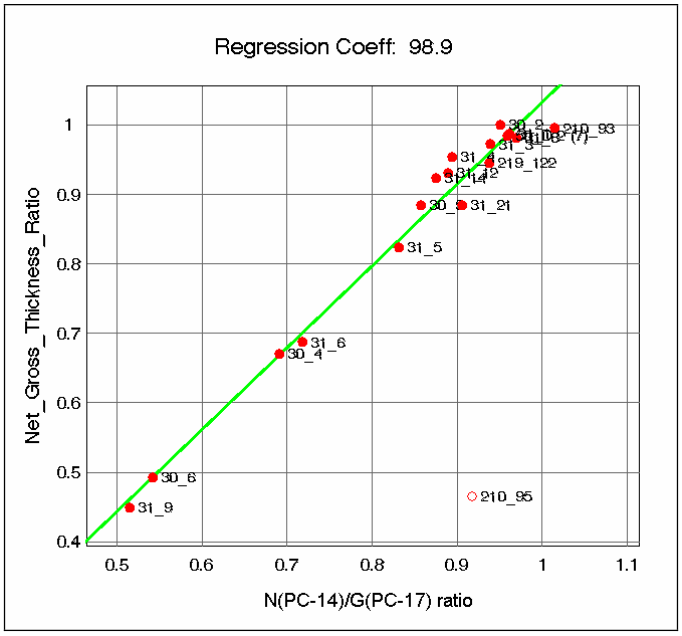

Figure 113. Scatter plot between measures N/G ratio and N(PC-14)/G(PC-17) ratio suggesting that the results of Figure 123 is more reliable than the results produced by maximum magnitude or PF-RT-2.

The spatial distribution of the log measured ϕ_{eff}h is shown in Figure 115. The maximum ϕ_{eff} of N-sand interval is seen at well 210-93 and 30-2 is located at the upper parts of the main channel. The western region of the lowstand delta shows higher values than its eastern reaches.

The spatial details of the distribution of the ϕ_{eff}h were achieved by an experimental semivariogram analysis using a lag interval of 805ft. The variogram model is a spherical function with a range of 15888.6ft and a sill of 0.00149 (Figure 116). The spatial distribution ϕ_{eff}h showed a general anisotropic spatial pattern similar to the model of gross effective porosity.

The major axis of continuity has an azimuth angle of 158 degrees from the north and an anisotropy ratio of 0.50. The ellipse plot of anisotropy is similar to the model presented by gross effective porosity property (Figures 91). Figure 117 presents a summary of the absolute values of the correlation coefficients between ϕ_{eff}h and the various seismic attributes.

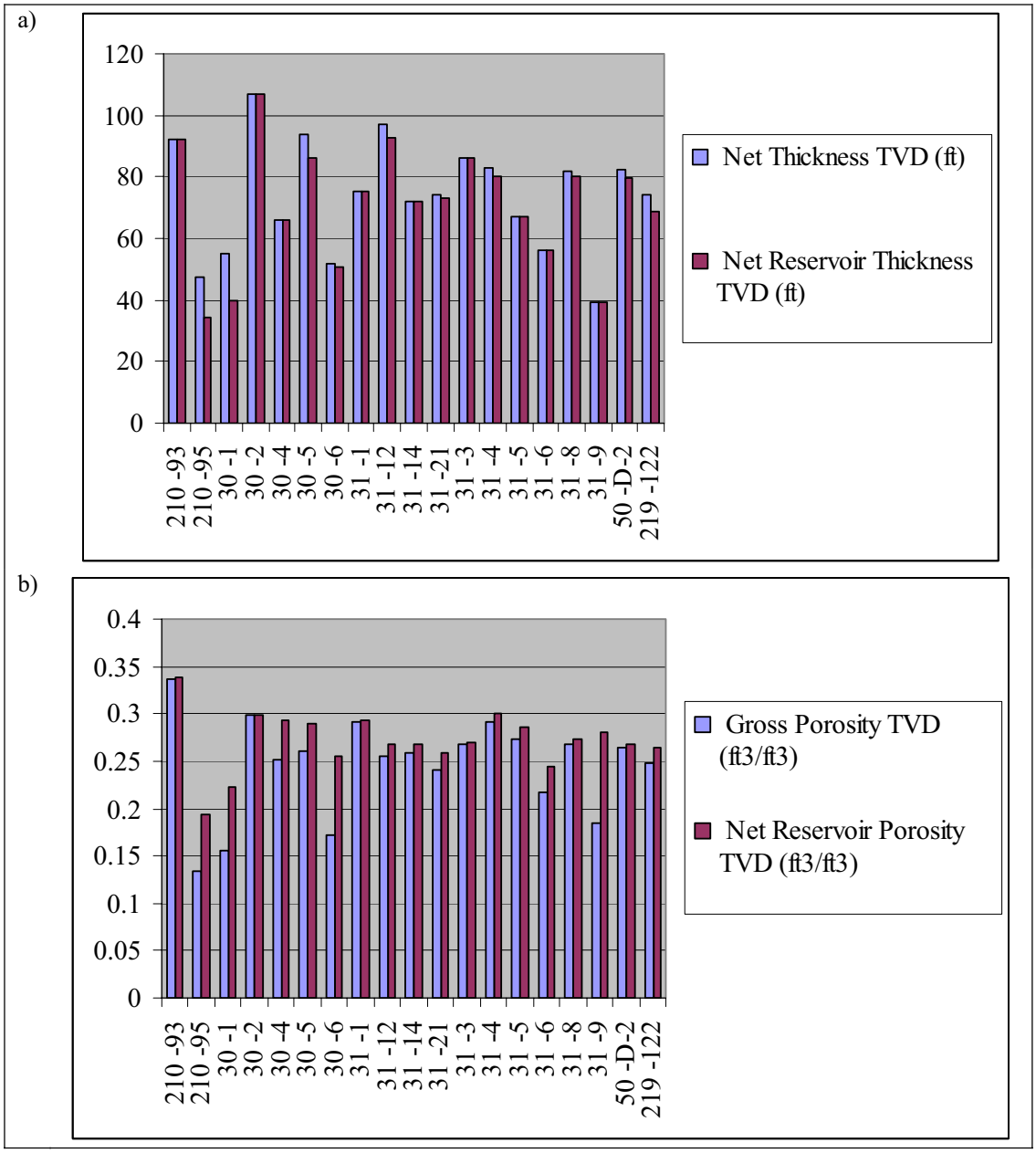

Figure 114. A) Comparison between net and net reservoir thicknesses (B) A comparison between gross and net reservoir porosities of Vermilion 50 wells. Net reservoir unit is characterized by less that 0.25 shale volume and porosity of more than 0.15.

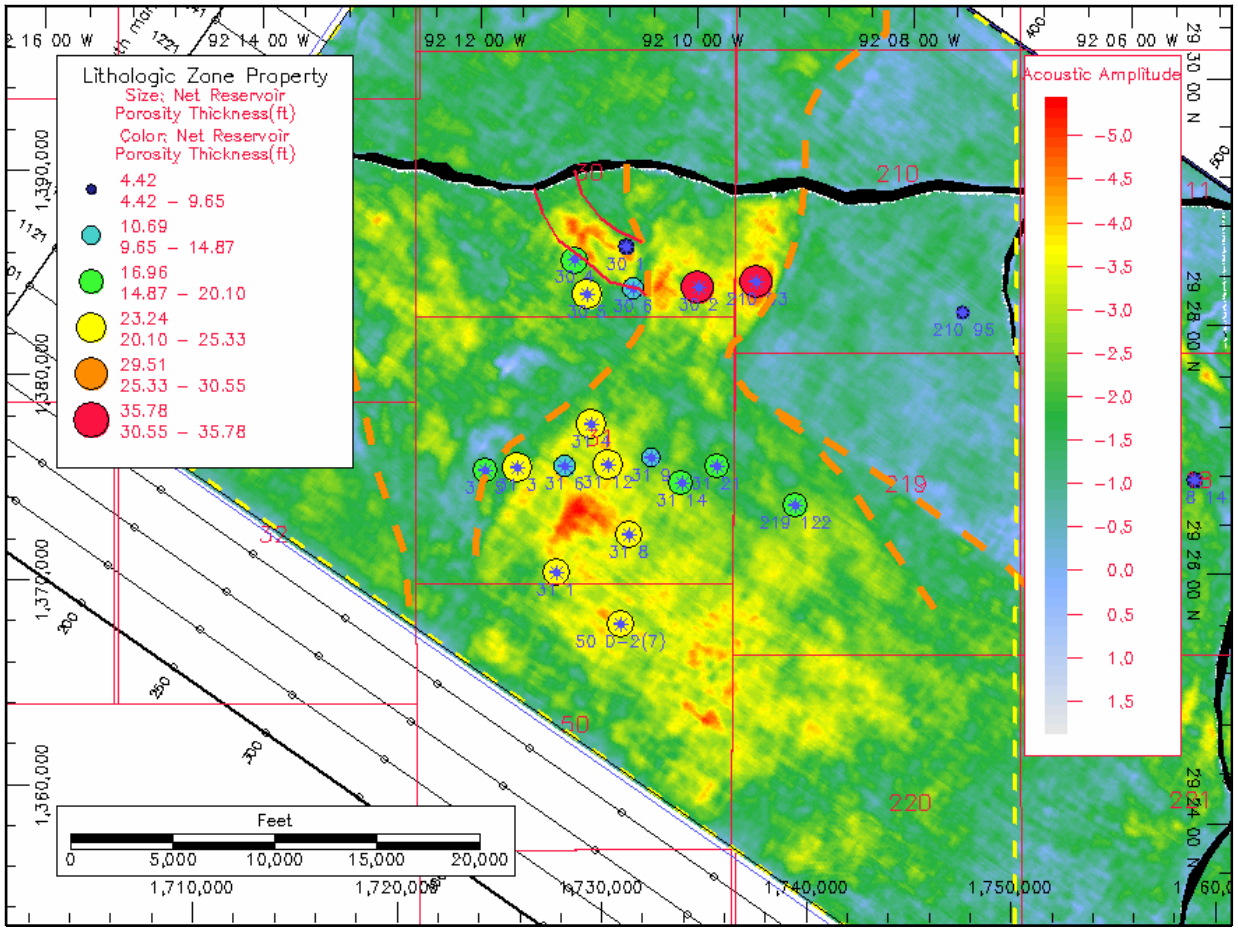

Figure 115. Amplitude map overlain by a bubble layout showing the spatial distribution $\phi_{eff}h$ estimates of the N-sand interval.

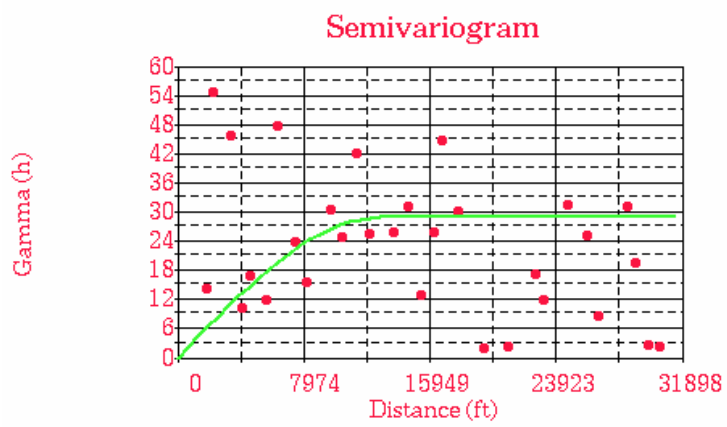

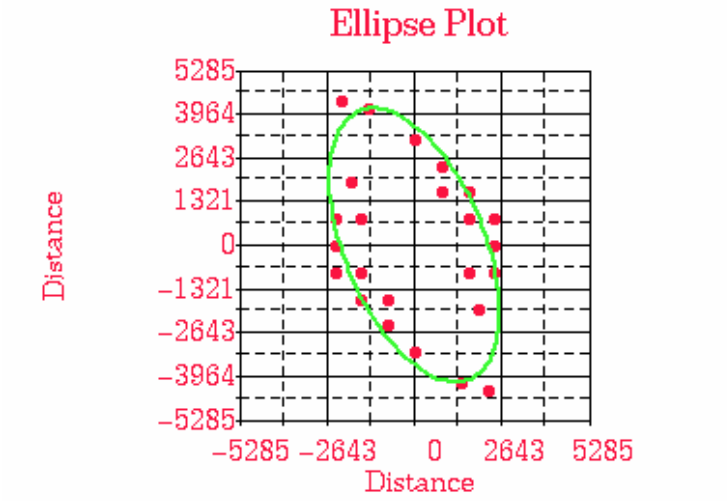

Lag Interval (h)	805ft	**Sill**	28.90
Max. Lag	30,000ft	**Nugget**	0
Model	Spherical	**Anisotropy Angle**	158°
Range	12823.92ft	**Anisotropy ratio**	0.5

Figure 116. Spatial analysis parameters of net reservoir ϕ_{eff}h of Vermilion 50 wells.

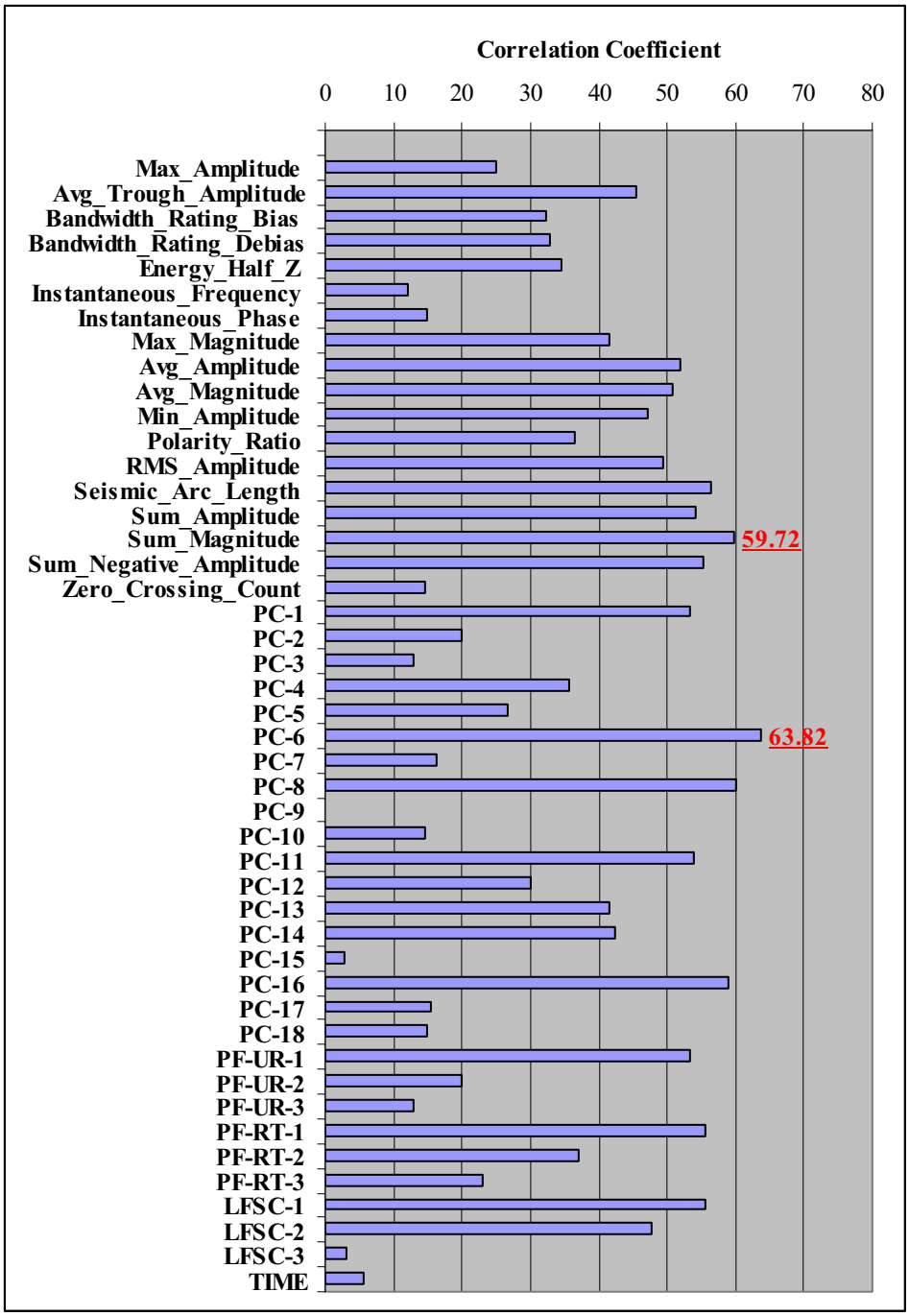

Figure 117. Correlation coefficient plot of the absolute correlation coefficients |r| between $\phi_{eff}h$ and the various seismic attributes for the wells located within the incised valley (n=17). $\phi_{eff}h$ showed a good correlation with the sum of magnitude (r=0.60) and the PC-6 (r=0.64). Original seismic attributes are normalized by subtracting the mean and division by the standard deviation value.

Among the original seismic attributes, the best correlation to $\phi_{eff}h$ was achieved with the sum of magnitude attribute (r=0.64) (Figures 117 and 118). It was expected that the sum of magnitude will show good correlation with $\phi_{eff}h$ since a similar association was seen earlier with net thickness property (Figure 79). Similarly, it is also anticipated that due the sensitivity of this attribute to the gas effect located within the lower reaches of the incised valley will overestimate the final results of $\phi_{eff}h$ mapping.

PC-6 showed the highest correlation coefficient value among the whole set of attributes (r=0.63) (Figures 117 and 119). It is a weighted linear combination of the maximum amplitude and the number of zero crossing seismic attributes (Figure 120 and Table 6).

The maximum amplitude represents the maximum value of peak or trough within a window. It is considered as a direct indicator for variation related in lithology and hydrocarbons (Chen and Sidney, 1997). On the other hand, the number of zero crossing is the average of zero crossings made by a seismic trace within a window of investigation (Table 3). A higher number of zero crossings indicate a higher frequency succession of sediment.

The inverse signs between the loadings of the maximum amplitude and the number of zero crossings indicate that these attributes it screening for the highest amplitude value located within a zone of minimum amount of vertical lithology variability or sand-shale cyclicity. This zone will be characterized by high net reservoir thickness and constant porosity. Accordingly, it is hoped that the use of PC-6 will enhance the final mapping results of $\phi_{eff}h$.

The maximum amplitude map shows anomalies of gas saturated sediments at localized positive relieves. PC-6 spatial map have an advantage over the maximum amplitude map by paying less attention to these anomalies located within the lower reaches of the incised valley (Figure 118).

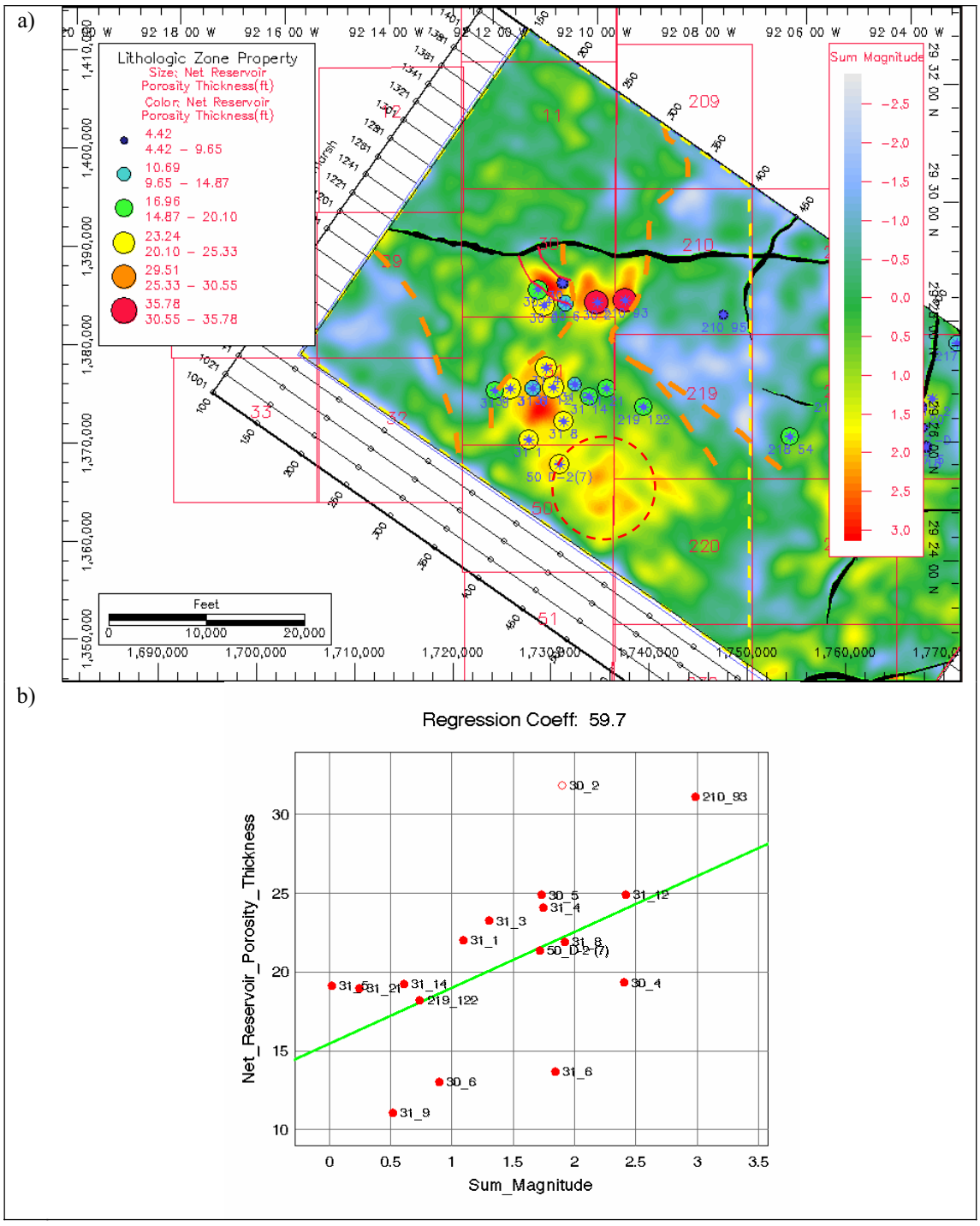

Figure 118. Standardized sum of magnitude seismic attribute map (a) showed the best correlation with net reservoir porosity thickness product (b). The dashed red defines gas related anomalies which is not seen in Figure 108.

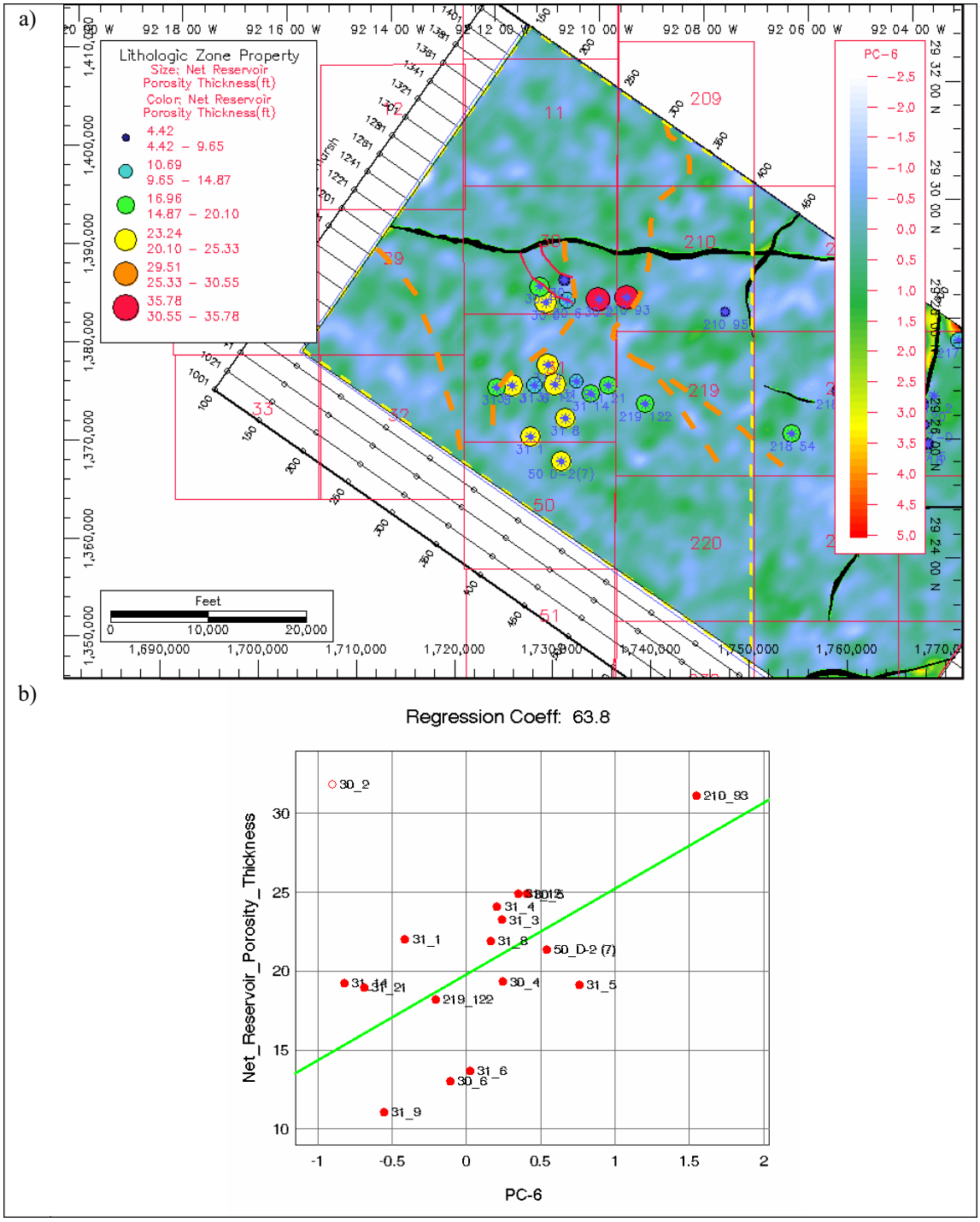

Figure 119. Multivariate seismic attribute PC-6 (a). Well 30-2 showed an outlier behavior in (b) and in Figure 118. Accordingly, it was left out of the study.

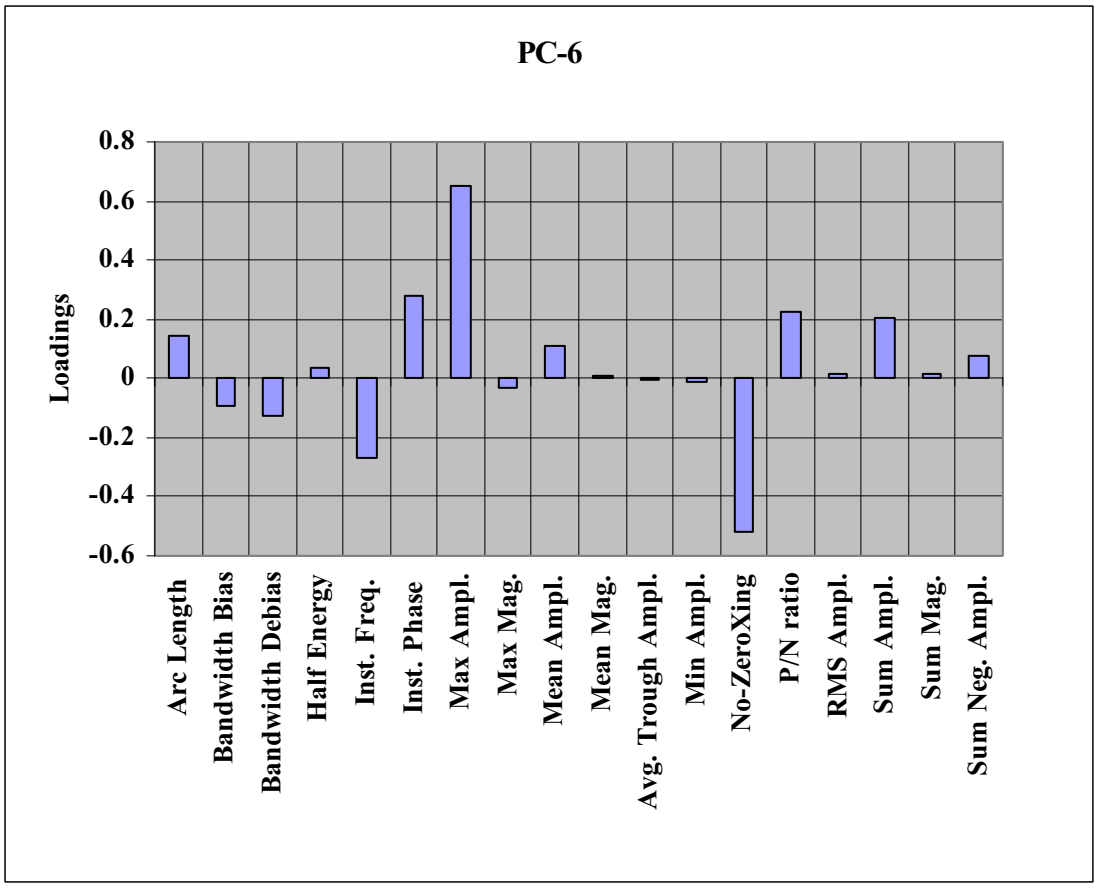

Figure 120. Bar chart illustrates the relative contribution of each seismic attributes to PC-6. It is obvious that maximum amplitude and no of zero crossings are the major contributors to PC-6.

The results of collocated cokriging estimates of ϕ_{eff} h using sum of magnitudes and PC-6 are presented in Figure 121. An enlargement of these maps is shown in Figures 122 and 123, respectively. These results indicate that the spatial estimates of ϕ_{eff} h of the multivariate seismic attribute PC-6 were more geologically acceptable. It is anticipated that the zone representing the highest reservoir pore footage will be localized within distributary channel systems of the deltaic sediments. These channels should cross the delta plain into the basin direction. The results of maximum magnitude showed very smooth spatial patterns for the distribution of ϕ_{eff} h (Figure 122), whereas, PC-6's spatial distribution of ϕ_{eff} h maintained the expected heterogeneity or roughness indicating a stronger control of geology over these estimates (Figure 123).

Well 30-2 showed an outlying behavior with maximum magnitude and PC-6 and it was left out during the course of the analyses. This behavior can be attributed to possible errors within the computed value of ϕ_{eff} h or the corresponding seismic attribute reading around the borehole. Figure 124 indicates that both approaches were able to predict accurate estimate of ϕ_{eff} h at well 30-2. As for the region located outside the incised valley both methods overestimated the results due to the lack of enough well control. The results of both approaches showed overestimated results of well 210-95 due to the lack of enough well control.

It can be concluded that multivariate seismic attributes are able to provide accurate estimates of reservoir proprieties at the limits of a reservoir level. The spatial estimates of ϕ_{eff} h based on the multivariate seismic attribute of PC-6 are more rigorous and geologically acceptable than the regular case involving the use of the single original seismic attribute of sum of magnitude (Figures 122 and 123).

Figure 123 shows that the results of the net reservoir porosity thickness product correlate well with previous drilling activities within the study area. The region located to the central part of the lowstand delta, highlighted by blue doted border, defines a proposed trend for future drilling projects.

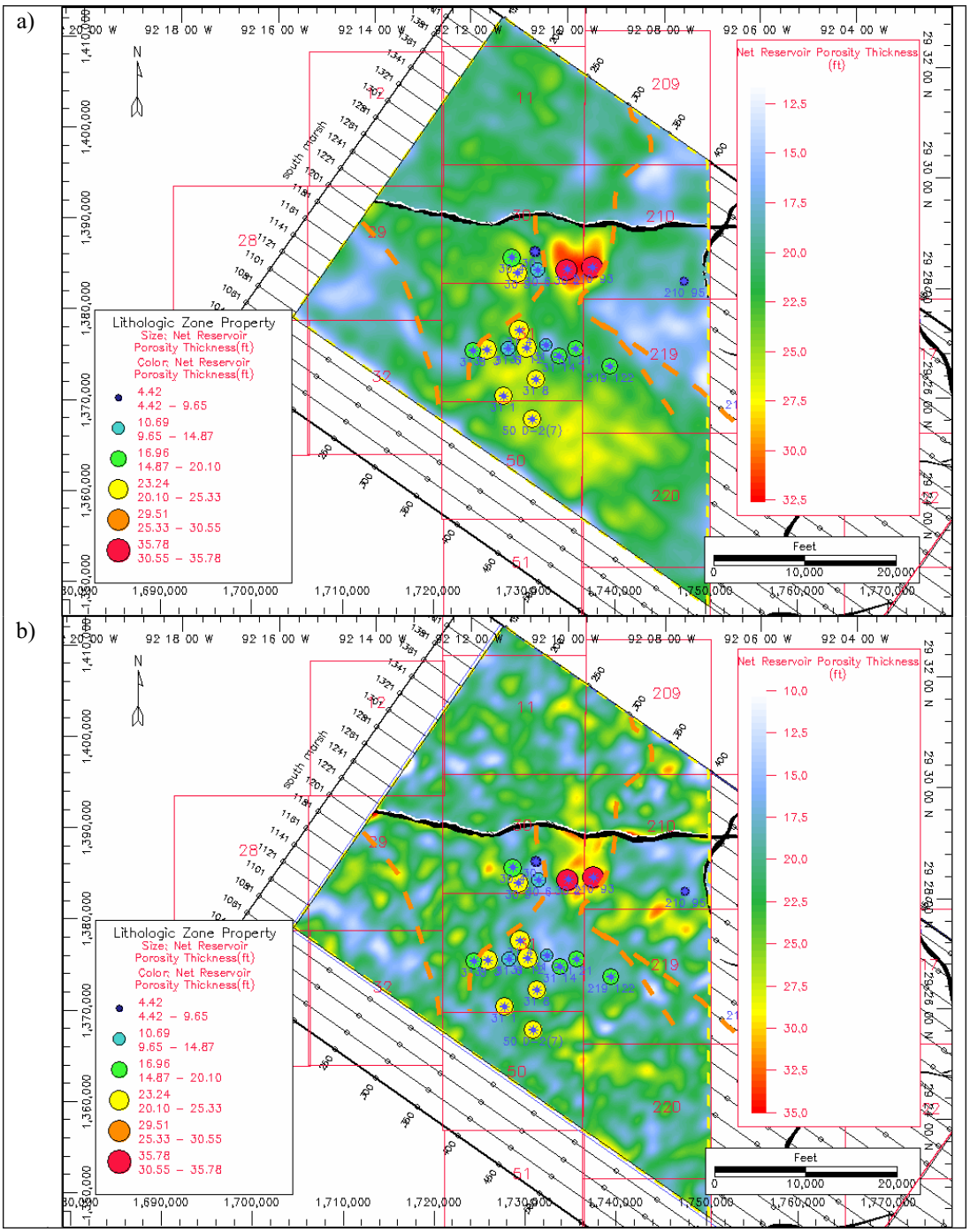

Figure 121. Comparison between $\phi_{eff}h$ estimates which was produced by using sum of magnitude (a) and by using P-6 (b). A blow up of these presentations is shown in Figures 122 and 123, respectively. Note that $\phi_{eff}h$ estimates of the sum of magnitude are very smooth compared to PC-6 results.

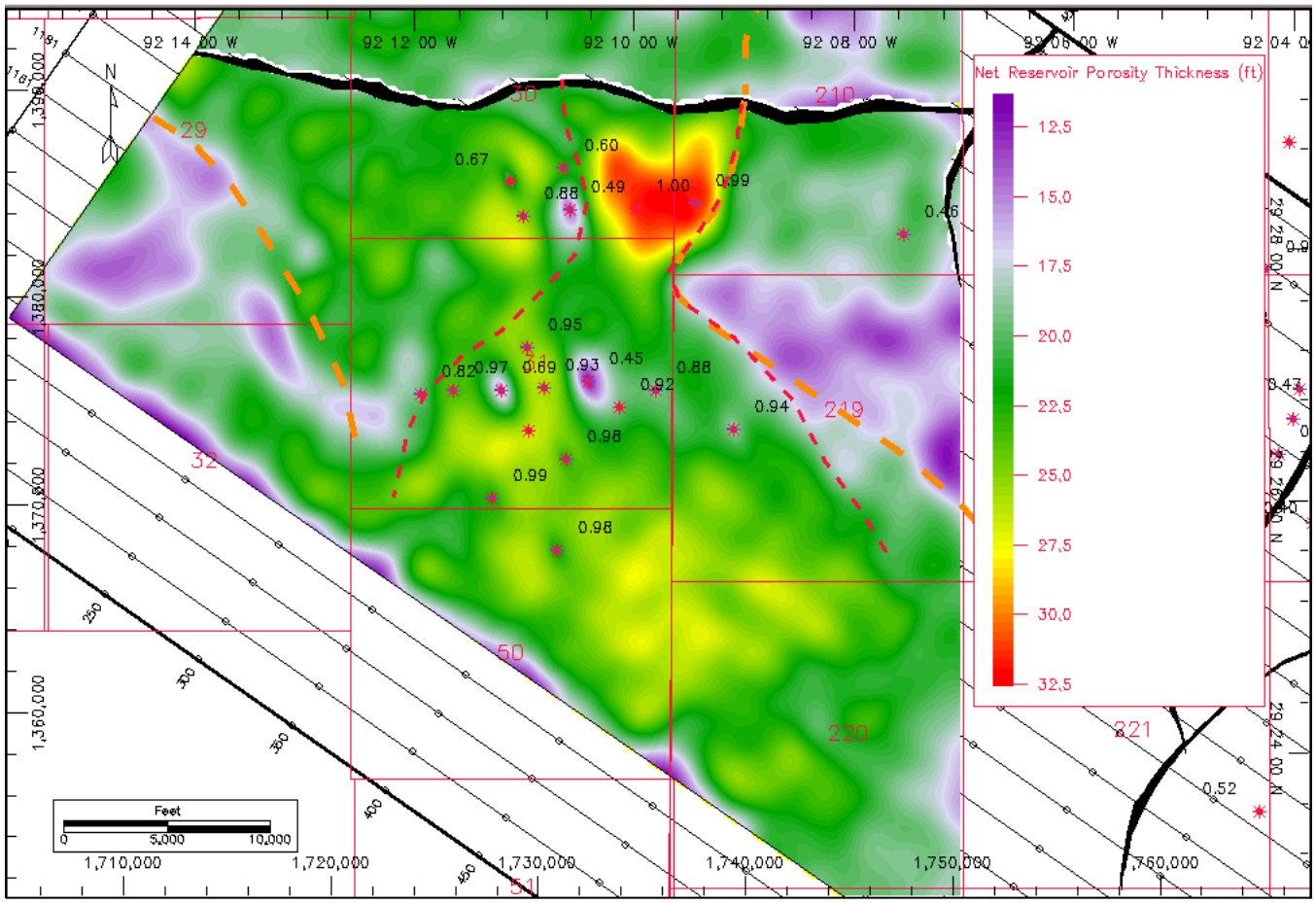

Figure 122. Net reservoir porosity thickness product estimate of the N-sand interval produced by sum of magnitude seismic attribute as a secondary data. The estimates are very smooth and do not reflect the geological identity of the incised valley system.

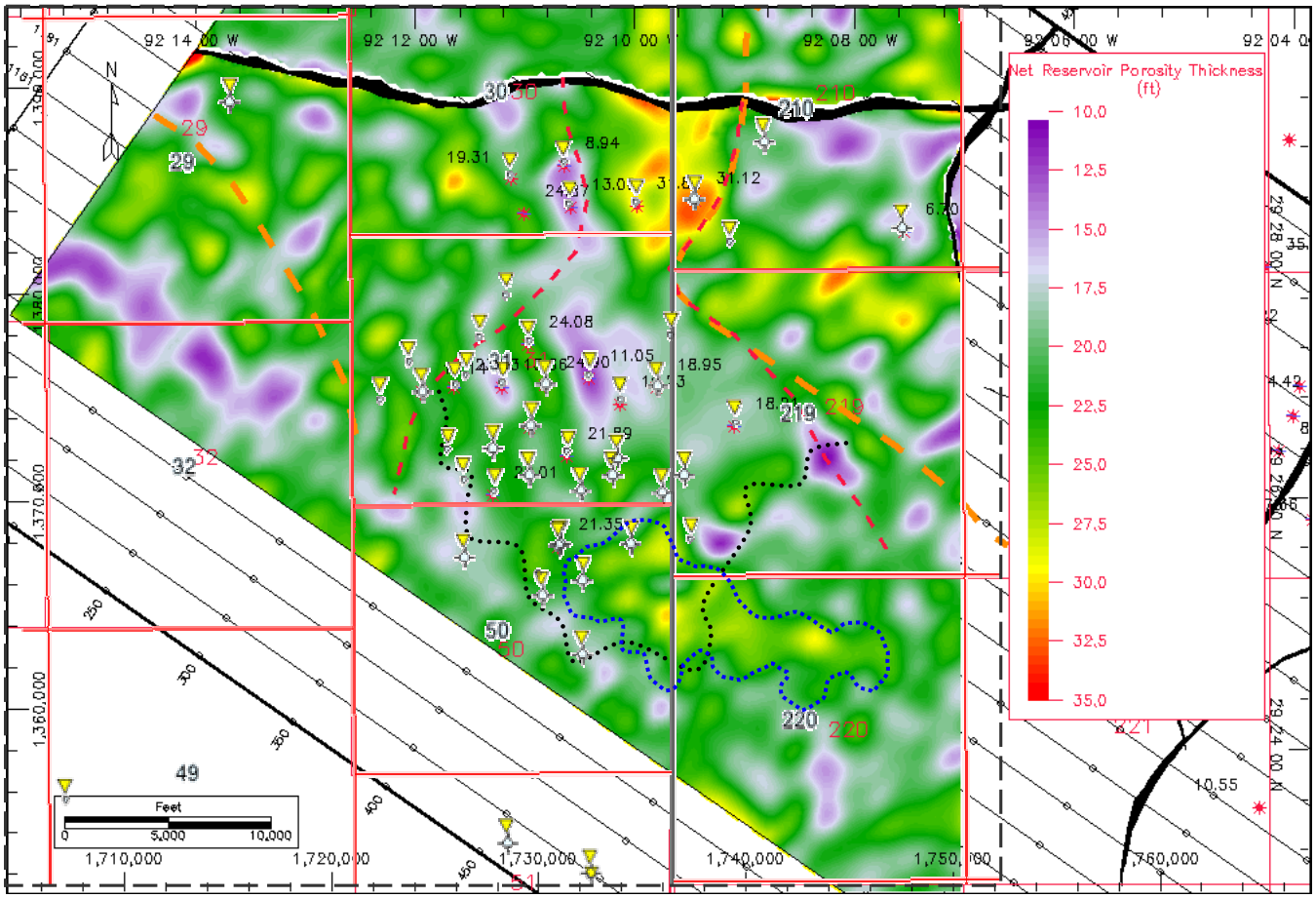

Figure 123. Net reservoir porosity thickness product estimate of the N-sand interval produced PC-6. The estimates of PC-6 maintained the lateral heterogeneity and roughness expected within the incised valley. The blue doted region represents new drilling potential location. The black dashed line highlights a possible boundary defining the edge of delta front deposits of the incised valley fill (Figure 86).

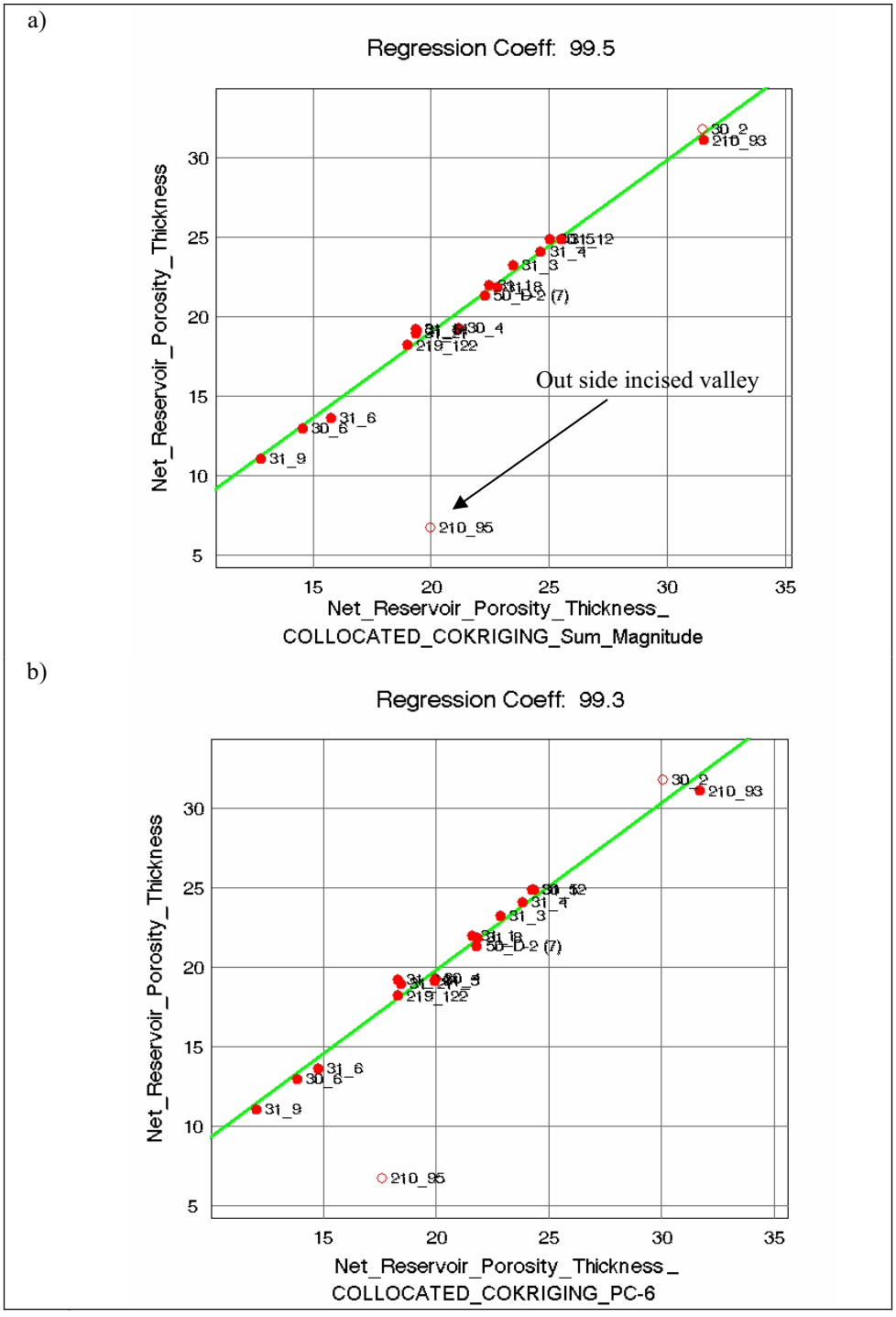

Figure 124. Correlation between measured values of ϕ_{eff} h and collocated cokriging estimates of ϕ_{eff} h produced by sum of magnitude attribute (a) and PC-6 (b). Both approaches gave similar results for the wells located within the incised valley. As for the region located out side the valley, the sum of magnitude approach highly overestimates the ϕ_{eff} h of well 210-95. Note also that both approaches gave accurate estimates for net thicknesses at the wells 30-2 which was left out of the study.

CHAPTER V

CONCLUSIONS

In this study, an integrated geology and geophysics study has been established to investigate the use of multivariate seismic attributes, against original seismic attributes, in predicting five reservoir properties including: gross thickness, net thickness, average gross effective porosity, N/G ratio and net reservoir porosity thickness product. The following conclusions are drawn from the study:

- Initial results of PCA and PFA indicated that multivariate seismic attributes can predict reservoir properties.
- The predictivity of multivariate seismic attributes depends on the variability between the original seismic attributes. In this study, the number of amplitude-based attributes (n=9) was relatively higher than other attributes which were reduced into a major principal component (i.e. PC-1). The use first PC/PF will show a smoothed spatial pattern of reservoir property map. Therefore, limiting the number of similar attributes can produce more distinct attributes and honor spatial variability.
- High order multivariate seismic PC's proved to contain valuable information that can be used to predict dependent reservoir properties. The degree of correlation between these attributes and the mapped properties defines the validity of their results. The higher and the meaningful the loadings of each PC's or PF's the stronger the ability of these components/factors to pinpoint certain reservoir properties associations.
- The use of a multivariate seismic attribute as a secondary variable in an integrated reservoir study depends on the degree of correlation between this attribute and the primary reservoir property as well as on the ability to give meaningful interpretation for its loadings.

- The cross-linked interpretation of multivariate attributes of related reservoir properties such as gross and net thicknesses supports the feasibility of the attributes to be used as a guide to map these properties and minimizes the risk of ambiguous relationships. For example, PC-17 and PC-14 were used as secondary seismic attributes to map the properties of gross thickness and net thicknesses, respectively. The interdependency of these PC's caused the correlation between PC-17 and net thickness to be very minimal while it was highly correlated to gross thickness property and vice versa.
- Multivariate seismic attributes are less sensitive to spurious anomalies produced due to the various interactions of reservoir properties.
- The collocated cokriging estimates of reservoir properties using multivariate seismic attributes provide more geological control on the estimates. These attributes are able to maintain the lateral geological heterogeneities imbedded within seismic data and strongly maintain the proposed geological model. On the other hand, original seismic attributes showed smoothed estimates due to the fact that these attributes are a product of many physical properties such as porosity, saturation, cyclicity etc (Brown, 1999).
- Finally, results suggest that multivariate seismic attribute technique can be used to predict various reservoir properties and can be applied to wide variety of geological and geophysical settings.

REFERENCES CITED

Alberty, M., 1992, Standard interpretation: Part 4, wireline methods, *in* D. Morton-Thompson, and A. M. Woods, eds., Development Geology Reference Manual: AAPG, Methods in Exploration Series 10, Tulsa, Oklahoma, p. 180 - 185.

Aly, A.M., Hunt, E.R., Pursell, D.A., and McCain, W.D., Jr., 1997, Application of multi-well normalization of open hole logs in integrated reservoir studies: 67th Western Regional Annual Meeting of the Society of Petroleum Engineers, Long Beach, California, 25-27 June 1997, SPE paper 38263, 7 p.

Anderson, N. L., and S. Cardimona, 2000, Forward modeling of reflection seismic and ground penetrating radar signals to aid in field survey design and data interpretation: Federal Highway Administration and Missouri Department of Transportation special publication, <http://www.utc.umr.edu/Publications/Proceedings/2000/modelingf.pdf> (Accessed February 15, 2004).

Archie, G. E., 1942, The electrical reseistivity log as an aid in determining some reservoir characteristics: Transactions of the American Institute of Mining Metallurgical and Petroleum Engineers, v. 146, p. 54 - 67.

Asquith, G.B., 1990, Log evaluation of shaly sandstones: A practical guide: AAPG, Continuing Education Course Note Series, no. 31, Tulsa, Oklahoma, 59 p.

Badescu, A. C., Reservoir characterization of the Miocene starfak and tiger shoal fields, Offshore Louisiana through integration of sequence stratigraphy, 3-D seismic, and well-log data, Ph.D. dissertation, University of Texas at Austin, Texas, 211 p.

Bahorich, M., and F. Steve, 1995, 3-D seismic discontinuity for faults and stratigraphic features: The Coherence Cube: The Leading Edge, v. 14, no. 10, p. 1053-1058.

Barnes, A. E., 1999, Seismic attributes past, present, and future: 69th Annual Meeting of the SEG Expanded Technical Program, Houston, Texas, 31 Octobar-5 November 1999, 4 p.

Barnes, A.E., 2001, Seismic attributes in your facies: CSEG Recorder, v. 26, no. 7, p. 41- 47.

Beard, J. H., J. B. Sangree, and L. A. Smith, 1982, Quaternary chronology, paleoclimate, depositional sequences, and eustatic cycles: AAPG Bulletin, v. 66, p. 158 -169.

Biot, M., 1956, Theory of propagation of elastic waves in a fluid saturated porous solid: I-low frequency range: Journal of the Acoustical Society of America, v. 28, p. 168-178.

Bouvier, J. D., C. H. Kaars-Sijpesteijn, D. F. Kluesner, C. C. Onyejekwe, and R. C. Van der Paal, 1989, Three-dimensional seismic interpretation and fault sealing investigations, Nun River Field, Nigeria: AAPG Bulletin, v. 73, no. 11, p. 1397 - 1414.

Bowen, D. W., P. Weimer, and A. J. Scott, 1993, The relative success of siliciclastic sequence stratigraphic concepts in exploration: Examples from incised valley fill and turbidite systems reservoirs, *in* P. Weimer and H. Posamentier, eds., Siliciclastic Sequence Stratigraphy: AAPG Memoir 58, p. 15 - 42.

Breard, S.Q., A.D. Callender, and M.J. Nault, 1993, Paleoecologic and biostratigraphic models for Pleistocene through Miocene foraminiferal assemblages of the Gulf Coast Basin: Gulf Coast Association of Geological Societies Transactions, v. 43, p. 493 - 502.

Brown, A., R., 1996, Seismic attributes and their classification: The Leading Edge, v. 15, no. 10, p. 1090 - 1091.

Brown, A., R., 2001, Understanding seismic attributes: Geophysics, v. 66, no. 1, p. 47-48.

Brown, A.R., 1999, Interpretation of Three-dimensional Seismic Data, 5th ed.: AAPG Memoir 42, p. 525.

Bryant, W. R., J. Y. Liu, and J. Ponthier, 1995, The engineering and geological constraints of intraslope basins and submarine canyons of the northwestern Gulf of Mexico: Gulf Coast Association of Geological Societies Transactions, v. 45, p. 95 - 101.

Castagna, J. P., 2001, Recent advances in seismic lithologic analysis: Geophysics, v. 66, no. 1, p. 42 - 46.

Chambers, R. L., and J. M. Yarus, 2002, Quantitative use of seismic attributes for reservoir characterization: CSEG Recorder, v. 27, no. 6, p. 14 – 25.

Chambers, R. L., J. M. Yarus, and K. B. Hird, 2000, Petroleum geostatistics for non-geostatisticians: Part 1: The Leading Edge, v. 19, no. 6, p. 592 - 599.

Chambers, R. L., Zinger M. L. and M. C. Kelly, 1994, Constraining geostatistical reservoir descriptions with 3-D seismic data to reduce uncertainty *in* J. M. Yarus and R. L. Chambers, eds., Stochastic Modeling and Geostatistics: AAPG Special Publication, p. 143 – 157.

Chawathé, A., A. Ouenes, and W. W. Weiss, 1997, Interwell property mapping using crosswell seismic attributes: Society of Petroleum Engineers Annual Technical Conference and Exhibition, San Antonio, Texas, 5-8 October 1997, SPE Paper 38747, 8 p.

Chen, Q., and S. Sidney, 1997, Seismic attribute technology for reservoir forecasting and monitoring: The Leading Edge, v. 16, no. 5, p. 445-456.

Clavier, C., G. Coates, and J. Dumanoir, 1977, The theoretical and experimental bases for the"Dual Water" model for the interpretation of shaly sands: Society of Petroleum Engineers Annual Conference and Exhibition, Denver, Colorado, 9-12 October 1997, SPE Paper 6859, 21 p.

Combellas-Bigott, R. I., and W. Galloway, 2002, Depositional history and genetic sequence stratigraphic framework of the Middle Miocene depositional episode South Louisiana (abs.): AAPG Annual Meeting, Houston, Texas, 10-13 March 2002, 1 p.

Crawford, T.G., B.J. Bascle, C.J. Kinler, and M.T. Prendergast, 2002, Estimated oil and gas reserves, Gulf of Mexico outer continental shelf, December 31, 1999: Mineral Management Services, U.S. Department of Interior, OCS Report MMS 2002-007, 28 p.

Deutsch, C.V., 2002, Geostatistical Reservoir Modeling: New York, Oxford University Press, 376 p.

Dewar, J., 2001, Rock physics for the rest of us, CSEG Recorder, v. 26, no. 5, p. 42 - 49.

Diegel, F. A., J. F. Karlo, D. C. Schuster, R. C. Shoup, and P. R. Tauvers, 1995, Cenozoic structural evolution and tectono-stratigraphic framework of the northern Gulf Coast continental margin, *in* M. P. A. Jackson, D. G. Roberts, and S. Snelson, eds., Salt Tectonics: A Global Perspective: AAPG Memoir 65, p. 109 - 151.

Doyen, P.M, den Boer, L.D., and W. R. Pillet, 1996, Seismic porosity mapping in the Ekofisk field using a new form of collocated kriging: Society of Petroleum Engineers Annual Technical Conference and Exhibition, Denver, Colorado, 6-9 October 1996, SPE Paper 36498, 9 p.

Dunteman, G. H., 1989, Principal Component Analysis: Thousand Oaks, California, Sage Publications Inc., 96 p.

Dutta, N. C., 2002, Geopressure prediction using seismic data: Current status and the road ahead: Geophysics, v. 67, no. 6, p. 2012 - 2041.

Dutton, S. P., and T. F. Hentz, 2002, Reservoir quality of lower Miocene sandstones in lowstand prograding wedge successions, Vermilion Block 31, offshore Louisiana: Gulf Coast Association of Geological Societies Transactions, v. 52, p. 217 - 228.

Fillon, R. H., and P. N. Lawless, 2000, Lower Miocene-Early Pliocene deposystems in the Gulf of Mexico: Regional sequence relationships: Gulf Coast Association of Geological Societies Transactions, v. L, p. 411 - 428.

Flores-Garnica1, J. G. and P. N. Omi, 2003, Mapping forest fuels for spatial fire behavior simulations using geomatic strategies: Agrociencia, v. 37, no. 1, p. 65 -72.

Galloway, W. E., P. E. Ganey-Curry, X. Li, and R. T. Buffler, 2000, Cenozoic depositional history of the Gulf of Mexico basin: AAPG Bulletin, v. 84, no. 11, p. 1743 – 1774.

Gassmann, F., 1951, Elastic waves through a packing of spheres: Geophysics, v. 16, no. 4, p. 673 -685.

Gastaldi, C., J. P. Biguenet, and L. De Pazzis, 1997, Reservoir characterization from seismic attributes: An example from the Peciko field (Indonesia): The Leading Edge, v. 16, no. 3, p. 263 - 266.

Goovaerts, P., 1997, Geostatistics for Natural Resources Evaluation: Oxford, Oxford University Press, 483 p.

Gregory, A. R., 1977, Aspects of rock mechanics from laboratory and log data that are important to seismic interpretation, *in* C. E. Payton, ed., Seismic Stratigraphy-applications to Hydrocarbon Exploration: AAPG Memoir 26, p. 15 - 46.

Hart, B., 1999, Geology plays key role in seismic attribute studies: Oil and Gas Journal, v. 12, p. 76 - 80.

Hart, B., and R. S. Balch, 2000, Approaches to defining reservoir physical properties from 3-D seismic attributes with limited well control: An example from the Jurassic Smackover Formation, Alabama, Geophysics, v. 65, no. 2, p. 368 - 376.

Hashmy, K., and M. Alberty, 1992, Difficult lithologies: *in* D. Morton-Thompson and A.M. Woods, eds., Development Geology Reference Manual: AAPG Methods in Exploration Memoir 10, p. 186 – 191.

Haskell, N. L., S. E. Nissen, M. Hughes, J. Grindhaug, S. Dhanani, R. Heath, J. Kantorowicz, L. Antrim, M. Cubanski, R. Nataraj, M. Schilly, and S. Wigger, 1999, Delineation of geologic drilling hazards using 3-D seismic attributes: The Leading Edge, v. 19, no. 3, p. 373 - 383.

Haskell, N. L., S. E. Nissen, J. A. Lopez, and M. S. Bahorich, 1995, 3-D seismic coherency and the imaging of sedimentological features: SEG Annual Meeting Expanded Technical Program Abstracts with Biographies, v. 65, p. 1532 - 1534.

Hentz, T. F., and H. L. Zeng, 2003, High-frequency Miocene sequence stratigraphy, offshore Louisiana: Cycle framework and influence on production distribution in a mature shelf province: AAPG Bulletin, v. 87, no. 2, p. 197 - 230.

Hilterman, F. J., 2001, Seismic Amplitude Interpretation: Society of Exploration Geophysicists, Tulsa, Oklahoma, 235 p.

Hirsche, K., S. Boerner, C. Kalkomey, and C. Gastaldi, 1998, Avoiding pitfalls in geostatistical reservoir characterization: A survival guide: The Leading Edge, v. 17, no. 4.

Hirsche, K., J. Porter-Hirsche, L. Mewhort, and R. Davis, 1997, The use and abuse of geostatistics: The Leading Edge, v. 16, no. 3, p. 253 - 260.

Hunt, E., 1997, Fundamentals of log analysis, Part 9, Determining water saturation: World Oil, v. 218, no. 9, p. 137 - 139.

Hunt, E., and D., Pursell, 1997, Fundamentals of log analysis, Part 8: Determining porosity from density, neutron and acoustic logs: World Oil, v. 218, no. 7, p. 173 -176.

Hunt, J. L. Jr., and G. Burgess, 1995, Depositional styles from Miocene through Pleistocene in the north-central Gulf of Mexico; an historical reconstruction: Transactions, Gulf Coast Association of Geological Societies, v. 45, p. 275-284.

Isaaks, E., and R. Srivastava, 1989, An Introduction to Applied Geostatistics: New York, Oxford University Press, 561 p.

Johnson, R. A., and D. W. Wichern, 1998, Applied Multivariate Statistical Analysis: Upper Saddle River, New Jersey, Prentice Hall, 816 p.

Jolliffe, I. T., 1986, Principal Component Analysis: New York, Springer, 271 p.

Kalkomey, C., 1997, Potential risks when using seismic attributes as predictors of reservoir properties: The Leading Edge, v. 16, no. 3, p. 247 - 251.

Kaufman, L., and P.J. Rousseeuw, 1990, Finding Groups in Data: An Introduction to Cluster Analysis: New York, New York, John Wiley & Sons, 342 p.

Kearney, T., 2001, Wavelet extraction -a black art?: GeoQuest Bulletin, 1st quarter, p. 2 -7.

Knapp, R. W., 1993, Energy distribution in wavelets and implications on resolving power: Geophysics, v. 58, no. 39, p. 39 - 46.

Kupfersberger, H., and C. V. Deutsch, 1999, Methodology for integrating analog geologic data in 3-D variogram modeling: AAPG Bulletin, v. 83, p. 1262 - 1278.

Lake, L. W., and H. B. Carroll, Jr., 1986, Preface, *in* L. W. Lake and H. B. Carroll, Jr., eds., Reservoir Characterization: Orlando, Florida, Academic Press, 659 p.

Latimer, R. B., R. Davison and P. Van Riel, An interpreter's guide to understanding and working with seismic-derived acoustic impedance data: The Leading Edge, v. 19, no. 3, p. 242 - 256.

Li, X. Y., Y. J. Liu, E., Liu, F. Shen, L. Qi, and Q. Shouli, 2003, Fracture detection using land 3D seismic data from the Yellow River Delta, China: The Leading Edge, v. 22, no., 7, p. 680 - 683.

Liner, C. L., 1999, Interpreting seismic data, *in* E. A. Beaumont and N. H. Foster, eds., Treatise of Petroleum Geology: Handbook of Petroleum Geology: Exploring for Oil and Gas Traps, American Association of Petroleum Geologists, Tulsa, Oklahoma, p. 1 - 30.

Lopez J. A., M. S. Bahorich, N. L. Haskell, and S. E. Nissen, 1996, 3-D seismic coherence mapping; a technological breakthrough (abs.): AAPG Annual Convention, San Diego, California, 19-22 May 1996, 1 p.

Lopez J. A., G. Partyka, N. L. Haskell, and S. E. Nissen, 1998, Identification of deltaic facies with 3-D seismic coherency and the spectral decomposition cube; a study from South Marsh Island area, Gulf of Mexico: Houston Geological Society Bulletin, v. 40, no. 5, p. 14 –15.

Lumley, D. E., 2001, Time-lapse seismic reservoir monitoring: Geophysics, v. 66, no. 1, p. 50 - 53.

Lynn, H. B., Simon, K. M. and Bates, C. R., 1996, Correlation between P-wave AVOA and S-wave traveltime anisotropy in a naturally fractured gas reservoir: The Leading Edge, v. 15,, no. 8, p. 931 - 936.

MacRae, G., and J. S. Watkins, 1993, Basin architecture, salt tectonics, and Upper Jurassic structural styles, DeSoto Canyon salt basin, northeastern Gulf of Mexico: AAPG Bulletin, v. 77, no. 10, p. 1809 -1824.

Marcoulides, G. A. and S. L. Hershberger, 1997, Multivariate Statistical Methods: Hillsdale, New Jersey, Lawrence Erlbaum Associates, Inc., 322 p.

Martin, R. G., 1978, Northern and eastern Gulf of Mexico continental margin: Stratigraphic and structural framework, *in* A. H. Bouma, G. T. Moore, and J. M. Coleman, eds., Framework, Facies, and Oil-trapping Characteristics of the Upper Continental Margin: Studies in Geology no. 7, AAPG, Tulsa, Oklahoma, p. 21- 42.

Morton, R. A., and L. A. Jirik, 1989, Origin depositional pattern, and reservoir characteristics of Middle Miocene shallow-marine sandstones, offshore South Louisiana, *in* R. A. Morton

and D. Nummedal, eds., Shelf Sedimentation, Shelf Sequences and Related Hydrocarbon Accumulation: Proceedings GCSSEPM Foundation 7th Annual Research Conference, New Orleans, Louisiana, p. 143 – 162.

Nehring, R., 1991, Oil and gas resources, *in* A. Salvador, ed., The Gulf of Mexico Basin: Geological Society of America, Decade of North American Geology, Boulder, Colorado Geological Society of America, p. 445 -494.

Nissen, S. E., N. L. Haskell, J. A. Lopez, T. J. Donlon, and M. S. Bahorich, 1996, 3-D seismic coherency techniques applied to the identification and delineation of slump features: American Association of Petroleum Geologists 1996 Annual Convention, American Association of Petroleum Geologists and Society of Economic Paleontologists and Mineralogists Annual Meeting Abstracts, v. 5, p. 106.

Paleo-Data Inc., 2003, Neogene Biostratigraphic Chart - Gulf of Mexico, <www.paleodata.com> (Accessed January, 2004.)

Posamentier, H. W., 2001, Lowstand alluvial bypass systems: Incised vs. unincised: AAPG Bulletin, v. 85, p. 1771 - 1793.

Ray, P. K., and J. R. Pearcy, 1988, An overview of the northern Gulf of Mexico: Geology, production trends, historical development and future potential, *in* J. R. J. Studlick, J. G. Bryant, J. A. Hartman, and R. D. Shew, eds.: New Orleans Geological Society, Offshore Louisiana Oil & Gas Fields, New Orleans, Louisiana, p. 7 - 36.

Reyment, R. A., and E. Savazzi, 1999, Aspects of Multivariate Statistical Analysis in Geology: Amsterdam, Elsevier, 285 p.

Russell, B., D. Hampson, J. Schuelke, and J. Quirein, 1997, Multiattribute seismic analysis: The Leading Edge, v. 16, no. 10, p. 1439 - 1443.

Saggaf, M. M., Toksöz, M. N., and Mustafa, H. M., 2003, Estimation of reservoir properties from seismic data by smooth neural networks: Geophysics, v. 68, no. 6, p. 1969 – 1983.

Scheevel, J. R., and Payrazyan, K., 1999, Principal component analysis applied to 3D seismic data for reservoir property estimation: 1999 SPE Annual Technical Conference and Exhibition, Houston, Texas, SPE Paper 56734, 14 p.

Schlumberger Wireline and Testing, 1999, Log Interpretation Principles/Applications: Sugar Land, Texas, Schlumberger Educational Services, 198 p.

Schultz, P. S., S. Ronen, M. Hattori, and C. Corbertt, 1994, Seismic-guided estimation of reservoir properties: SPE 69th Annual Technical Conference and Exhibition, New Orleans, Louisiana, September 25-28, 1994, SPE Paper 28386, 7 p.

Seni, S. J., 1997, Introduction, *in* S. J. Seni, T. F. Hentz, W. R. Kaiser, and E. G. Wermund Jr., eds., Atlas of Northern Gulf of Mexico Gas and Oil Reservoirs: Volume 1. Miocene and Older Reservoirs: University of Texas at Austin, Bureau of Economic Geology, p. 1 - 6.

Seni, S. J., and D. J. Bebout, 1997, Introduction to the upper Miocene plays, *in* S. J. Seni, T. F. Hentz, W. R. Kaiser, and E. G. Wermund Jr., eds., Atlas of northern Gulf of Mexico Gas and Oil Reservoirs: Volume 1. Miocene and Older Reservoirs: University of Texas at Austin, Bureau of Economic Geology, p. 159 - 164.

Shelby, W. S., 1988, Tiger Shoal Field offshore Louisiana, *in* J. R. J. Studlick, J. G. Bryant, J. A. Hartman, and R. D. Shew, eds., New Orleans Geological Society Offshore Oil & Gas Fields: v. II, New Orleans, Louisiana, p. 173 - 177.

Sheriff, R.E., 1991, Encyclopedic Dictionary of Exploration Geophysics, 3rd ed.: SEG Geophysical References Series 1, Tulsa, Oklahoma, p. 384.

Smith, R.L. and McGarrity, J.P., 2001, Cracking the fractures from seismic anisotropy in an offshore reservoir: The Leading Edge, v. 20, no. 1, p. 19 - 26.

Sukmono, S., 2001, Seismic Attributes for Reservoir Characterization: Jakarta, Indonesia, Network of Excellence in Training (NExT), 94 p.

Taner, M. T., 2001, Seismic attributes: CSEG Recorder, v. 26, no. 9, p. 48 - 56.

Van Bemmel, and R. Pepper, 2000, Seismic Signal Processing Method and Apparatus for Generating a Cube of Variance Values, Patent Number US06151555, 24 p.

Van Heijst M. W. I. M., G. Postma, W. P. Van Kesteren, and R. G. De Jongh, 2002, Control of syndepositional faulting on systems tract evolution across growth-faulted shelf margins: An analog experimental model of the Miocene Imo River field, Nigeria: AAPG Bulletin, , v. 86, no. 8, p. 1335 - 1366.

Van Wagoner, J. C., R. M. Mitchum, K. M. Campion, and V. D. Rahmanian, 1990, Siliciclastic Sequence Stratigraphy in Well Logs, Cores, and Outcrops: AAPG Methods in Exploration Series, v. 7, AAPG, Tulsa, Oklahoma, p. 155.

Wackernagel, H., 2003, Multivariate Geostatistics: Berlin, Springer Verlag, 387 p.

Wang, Z., 1997, Feasibility of time-lapse seismic reservoir monitoring: The physical basis: The Leading Edge, v. 16, no. 9, p. 1327 - 1329.

Wang, Z., 2001, Fundamentals of seismic rock physics: Geophysics, v. 66, no. 2, p. 398 -412.

Watkins, J. S., W. R. Bryant, and R. T. Buffler, 1996, Structural framework map of the northern Gulf of Mexico, *in* J. O. Jones and R. L. Freed, eds., Structural Framework of the Northern Gulf of Mexico: Austin, Texas, Gulf Coast Association of Geological Societies, p. 95 - 98.

Waxman, M. H., and L. J. M., Smits, 1968, Electrical conductivities of oil-bearing shaly sands, SPE Paper 1863-A, Soc. Pet. Eng. J., v8, no.2, p.107 - 122.

Winker, C. D., 1982, Cenozoic shelf margins, northwestern Gulf of Mexico: Gulf Coast Association of Geological Societies Transactions, v. 32, p. 427 - 448.

Woodbury, H. O., I. B. Murray, Jr., P. J. Pickford, and W. H. Akers, 1973, Pliocene and Pleistocene depocenters, outer continental shelf, Louisiana and Texas: AAPG Bulletin, v. 57, no. 12. p. 2428 - 2439.

Worrall, D. M., and S. Snelson, 1989, Evaluation of the northern Gulf of Mexico, with emphasis on Cenozoic growth faulting and the role of salt, *in* A. W. Bally, and A. R. Palmer, eds., The Geology of North America—An Overview, The Geology of North America, Boulder, Colorado Geological Society of America, p. 97 - 137.

Xinxia W. and W. E. Galloway, 2002, Upper Miocene depositional history of central Gulf of Mexico Basin (abs.): AAPG Bulletin, v. 86, no.13. 1 p.

Xu, W., T. Tran, R. M. Srivastava, and A. G. Journel, 1992, Integrating seismic data in reservoir modeling: The collocated cokriging alternative: Proceedings of Society of Petroleum Engineers 67th Annual Technical Conference and Exhibition, Washington, DC, 4-7 October 1992. p. 833 - 842.

Yang G. Y, C. and R. R. Stewart, 1997, Linking petrophysical parameters (ρ, σ, μ, λ, κ, φ) with seismic parameters (α, β, R_{PP}, R_{PS}, R_{SS}): CREWES Research Report, v. 9, p. 1 - 7.

Yang, S. Y., J. S. Watkins, M-J. Jiang, X. DU and B. E. Bradshaw, 1992, Miocene systems tracts of east and west Cameron ocs areas, offshore western Louisiana, Gulf Of Mexico: AAPG Bulletin, v. 76, no. 9, p. 1471 – 1472.

Zeng, H. L., T. F. Hentz, and L. J. Wood, 2001, Stratal slicing of Miocene-Pliocene sediments in Vermilion Block 50-Tiger Shoal area, offshore Louisiana: Leading Edge, v. 20, no. 4, p. 408 - 418.

APPENDIX

ORIGINAL SEISMIC ATTRIBUTE MAPS OF THE N-SAND INTERVAL

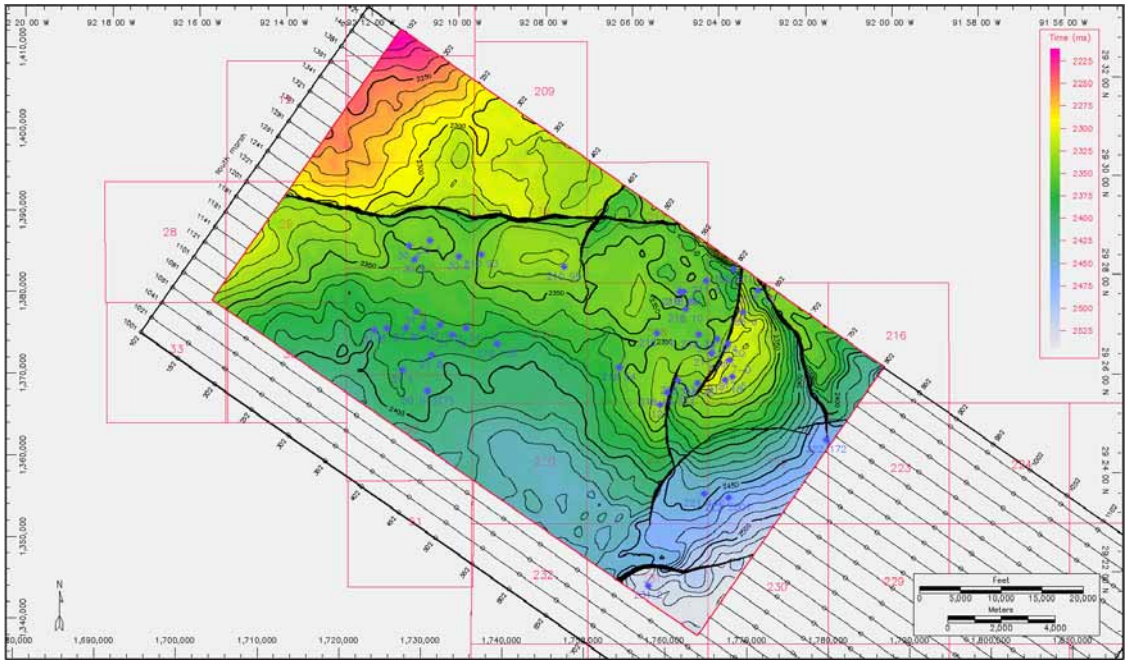

Figure 125.Time structure map of the N-sand interval. Contour interval equals to 10msec.

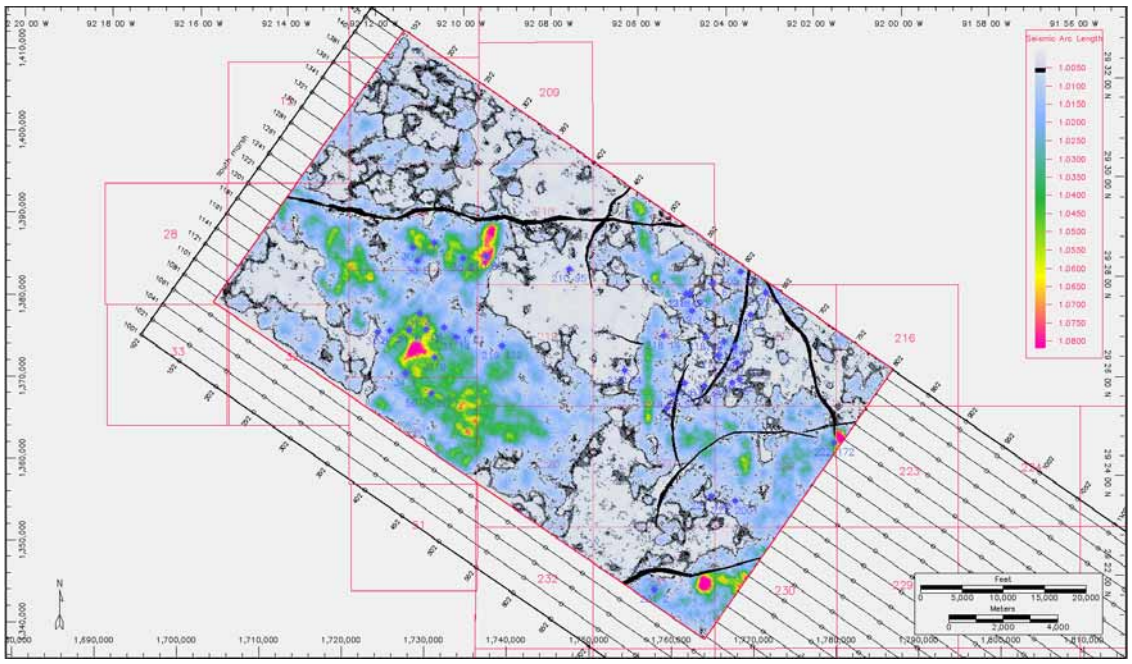

Figure 126. Seismic arc length attribute map of the N-sand interval. Note that in order to expose spatial variability which is a product of geological and petrophysical factors, the color spectrum is highlighted with black color. The same procedure was used in subsequent seismic attributes.

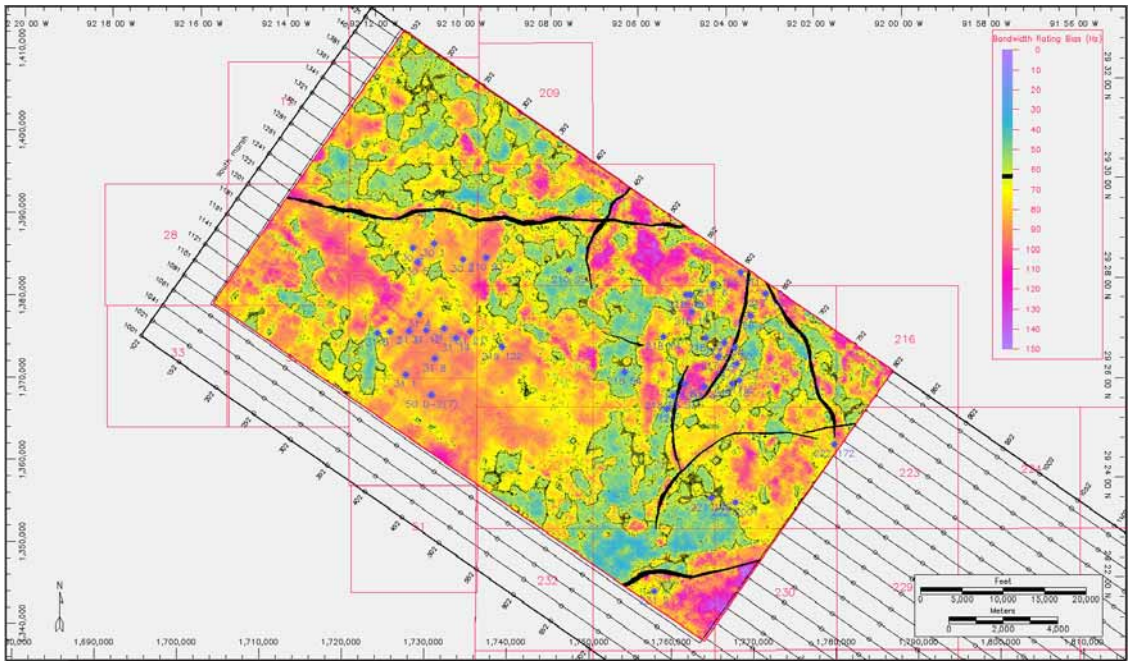

Figure 127. Seismic bandwidth rating with (bias) attribute map of the N-sand interval.

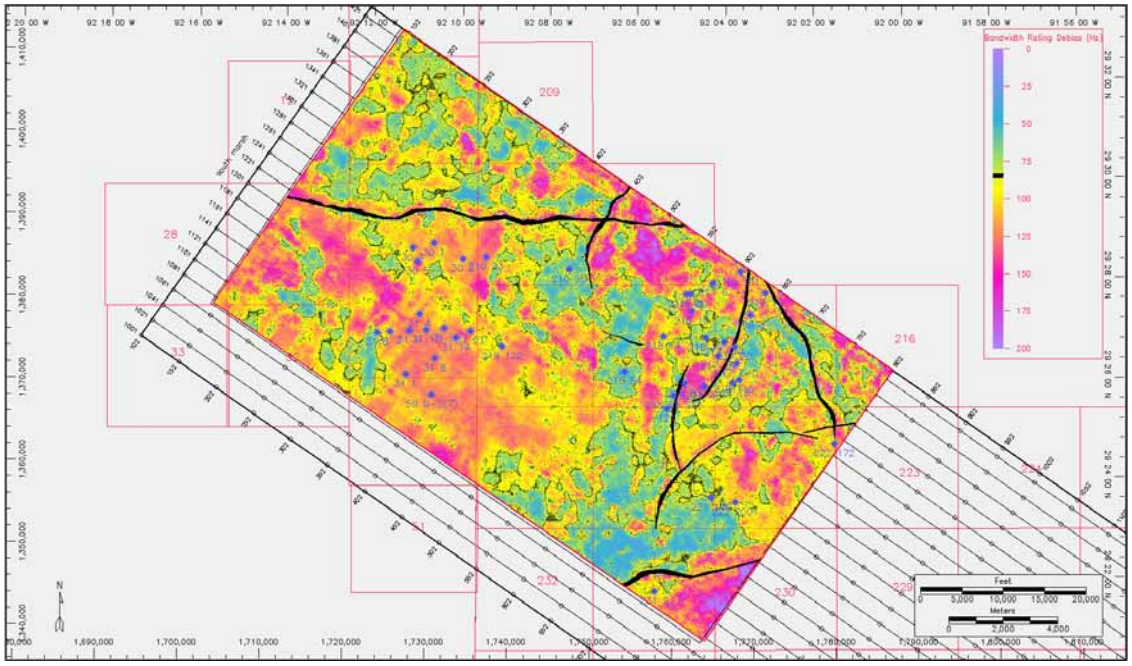

Figure 128. Seismic bandwidth rating with (debias) attribute map of the N-sand interval.

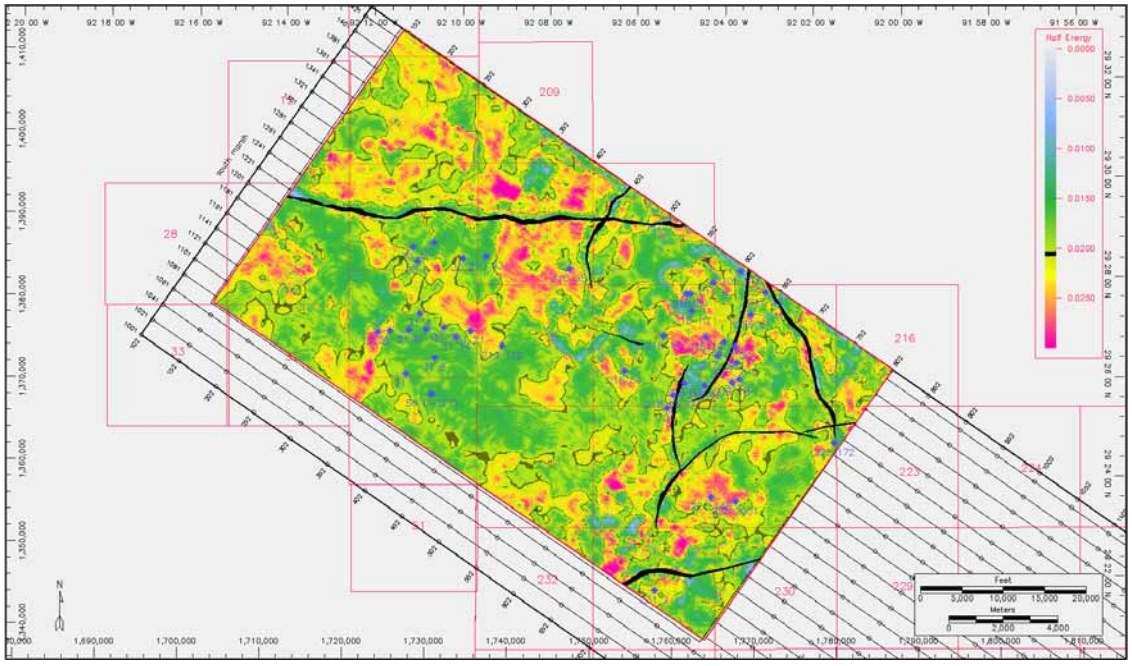

Figure 129. Seismic half energy attribute map of the N-sand interval.

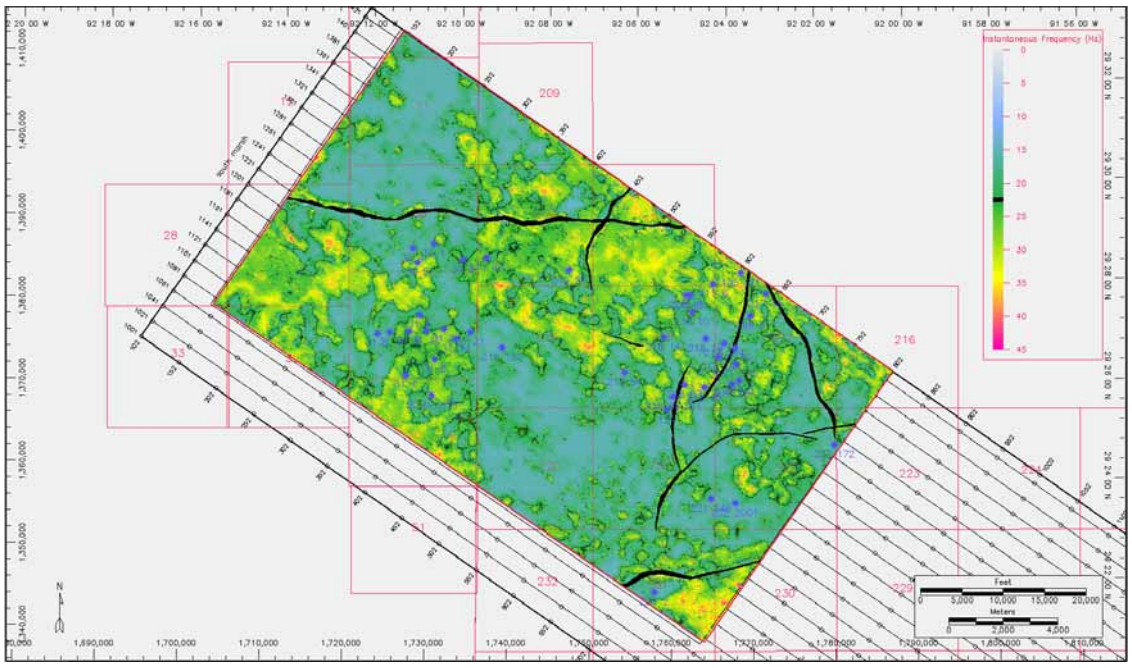

Figure 130. Average seismic instantaneous frequency attribute map of the N-sand interval.

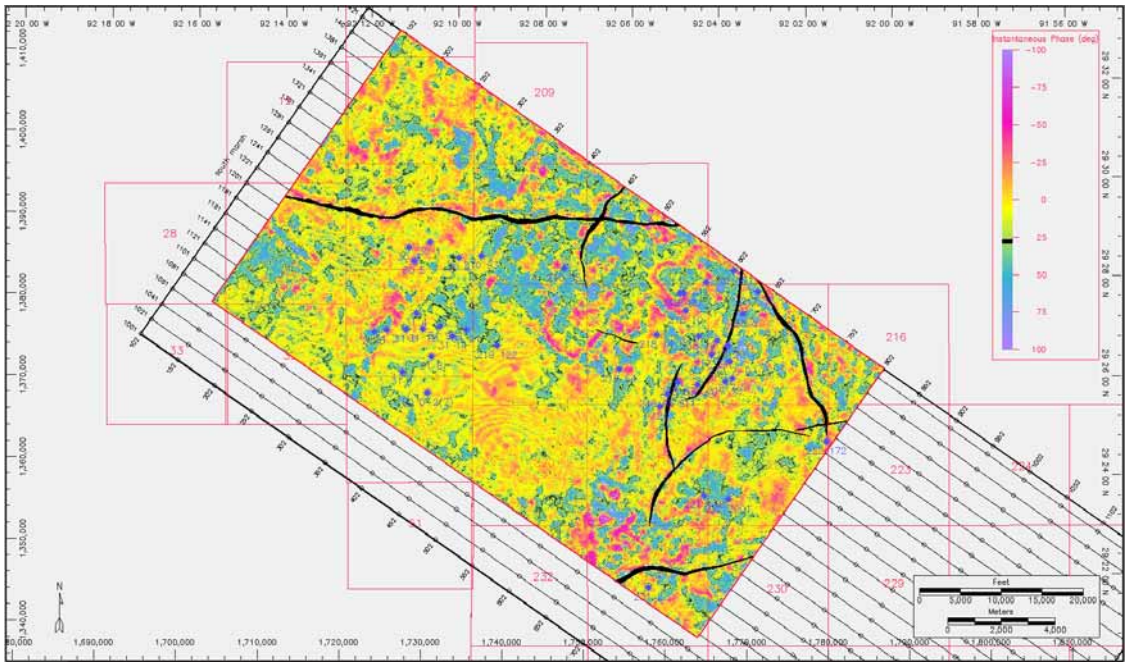

Figure 131. Average seismic instantaneous phase attribute map of the N-sand interval.

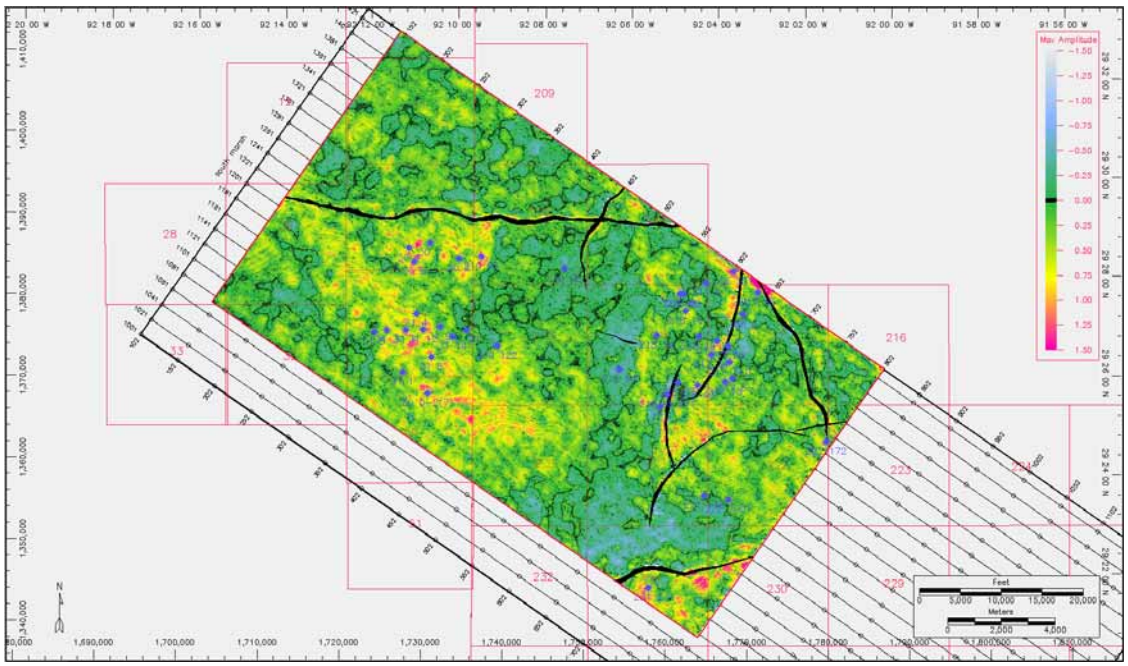

Figure 132. Maximum amplitude attribute map of the N-sand interval.

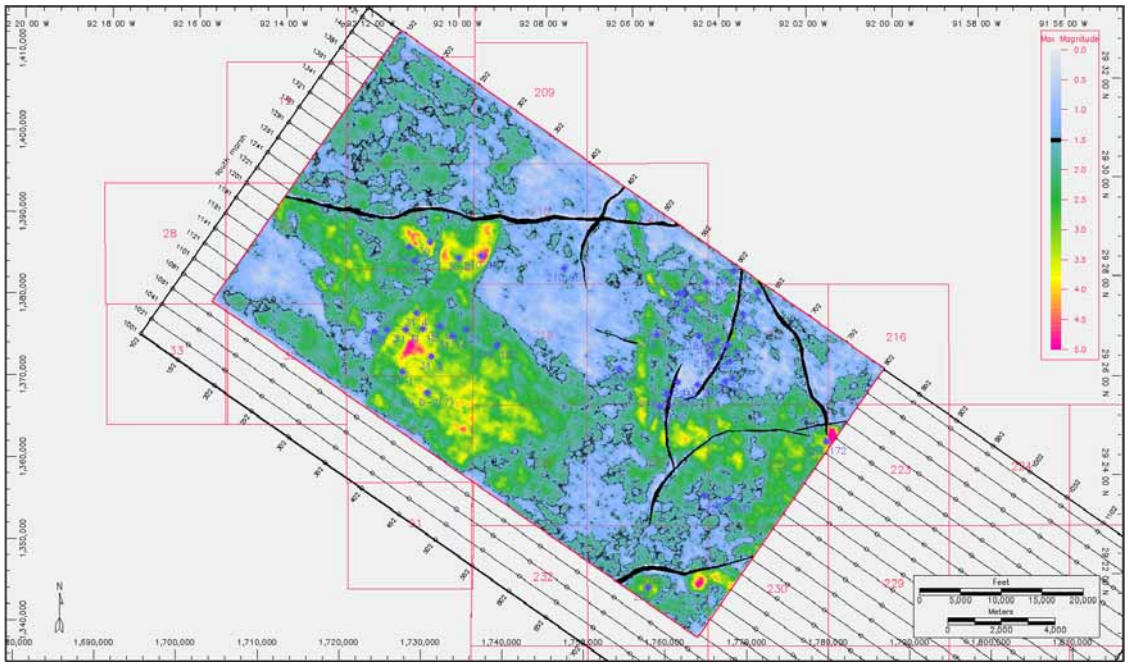

Figure 133. Maximum magnitude attribute map of the N-sand interval.

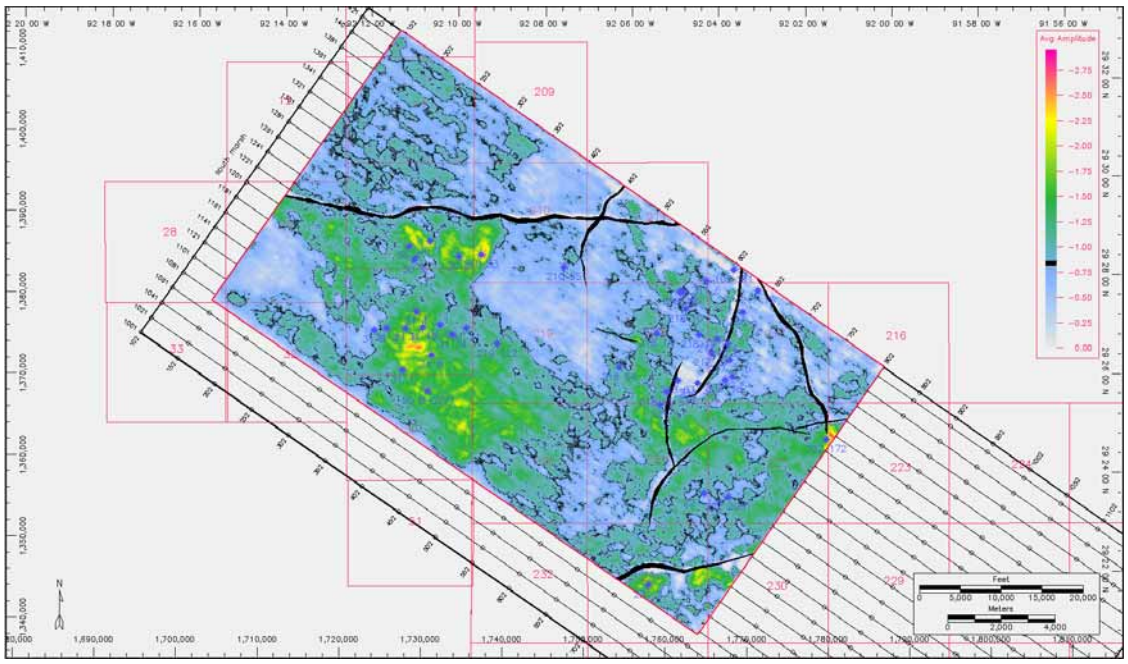

Figure 134. Average amplitude attribute map of the N-sand interval.

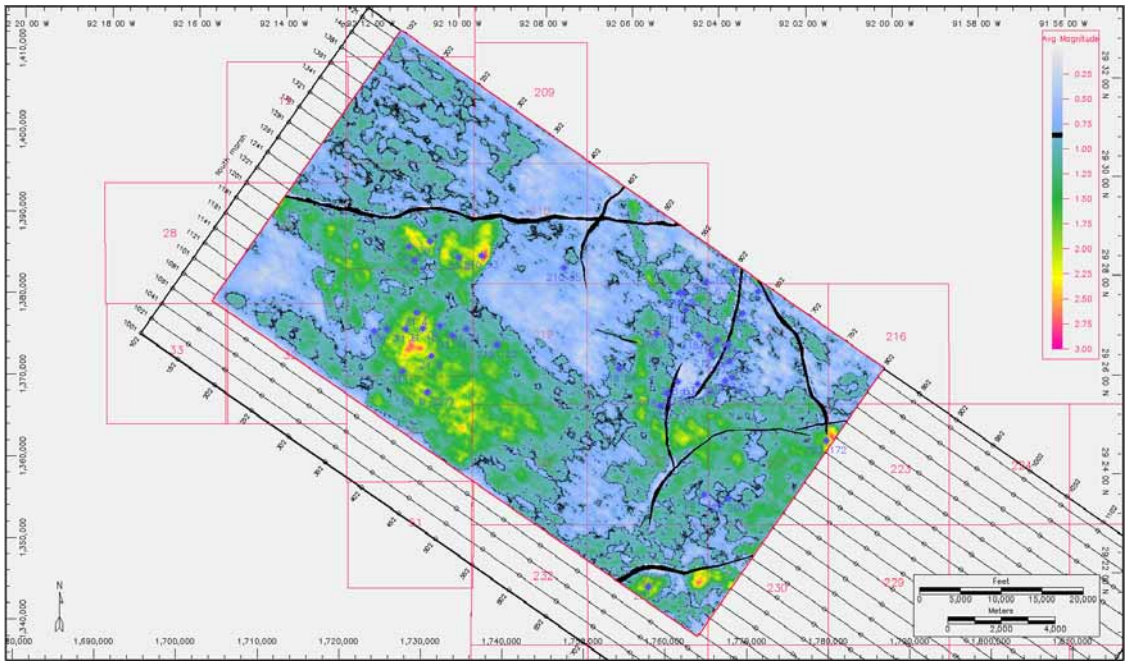

Figure 135. Average magnitude attribute map of the N-sand interval.

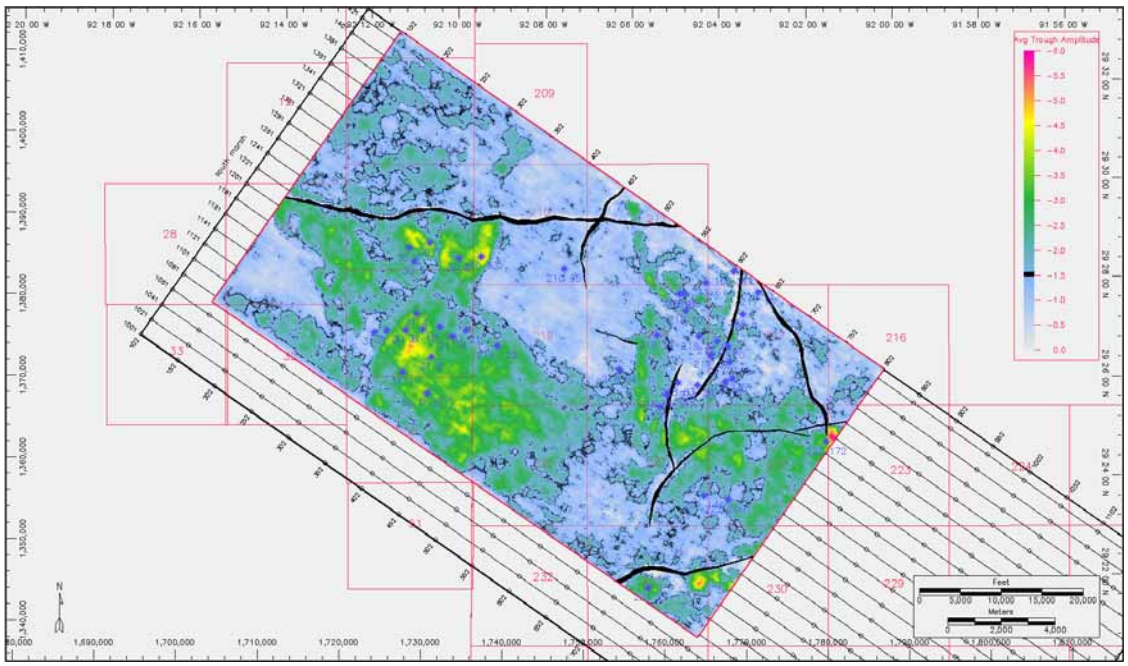

Figure 136. Average trough amplitude attribute map of the N-sand interval.

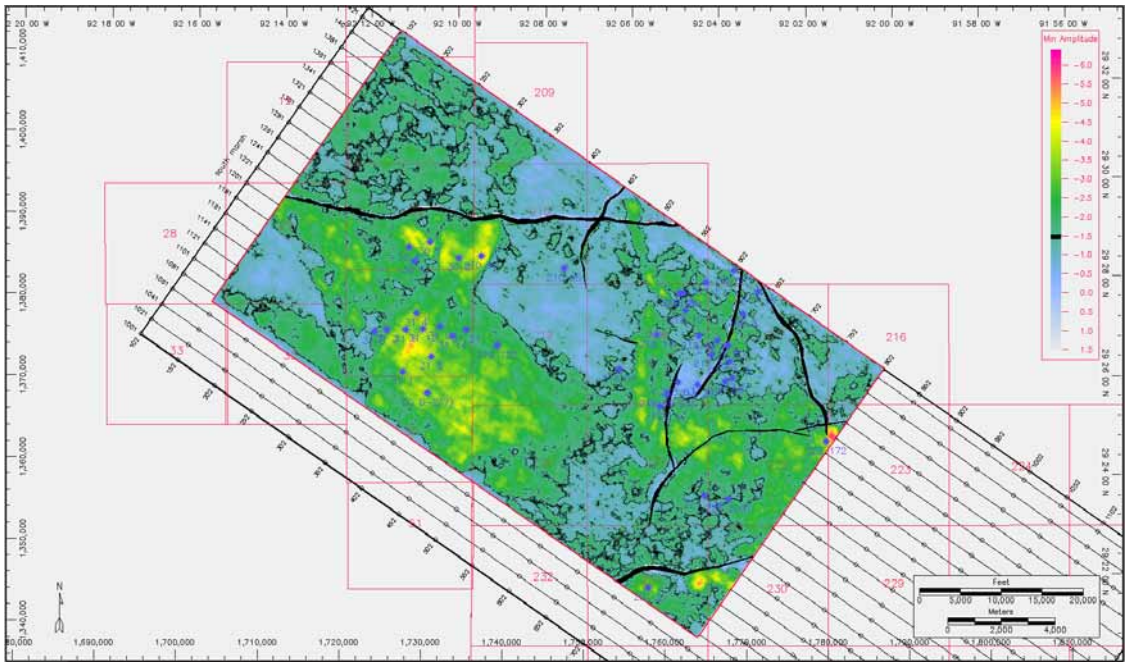

Figure 137. Minimum amplitude attribute map of the N-sand interval.

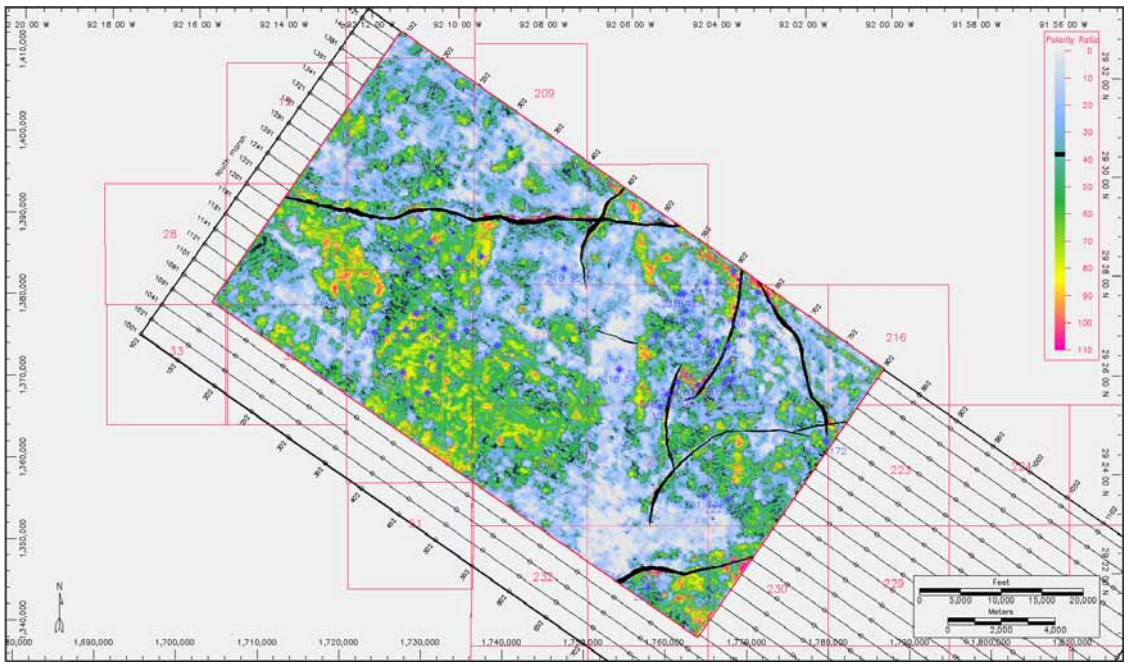

Figure 138. Polarity ratio attribute map of the N-sand interval.

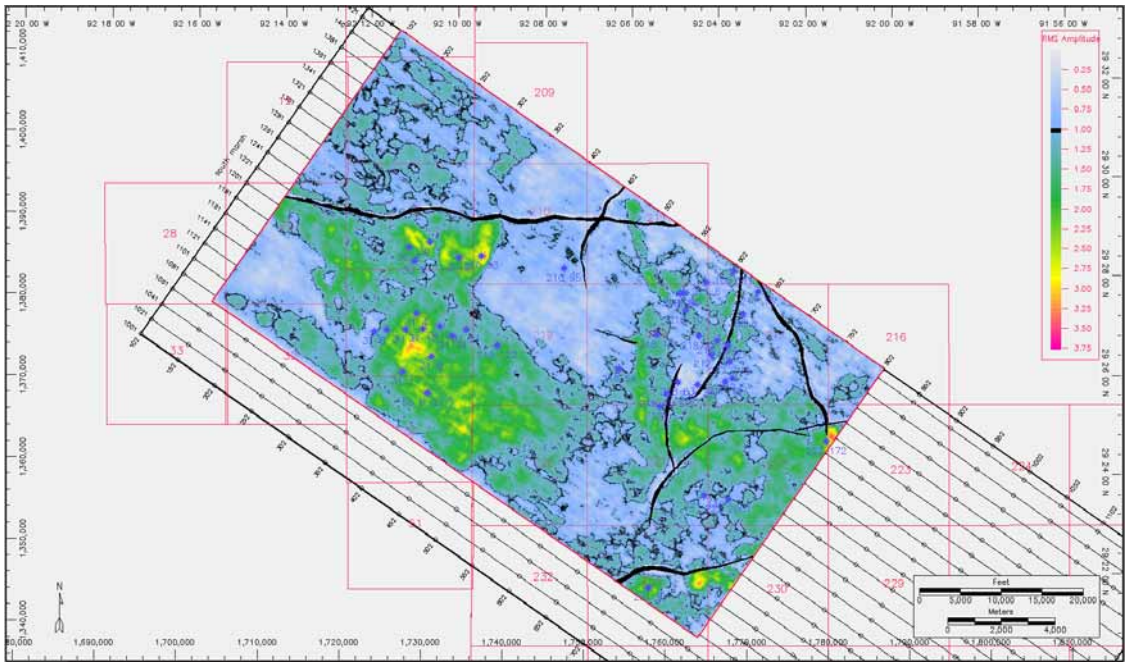

Figure 139. RMS amplitude attribute map of the N-sand interval.

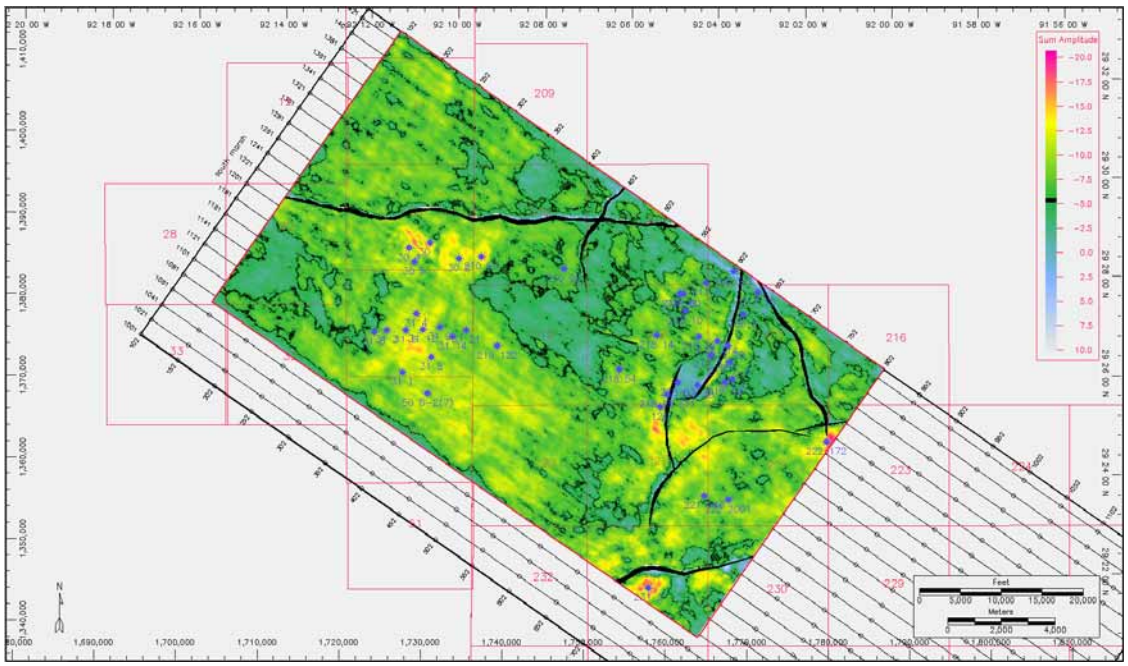

Figure 140. Sum of amplitudes attribute map of the N-sand interval.

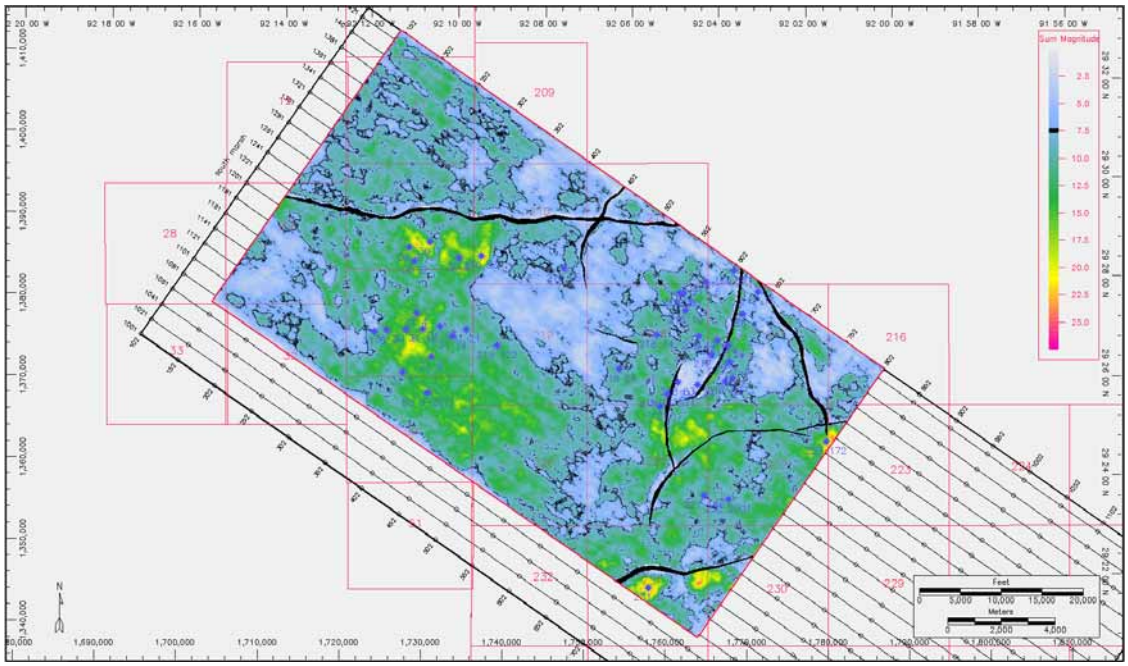

Figure 141. Sum of magnitudes attribute map of the N-sand interval.

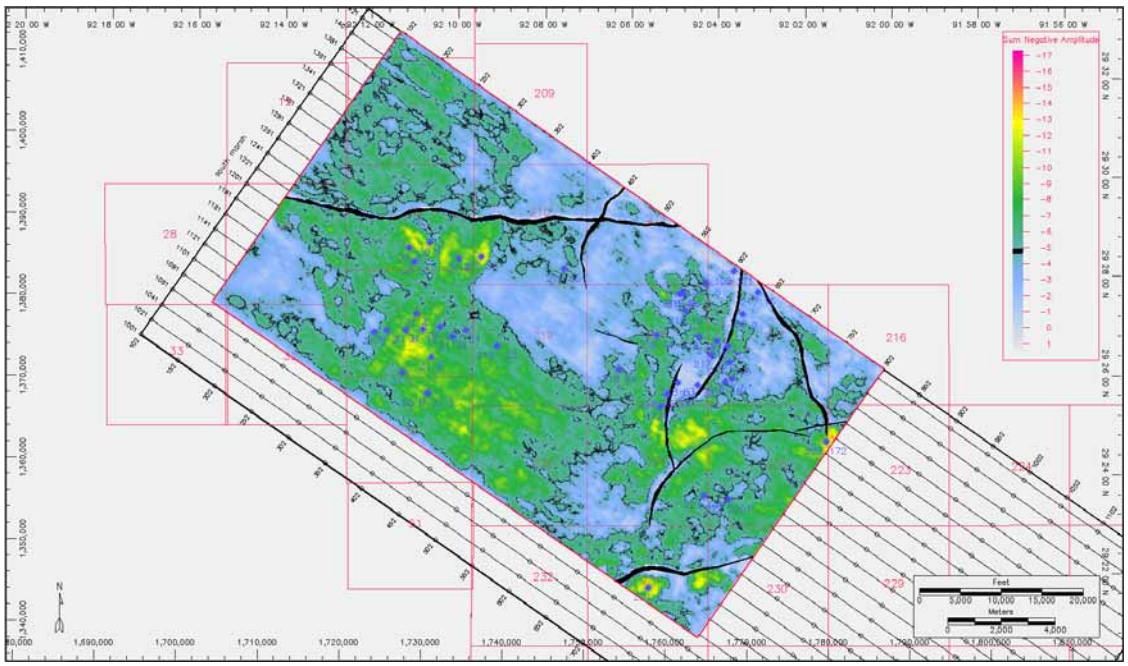

Figure 142. Sum of negative amplitude attribute map of the N-sand interval.

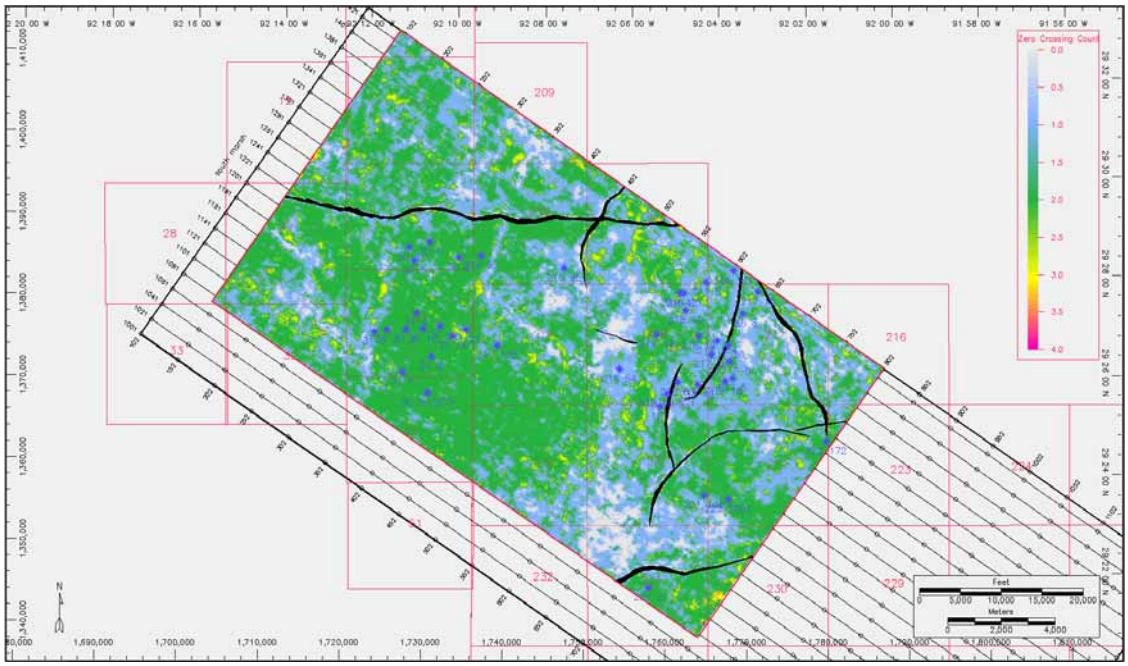

Figure 143. Number of zero crossings attribute map of the N-sand interval.

VITA

Rasheed Abdelkareem Jaradat was born in Amman-Jordan in 1970. He holds a Ph.D. in Geophysics from Texas A&M University (2004), M.S. in geology from Yarmouk University (1996), and B.S. in geology (major) and computer sciences (minor) from Yarmouk University (1992). During his Ph.D., he joined the Department of Geology and Geophysics at Texas A&M University as a geophysics graduate student with a focus on reservoir seismology. Concurrently, he served as a teaching assistant for a graduate class of interactive seismic interpretation. During the summers of 1998, 1999 and 2000, he worked for Schlumberger/GeoQuest, Houston-USA as a geoscientist intern in software commercialization group with respectabilities including testing GeoFrame Reservoir Characterization software, data preparation and management, documentation review, and writing test plans. Previously, he worked for United Arab Emirates Central Directorate of Education (1994-1996) as an instructor of geology. In summer 1997, he joined Halliburton Ltd., Abu-Dhabi-UAE as a trainee surface data logging engineer.

Jaradat is a member of the American Association of Petroleum Geologists, the Society of Exploration Geophysicists and the Jordanian Geological Association. He received the World Laboratory Scholarship, Lausanne, Switzerland (1999-2000), Houston Oil & Minerals Scholarship (1999), Chevron Oil Scholarship (2000), Yarmouk University Scholarship for his Ph.D. study at Texas A&M University (1998-2001), Honor Medal of Scientific Excellence, Yarmouk University (1996) and (1992).

Jaradat is currently working as a professor of geophysics at the Department of Earth and Environmental Sciences, Yarmouk University. His permanent address is:

Department of Earth and Environmental Sciences
Yarmouk University
Irbid-Jordan
Tel: 962-2-721-1111 ext. 2929
Mobile: 962-795-068-442
rasheedjaradat@hotmail.com